UNIVERSITY OF CAMBRIDGE

Photon-mediated entanglement of electron spins in a dynamic solid-state environment

Megan Jane Stanley

Clare College

This dissertation is submitted for the degree of Doctor of Philosophy
December 21st, 2016

Abstract

Self-assembled quantum dots can act as an interface between single spins and photons. They combine the flexibility and scalability of semiconductor systems with near-perfect two level systems, emitting highly coherent single photons. In potential quantum information processing architectures based upon optical networks, quantum dots permit light-matter coupling between matter qubits and photonic links. Single trapped charge carriers in quantum dots can be addressed optically, generating spin-photon entanglement between the matter qubits and 'flying' photon qubits, a key first step in creation of a network.

Such an optically linked network of spins in quantum dots has yet to be realized. The semiconductor environment presents a key challenge; it broadens the spectrum of the emitted light, which reduces the fidelity of schemes based upon photon exchange or interference. In addition, these quantum dots are subject to hyperfine coupling to a bath of $> 10^5$ nuclear spins. While this presents an opportunity to study the physics of a central spin in a spin bath, it degrades the spin coherence of a trapped electron or hole. The suggested gate operations to generate entanglement, and the spin measurements to verify a created state, rely upon photon detection. Thus a second limitation occurs due to low efficiency of detectors and photon collection probability. Recent developments in detector technology have enabled us to bring generation and verification of entangled states with quantum dots into the realm of possibility.

This dissertation begins with a detailed study of the interaction of a single electron spin with the solid state environment of the quantum dot, analysing the intensity noise of scattered light under resonant excitation to uncover the timescales and relative amplitudes of identified noise sources. A technique for rapid characterization of samples is presented, focusing in particular upon comparison of spectral broadening of the optical transitions relevant to a spin-photon interface.

Having identified the extent of environmental factors acting upon the quantum dots, we turn to a demonstration of photon-mediated entanglement between two distant electron spins using a probabilistic scheme. We are able to generate entangled states at 7 kHz, the fastest yet reported for photon-mediated protocols. The average state fidelity of the created Bell states is 63.5 ± 3.0 %., violating the classical limit by over 4 standard devia-

tions of the mean. In addition, we demonstrate full optical phase tuning of the Bell state $|\Psi\rangle = \frac{1}{\sqrt{2}}\left(|\uparrow\rangle|\downarrow\rangle + e^{i\phi}|\downarrow\rangle|\uparrow\rangle\right)$. This is a proof of principle experiment, and sets a fidelity benchmark upon which gains can be made by mitigation of environmental dynamics.

Declaration

This dissertation is my own work and contains nothing which is the outcome of work done in collaboration with others, except where specified in the text. This dissertation is not substantially the same as any that I have submitted for a degree or diploma or other qualification at any other university. This dissertation does not exceed the prescribed limit of 60 000 words.

Megan Jane Stanley
December, 2016

Acknowledgements

I am lucky enough to have been able to count upon a great many supporters, friends and family alike, whom I wish to acknowledge and thank.

First of all, I am greatly indebted to my supervisor Mete Atatüre for all of the support and guidance given to me over the years. Mete fosters an environment of enthusiastic discovery, and encourages us all to work to the highest standard, take on challenging experiments, and persevere in the face of apparent disaster. He also ensures that we have fun at the same time. Mete's commitment to doing things differently means that I can count 'performing physics experiments in a field at a music festival' amongst the experiences of my PhD, and I am glad to do so.

Special thanks go to our postdoctoral researcher Claire Le Gall, not only for being a wonderful working companion in the laboratory and mentor in general, but for her support during the writing of this dissertation and dedicated proofreading. I also wish to thank Clemens Matthiesen for his patient teaching in my early days as a PhD student, and for working with me on the analysis of resonance fluorescence noise. Clemens laid many of the foundations for the work in this dissertation and his expertise regarding everything in the laboratory was essential to our progress.

The experiments described in this work were challenging, and required a number of team members. I want to acknowledge the incredibly hard work of the quantum dot team in bringing entangled states of electron spins from an idea to reality. Both Claire and Clemens were essential to these efforts, and guided the less experienced of us through this complex task. Robert Stockill developed our ability to optically rotate electron spins, to put together optical pulse sequences and integrate the disparate parts of the experiment. It would simply have been impossible to have made it through what turned out to be over a year of hard work on the experiment without his cheery demeanour, extreme perseverance, and excellent musical tastes. Lukas Huthmacher developed the acquisition and analysis of the resulting enormous quantities of data, and without his contribution we would have foundered, so we are all very glad that he took the challenge on! I am very grateful to have worked as part of such an excellent team.

I also wish to thank the previous group members with whom I have worked: Carsten

Schulte, Jack Hansom, and Paul Geller. Studying quantum dots in this laboratory has been to work with colleagues in a constant state of good humour and enthusiasm.

Thanks go to all of my colleagues, old and new, for making this group an inspiring and enjoyable place to work. I must include thanks to Helena Knowles, Benjamin Pingault, Joshua Barnes, Dhiren Kara, Carmen Palacios-Berroquero, Jan Beitner, Mustafa Gündogan, Camille Stavrakas, Tina Müller, Jeff Holzgraffe, Matteo Barbone, Alejandro Rodriguez-Pardo Montblanch, David-Dominik Jarausch, Lucio Stefan, and our latest quantum dot team members Dorian Gangloff and Gabriel Éthier-Majcher.

I also would like to thank my long-time mentor Richard Phillips for well-timed coffee with a side of sage advice in my early days as a PhD student.

To Stephen Topliss for all of the contributions to our suite of custom-made electronic equipment, many thanks are due. Also, special thanks go to Pam Smith, our group administrator, who keeps the entire group running smoothly with incredible efficiency.

Finally, my love to to all of my friends and family for the support they have shown me, and for putting up with times when I have been very busy over the past few years.

Contents

1 Introduction **17**

1.1 Quantum entanglement 19

1.1.1 Entangled states as a resource in computation, communication and metrology 20

1.1.2 Experimental generation of entangled states 22

1.2 Self-assembled quantum dots 25

1.2.1 Energy levels, selection rules and excitons in quantum dots 25

1.2.2 Photoluminescence, charge tuning and quantum-confined Stark effect of quantum dots 28

1.2.3 Single trapped electrons in quantum dots 30

1.2.4 Device design and heterostructures 32

1.3 Resonance fluorescence in theory and in practice 33

1.3.1 Two and four-level systems interacting with light 34

1.3.2 Scattered light intensity and correlations of resonance fluorescence . 37

1.3.3 A resonance fluorescence microscope 39

2 The solid-state environment of a quantum dot **42**

2.1 Electron spin-nuclear spin interactions and nuclear spin dynamics 43

2.1.1 The hyperfine interaction 43

2.1.2 Mean field approach to nuclear spin bath 44

2.1.3 Nuclear spin bath dynamics 45

2.2 Sensitivity of a quantum dot transition to electric and magnetic field fluctuations 48

2.3 Resonance fluorescence fluctuation spectroscopy 51

2.3.1 Unambiguous discrimination of magnetic field noise 54

2.4 A quantitative model of electric- and magnetic-field fluctuations 57

2.4.1 Application of the model to electric-field-related bunching amplitudes 60

2.5 Power dependence of nuclear-spin correlation times 63

2.6 Further discussion . . . 65
2.6.1 Identification of noisy samples . . . 65
2.6.2 Comparison to quantum dot hole spin behaviour . . . 66
2.6.3 Summary . . . 67

3 Photon counting statistics: a technique for rapid QD characterization 70
3.1 Diffused Poisson distribution model . . . 70
3.2 Application of the model to quantum-dot histograms . . . 75
3.2.1 Limitations of photon-counting analysis . . . 77
3.3 Survey of photon counting statistics . . . 81
3.3.1 Power dependence of spectral diffusion . . . 81
3.3.2 Comparison of QDs . . . 83
3.3.3 Spectral switching . . . 83
3.4 Conclusion . . . 85

4 An entangled state of two electron spins 87
4.1 Photon-mediated entanglement schemes . . . 88
4.2 A single-photon detection scheme . . . 90
4.3 Indistinguishable photons from two quantum dots . . . 94
4.3.1 Ramsey interferometry . . . 95
4.3.2 Hong-Ou-Mandel interferometry . . . 97
4.4 An optical entanglement-generation machine . . . 100
4.4.1 Spin read-out . . . 105
4.4.2 Optical spin rotation . . . 106
4.4.3 Two-photon correlation measurements . . . 106
4.5 Results of two-spin state measurement . . . 108
4.5.1 Measurement in the population basis . . . 108
4.5.2 Measurement in an orthogonal basis . . . 110
4.5.3 Fidelity of created states . . . 113
4.5.3.1 Limitations to state fidelity . . . 113
4.6 Discussion and conclusions . . . 115

5 Entangled state control through optical phase tuning 119
5.1 Phase of the entangled state: optical-path-length mapping to a spin state . 119
5.1.1 Phase noise of the scattered photons and the entangled state . . . 122
5.2 Phase-stabilization of a fibre-based interferometer . . . 124
5.2.1 Homodyne measurement of phase noise . . . 126
5.2.2 Characterisation of phase reference detection . . . 127
5.2.3 Phase stabilisation performance . . . 128
5.2.3.1 Phase stabilisation at quantum dot frequencies . . . 130
5.2.3.2 Setting the zero-delay point of the interferometer . . . 130

5.3 Phase-controlled interference of elastically scattered photons 132
5.4 Larmor frequency variation 136
5.5 Phase-controlled measurements: a tunable two-electron spin-entangled state 139
5.6 Conclusions: phase tunable entanglement generation. 142

6 Conclusion **145**

Bibliography **151**

List of Figures

1.1 The band structure of strained InGaAs and neutral excitons in quantum dots. . . . 26
1.2 Charge tuning of a quantum dot in a diode structure. . . . 29
1.3 Ground and excited states of single trapped electrons. . . . 31
1.4 The full sample structure of quantum dot devices. . . . 33
1.5 Energy levels in two and four-level description of resonance fluorescence. . . . 36
1.6 A cryogenic resonance fluorescence experimental set-up 39

2.1 Fluctuations in time resolved resonance fluorescence 48
2.2 Sensitivity of the X^{1-} transitions to noisy electric and magnetic fields. . . . 50
2.3 Resonance fluorescence autocorrelations 52
2.4 Detuning-dependent bunching decay amplitudes 53
2.5 Subtraction of systematic background from QD RF autocorrelations 55
2.6 Unambiguous discrimination of magnetic field noise 56
2.7 Model of X^{1-} interacting with the Overhauser field 57
2.8 Absorption lineshape of two and four-level systems. . . . 59
2.9 Radiative lifetimes of QD A, B and C 60
2.10 Fit of four-level electric field noise model to bunching amplitudes. . . . 61
2.11 Power dependence of nuclear spin correlation times 63
2.12 Autocorrelations from an alternative sample. . . . 65

3.1 Influence of spectral diffusion on resonant photon counting statistics 74
3.2 Fitting quantum dot resonance fluorescence histograms using full counting statistics. . . . 75
3.3 Fitting quantum dot resonance fluorescence histograms using full counting statistics - errors 76
3.4 Signatures of electric field fluctuations in photon counting histograms with varied detuning 78
3.5 Summary of spectral diffusion width for QD C X^{1-} 79
3.6 Summary of spectral diffusion width for QD C X^{0} 80

3.7 Identification of noise timescales for QD C. 81
3.8 Electric field noise in QD Q. 82
3.9 Comparison of spectral diffusion widths for three QDs 83
3.10 Identifying spectral jumps through the photon statistics 85

4.1 Schematic of the single-photon detection scheme. 91
4.2 Radiative lifetime measurements of QD A and QD B. 94
4.3 Intensity autocorrelation measurements for QDs A and B. 95
4.4 Ramsey interferometry of a single electron spin. 96
4.5 Ramsey interferometry of QD A and QD B 97
4.6 Hong-Ou-Mandel indistinguishability measurement for photons scattered from QD A and QD B. 98
4.7 Zero time delay of HOM measurement, detail. 99
4.8 The experimental realization of the Cabrillo scheme. 101
4.9 An entanglement generation and confirmation pulse sequence. 102
4.10 Experimental arrangement of the pulse sequence. 103
4.11 Detection of entanglement pulse sequence. 104
4.12 Optical spin read-out of a single quantum dot. 105
4.13 Optical electron spin rotation; Rabi oscillations. 107
4.14 Two-photon correlations during the pulse sequence. 108
4.15 Population basis measurement of generated two-spin state. 109
4.16 Two-photon correlations during the pulse sequence, measurement in rotated basis. 110
4.17 Measurement of entangled state creation in a rotated basis. 112
4.18 Comparison of results to current literature reports. 115

5.1 Schematic of phase origin in single-photon detection scheme. 120
5.2 Experimental phase stabilization and control. 125
5.3 Two-cryostat Mach-Zehnder interference detected on a fast photodiode. . . 127
5.4 Reponse of pulse counters to single APD inputs. 128
5.5 Phase stabilization before an entanglement measurement 129
5.6 Phase stabilization of the Mach-Zehnder interferometer. 129
5.7 Phase stabilization at quantum dot frequencies. 130
5.8 Setting the zero delay path of the interferometer. 131
5.9 Two QD Rayleigh photon interference in the unstabilized interferometer. . . 133
5.10 The phase of quantum dot resonance fluorescence in a stabilized interferometer. 135
5.11 Variation of Larmor frequencies: QD C Ramsey interferometry. 137
5.12 QD A Larmor frequency variation with gate voltage. 137
5.13 Investigation of Larmor frequency variation. 138
5.14 Two electron spin measurements in the rotated basis; full phase tuning. . . 140

5.15 Summary of the phase-tunable entangled states. 141

Chapter 1

Introduction

The longstanding dream of a new paradigm in technology, where quantum mechanical effects are harnessed to enhance current capabilities or permit entirely new approaches to communication and computation, has resulted in an ongoing search for physical systems that meet strict requirements. It is necessary for any physical representation of an abstract 'qubit', that is to say a bit of a quantum computer, to be sufficiently isolated from decoherence through interaction with the environment. However, a qubit must also couple strongly enough to specific channels that it can be controlled and measured by classical technology [1]. Thus far there are numerous avenues of enquiry regarding potential physical systems that can contain or represent qubits [2], or present enhanced sensing capabilities, including but not limited to: trapped ions and atoms [3], defect centres in both bulk and nano-sized diamond [4–6], single dopant atoms in silicon [7], a range of superconducting qubit architectures [8], single photons [9], metallic gate-defined quantum dots [10], and the system of interest in this work, single self-assembled quantum dots in GaAs.

Self-assembled quantum dots combine the flexibility and scalability of semiconductor systems with all optical access and control. The optical properties are 'atom-like', where emission is spectrally narrow or highly coherent, much like that of an ideal two-level system [11]. In addition, these quantum dots can be processed into diode structures to allow discrete charge control and electrical tuning of energy levels [12], and as such single charge carriers can be trapped. These charge carriers can be addressed optically due to their position as the ground state in allowed dipole transitions. In an applied magnetic field, the charge carriers can have well-defined spins that can be optically pumped and measured [13, 14]. More recently, all-optical coherent control of a trapped single electron spin has been demonstrated [15], permitting detailed study of the coherence properties of the electron spin [16, 17]. In general, this type of quantum dot is a promising light-matter interface for use in quantum optical networks [18], and many steps have been made in this direction including entanglement of ground state spins with emitted photons [19–21].

Applications in quantum networks of more than one matter qubit require the photonic 'flying-qubits' to be spectrally consistent, and the coherence of the spins themselves fundamentally limits the timescale available for any computational operations. However, the trapped spins and the optically excited states in InGaAs quantum dots are necessarily subject to the solid-state environment. The spectra of quantum dots are known to wander [22], which if more than one emitter is in use is detrimental to protocols relying upon mutual indistinguishability. Likewise, all of the atoms ($N \sim 10^5$) in a quantum dot have non-zero nuclear spin and as such a single trapped charge is sitting in a fluctuating magnetic field due to the hyperfine interaction [23]. The effects of this are observed in the coherence of the electron spin [24] as well as in the emitted resonance fluorescence [25].

In this dissertation, we study the impact of the solid-state environment through the signature it leaves in resonance fluorescence. In doing so we wish to elucidate some of the mechanisms by which the environment influences our spins and optical transitions, and also quantify the impact such that comparisons can be made between samples. A technique based upon photon statistics provides a rapid and robust way of doing so, so as to identify samples with the minimal spectral diffusion of those available to us. With knowledge of these limitations, we demonstrate that it is possible to create an entangled state of distant electron spins in single quantum dots. We use a single photon detection method which permits tuning of the precise state we create, and we generate an entangled state with the fastest rate reported thus far.

To this end, in Chapter 2 we present a detailed study of the semiconductor environment of our quantum dots and in particular the interaction of the nuclear spin bath with a single trapped electron spin. This study utilises the technique of resonance fluorescence to perform noise spectroscopy. A useful method of magnetic and electric field noise differentiation is presented, and in addition a model of the noise amplitudes allows us to quantify the environmental magnetic and electric fields operating on the single electron system. In particular, we find evidence for electron-dependent dynamics of the nuclear spin bath. This work is presented in publication in Reference [26].

In Chapter 3, a method for rapid characterization of the dominant electric field noise is developed and applied. We use a model of spectral diffusion applied to photon counting statistics in resonance fluorescence. The model is useful in comparing systems and we are able to identify particular interesting cases such as clear spectral switching. This work is published in Reference [27].

A first demonstration of entanglement between electron spins confined to distant semiconductor quantum dots is presented in Chapter 4. We assess whether the quantum dots meet basic requirements, and outline the experimental protocol. We present two-electron spin correlations measured along two orthogonal axes, and show the distribution of entanglement between two spins with a repetition rate of ≈ 7 kHz. The single-photon detection protocol we use allows for phase tuning of the state, and thus in Chapter 5 we discuss the impact of environmental noise on our scheme, how we monitor the phase, and achieve

phase stability. We are able to present entangled states with fully tunable phase.

For the remainder of this introduction, we outline key ideas and sample details to form a necessary background for the remainder of the work. The concept of entanglement, its potential uses, and to date experimental realizations are discussed in Section 1.1. In Section 1.2 we give a description of quantum dots, and introduce the excitonic species we are interested in, as well as the sample design. In Section 1.3 we outline a simple theoretical picture of resonance fluorescence, as it is particularly useful for the discussion of the model in Chapter 2 and a necessary spectroscopic tool throughout. The introductory material is finished by an outline of the basic methods used to access photonic, electrical, and magnetic field control of the quantum dot in a bath cryostat at 4.2 K.

1.1 Quantum entanglement

A key resource in quantum computation is the presence of quantum entanglement between separate components. In general, an entangled state of two or more qubits is one which cannot be separated simply into a product state [28]. An implication of this is that even if two qubits are separated in a space-like manner, a measurement of one qubit necessarily determines the outcome of a measurement upon the other. Initially, this was taken to suggest that quantum mechanics could not be a complete description of reality; famously, Einstein, Podolsky and Rosen suggested that there must exist 'hidden variables' that predetermine the state of every qubit, such that the states are 'real' in the sense of existing prior to a measurement. Therefore, any information regarding the state must be held local to the qubit itself [29]. Entangled states violate this concept of *local realism* by allowing the observation of a distant qubit to set the state of a nearby qubit, where prior information regarding this observable is not available independently of this other system. Bell demonstrated that local hidden variable theories were incompatible with the predicted statistical outcomes of measurements in a universe run on quantum mechanics [30], the result of which is often termed 'Bell's inequality'. If Bell's inequality is satisfied, it cannot be said that local realism is violated. This was reformulated by Clauser-Horne-Shimony-Holt [31], and indeed many other such tests used in experiments exist.

In a real, local universe, locality is imposed by requiring the result of a measurement of one system to be independent of a system with which it cannot classically communicate. Realism permits measurements with two non-commuting observables that repeatedly return the same results, suggesting that the system has some 'real' underlying value of a parameter. In quantum mechanics, one cannot measure a qubit with two incompatible operators in this way; eigenstates of these operators are not simultaneous and measurement of one observable will project the state into a superposition of eigenstates of the other operator. As a simple example, if one measures a photon's polarization in a 'vertical-horizontal' basis the photon is now in a superposition from the perspective of a 'diagonal' polarization measurement. Realism, however, argues that there is a polarization of the

photon that exists for all time, where the measurement does not generate 'collapse' of the wave-function onto an eigenstate of the measurement operator.

In this work, we aim to create maximally entangled states of two qubits as a starting point for more complex entangled networks. Maximally entangled states are those where, having undergone a partial trace over the density matrix for one component, the remaining density operator is proportional to the identity. In other words, there are no parts of the state for which the qubits are independent of each other and can be written as additional components with their own 'private' coherences. The maximally entangled states for two qubits, here called A and B, are the Bell states and are written:

$$|\Psi\rangle_+ = \frac{1}{\sqrt{2}}\left(|1\rangle_A|0\rangle_B + |0\rangle_A|1\rangle_B\right), \tag{1.1a}$$

$$|\Psi\rangle_- = \frac{1}{\sqrt{2}}\left(|1\rangle_A|0\rangle_B - |0\rangle_A|1\rangle_B\right), \tag{1.1b}$$

$$|\Phi\rangle_+ = \frac{1}{\sqrt{2}}\left(|0\rangle_A|0\rangle_B + |1\rangle_A|1\rangle_B\right), \tag{1.1c}$$

$$|\Phi\rangle_- = \frac{1}{\sqrt{2}}\left(|0\rangle_A|0\rangle_B - |1\rangle_A|1\rangle_B\right). \tag{1.1d}$$

In Chapters 4 and 5 of this work we shall demonstrate generation of the states Ψ_+ and Ψ_- where our two qubits are the electron spins trapped in quantum dots.

1.1.1 Entangled states as a resource in computation, communication and metrology

Initial experiments focused upon whether or not quantum mechanics is a good description of reality, that is, whether Bell's inequality could be violated. Alain Aspect et al. [32] provided a demonstration of the invalidity of hidden-variable theories with polarization-entangled photons. The measurement operators could be switched during the time of flight of the photons to ensure the state was not predetermined, and measurement occured at points with sufficient separation that information could not be communicated classically between them while the measurement was being performed.

There are loopholes in such experiments including locality (the two systems are never space-like separated which could theoretically permit information transfer between them), and detection (discarding events that are not detected may allow selection of a biased subset which violate the inequalities, when all events taken together do not). These two could not be simultaneously closed until the demonstration of distant entanglement between two electron spins in nitrogen-vacancy defects in diamond [33]. In particular, this closed the detection loophole because the method for obtaining entanglement satisfied the so-called 'event-ready' requirement of Bell, whereby some signal is available that tells the observer for which trials a Bell state was successfully created, and therefore which trials can be fairly discarded with no biasing of the results [34]. Additionally, there exists a

cycling transition which enables the spin to be read out in a 'single-shot' fashion with high detection efficiency [35].

Following these experiments, it is generally accepted that quantum entanglement is 'real' and we turn instead to the question of how it can be used as a resource in future technologies. Entanglement is fundamental to quantum computation [36], and underpins the quantum computing algorithms that are known to allow a speed-up of computation time over their classical counterparts [37, 38]. For example, one of the most famous of these is Shor's algorithm for factoring numbers [39], which if realized would enable decryption of currently secure communications. In addition, it may be possible to make computation robust against local single-qubit errors by using entanglement, as the information is encoded in the entangled state distributed over several qubits rather than at an individual site [40, 41].

Entanglement may also play a useful role in quantum communication [42, 43], although the famous BB84 protocol [44] does not rely upon entanglement but simply upon the inability to measure two incompatible observables and the collapse of the wave-function upon measurement. However, it is possible to increase the security of very similar protocols by creating entangled states between the two communicating parties [45]. For example, the security of a channel can be ascertained by checking for the presence of the shared Bell states; any eavesdropper destroys the state and alerts the users to their presence [46]. Such protocols have already been implemented experimentally [47–49].

The measurement and distribution of Bell states has important consequences for another use of entanglement: quantum teleportation [50]. Quantum mechanics does not allow a quantum state to be cloned [51], and state cloning would permit direct violation of universal principles. For example, cloning would allow incompatible observables to be measured simultaneously by observing each on a different identical copy of the state. In fact, it would also allow for super-luminal communication, were one of the constituent qubits of a Bell state (qubit 'B') to be cloned multiple times. Following a measurement of the qubit 'A', 'B' could be completely determined, which gives information about the measurement basis used on qubit A through its action on the total entangled state. Consequently, information regarding the *choice of measurement* is transmitted faster than the speed of light. It is undoubtedly a disappointment to science fiction authors (and their fans) everywhere that quantum mechanics forbids such work-arounds of the universal speed limit.

Quantum teleportation in reality is a way of sending a quantum state from *here* to *over there* through a classical channel. An entangled state is distributed between sender and receiver, and the sender measures the qubit to be transferred and the local component of the Bell state together, determining the maximally entangled state these two qubits represent. Classical communication of this information allows the receiver to transform the qubit they hold into the original qubit. There are two main challenges of such protocols: the sender has the challenge of determining which Bell state is present with complete certainty in a single measurement, which we are not going to tackle here. The other

challenge, that of how to produce and distribute an entangled state, we will focus upon in the latter half of this work as it is generally applicable to a wide range of applications.

In addition to quantum communication and information processing there is also the possibility of improved metrology [52]. For example, the input into a Mach-Zehnder interferometer of an entangled state of light allows the Heisenberg limit of uncertainty to be reached in phase estimation [53, 54]. A natural extension is improving estimates of atomic transition frequencies within optical clocks [55, 56]. With entangled states of light it is also possible to improve the resolution of optical imaging and lithography beyond the apparent Rayleigh diffraction limit [57–59]. However, here we focus specifically upon building networks of entangled nodes.

1.1.2 Experimental generation of entangled states

The first demonstrations of entangled states were photonic, where polarization-entangled photons can be produced during atomic decay cascades [60], or in photon down-conversion processes [61]. Generating bright sources of entangled photons has been a recent area of much research; in InGaAs quantum dots the decay of the biexciton creates polarization-entanglement [62–64]. Alternatively, ambiguity regarding the time bin in which photons are created produces time-bin entanglement [65]. The advantage of an atom-like entangled photon source is that only one excitation can be achieved at a time and therefore the emission is anti-bunched; they are a good source of single entangled photon pairs.

While photons are very good 'flying qubits', being rather weakly interacting with the environment, they are difficult to store for long periods of time and do not directly interact with each other. Quantum states cannot be stored in photons to be manipulated when it is convenient. It appears that some use of matter qubits is necessary to have quantum memories. There are methods to enact computation entirely with the use of photons via linear optics, with phase shifters and beam-splitters between a number of modes, relying finally upon the detection of a large number of photons [9]. However, it has been shown to require five orders of magnitude more components than a matter-based processor performing the same protocol [66].

The requirements of a quantum computer were stated by DiVincenzo as: a well-defined and scalable qubit register, where states can be reliably prepared and projectively-measured. There must be an accurate, universal set of gate operations and in addition, the decoherence time of the qubits must be much longer than the gate operations [1]. In general these are well met by trapped ions and atoms in optical lattices [3, 67] under optical control. In addition, single trapped ions and atoms are isolated from their environment and so maintain the coherence of the quantum state over the time of many qubit operations. Entanglement can be created between adjacent ions in a trap, for example, by using shared motional excitations in the harmonic potential to mediate a CNOT operation [68–70]. Such a phononic link enabled the first demonstration of entangled states of matter [71]. Shor's algorithm was originally demonstrated using magnetic resonance of

the nuclei of an organic iron complex [72], but ion-trap technologies have advanced and factorization of 15 was demonstrated with a total of eleven qubits very recently [73].

Likewise, controlled interactions between adjacent gate-defined semiconductor quantum dots, with qubits defined as singlet and triplet states of the electrons shared between the dots [74], have allowed entanglement of two adjacent double quantum dot systems [75]. The states are relatively weakly coupled with the environment so that decoherence times can be extended to hundreds of nanoseconds with Hahn-echo pulse sequences. However, the material in use is GaAs in which it is difficult to avoid the impact of nuclear spins. The influence of nuclear spins on our self-assembled quantum dots will be discussed in Chapter 2.

Such direct interaction entanglement operations work well, and forms of quantum computing based upon large two-dimensional arrays of nearest-neighbour interacting qubits have been envisaged [76]. However, it is a practical challenge to place very large numbers of qubits adjacent to each other and obtain all qubits functioning perfectly. Therefore, the concept of optical networks is attractive because it provides great flexibility in qubit arrangement [18].

In an optical network matter qubits sit at nodes, which store quantum information and permit manipulation and measurement of states. Optical interconnects are created between the nodes, not merely functioning as classical communication links, but rather transmitting quantum information. In this way, instead of a series of small quantum processors each performing small scale computation, there can be one large quantum processor distributed over many sites. An example system in which this could be carried out is an array of ion traps each containing a few ions [77]. A challenge of optical networks is how to reliably distribute entanglement between nodes where collection of photons from single emitters is limited by the effective numerical aperature of the collection optics, and photons are absorbed by fibres and other optical elements.

One approach relies upon cavity QED, where a single atom interacts strongly with a specific photonic mode of a cavity. The mode leaks out and is then able to enter without reflection another cavity, and may be mapped directly onto the same mode present there [78, 79]. By combining strong light-matter interaction with spin-photon entanglement between an atom in the cavity and a photon [80], the atoms within two cavities can be deterministically entangled [81], constituting a demonstration of the basic building blocks of a quantum network.

Cavity systems may be difficult to scale due to their size in current iterations, and the schemes rely upon strong cavity coupling to the atom-like system in order to be deterministic. In this work, we shall explore the implementation of an alternative approach, that of probabilistic entanglement generation [82] where detection of one or more photons creates the state, thus heralding its existence. However, to distribute entanglement across a network requires more than one probabilistic step, or in other words one must wait for more entanglement heralds to arrive. In the meantime, it must be possible to have stored

the state created in the previous step. Therefore, such schemes require the memory at the nodes to be longer than the time interval between the pairwise entanglement-generation events. In general this time is limited by photon-collection efficiency, and is further increased by schemes which do not scatter the state-projecting photons with unit probability as is the case in the work presented here. Increasing the entanglement generation rate is essential to making such schemes a viable option, as an entangled network must be generated must faster than the created state decoheres. By relying upon interference of photons from separate systems, we also require that the photons emitted by all components are spectrally narrow and therefore can well overlapped at all times in order to generate entangled states with high fidelity.

To create an entangled state of two spins, we require the key ingredients of generation of highly indistinguishable photons from two separate systems, spin initialization and read-out, and a well as a method of coherent spin rotation in order that the entangled state can be verifed. In quantum dots the tools of spin initialization and read-out are provided by the optical transitions of the singly charged exciton species X^{1-} and X^{1+}, which additionally permit entanglement of the state of an emitted photon and the ground state spin [19–21]. However despite having been studied for over 15 years, entanglement was only recently achieved for hole spins in QDs [83]. For the quantum dot community, a critical limiting factor in generation of an entangled state and subsequent verification is that in the configuration required for coherent spin rotation we do not have access to single-shot read-out of the spins. This has prevented us so far from achieving a verified entangled state because the rate at which confirmed events could be generated would be impractically slow. Now, we have single-photon detectors with efficiencies exceeding 80 % due to new superconducting nanowire technology. In a protocol based upon single-photon heralding, two additional photons must be detected to verify the state; one from each spin. Therefore, with an example increase of a factor 4 in the photon detection efficiency afforded by these detectors we should gain a factor of 64 increase in the rate of verified entangled state production.

With the tools to achieve entanglement generation now available, we attempt to entangle two electron spins in two separate quantum dots in this dissertation. Another critical limitation is due to the quantum dot placement in a solid state system. Quantum dots are well known to emit high rates of single photons but it has long been apparent that they suffer from significant spectral wandering [22], which degrades the indistinguishability of photons so critical for the fidelity of any entangled state. In addition, they are subject to the nuclear spin bath inherent to InGaAs, which creates a fluctuating effective magnetic field. The challenges of working in a complex solid state environment must be recognized and mitigated if we are to understand what limits the fidelity of a spin-spin entangled state of two electrons and improve it to reach a useful value.

We shall examine the impact of the solid state environment on quantum dots, paying particular attention to the electron spin and X^{1-} species necessary for entanglement gen-

eration. In addition, we present a method to compare the spectral diffusion that occurs within different samples, which can act as feedback in growth and in choice of samples. We aim to demonstrate an entangled state of two electron spins, where we use knowledge of the environment dynamics to inform the details of how the experiment must be performed. In addition, obtaining quantitative knowledge of the noise processes impacting our sample and therefore entangled state will allow us to set a fidelity benchmark; improvements to the solid state environment with regards these measured parameters should increase the fidelity of our created state.

To this end, we now turn to an introduction of the basic semiconductor properties of quantum dots, the devices that have been developed to permit charge control and energy level tuning, and the energy levels under magnetic field that allow optical spin control, read-out and initialization.

1.2 Self-assembled quantum dots

1.2.1 Energy levels, selection rules and excitons in quantum dots

Self-assembled InGaAs quantum dots (QDs) form as islands of $In_xGa_{1-x}As$ on a GaAs substrate. During molecular-beam-epitaxy (MBE) growth of InAs onto GaAs, the lattice mismatch is initially accommodated by the new layers, but at a point of ≈ 1.5 monolayers, collections of In-rich alloy assemble in an energy-minimizing step [84]. This is called the Stranski-Krastonov growth mode and its use is not unique to InGaAs; it is the growth method for a whole range of III-V semiconductor quantum dots to very high quality, ideally free of crystal defects.

The resulting QDs are described as 'lens-shaped' being approximately 20 nm in diameter and 5 nm along the growth axis. Confinement of carriers is created by the reduced band gap within the quantum dot as compared to the surrounding GaAs crystal. However, before expanding upon the details of the single carrier states within a quantum dot it is useful to look at the underlying semiconductor physics of the material.

In InGaAs it is necessary to take account of spin-orbit coupling of the electron; there is an additional term in the electronic Hamiltonian of the form $H_{so} \approx \lambda_{so}\mathbf{L}\cdot\mathbf{S}$. Therefore, $\mathbf{L}$ and $\mathbf{S}$ are no longer good quantum numbers, instead we must describe the system in terms of total angular momentum $\mathbf{J}$, where $\mathbf{J}^2 = (\mathbf{L}+\mathbf{S})^2$. The lowest energy states are found around the Γ point ($\mathbf{k} = 0$), where there is a direct band gap. Here, the valence band state closest in energy to the band gap has J = 3/2, while the J = 1/2 states lie lower in energy as H_{so} = -λ_{so}/2. This is band is termed 'split-off' by the spin-orbit interaction.

In the case of the valence band, the two projections of J = 3/2 are termed 'heavy' ($|m_j| = 3/2$) or 'light' ($|m_j| = 1/2$) due to the curvatures of the bands around the Γ point. The inherent strain in quantum dots also modifies the band structure, such that the light and heavy-hole bands are further split from each other even at $k = 0$. The precise details

of the strain and vertical confinement alters the contribution to the final hole states from light holes. In the type of quantum dots considered here, the holes are of predominantly heavy-hole character, as this is the band lying closest to the Fermi energy and strain is sufficient to prevent a strong admixture of the other hole types [85]. A schematic of the band structure under strain around the Γ point is illustrated in Figure 1.1(a). As a result of the dominant $|j = 3/2, m_j = \pm 3/2\rangle$ contribution to the hole states, the discussion of the optically active species in these quantum dots is focused upon holes with wave-functions of p-type character, inherited from the atomic orbitals. However, we must note that in this form of quantum dot the admixture of holes has a small contribution of light hole character (< 5 %) which has important consequences for the behaviour of these quantum dots under resonant excitation. Meanwhile, the lowest energy conduction band has J = 1/2 (S = 1/2, L = 0), thus the electrons have s-type character [86].

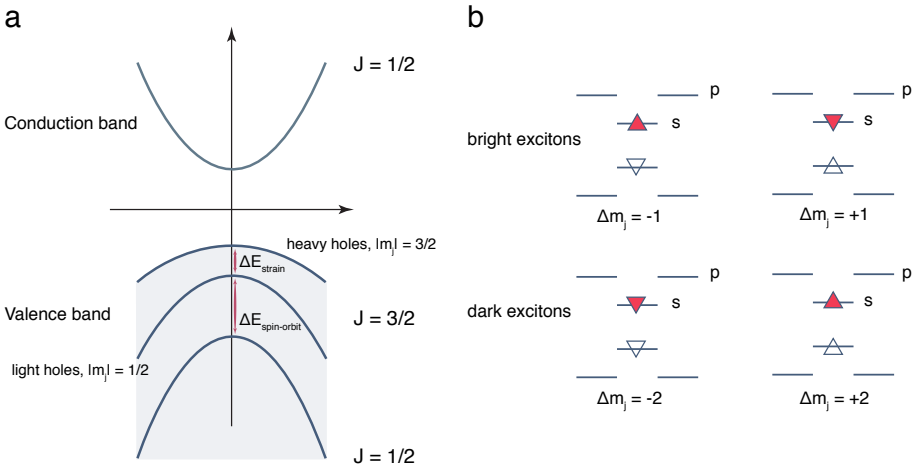

Figure 1.1: The band structure of strained InGaAs and neutral excitons in quantum dots. (a) The band structure of strained InGaAs around the Γ point, as expected in quantum dots. The conduction band is of entirely J = 1/2 character, while the valence band consists of J = 3/2 and J = 1/2, although the J = 1/2 component is removed from the valence band edge by the spin-orbit energy. Heavy holes and light holes create the J = 3/2 band, where heavy holes dominate due to their lower energy under strain. (b) Neutral excitons in a quantum dot. The optical dipole selection rules result in two bright excitons, where the heavy-hole band dominates the character of holes in general.

The band structure of the underlying zincblende crystal structure (alloy of $In_xGa_{1-x}As$) provides the atomic symmetries that determine the selection rules of optical transitions. In the presence of spin-orbit coupling the typical selection rules for electric-dipole transitions are: $\Delta J = 0, \pm 1$, $\Delta l = \pm 1$, and $\Delta m_j = 0, \pm 1$. It is clear that transitions of electrons between the valence band where $J = 3/2$ and the conduction band $J = 1/2$ are allowed, since $\Delta J = 1$.

It is quantum confinement which lies at the origin of the discrete nature of the energy levels found in quantum dots. Carrier wave-functions are localised to the quantum dot, somewhat like those of individual atoms, but here they are built up as linear combinations

of the underlying atomic contributions. The precise spatial arrangement of these wave-functions is dependent upon the confining potential, but in general they are somewhat like very spatially large atomic wave-functions spanning the quantum dot. The small size of these quantum dots means that the energy levels are separated by $\sim$ 10 meV, corresponding to $k_B T$ where T $\sim$ 100 K. Therefore, provided the quantum dots reside at low temperatures, we now have a series of discrete energy levels analogous to that of atoms, where we label the lowest discrete energy level as the 's-shell' and so forth. Similar to the basic atomic picture, shell filling is subject to Pauli's exclusion principle; for example, electrons can only occupy the first s-shell in a spin singlet. Likewise, the heavy-holes can only occupy the s-shell of the valence band in a pseudo-spin singlet.

The underlying solid-state nature is inherited by the discrete energy levels of the quantum dot. J remains a good quantum number to use in describing the behaviour of electrons and holes in these confined systems. Optical excitation results in a trapped electron-hole pair, an exciton. The 'bright' excitons are those for which optical excitation and recombination is permitted by the electric dipole selection rules. A bright neutral exciton (X^0) is formed by excitation of an electron-hole pair such that the total angular momentum change is $\pm$ 1, which is true for the cases of m_j^e = -1/2(1/2) and m_j^h = +3/2(-3/2). If one of the two carriers has m_j of opposite sign however, then the exciton is termed 'dark' as it cannot recombine in, or be directly formed by, an electric dipole transition. The bright and dark excitons are illustrated in Figure 1.1(b) for clarity.

The Coulomb interaction between the electrons and holes becomes a perturbation to these energy levels. In particular, the exchange interaction is crucial to an understanding of excitonic energy levels. The exchange interaction occurs because overall fermionic wave-functions are required to be antisymmetric by Pauli's exclusion principle. As a result, there is an effective interaction between, for example, and the electron spin S^e and hole overall angular momentum J^h. For a quantum dot with any structural asymmetry in the in-plane direction [87], the exchange interaction couples the two circularly polarized bright exciton states ($|m_j^h, m_j^e\rangle$), $|\frac{3}{2}, -\frac{1}{2}\rangle$ and $|-\frac{3}{2}, \frac{1}{2}\rangle$) into two exchange-energy split, linear combinations [88]. This is called the fine-structure splitting, and typical values of $\approx$ 30 μeV [89] are easily resolvable with resonant spectroscopy. The ability to discriminate the energy of photons emitted in a biexciton cascade means that fine-structure splitting is detrimental to schemes aiming to produce otherwise indistinguishable polarization-entangled photons from quantum dots [90]. However, significant progress can be made through careful growth control of the asymmetry and in-plane electric and magnetic field tuning of the effective confinement potential [63].

In summary, self-assembled quantum dots provide a discrete energy spectrum of electron and holes states much like that of atoms. However, the underlying solid-state nature is expressed through the details of the optical selection rules. We now turn to a discussion of a very useful initial characterization technique, photoluminescence, and the method of energy-level tuning through electric fields that is essential to the work presented here.

1.2.2 Photoluminescence, charge tuning and quantum-confined Stark effect of quantum dots

Photoluminescence is generated by the recombination of electrons and holes with associated photonic emission. Typically, the electrons and holes are generated by non-resonant excitation, that is, excitation at an energy above the band gap of GaAs. Alternatively, excitation can be performed into the 'wetting layer' of the sample; this is a residual two-dimensional layer of InGaAs left behind when the quantum dots are grown, which emits at $\approx$ 870 nm, blue-shifted from the QDs themselves. The photo-created carriers rapidly lose energy through non-radiative processes in less than 50 ps [91] and relax to the lowest available energy levels, populating the quantum dot. Subsequently the carriers recombine, emitting photonic signatures of each excitonic species [92].

Figure 1.2(a) presents a typical photoluminescence spectrum of a single quantum dot emission at $\approx$ 10 K. This emission was imaged by a 1200 g/mm grating spectrometer (Acton) with a liquid N_2-cooled CCD following excitation with an above band-gap laser source (at 785 nm). The neutral exciton emission is labelled, as well as the X^{1-} and X^{2-} species, where each is associated with a different electron number occupying the quantum dot prior to electron-hole pair capture, see Figure 1.2(b). The species-dependence upon the externally applied gate voltage indicates that these samples are charge-tunable; there is in fact a controlled vertical electrical field along the direction of the growth axis. In Figure 1.2(c) we present a schematic of the structure. The Fermi energy is pinned to the n^+-doped layer of the back contact. The quantum-dot layer is sandwiched between intrinsic GaAs layers, where an additional AlGaAs blocking barrier acts to prevent current flow in the forward direction. On the top surface of the sample a transparent metallic gate forms a Schottky contact, and allows a voltage to be applied, where the consequent band-bending is illustrated.

An increase in gate voltage brings the discrete quantum-dot levels below the Fermi energy of the back contact. The addition of electrons to a quantum dot is prevented by the confinement energy, with the additional perturbation of the Coulomb energy present for more than one carrier in a quantum dot. The gate voltage tunes the energy levels to overcome these contributions. This allows in-tunnelling of electrons from the Fermi sea. As a consequence, there is a sequential increase in the number of electrons resident in the QD achievable by applying larger gate voltages. In Figure 1.2(a) as the gate voltage is increased from 100 to 600 mV it becomes most likely that the ground state of the QD is single electron occupation. Electron-hole recombination energy is red-shifted due to the Coulomb interaction present in the X^{1-} species, where attractive electron-hole interaction dominates the additional repulsive interaction between the two electrons [93]. This type of structure allows us to select an excitonic species with which to work [12, 94]. In these particular samples there is weak coupling to the back contact due to a relatively long tunnel barrier of 35 nm, which means that the case of no electron occupying the quantum

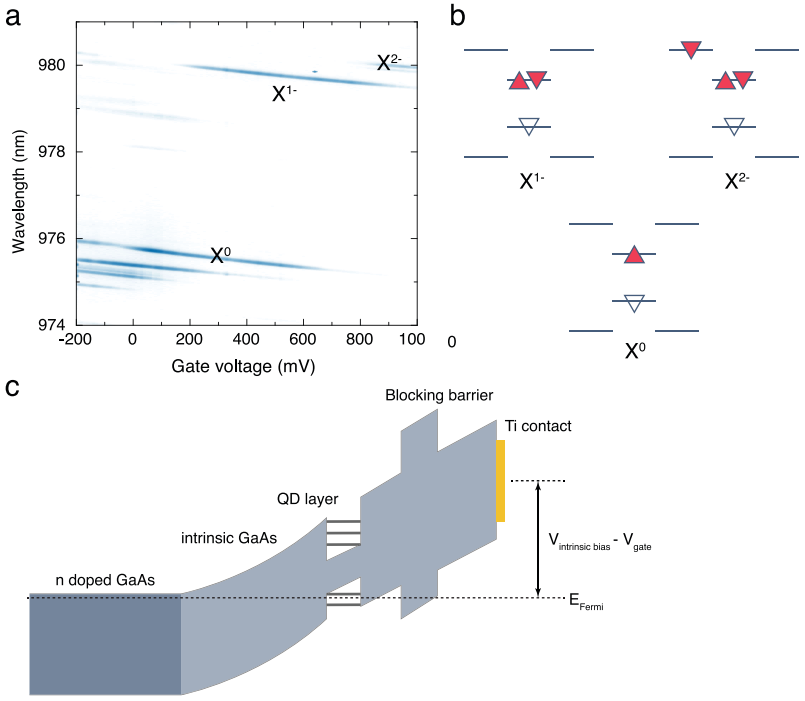

Figure 1.2: Charge tuning of a quantum dot in a diode structure. (a) Photoluminescence spectra of a quantum dot recorded on a spectrometer as the applied gate voltage, or electric field, across a device is swept. The charging steps from X^0 to X^{2-} are indicated as the Coulomb blockade is overcome to allow more electrons to tunnel in to the dot. (b) The excitons for which the emission lines are described in figure (a). (c)The basic form of a Schottky diode device incorporating a QD layer.

dot persists long past the gate voltage at which it becomes possible to add an electron to the ground state. In samples with a shorter tunnel barrier the charge steps are more distinct [12], but for our purposes it is important to maintain long spin lifetimes afforded by weak coupling to the Fermi sea.

In addition to charge tuning, the applied electric field is essential to a small wavelength tuning through the quantum-confined Stark effect [95]: the electron-hole pair forms a dipole $\boldsymbol{p}$ which has an energy associated with applied electric fields $\boldsymbol{F}$, $\Delta E_{Stark} = -\boldsymbol{p} \cdot \boldsymbol{F}$. This energy is given by:

$$E = E_0 - \boldsymbol{p}_0 \cdot \boldsymbol{F} - \beta \boldsymbol{F}^2, \tag{1.2}$$

where E_0 is the zero-field energy, $\boldsymbol{p}_0$ is the inherent electric dipole of an exciton, and β is the polarizability, or effectively how much the exciton can be spatially separated by increasing the electric field. This is not a strong effect within the confined environment of the QDs under discussion here, but it results in a strong parabolic dependence in larger quantum-well structures [96]. The quantum-dot states of interest here undergo primarily linear energy shifts with gate voltage (as evident in Figure 1.2(a)). The ability to tune energy levels is critical in the remaining work of this dissertation. However, the large dipole moment also results in sensitivity to stray electric fields due to trapped charges in

the surrounding solid-state matrix, resulting in unwanted spectral diffusion. This is a key topic of study in chapters 2 and 3.

1.2.3 Single trapped electrons in quantum dots

In this work we shall resonantly address the X^{1-} species, treating it independently of the other possible quantum dot states. We select the correct applied gate voltage and typically remain in this region. In this way, we are able to work with single trapped electrons, the spins of which will be used as matter qubits in Chapters 4 and 5. To form a background for this discussion, we now outline the optical transitions incorporating the single-electron ground state, and how these are subject to externally applied magnetic fields. This also forms the basis of the discussion surrounding the solid-state environment sensing of Chapter 2.

In Figure 1.3(a) we present the energy levels of a quantum dot in the case of a single trapped electron subject to an externally applied magnetic field along the growth axis, known as the Faraday geometry. This lifts the degeneracy of two possible X^{1-} transitions. In the ideal case, the ground state now consists of a well-defined electron spin with a typical spin relaxation time of 30 ms at 2T [97]. Only vertical transitions are permitted by the optical selection rules, with $\Delta m_j = \pm 1$, corresponding to a circular polarization of light.

A map of the resonantly excited emission at 2 T externally applied field is shown in Figure 1.3(b), where the two circularly-polarized transitions are highlighted by dotted lines. The map is of excitation frequency as a function of gate voltage, and where the peaks in signal should occur when the laser frequency coincides with that of the transition, as expected for resonance fluorescence (see Section 1.3). The combination of excited and ground state splitting is ≈ 23 GHz T^{-1}. In the centre of the plateau the emission vanishes as the spin population is shelved in the ground state that is not resonant with the driving laser. This is a method of spin initialization also known as optical spin pumping. It occurs through a diagonal transition (e.g. $|\Uparrow\downarrow\uparrow\rangle_z \rightarrow |\downarrow\rangle_z$), which is forbidden by the selection rules, but nonetheless they have a rate $\gamma \ll \Gamma$ associated with a small component of light-hole states in the overall hole state admixture. This relaxes the optical selection rules and enables spin pumping [14], with a spin pumping time of a few microseconds [97]. Therefore, the transition is much like a cycling transition, with many photons scattered before a spin flip event. The arrangement permits single-shot readout of the spin state if the photon collection efficiency is sufficiently high [98].

Away from the centre of the plateau the gate voltage is such that the electron energy levels are brought into the 'cotunnelling' regime: coupling to the Fermi sea in the back contact thermalizes the spin and prevents effective spin pumping [99], resulting in a recovery of the signal.

In order to have a suitable basic component for quantum information, we need to have a qubit that can be initialized, controlled and read out [1]. In general, we wish

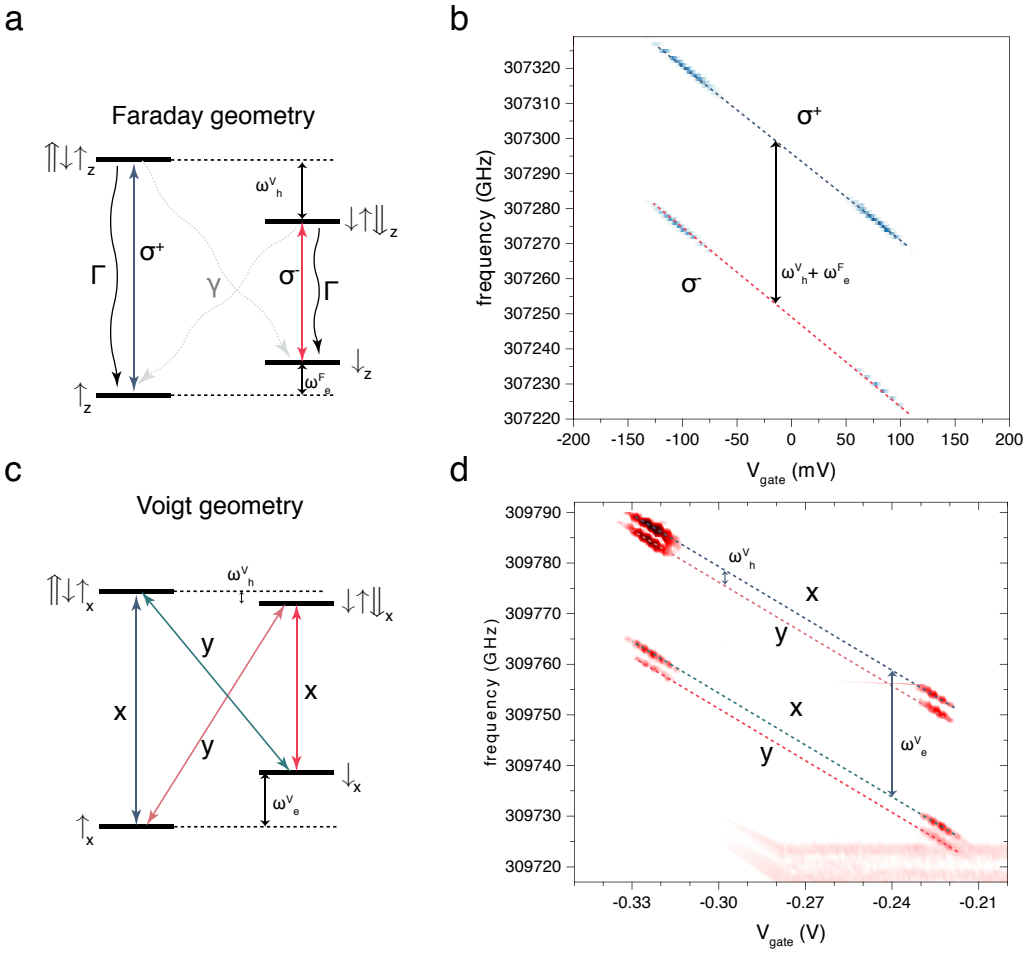

Figure 1.3: Ground and excited states of single trapped electrons. (a) The energy levels of a single trapped electron and the first optically excited states in Faraday geometry. Two circularly polarized electric-dipole transitions are available, and slow diagonal transitions may occur with a rate γ as permitted by a small admixture of light hole character into the excitonic states. (b) A map of resonantly driven fluorescence from the states indicated in (a), where the centre of the plateau vanishes due to spin-pumping into the undriven ground state, and is enabled at the extremes by the spin-randomization process of co-tunneling. (c) The energy levels of a single trapped electron and the first optically excited states in Voigt geometry. All four transitions are allowed by electric-dipole optical selection rules, where vertical and diagonal transitions have opposite polarization. (d) A map of resonantly driven fluorescence from the states indicated in (c), where all four transitions are apparent, but spin pumping is evident in the central region.

to have full and fast control over our electron spin, and having only a forbidden optical transition available for spin pumping reduces the repetition rate at which we can operate. Also, the proposed scheme to perform fast optical coherent rotation of an electron spin requires a λ-scheme with two strong optical transitions [100]. By applying the magnetic field in the plane of the sample, known as the Voigt geometry, the new spin eigenstates for the adjusted Hamiltonian are linear combinations of the previous electron spin ground

states. All four transitions are now equally permissible, as illustrated in Figure 1.3(c). The map of resonant emission in Figure 1.3(d) shows the four transitions at 4T, where the ground-state splitting is 6.25 GHz T^{-1} and the excited-state splitting is close to 0.5 GHz T^{-1}.

In Chapter 4 we use the X^{1-} in the Voigt geometry to access this spin qubit. The presence of optically allowed diagonal transitions results in rapid (sub-10 ns) optical spin pumping, and allows coherent spin rotation [16, 101, 102]. In general, the origin of all of this functionality is the λ-scheme that can be created by selecting one excited state between the two ground states. λ-schemes are a key component in schemes for the physical implementation of quantum information operations, as they allow a spin-photon interface [19, 20]; in the Voigt geometry we obtain many of the ingredients of an optical quantum network mode. We will, however, lose the ability to read out our electron spin in a near single-shot manner, which reduces the rate at which we can both create and then verify entangled states of spins.

1.2.4 Device design and heterostructures

Beyond simple self-assembly, the properties of the QDs are carefully tuned. For example, a capping layer of GaAs is grown on top of the QDs and the temperature of post-growth annealing alters the alloying and strain at the dot-capping layer interface [103]. This allows the as-grown wavelength of emission at $\approx$ 1200 nm to be tuned down to below 1000 nm, where photon detectors are readily available. We note that in addition to quantum dots a spectrally-broad higher energy emission occurs at $\approx$ 870 nm. This is due to the presence of a residual wetting layer, which behaves as a 2D quantum well, but does not have significant impact in our work as we study quantum dots under resonant excitation.

Within the growth process a number of different layers are also included to improve device properties and produce the structure indicated in Figure 1.2(c). Not only do these layers give us electrical tuning, they also assist in the improvement of the photon outcoupling efficiency. The high refractive index of GaAs ($\sim$ 3.5) results in much of the emission being totally internally reflected rather than reaching the collection optics. Our complete sample heterostructure is illustrated in Figure 1.4(a). The QDs are incorporated into a Schottky diode structure with a 35-nm tunnel barrier between the QD layer and an n+-doped layer. The diode heterostructure is grown above a distributed Bragg reflector to maximize our photon outcoupling efficiency. Further enhancement of photon collection is obtained by the presence of a super-hemispherical solid immersion lens (SIL) placed directly on the semi-transparent Titanium Schottky contact on the surface of the sample. For the sample and SIL combination used in Chapters 2 and 3 we estimate a photon outcoupling efficiency $>$ 10 % for QDs with emission wavelengths around 970-980 nm, although this is achieved only when the SIL sits flush with the sample.

In Figure 1.4(b) the sample is shown incorporated into a device, where an etch down to the n-doped back contact with subsequent deposition of AuGeNi alloy is used to provide an

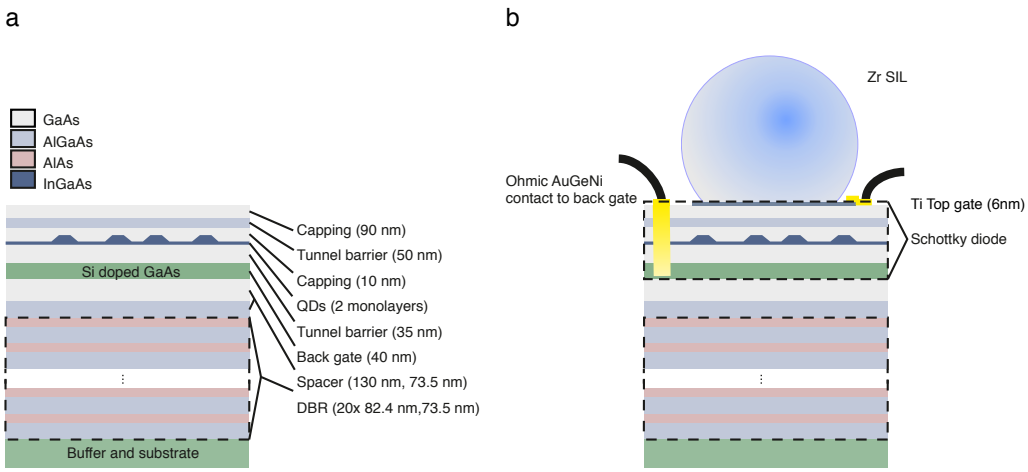

Figure 1.4: The full sample structure of quantum dot devices used in this dissertation. (a) The heterostructure layers grown via Molecular Beam Epitaxy at the Sheffield Centre for III-V Technologies by M. Hugues and E. Clarke. (b) The heterostructure incorporated into a final device by post-growth processing, inclusive of a AuGeNi Ohmic contact and transparent Ti Schottky contact on which is mounted a Zr superhemispherical Solid Immersion Lens (SIL).

Ohmic contact. The semi-transparent Titanium Schottky contact is deposited via e-beam evaporation to an estimated thickness of 6 nm.

With this background regarding the structure and behaviour of quantum dots outlined, we finally introduce a description of light-matter interactions in systems such as quantum dots. That is, those which can be considered to have discrete energy levels connected by strong electric dipole transitions. In particular, we wish to describe the theory underpinning resonance fluorescence, before focusing upon the practical implementations of this in the laboratory.

1.3 Resonance fluorescence in theory and in practice

A description of resonance fluorescence (RF), the light scattered from one or more transitions excited on or close to the resonant condition, is fundamental to understanding light-matter interactions in general. The spectrum of resonance fluorescence was first given by Mollow in 1969 [104], and numerous properties have since been demonstrated experimentally including the Mollow triplet [105], or spectral evidence of Rabi oscillations, single-photon emission evidenced by anti-bunching [106], highly coherent elastically scattered photons [11, 107] and most recently, the quadrature-squeezed nature of the emitted light [108]. Resonantly-scattered photons have many potential applications including the 'flying qubits' connecting a quantum network, where single photon-single matter qubit coherent interactions enable the faithful transfer of information between nodes [18, 81, 109].

1.3.1 Two and four-level systems interacting with light

Much of this work calls upon an understanding of resonance fluorescence and an appropriate theoretical description is outlined here, following a number of standard textbooks [110–113]. As the work is carried out on a negatively charged exciton (X^{1-}) in the presence of a magnetic field, we are specifically interested in the generalization of the two-level model to incorporate four levels with non-radiative relaxation processes. This description is used in chapter 2 to describe the X^{1-} under small fluctuating magnetic fields.

Two-level system A two-level system interacting with a single-frequency (ω_{laser}) light field illustrated in Figure 1.5(a), where the ground and excited states are labelled 1 and 2. The interaction Hamiltonian in the dipole approximation is:

$$\hat{\mathrm{H}}_{\mathrm{int}} = -\hat{\mathbf{d}} \cdot \mathbf{E}(t). \tag{1.3}$$

Here the electric field $\mathbf{E}(\mathbf{r}, t)$ at the position of the system determines the energy of a dipole, where the dipole operator is $\hat{\mathbf{d}} = \mathrm{q}\hat{\mathbf{r}}$ for charge q, with a dipole formed along vector $\mathbf{r}$. Taking a semiclassical description where the optical field is not quantized and is described as a sinusoidally oscillating electric field $\mathbf{E}(t) = \epsilon E_0 \cos(\omega_{laser} t)$, the Hamiltonian can be rewritten in terms of the projection operators of the system:

$$\hat{\mathrm{H}}_{\mathrm{int}} = -\hbar\Omega_{\mathrm{R}} \left[|2\rangle \langle 1| + |1\rangle \langle 2| \right] \cos(\omega_{laser} t) \tag{1.4}$$

where the Rabi frequency Ω_{R} is given by $\Omega_{\mathrm{R}} = \frac{eE_0}{\hbar} \langle 2| \mathbf{r} \cdot \epsilon |1\rangle$ and in the interaction representation this becomes [113]:

$$\hat{\mathrm{H}}_{\mathrm{int}} = -\frac{\hbar\Omega_{\mathrm{R}}}{2} \left[\mathrm{e}^{-i\delta \mathrm{t}} \sigma_{12} + \mathrm{e}^{i\delta \mathrm{t}} \sigma_{21} \right] \tag{1.5}$$

where the projection operators are rewritten as:

$$\sigma_{ij} = |i\rangle \langle j| \text{ such that } |i\rangle \langle j| |l\rangle = |i\rangle \delta_{jl} \tag{1.6}$$

Here we use the rotating wave approximation, which assumes that a component of the Hamiltonian rotating at the sum of the atomic and laser frequencies may be neglected. This is due to its rapid oscillation resulting in an effective averaging to zero in any measurement, or equivalently it represents non-energy conserving transitions in a fully quantized picture [110].

It is useful to work with the density matrix formalism to describe the populations and coherences of a system, where a density matrix, ρ, in general represents a weighted sum over pure states Ψ, each occupied with probability P_Ψ:

$$\rho = \sum_{\Psi} P_\Psi |\Psi\rangle \langle \Psi| \tag{1.7}$$

and the density matrix elements in terms of a chosen basis $\{i, j\}$ are given by:

$$\rho_{ij} = \langle i| \rho |j\rangle . \tag{1.8}$$

The time evolution of the density matrix is described by the Von Neumann equation:

$$\frac{d\rho}{dt} = -\frac{i}{\hbar}[\mathrm{H}, \rho] + \mathcal{L}(\rho) \tag{1.9}$$

where the Lindblad superoperator, $\mathcal{L}(\rho)$, includes the irreversible dynamics. In the case of a two-level system this includes the spontaneous emission from the excited state, which occurs with a decay rate $1/\mathrm{T}_1$ (T_1 being the excited state lifetime). It also includes a pure dephasing rate γ_p, which is phenomenologically introduced by supplementing the lifetime to gain a dephasing time T_2:

$$\frac{1}{T_2} = \frac{1}{2T_1} + \gamma_p. \tag{1.10}$$

For the excited state of a neutral exciton, potential excited state pure dephasing is available due to an elastic-scattering interaction with phonons on a timescale shorter than the radiative lifetime. However, it has been shown that the transitions in quantum dots are in general highly coherent, with slow pure dephasing under resonant excitation [11]. In Chapter 2 we discuss slow dephasing processes, where these are treated as stationary during the radiative dynamics of the quantum dot states. Thus, we here make the assumption $\mathrm{T}_2 \sim 2\mathrm{T}_1$. A simple expression for the relaxation can be written in terms of a relaxation matrix of elements [113]:

$$\Gamma_{nm} = \langle n| \Gamma |m\rangle = \gamma_n \delta_{nm} \tag{1.11}$$

of which $\Gamma_{11} = \Gamma_{12} = \Gamma_{21} = 0$ and $\Gamma_{22} = \frac{1}{T_1}$. In a simplified form the relaxation term appears as an anti-commutator between the density and relaxation matrices, $\mathcal{L}(\rho) = -\frac{1}{2}\{\Gamma, \rho\}$. The expression for the Lindblad term in the equation of motion can then be written as a matrix:

$$\mathcal{L}(\rho) \equiv \begin{pmatrix} 0 & \frac{\rho_{12}}{T_1} \\ \frac{\rho_{21}}{T_1} & \frac{2\rho_{22}}{T_1} \end{pmatrix}. \tag{1.12}$$

A substitution of T_1 with T_2 in the coherence terms introduces pure dephasing. Substitution of equations 1.5 and 1.12 into the Von Neumann equation 1.9 gives the density matrix equations of motion, or the optical Bloch equations of a two-level system:

$$\dot{\tilde{\rho_{22}}} = \frac{i\Omega}{2}(\tilde{\rho_{12}} - \tilde{\rho_{21}}) - \frac{\tilde{\rho_{22}}}{T_1} \tag{1.13}$$

$$\dot{\tilde{\rho_{12}}} = \frac{i\Omega}{2}(\tilde{\rho_{22}} - \tilde{\rho_{11}}) - \tilde{\rho_{12}}\left(\frac{1}{T_1} - i\delta\right) \tag{1.14}$$

here δ is the detuning between the driving laser and the resonance, and this is written in a frame rotating at ω_{laser} with respect to the lab frame. These equations include the population decay due to radiative relaxation, and the decay in the coherences also due to

relaxation. The equations also allow for a coherent driving between ground and excited states due to the excitation field.

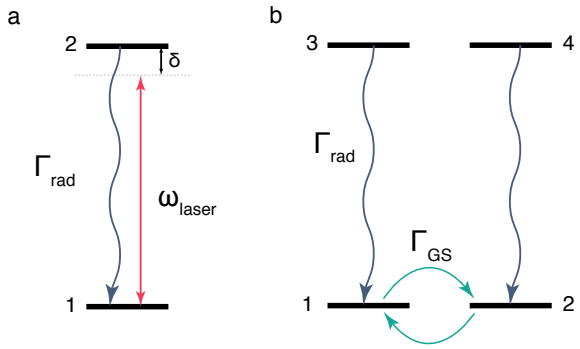

Figure 1.5: Energy levels in two and four-level description of resonance fluorescence. (a)A simple two-level system, driven by an excitation field at ω_{laser}, with detuning δ. The rate of radiative decay is denoted Γ_{rad}. (b)The four-level system is initially modelled as two two-level systems coupled only by relaxation between their ground states with rate Γ_{GS}. Essentially, this represents an X^{1-} system in Faraday geometry. The effect of Voigt geometry is included in the detailed model introduced in Chapter 2.

Four-level system A generalization is made to the four-level system illustrated in Figure 1.5(b) with the interaction Hamiltonian:

$$\hat{\mathrm{H}}_{\mathrm{int}} = -\frac{\hbar\Omega_{\mathrm{R}}}{2}\left[\mathrm{e}^{-i\delta \mathrm{t}}\left(\sigma_{13}+\sigma_{24}\right)+\mathrm{e}^{i\delta \mathrm{t}}\left(\sigma_{31}+\sigma_{42}\right)\right]. \tag{1.15}$$

Here the projection operators are the same as before, and the terms just describe two independent, uncoupled and identical two-level systems as the diagonal transitions are not permitted. It should be noted that the transitions have identical detunings with respect to the excitation field because denoting two transitions at this point is in essence a bookkeeping exercise; in Chapter 2 a magnetic field is included which relaxes the strict selection rules and mixes the energy levels, permitting more interesting behaviour. It remains to add the generalised population relaxation through the Lindblad term:

$$\frac{d\rho}{dt} = -\frac{i}{\hbar}[\mathrm{H},\rho] + \sum_m \mathcal{L}(\rho, L_m) \tag{1.16}$$

The operator for each of the four levels (m = 1,2,3,4) can be written $\mathcal{L}(\rho, L_m) = L_m \rho L_m^\dagger - \frac{1}{2}\{L_m^\dagger L_m, \rho\}$. In the absence of pure dephasing the spontaneous emission must be included as before, but now the spin relaxation in the ground state, for example due to

spin-orbit coupling [97, 114], must be taken into account. The resulting terms are:

$$L_1 = (\Gamma_{\mathrm{GS}})^{\frac{1}{2}}\sigma_{12}, \tag{1.17a}$$

$$L_2 = (\Gamma_{\mathrm{GS}})^{\frac{1}{2}}\sigma_{21}, \tag{1.17b}$$

$$L_3 = (\Gamma_{\mathrm{rad}})^{\frac{1}{2}}\sigma_{13}, \tag{1.17c}$$

$$L_4 = (\Gamma_{\mathrm{rad}})^{\frac{1}{2}}\sigma_{24}. \tag{1.17d}$$

$\Gamma_{\mathrm{rad}} = (2\pi T_1)^{-1}$ and the radiative lifetime of states can be measured as detailed in Section 4.3.

1.3.2 Scattered light intensity and correlations of resonance fluorescence

Experimentally, we are not observing populations and coherences of the QD energy levels but the intensity and correlations of light scattered by them. The intensity is proportional to the first-order correlation of the field at a single time,

$$I(t) \propto \int_o^t \langle E^+(t)E^-(t)\rangle dt \tag{1.18}$$

where the field is expressed in terms of positive and negative components, which are directly related to the raising and lowering operators for electromagnetic modes. The source-field expression [111], which simply states that the far-field radiation emitted by a dipole is proportional to the dipole itself, allows us to make the replacement $E^+(\mathbf{r},t) \propto \frac{1}{r}\sigma_-(t-r/c)$. The raising operator for the field goes with the atomic lowering operator as would be expected, and vice versa. Here $\sigma_+ = |2\rangle\langle 1|$ so,

$$\sigma_+(t)\sigma_-(t) = |2\rangle\langle 2| \quad \Rightarrow \quad \langle\sigma_+\sigma_-\rangle = \tilde{\rho_{22}} \tag{1.19}$$

for the two-level system. Therefore, the intensity of scattered RF on timescales much longer than the excited-state lifetime is simply the steady-state excited-state population, which requires that the density matrix is not evolving, $\dot{\tilde{\rho}} = 0$. The resulting solution of the optical Bloch equations gives the emission rate from a two-level system as the product of the decay rate and the excited state population:

$$\Gamma_{\mathrm{RF}} = \rho_{22} \times \frac{1}{T_1} = \frac{1}{T_1} \times \frac{1}{2}\frac{\Omega^2}{(T_1T_2)^{-1} + 2\delta^2 + \Omega^2}. \tag{1.20}$$

The Lorentzian dependence with respect to laser detuning is power broadened [112]. However, the rate of fluorescent emission does not continue to increase with power, as it saturates at $\Gamma_{\mathrm{max}} = 1/2\mathrm{T}_1$. This is expected for a single emitter when the rate at which the excited state can be populated is balanced by the spontaneous emission rate.

Throughout this dissertation the saturation parameter s will be used, where $s = 1$ for excitation powers that result in half the maximum RF intensity, corresponding to a Rabi

frequency $\Omega^2 = 1/\mathrm{T_1T_2}$. The parameter s can be found by fitting the scattered intensity as a function of power at zero detuning to:

$$\Gamma_{\mathrm{RF}} = \frac{1}{2T_1} \times \frac{s}{s+1} \tag{1.21}$$

In this work we do not consider the short-time population dynamics of the two-level or four-level system, and the inherently linked spectral properties of emitted light, rather the interest here is in the steady-state solutions alone.

Second-order correlations of resonance fluorescence In Chapter 2 we study the autocorrelation of resonance fluorescence on timescales much longer than the population dynamics. There, we shall work in a regime of steady-state population where the Hamiltonian is permitted to change on a 'shot-by-shot' basis.

The autocorrelation, or second-order correlation of resonance fluorescence, is defined in terms of the measured electric field and once more the source-field expression directly relates this to the atomic dipole lowering and raising operators:

$$g^{(2)}(\tau) = \frac{\langle E^-(t)E^-(t+\tau)E^+(t)E^+(t+\tau)\rangle}{\langle E^-(t)E^+(t)\rangle^2} \tag{1.22}$$

$$= \frac{\langle \sigma_-(t)\sigma_-(t+\tau)\sigma_+(t)\sigma_+(t+\tau)\rangle}{\langle \sigma_-(t)\sigma_+(t)\rangle^2} \tag{1.23}$$

It is clear that the normalization is given by the steady state value of the excited population. The full expression for the dynamics of the system on a timescale comparable to the radiative lifetime is omitted here for simplicity. In the case of $\tau = 0$ it is simple to see that $g^{(2)}(0) = 0$. This is known as antibunching and is a characteristic of photon emission by atomic systems long observed in QDs which confirms their two-level nature [115]; it is also therefore crucial to identifying single-photon emitters, as detailed in Section 4.3.

A measurement of the second-order correlation of a stream of emitted photons is equivalent to measuring the probability of photon detection, given a prior photon detection. In other words, the first detection at time $t = 0$ conditions the population to lie initially in the ground state. The probability of some later photon emission at time τ is directly proportional to the excited-state population $\rho_{22}(\tau)$. Over time, photon emission becomes uncorrelated as the current state of the system becomes independent of prior dynamics of a system [116], so that:

$$g^{(2)}(\tau \to \infty) = 1 \text{ or } g^{(2)}(\tau \gg \tau_c) = 1, \tag{1.24}$$

where τ_c is the coherence time of the system.

1.3.3 A resonance fluorescence microscope

Access to light resonantly scattered by single quantum dots is key to the experimental work presented in this dissertation. Therefore, we outline the basic experimental set-up of a microscope in combination with a cryostat.

Figure 1.6(a) presents a schematic of the generalized experimental set-up including the optically accessible magnetic bath cryostat. The sample is positioned at the bottom of the insert, bathed in low pressure Helium gas, itself surrounded by liquid Helium at 4.2 K. At this temperature carriers occupy the lowest available energy levels, and the contribution of the phonon sideband to photonic emission is limited to ≈ 15 % [117]. The electrical gates on the sample are accessed by wires leading to room temperature at the top of the insert, and additionally the sample position can be controlled by piezo-driven stages (Attocube) with three axes available. In addition, a superconducting magnet allows a fixed-direction magnetic field to be applied along the direction of the insert at the position of the sample.

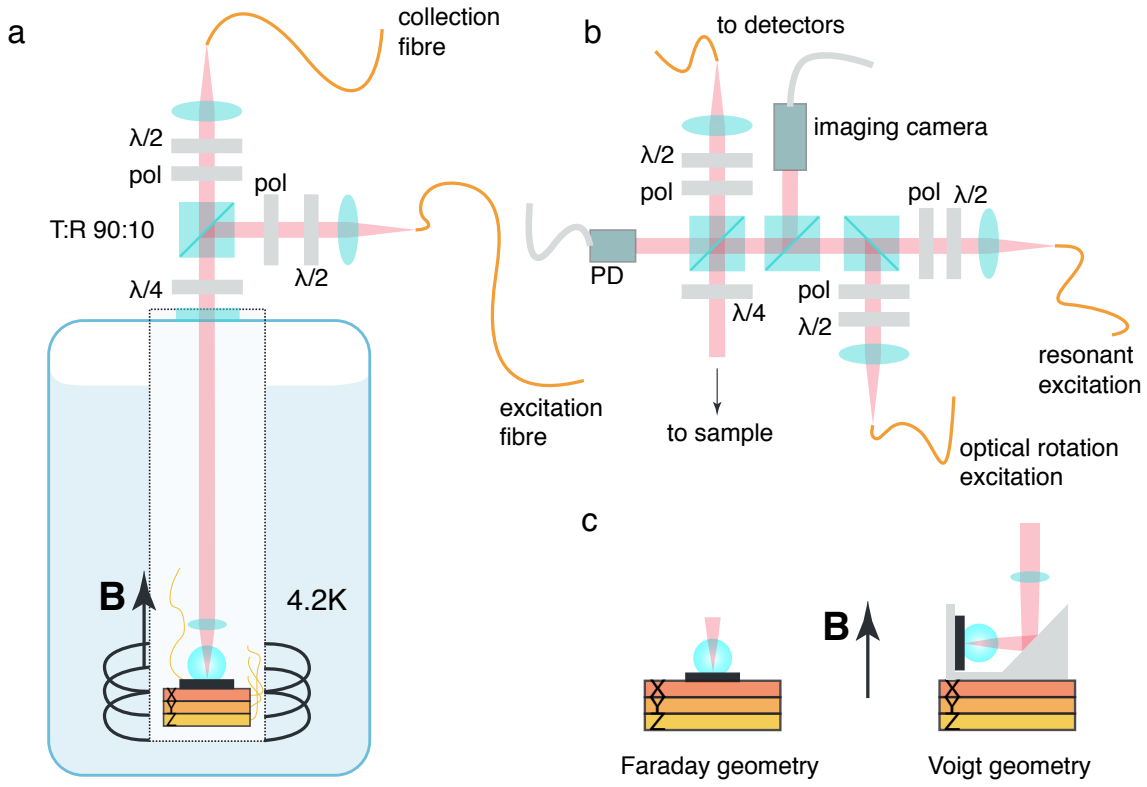

Figure 1.6: A cryogenic resonance fluorescence experimental set-up. (a) A Helium bath cryostat, inclusive of a fixed superconducting magnet, contains a sample at 4.2K. The sample is positioned within the magnetic field area on stick-slip piezo driven stages, and the microscope is mounted above the cryostat except the objective lens which sits near the sample. (b) A complete multi-purpose resonance fluorescence microscope. Two excitation inputs allow for resonant excitation simultaneous with coherent optical spin rotation. (c) Faraday and Voigt geometry sample mounting in a fixed-direction external magnetic field.

Optical access is provided by the top-mounted microscope, where the 0.5 NA aspheric objective lens is held within the insert close to the sample. The microscope is in a confocal configuration, where spatial mode rejection at the end of the light-collection fibre in concert with the objective allows us to collect light from the refraction-limited spot of ~ 1 μm diameter. Consequently we ensure that the density of quantum dots on the sample falls within this range, in order to perform single quantum dot experiments. The microscope is fibre-coupled, such that excitation light can be prepared elsewhere, and the collected photons are directed towards the detector of choice, whether a spectrometer or single photon detector. A beam-splitter with 90 % transmission is used to direct photons collected from the quantum dot to the collection fibre, while allowing the excitation to be coupled in along the same path.

Details of the microscope configuration used to measure resonance fluorescence, and perform optical control of the quantum dots, are included in Figure 1.6(b). The microscope is operated in the dark-field configuration [118] where the crossed polarization of excitation and collection is used to reject laser background and enable only the resonantly scattered photons to be collected. The microscope is operated in a confocal manner, and as such the modes of excitation and collection can be well matched, which assists in background rejection. The total best achieved signal-to-background ratio of resonance fluorescence to 1000:1 for particularly bright emitters, where 100:1 is found under everyday operation. We note that polarization-based suppression of the laser background is highly sensitive to laboratory temperature and mechanical stability of the microscope, hence the variability in these quoted figures.

Each input is preceded by a polarizer to permit dark-field operation, and in addition a half waveplate to ensure the polarization of the incoming light is matched to the polarizer axis. In combination with polarization-maintaining fibres the input intensity is maintained by active feedback control. The error signal is provided by a microscope-mounted photodiode (PD) and is actioned by acoustic optical modulators (AOMs), where the intensity in the first-order diffraction beam is adjusted by the output of a PID control box (Stanford SIM960). The two inputs included on this microscope configuration allow simultaneous resonant driving and read-out, with optical spin rotation by far off-resonant pulses (see Chapter 4). The necessary circular polarization of the optical spin rotation pulses is acheived using the quarter waveplate prior to the cryostat window.

The collection fibre is directed towards the detection set-up of interest. This may be, as in the case of Chapters 2 and 3, directly a single photon-counting detector. However, in the work we describe in Chapters 4 and 5 this is a more complicated filtering set-up prior to the detectors. Analysing photoluminescence (Section 1.2.2) simply requires the output to be coupled into a spectrometer.

Finally, in Figure 1.6(c) we indicate the arrangement whereby Voigt geometry is achieved in a fixed-field cryostat. A custom sample mount with inclusive mirror is positioned on the piezo-stages, offset to allow coupling of the collection mode onto the surface

of the sample.

The experimental set-up described here provides a versatile basis for a wide range of resonant quantum-dot studies. A fibre-coupled microscope allows for flexibility in experiment positioning, and to some extent allows us to 'plug and play' with both excitation sources and the precise downstream processing of our collected photons. We will see that this is particularly important in the case of entanglement generation, where we must assemble a large 'machine' from many parts, of which only one is the microscope-cryostat component.

Chapter 2

The solid-state environment of a quantum dot

Optical transitions in single quantum dots have been established as model two-level systems in the solid state; individual QDs emit single photons [115] and highly coherent elastic scattering has demonstrated the absence of pure dephasing of the optical transitions at low temperature [11]. Photons emitted from a QD under resonant excitation can be highly indistinguishable shot-to-shot [119, 120]. In addition a single trapped electron with a quantization axis defined by an external magnetic field is a potential spin qubit; both optical pumping of spin population [14] and coherent optical rotation of a single spin have been demonstrated [15]. Combined with the ability to resolve spin population through resonance fluorescence [13], and indeed entangle the state of a single spin with a single photon [19, 20], the X^{1-} species in InGaAs QDs shows great promise in quantum communication and information processing applications.

However the key requirements for entanglement, namely indistinguishability between photons emitted by two separate QDs and maintaining electron spin coherence, are challenging. A high degree of indistinguishability (81% wavepacket overlap) was originally demonstrated between photons emitted from the *same* QD in response to non-resonant excitation [121], and resonant excitation has increased this indistinguishability to 97% [120]. However, the spectra of fluorescence from QDs have long been recognised to suffer spectral diffusion [22], and as such even if two QDs are found with the same resonant frequency, the time-dependent relative detuning will result in a reduction of two-photon indistinguishability. This has been found to be only 18% with non-resonant pulsed excitation [122], increased to 39% with excitation resonant with the p-shell of a QD [123] and further to 82% [124] under resonant excitation. It is thought that non-resonant excitation results in excess, unwanted carrier creation in the vicinity of a QD and increased spectral diffusion due to noisy electric fields. In general, spectral diffusion is not apparent on short timescales for a single QD [125], but it is the longest timescales that are important when

one wishes to consistently generate indistinguishable photons from two separate QDs.

Using coherent optical rotation the spin coherence of electrons can be measured directly; a Ramsey interference experiment reveals a typical electron spin dephasing time $T_2^* \approx 2$ ns, and with a Hahn spin echo pulse sequence the coherence time T_2 is extended to few μs timescales [16]. The hyperfine interaction of the electron with the bath of non-zero nuclear spins present in an InGaAs QD is the most likely limiting factor [126]; this 'central spin' problem is complex. The imprint of ground state spin dephasing is also seen in the reduced coherence of Raman scattered photons [127], and the spectrum of scattered resonance fluorescence is sensitive to the presence of a nuclear spin bath [128].

With a view to understanding how the solid state environment affects the behaviour of a QD, and in particular the X^{1-} system that is so important as our spin-photon interface, this chapter explores intensity correlations within time-resolved resonance fluorescence. This approach does not directly probe the nuclear spin bath or charging of the sample but instead uses the effect of the resulting 'noisy' fields upon the optical transition.

This chapter first describes the interaction between a single electron and a bath of nuclear spins from a theoretical point of view and reviews recent literature, in particular focusing on the evolution of the nuclear spins in Section 2.1. In Section 2.2 the signature of noisy electric and magnetic fields in resonance fluorescence is discussed, and this is applied in Section 2.3 to identify the origins and timescales of each contribution to the noise of three QDs from the main sample discussed in this dissertation, 'Chef 2'. Magnetic field noise is clearly distinguished through an additional two-laser excitation experiment. A four-level optical Bloch equation model is applied in Section 2.4 to quantify the noise and distinguish the effects of power broadening from QD-to-QD variation. Furthermore, Section 2.5 studies the power dependence of the nuclear spin bath dynamics, determining that in the absence of applied magnetic field the presence of an electron spin has a significant impact upon the correlation times observed. Finally, the properties of another sample are surveyed, demonstrating the utility of RF intensity autocorrelation measurements as a rapid characterization technique.

The main results detailed in this Chapter are published in Ref. [26].

2.1 Electron spin-nuclear spin interactions and nuclear spin dynamics

2.1.1 The hyperfine interaction

The interaction of an electron or hole spin with a single nuclear spin is composed of three terms [129]: the Fermi contact hyperfine interaction of form $\hat{\mathrm{H}}_{\mathrm{hyp}}^{\mathrm{fc}} \sim \delta(\mathbf{r})\,\mathbf{S}\cdot\mathbf{I}$, a direct magnetic dipole-dipole coupling between the two spins of form $\hat{\mathrm{H}}_{\mathrm{hyp}}^{\mathrm{dip}} \sim (3(\mathbf{n}\cdot\mathbf{S})(\mathbf{n}\cdot\mathbf{I}) - \mathbf{S}\cdot\mathbf{I})/r^3$, and a spin-orbit term representing the interaction of the nuclear spin with the carrier's orbital angular momentum which therefore takes the form $\hat{\mathrm{H}}_{\mathrm{hyp}}^{\mathrm{SO}} \sim \mathbf{L}\cdot\mathbf{I}/r^3$. $\mathbf{I}$ is the nuclear

spin and **S** and **L** represent the carrier spin and orbital angular momentum respectively. Here **r** is the vector pointing from each nucleus to the electron and $\mathbf{n} = \mathbf{r}/|\mathbf{r}|$. The spin-orbit interaction of the electron alone is inherent to the energy levels of a quantum dot and was discussed in Section 1.2.

The relative contributions of these terms differ between electrons and holes due to the wavefunction symmetry; the s-type electrons can experience an isotropic Fermi contact interaction, whereas the p-type holes are free of the Fermi contact interaction as the wavefunction vanishes at each of the lattice sites. The dipole-dipole coupling dominates in the hole spin case, however it is found to be an order of magnitude weaker than the Fermi contact interaction for conduction band electrons [130–132]. A more detailed discussion of the hole spin case is undertaken in Section 2.6.2.

The Fermi contact interaction of the electron spin with the nuclear bath can be written as [133, 134]:

$$\hat{\mathrm{H}}_{\mathrm{hyp}}^{\mathrm{fc}} = \frac{\nu_o}{2} \sum\nolimits_j A^j |\psi(\mathbf{r}_j)|^2 \left(\hat{I}_z^j \hat{\sigma}_z^e + \frac{\hat{I}_+^j \hat{\sigma}_-^e + \hat{I}_-^j \hat{\sigma}_+^e}{2} \right) \tag{2.1}$$

where the sum is over all nuclei that can interact with the electron, ν_o is the volume of the unit cell and the magnitude of the electron wavefunction at each of the lattice sites $\mathbf{r}_j$ is given by $|\psi(\mathbf{r}_j)|^2$. A^j is the hyperfine coupling constant for each nucleus, and is found to be 40-50 μeV for InGaAs dots [135]. The operators $\hat{\sigma}_+$ and $\hat{\sigma}_-$ are raising and lowering operators for the electron spin ($\hat{\sigma}_+^e = \left|m_{z+1}^e\right\rangle \langle m_z^e|$), in general represented by Pauli spin operators $\hat{\sigma}_x, \hat{\sigma}_y, \hat{\sigma}_z$. The spin of each nucleus is similarly represented by the $\hat{I}$ operators.

2.1.2 Mean field approach to nuclear spin bath

The interaction of a single electron with around 10^5 nuclear spins is represented in a first approximation as a single effective magnetic field, the Overhauser field $\mathbf{B}_N$ [23]:

$$\mathbf{B_N} = \frac{\nu_o \sum_j A^j |\psi(\mathbf{r}_j)|^2 \langle \mathbf{I}^j \rangle}{g_e \mu_B}. \tag{2.2}$$

This is the sum of the effective field due to the mean nuclear spin at each site. The total field acting upon an electron is then $\mathbf{B} = \mathbf{B_z} + \mathbf{B_N}$ where $\mathbf{B_z}$ is an externally applied field. Were the nuclei uniformly polarized ${\mathbf{B_N}}^{max}$ would be equivalent to several Tesla of externally applied field. For example, assuming a uniformly distributed wavefunction, $|\psi(\mathbf{r}_j)|^2 = \frac{1}{\sqrt{N}}$ and an $\mathrm{In}_x\mathrm{Ga}_x\mathrm{As}$ QD where $x = 0.5$, $\mathbf{B_N} = 6.5$ T.

The electron spin similarly exerts an effective magnetic field upon each nucleus: this field is then referred to as the Knight field and the time averaged value is given by

$$\mathbf{B_K}_j = f_e \frac{\nu_o A^j}{g_N \mu_N} |\psi(\mathbf{r}_j)|^2 \langle \hat{\mathbf{S}}^e \rangle. \tag{2.3}$$

Here the time-averaged electron spin is the origin of the field, and the filling factor f_e

allows for the dot to be unoccupied. The maximum measured local effective field acting on a single nucleus is 30 Gauss (3×10^{-3} T) for a QD with an estimated 30 % electron spin polarization in a time-averaged measurement [136]. It is reduced compared to the maximum Overhauser field as it is the effect of a single particle rather than a collection. Due to the wavefunction variation over the dot it is inherently spatially inhomogeneous.

In the absence of a magnetic field there is no preferred polarization of the nuclear spins, such that $\langle \mathbf{B_N} \rangle = 0$. However, the operators representing the nuclear spins along each orthogonal axis do not commute; they cannot be simultaneously determined to be exactly zero such that fluctuations of the Overhauser field, $\sigma_B = \sqrt{\langle \mathbf{B_N}^2 \rangle - \langle \mathbf{B_N} \rangle^2}$, have a non-zero value. In a typical instantaneous Overhauser field at 0T external magnetic field, the electron spin precesses on a timescale $\sim$ 100ns, where the corresponding nuclear spin precession in the equivalent Knight field is $\sim 1\mu$s. Therefore, the dynamics of the Overhauser field are expected to be much slower than an electron spin precession. The electron can therefore be treated as though in each measurement attempt it is precessing in a fixed Overhauser field, this is called the *frozen fluctuation model* and in this work we follow the picture developed in Ref. [126] that describes the magnitude and direction of the Overhauser field as random, with a value drawn from a 3-dimensional Gaussian probability distribution:

$$\mathrm{W}\left(\mathbf{B_N}\right) = \frac{1}{\left(2\pi\sigma_B^2\right)^{3/2}} \exp\left[-\frac{1}{2}\left(\frac{\mathbf{B_N}}{\sigma_B}\right)^2\right] \tag{2.4}$$

The standard deviation of the Overhauser field is the unknown parameter; previous work on hyperfine effects at zero field performed by my colleagues Jack Hansom, Carsten Schulte and Claire Le Gall suggests $\sigma_B \approx$ 20mT [128], Ref [137] suggests 10 mT, and a rough estimate based upon the theory presented in Ref [126] suggests $\sigma_B \sim$ 40 mT.

2.1.3 Nuclear spin bath dynamics

Through the Overhauser field, the dynamics of the collection of nuclear spins are evidenced directly in the electron Zeeman splitting. There are several competing mechanisms that influence how this nuclear spin bath evolves:

- The Knight field due to the electron generates an effective magnetic field acting on each nucleus as discussed above. The inhomogeneity of the Knight field means that the nuclei do not evolve in a concerted way, and an estimate for the evolution time is $\mathrm{T}_K \sim 1$ μs [126]. We note that this applies for the case of a fully polarized electron spin exerting the maximum possible Knight field on the nuclei.

- Direct transfer of the spin angular momentum from the electron to a single nuclear spin allowed by the second term of the Hamiltonian 2.1, called a 'flip-flop' process. If a particular electron spin population is optically pumped with circularly polarized

light, for example, this leads to a continual transfer of a spin polarization to the nuclear spins and consequent polarization of the entire bath, which is detectable as an Overhauser shift in the optical transitions [138].

- The nuclei interact amongst themselves via direct dipole-dipole interaction [23] which may be described as a fluctuating field ($B_L \approx 0.15$ mT) at each nucleus around which the lattice site spin can precess with $T_d \sim 100$ μs, or equivalently $\nu_{dd} \sim 1$ kHz.

- Inter-nuclear spin flip-flop processes that require energy conservation and scale as $1/r^3$ where r is the inter-nuclear separation [134].

- Nuclear quadrupole coupling to the electric field gradients inherent to a strained InGaAs dot [139]. The resulting effective magnetic field acting on the nuclei is site-dependent, but overall this 'quadrupole field' B_Q is of order 100 mT, or $\nu_Q \sim$ 1-10 MHz. Therefore, it can dominate over the Knight field subject to the precise details of the strain in the quantum dot.

Due to incommensurate electron and nuclear Zeeman energies, electron-nuclear spin exchange should be suppressed by an external magnetic field. However, any process that reduces the interaction time of the electron and nuclear spins, or effectively broadens the electron energy levels, allows the flip-flop process to occur. For example, this can be thermal broadening, increased tunnelling of an electron with a back contact, or in the case of the electron being present only in the excitonic species such as the X^+, a decrease of the exciton's radiative lifetime [140]. It is also clear that any electron-mediated nuclear spin polarization can become quite complicated; the polarization of nuclear spins leads to an Overhauser field acting to suppress the flip-flop processes that brought it into existence [141, 142].

The inter-nuclear flip-flop processes allow spin diffusion away from a point of high nuclear polarization, and were this the dominant process it would not be possible to polarize the nuclear spins of a single dot. It has however been shown that the dipole-dipole interaction could be quenched in small externally applied fields of 1mT [143] and the initial observations of nuclear polarization even in the absence of an externally applied magnetic field were attributed to the electron Knight field acting on the nuclei [136]. However, it has since been determined that the nuclear polarization can be maintained for timescales exceeding an hour in the absence of a trapped electron, and that the presence of an electron can actually lead to depolarization [144]. This indicates that nuclear spin diffusion via the dipole-dipole interaction is suppressed, even in the absence of a Knight field, and the culprit is likely to be the nuclear quadrupole effect.

Nuclear quadrupole effects A self-assembled quantum dot is inherently strained due to the lattice mismatch of $\sim 7\%$ between InAs and GaAs which drives the growth. Partial strain relaxation and random alloying result in inhomogeneous electric fields within the dot [145] that couple to quadrupole electric moments of the prolate-shaped nuclei for

I>1/2 (where we have $I_{In} = 9/2$, $I_{Ga} = 3/2$ and $I_{As} = 3/2$). This creates an additional term in the Hamiltonian of nuclear spins [146]:

$$\hat{H}_Q = \frac{\hbar\omega_Q}{2}\left(\hat{I}_z'^2 - \frac{I\,(I+1)}{3}\right), \tag{2.5}$$

where $I_z^{'}$ is the nuclear spin projection along the electric field gradient at the lattice site, where the electric field gradient changes across the dot and is not necessarily coincident with the growth axis or an external magnetic field. The electric field gradient can be considered a local quantization axis where the $|m_z^{'}|$ values sit on a ladder of unevenly spaced energies due to the term $I_z'^2$. The spacing of the ladder also depends upon the specific electric field gradient at that lattice site through ω_Q, and the nuclear spin I of the species involved. Nuclear dipole-dipole spin flips are energetically forbidden due to the anharmonic ladder even if they conserve spin, unless the spin transitions happen to be equal in energy. Matched energies arises in a number of possible cases: the overall populations of each $m_z^{'}$ state is maintained, as two nuclei simply swap the value of their spin projection with $\Delta m_z^{'} = 1$; the energy spacing of two completely different $m_z^{'}$ transitions happens to match [146]; there is a transfer of spin between two local nuclear spins where $m_z^{'} = \pm\,1/2$. By limiting the number of such scenarios, quadrupolar coupling suppresses nuclear spin diffusion through the QD.

A typical value for the effective magnetic field due to the quadrupolar coupling, $B_Q = \frac{\hbar\omega_Q}{g_N\mu_N}$, is 100 mT or equivalently nuclear spin precession at 1-10MHz [147]. The strain profile and elemental composition are not homogeneous, thus the dipolar coupling is strongly suppressed leading to a well-maintained nuclear spin polarization [148]. The mismatch between the dot and its surroundings reduces the spin out-diffusion that can occur in particular. This is demonstrated by the cycles of polarization and allowed diffusion leading to gradual polarization of the entire dot in Ref. [144]. Even at high magnetic fields this perturbation remains significant and the spectra of nuclear spins does not become perfectly harmonic or independent of the local environment of an individual nucleus [146].

The interplay of different processes in nuclear spin dynamics is complex and subject to variation dependent on external magnetic field, the specific geometry of a dot, and the presence of an electron spin. In the general case, an electron spin is subject to the total of the Overhauser and externally applied fields. The Overhauser field itself is due to the sum of all nuclei, which precess in any external magnetic field but also are subject to the quadrupolar coupling to electric field gradients, dipolar coupling amongst themselves, and hyperfine coupling to the spin of an electron if it is present. A power-dependent study of potential Overhauser field dynamics in Section 2.5 attempts to shed further light on the competition between processes contributing within the quantum dots studied here.

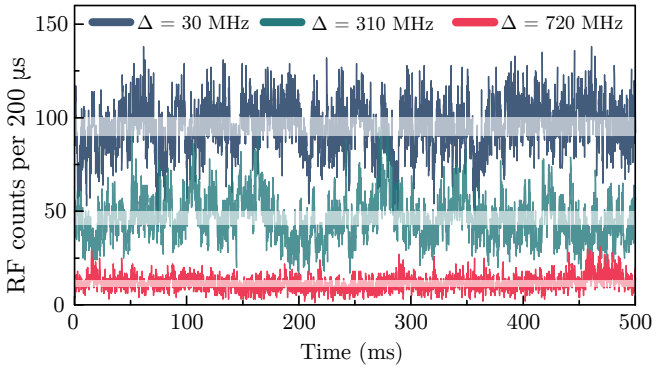

Figure 2.1: Fluctuations in time-resolved resonance fluorescence (RF) from QD A, driven below saturation at s = 0.28. White bars indicate the expected distribution of counts for shot noise alone.

2.2 Sensitivity of a quantum dot transition to electric and magnetic field fluctuations

The interaction of quantum dot resonances with electric and magnetic fields was outlined in Section 1.2, where they act as external control parameters to tune resonances and define spin quantization axes. However, uncontrolled fields are at the heart of reduced photon quality and spin coherence in quantum dots. Figure 2.1 displays time-resolved resonance fluorescence for a single quantum dot, QD A, driven far below saturation, s = 0.28. The mean count rate decreases with increasing detuning of the laser from the resonant condition as expected, but the noise of the fluorescence is far greater than the white bars that indicate the expected shot noise, $\sigma = \sqrt{N}$ where N is the number of counts in a time bin. This kind of signal is typical for resonance fluorescence from an InGaAs quantum dot [149]. Additionally, the QD absorption linewidth depends upon the rate of scanning across a resonance [22]. Both of these effects are associated with spectral diffusion; the aim of this chapter is to identify the processes that contribute to this noisy fluorescence in more detail. The optical transitions of quantum dots have been previously used as a local charge sensor [150–152] and here this is extended to also include noisy magnetic fields.

In this work the system of interest is the X^{1-} species. In addition to providing optical access to a potential spin qubit the transition serves as a fluctuation sensor that can distinguish electric and magnetic fields.

The impact of a noisy electric field on QD excitons is illustrated in Figure 2.2, where charge traps, either local or at an interface within the sample heterostructure, are envisioned as potential field sources [151, 153], Fig 2.2(a). The large permanent dipole [154] of the QD exciton renders the transition frequency of both the X^{1-} and the X^0 sensitive to the parallel component of this field $[E_z(t)]$. Any instability in the local electric field leads to a time-dependent linear Stark shift, thus the local electric field strength is reflected in

the instantaneous resonance frequency of the QD transition, Fig. 2.2(b). The result of a spectral measurement of absorption over a much longer timescale than the fluctuations is a broadened profile approaching a Gaussian, rather than a Lorentzian.

We therefore use a Gaussian distribution of resonant frequencies to model the resonance fluorescence intensity 'jitter' in the QD absorption, Figure 2.2(b). A single narrow-linewidth laser is represented in two cases by the red arrows. The resultant resonance fluorescence samples a range of resonance conditions; a laser at the centre of the distribution will yield a higher mean intensity with a lower distribution of values than is the case for a more detuned laser. This is generally true for linear shifts of the resonant frequency, and the sensitivity to a sub-linewidth change is approximately the derivative of the underlying absorption profile. It does not vanish at the resonance, however, since the spectral wandering is large enough to render this first-order approximation inappropriate. The amplitude of the fluctuations is given by the range of possible values sampled over by a fixed excitation laser, and is presented in Figure 2.2(e).

This behaviour is in contrast to that seen in response to magnetic fields: the Zeeman splitting of both the spin ground state and unpaired hole in the excited state creates a four-level system for an X^{1-}. In contrast, the resonance of the X^0 will undergo a shift dependent upon which of the two excitons is addressed [88, 155] which will appear qualitatively similar to a Stark shift of the resonant frequency.

Figure 2.2(c) illustrates the effect of a noisy sub-linewidth Zeeman splitting on the X^{1-} absorption profile. The single laser drives a four-level system, where the quantization axis direction shifts from Faraday-like to Voigt-like; consequently the selection rules are not fixed [128]. Figure 2.2(d) illustrates a series of absorption profiles for different Overhauser fields drawn from a Gaussian distribution, representing the absorption probability at a series of points in time. Therefore, a laser driving on the zero-field resonant frequency will result in resonance fluorescence with *more* fluctuations than at an off-resonant point in contrast to the case of electric-field fluctuations. This difference in sensitivity to electric and magnetic fields enables the sources of noise in RF to be distinguished by plotting the detuning dependence, and is indicated in the contrast between Figures 2.2(e) and (f). This technique was used in Ref. [25] to make a similar identification of noise sources.

We note also that these figures display the results of optical Bloch equation simulations for a four-level system, where Gaussian distributions of the Overhauser field ($\sigma_B = 25$ mT) and resonant frequency ($\sigma_E = 250$ MHz) are applied to a system with radiative lifetime $T_1 = 700$ ps. Figures 2.2(e),(f) are derived from the width of intensity distributions at a single laser frequency as indicated in Figures 2.2(b),(d), and can be recovered directly in experiments as bunching amplitudes in the autocorrelation of the resonance fluorescence, as we discuss below.

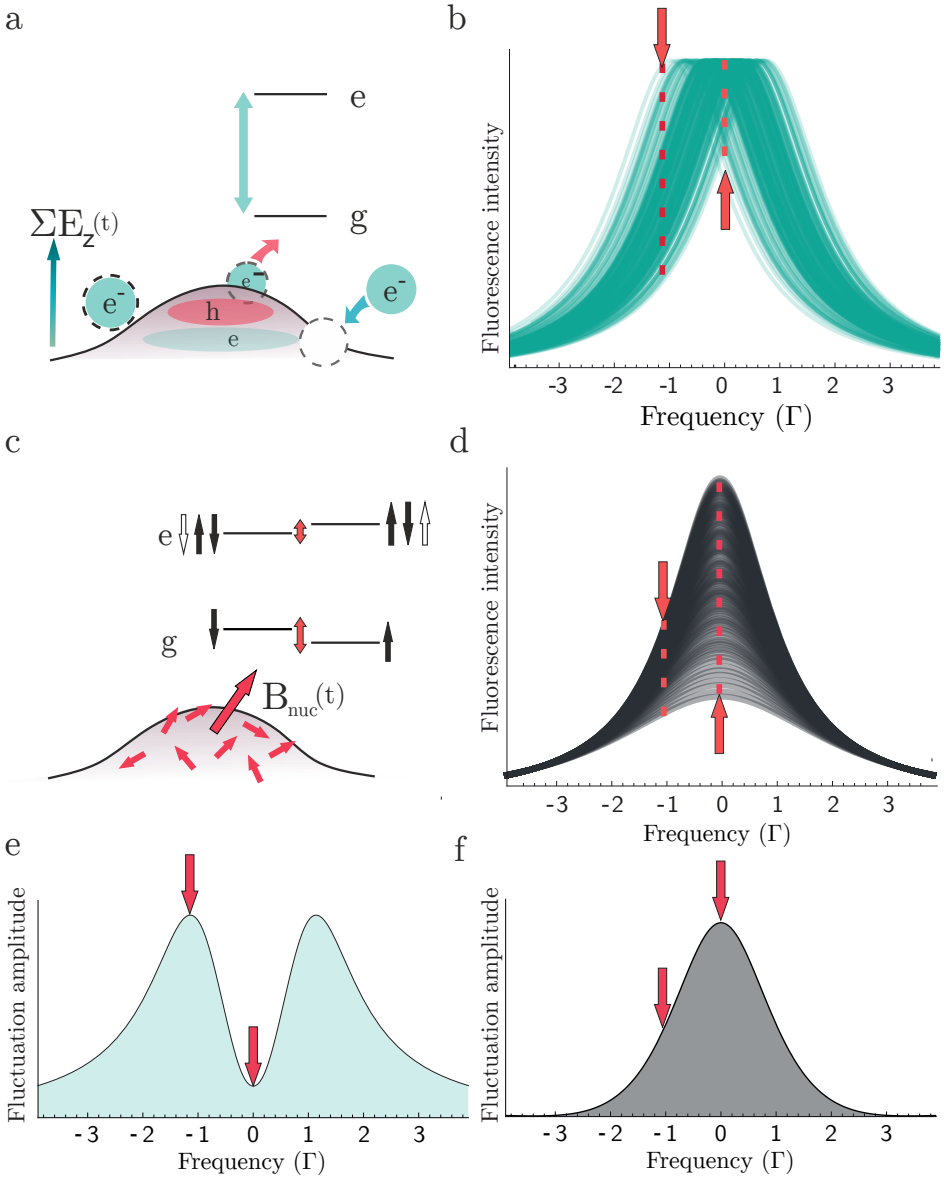

Figure 2.2: Sensitivity of the X^{1-} transitions to noisy electric and magnetic fields. a) The optical transition is sensitive to linear Stark shifts due to electric field components aligned with the optical dipole. b) A 'jitter plot' of a Lorentzian absorption lineshape where the resonant frequency is dispersed by a Gaussian distribution, as a model of electric-field induced spectral diffusion. c) The X^{1-} becomes a four-level system in the effective magnetic field resulting from the Overhauser field of the nuclear spins. d) This 'jitter plot' shows the absorption calculated where multiple Overhauser fields are sampled from an isotropic Gaussian distribution, with field capable of producing only a sub-linewidth splitting of the absorption. e) The expected amplitude of fluorescence fluctuations due to a noisy electric field is derived from the distribution of intensities sampled when driving with a narrow-linewidth laser in b), and is minimised when driving at the central frequency. f) In contrast, a noisy sub-linewidth splitting of the electron spin ground state results in maximum fluorescence fluctuations at the resonant frequency.

2.3 Resonance fluorescence fluctuation spectroscopy

To extract fluorescence dynamics over a wide range of timescales we record a time-trace of the fluorescence on a single detector and calculate the intensity autocorrelation function $g^{(2)}(\tau)$, where the variable τ specifies the time delay between photodetections. This is not the same as a typical $g^{(2)}(\tau)$ measurement as we do not use two separate detectors, and are thus prohibited from recording the very small τ dynamics due to the dead time of the detector ($\sim$ 50 ns). Obtaining and analyzing the autocorrelation of a fluorescence signal is a well-known spectroscopy technique used to study conformational changes of molecules, molecular binding in solution and to quantify molecular diffusion dynamics [156–158], for example. In the autocorrelation function the shot noise limit corresponds to $g^{(2)}(\tau) = 1$, where the detection of a photon is uncorrelated with any other detection. Super-Poissonian statistics are associated with chaotic light; the correlation between photons will result in bunching, that is, $g^{(2)}(\tau) > 1$. In general, at times greater than the coherence time, τ_c, the autocorrelation reaches unity. The timescales over which the autocorrelation amplitudes decay reflect the rates of the processes at the origin of intensity fluctuations.

We make use of the setup introduced in the introduction to this dissertation; resonance fluorescence (RF) is collected by means of a confocal microscope in a dark-field configuration [11] and detected by a single photon counting avalanche photodiode (APD). Here we work with no externally applied field. Frequency- and power-stabilized lasers resonantly excite single QDs in continuous-wave mode with linear polarization. Photon arrival times are registered by a time-to-digital converter (quTau) with a timing resolution of 162 ps where data is rebinned in post-processing. A laser frequency is chosen such that the QD is excited in the centre of the X^{1-} charge plateau; the resonance is tuned with respect to the laser through the gate voltage on the diode structure.

Three example photon detection time traces from QD A were displayed in Figure 2.1 for excitation on resonance and detunings of $\Delta = 310$ MHz and $\Delta = 720$ MHz, where the natural linewidth of the transition, Γ, is 270 MHz in linear frequency. The excitation power corresponds to $s = 0.28$, where $s = 1$ corresponds to $I/I_{sat} = 1/2$. Fig. 2.3 displays the corresponding autocorrelations where in total $\sim 10^7$ time-tagged detection events were acquired for each measurement, lasting $100 - 200$ s, dependent upon the laser detuning. The autocorrelation is not calculated for timescales as short as the radiative lifetime of the quantum dot due to the single-detector nature of the experiment, thus the single-photon nature of QD resonance fluorescence typically evidenced by $g^{(2)}(\tau = 0) = 0$ will not apparent here. Instead, there is a prominent bunching $g^{(2)}(\tau) > 1$ indicative of intensity noise. On timescales approaching 1 s or above, $g^{(2)}(\tau)$ decays to 1. Here, the very long-time behaviour is not explored, and in general has been found to be noisy and subject to day-by-day change [25].

Fits of the experimental autocorrelations to a sum of exponential decays, shown as dark grey lines in Fig. 2.3, reveal a set of distinct correlation times. In the case of simple

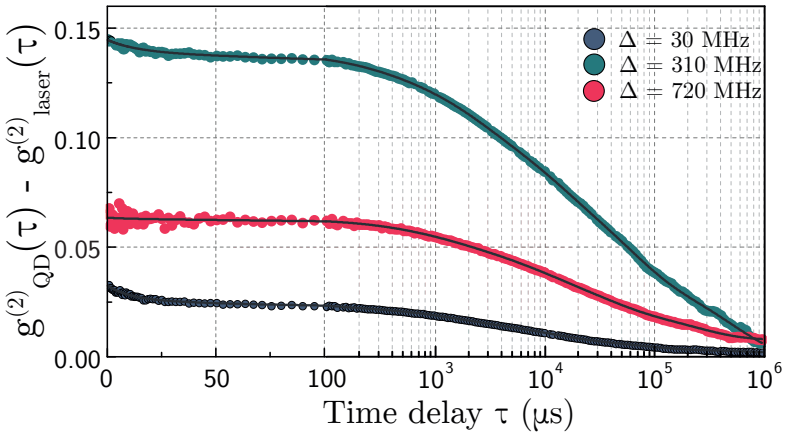

Figure 2.3: Resonance fluorescence autocorrelations for QD A driven at three detunings, at s = 0.28 (corresponding to the data of Figure 2.1. Multi-exponential fits to the data are also displayed.

telegraph noise a single exponential decay is expected [159] and a set of correlation times indicates several fluctuation processes are present: for QD A we resolve six timescales ranging from about 10 μs to 1 s in the fit. Detailed data on timescales and amplitudes of the individual correlation decays for both QD A and QD B are presented in Fig. 2.4. QD B exhibits very similar timescales to QD A suggesting that the underlying processes are common to this sample. Six exponential decays were consistently found for the data of both QDs at all detunings.

For both QDs, amplitudes (left column) corresponding to correlation times (right column) of $\sim$ 1 ms and longer are clearly reduced on resonance. In contrast, the shortest correlation time amplitudes are maximal on resonance. We compare this detuning dependence with the discussion of noise amplitudes around Fig. 2.2, and discern that electric field fluctuations make the dominant contribution to noise on timescales of 1 ms and longer. We label these timescales $\tau_3 - \tau_6$. In contrast, the detuning dependence of the τ_1 process points to magnetic field fluctuations as source of noise. However, the large number of noise sources present for both QDs can give rise to dependencies between fit parameters and make a direct identification challenging. The correlation amplitudes corresponding to τ_2 ($\sim$ 30 - 300 μs) highlight the ambiguity in this approach: the detuning dependence does not fit into a single category, suggesting contributions from both noise sources. Similarly, we cannot exclude the presence of electric field noise in the fastest decay (10 μs) in this measurement, while Overhauser field fluctuations could also be contributing to longer-correlation decays.

There are two notable differences between QD A and QD B. The first is easily explained in terms of power broadening as QD B is driven at s = 0.92, resulting in a somewhat smoother and broader decay amplitude profile with respect to detuning than in the case of the weakly driven QD A. The second is that the amplitudes themselves are reduced

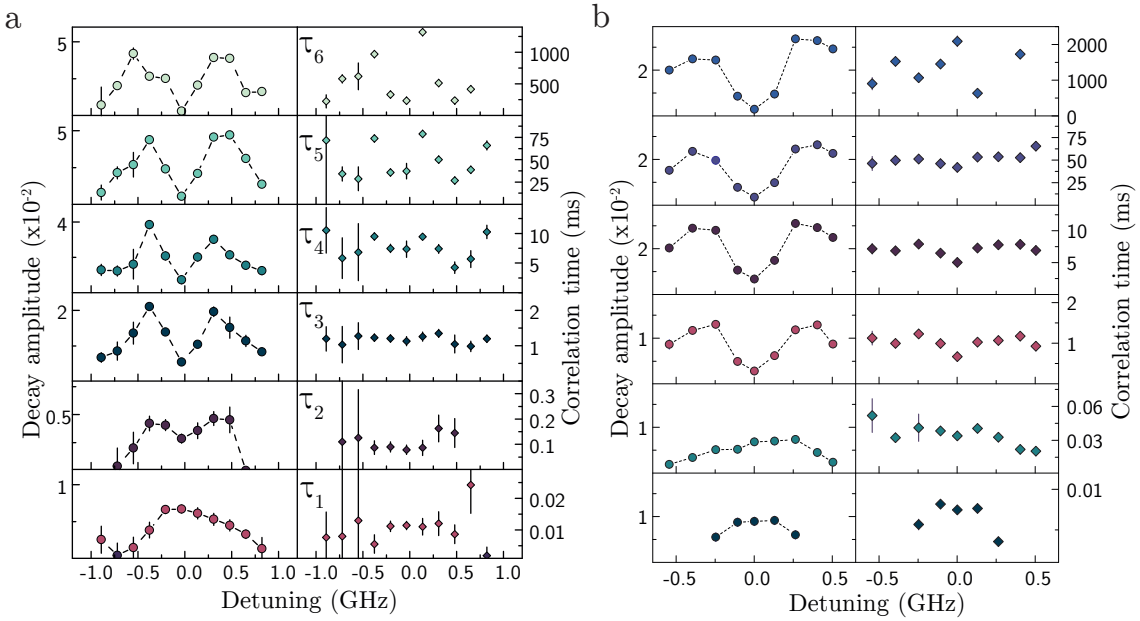

Figure 2.4: Detuning-dependent bunching decay amplitudes. a) The results of multi-exponential fits to detuning-dependent data at a laser power corresponding to s = 0.28 for QD A. The left-hand column indicates the amplitudes of each component, and the right the associated time constant. b) Similarly obtained results for QD B driven at s = 0.92.

for QD B. There are several possible explanations: this could be a manifestation of the power broadening of the resonance which leads to reduced sensitivity as the detuning fluctuates. It could also be that QD B has a somewhat smaller Stark shift (260 MHz/mV) than QD A (340 MHz/mV) and is inherently not as sensitive to electric field fluctuations. Finally, QD B may be subject to reduced electric field fluctuations simply due to being in a slightly different location on the sample. An attempt to distinguish these effects and make quantitative statements about the local electric field is pursued in Section 2.4.

The timescales we associate with electric field processes here are relatively slow in comparison to the case of non-resonant excitation, where timescales ranging from tens of picoseconds [160] to a few microseconds [161] have been measured, and are attributable to a variety of carrier trapping and escape processes that are activated by the non-resonant excitation. However, the slow noise we uncover is in good agreement with other work using solely resonant excitation [25] where the addition of non-resonant excitation produces the faster electric field noise processes on top of what is measured here. In general, this indicates that using RF as a weak probe of QDs is a good way to study the electrostatic environment in an 'undriven' regime.

A single exponential decay with correlation time τ_c is indicative of a single relaxation process [161], where the corresponding power spectrum (directly related via the Wiener-Khinchin theorem) is a single Lorentzian peak with a width that is proportional to $1/\tau_{process}$ [159]; such Lorentzian power spectra have been identified in Ref. [25]. In

our data we are able to consistently extract between 4 and 6 exponential decays, which suggests this is the number of distinct processes contributing to noise. It is possible to model the electric field fluctuations by a Gaussian distribution of local electric fields; this is a good description for the effect of noise upon photon counting statistics as discussed in Ref. [27], also discussed in Chapter 3, and used below in Section 2.4. However, a Gaussian distribution is consistent with a larger number of electric field values, and not obviously in keeping with a small number of processes. One picture is that a relatively small number of independently fluctuating charge traps, N, can be occupied or unoccupied leading to 2^N possible electric field values at the position of the dot. In addition, single decay timescales in the autocorrelation may be associated with many similar charge traps rather than single locations, potentially increasing N.

In our model of autocorrelation bunching amplitudes, however, we choose not to focus upon individual noise processes, but to represent them by the total amplitude alone. The effects at different timescales are considered to be independent of each other.

Background subtraction Systematic errors were accounted for by taking reference measurements of laser photon streams at comparable count rates, and subtraction of the corresponding autocorrelation from that of the QD RF. Figure 2.5 shows the treatment of data for two examples. This background data is taken with the QD transition detuned from the resonant laser and the polarization suppression is relaxed to gain the same photon count rates. While APD afterpulsing appears to have a pronounced effect at time delays up to about 1 μs, small corrections resulting from the subtractions are visible for time delays as large as 100 μs, rendering it necessary to take into account background for all data. The longer time correlations are likely due to intensity fluctuations of the laser coupled into the microscope. Thus, the autocorrelation function depends sensitively on experimental settings, such as APD count rate or laser power stabilization, and changes when equipment is exchanged. For this reason, the reference measurement of the laser autocorrelation was measured systematically to replicate experimental conditions as closely as possible.

2.3.1 Unambiguous discrimination of magnetic field noise

In order to discriminate the noise sources unambiguously it is possible to isolate magnetic field noise in the QD fluorescence using two-color excitation. The concept is illustrated in Fig. 2.6(a). Two lasers of equal power drive the QD transition at equal and opposite detuning from resonance. Linear Stark shifts due to changes in the ambient electric field (right) cause opposite changes in intensity of resonance fluorescence at each frequency. Magnetic field noise (left), however, changes the splitting of the resonance and affects absorption equally at both laser frequencies (c.f. white arrows).

Figure 2.6(b) presents a resonance fluorescence time trace for excitation of QD A with a single laser (top) at a detuning $\Delta \sim 250$ MHz, which yields half the fluorescence intensity compared to excitation on resonance. The bottom time trace corresponds to excitation with two lasers at detunings $\pm\Delta$. The total laser power incident on the sample

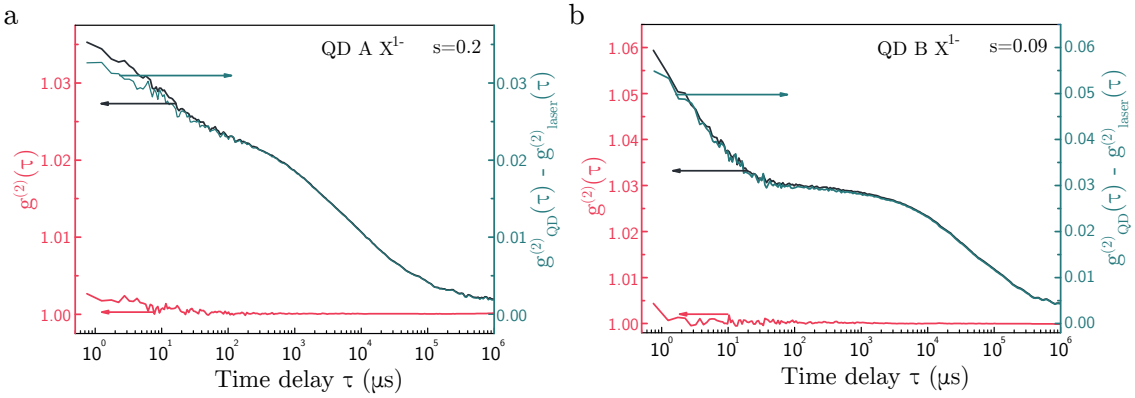

Figure 2.5: Subtraction of systematic background from QD RF autocorrelations a)(red)The autocorrelation for background only at a count rate equal to the mean fluorescence of QD A, with the raw data in blue (left hand axis), and corrected data in turquoise (right hand axis) b)The same process for QD B where the higher count rate was taken into account when recording the background.

corresponds to $s \approx 0.1$ in the single-laser case. In Fig. 2.6(c) the autocorrelation for the two-laser excitation demonstrates a reduction of slow ($\tau > 500$ μs or longer) decay processes by up to two orders of magnitude in amplitude, while noise with short correlation times remains.

The suppression of electric field-related noise in the fluorescence exposes the magnetic field fluctuations, revealing two distinct decays of $\tau_{\mathrm{N1}} = 6$ μs and $\tau_{\mathrm{N2}} = 40$ μs with similar amplitudes, where the subscript N tentatively specifies the origin as nuclear spin noise. In comparison to the single-laser experiment, the amplitudes are similar to those extracted for these timescales, but the ambiguous contribution of electric field noise has been removed. The next fastest correlation decay happens on a 1.5 ms timescale and is reduced by a factor of 50 in comparison to single laser excitation, consistent with residual electric field fluctuations, evident since the placement of the lasers at equal and opposite detuning with respect to a wandering transition cannot be perfectly accurate. The timescales τ_N are discussed in more detail in Section 2.5.

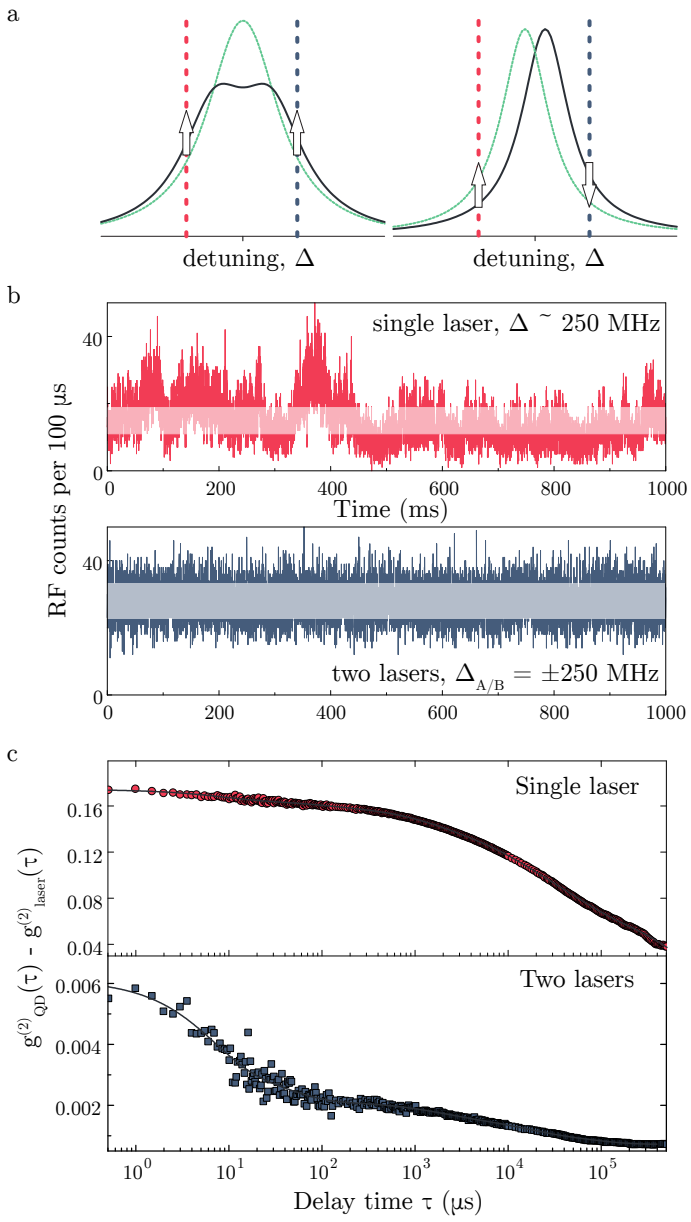

Figure 2.6: Unambiguous discrimination of magnetic field noise. a) Comparison of driving a QD with two lasers equally detuned from a central resonance frequency; a sub-linewidth splitting as induced by a magnetic field should result in intensity noise as indicated by the white arrows (left), where a Stark shift of the central frequency is rendered ineffectual (right) b) Time-resolved resonance fluorescence from the case of a transition driven at a detuning with a single laser, and with two equally detuned lasers. The driving power is maintained to avoid power broadening effects, and white bars indicate the expected standard deviation of the signal where shot noise only is apparent. c) Autocorrelations of the data in part (b), with fits which confirm that the slow noise processes ($\tau > 500$ μs or longer) are reduced by two orders of magnitude by two-laser excitation.

2.4 A quantitative model of electric- and magnetic-field fluctuations

Magnetic and electric field correlation times for QDs in our device are well separated (up to $\approx$ 100 μs for nuclear spin bath fluctuations, beyond 1 ms for electric fields) so that electric field fluctuations can be considered frozen on the timescale of Overhauser field evolution. Here we employ this separation to quantify noise and distinguish the effect of power broadening, different Stark shifts and local effective field fluctuations for three individual QDs.

The model We first calculate the time-averaged effect of a nuclear spin bath with isotropic distribution function on the excited state populations. This results in underlying absorption profile with respect to detuning for a single value of the electric field. The parameters of this four-level model, first shown in the introduction to this work, are reintroduced in Figure 2.7(a), where a small magnetic field Zeeman splits both the ground and excited states. In this model the excited-state splitting, governed by the hyperfine interaction of the nuclear spins with an unpaired hole, is neglected as it is an order of magnitude smaller than the ground-state splitting. As a reference, the ground states are the eigenstates in Faraday geometry, where $m_s = \pm 1/2$ as $|\uparrow\rangle = |1\rangle$ and $|\downarrow\rangle = |2\rangle$. In this situation diagonal transitions are forbidden, where light hole-heavy hole mixing is neglected here. However, due to changes in the Overhauser field vector the electron ground state spin quantization axis shifts over time and hence the selection rules are not fixed. In general, the instantaneous eigenstates will be superpositions of the spin states $|\uparrow\rangle$ and $|\downarrow\rangle$, allowing diagonal transitions for most Overhauser field configurations.

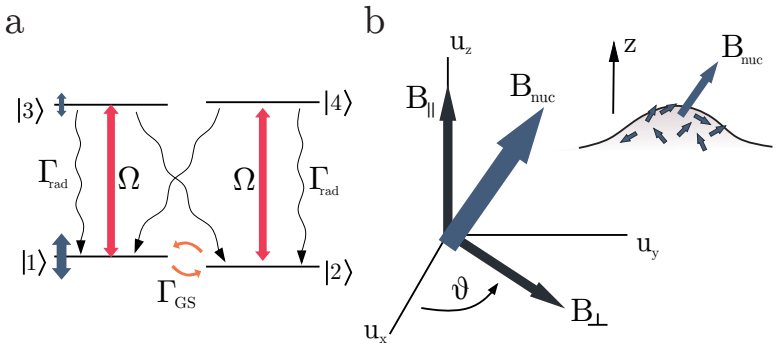

Figure 2.7: Model of X^{1-} interacting with the Overhauser field. a) The four-level system resulting from the X^{1-} interaction with the Overhauser field in the absence of external magnetic field. Γ_{rad} is the radiative decay rate, Ω represents the optical driving frequency, or power, and Γ_{GS} is the ground state electron spin relaxation rate. b) The Overhauser field can be represented by components perpendicular and parallel to the growth axis, or equivalently the optical excitation axis, and is assumed to be isotropic in zero magnetic field.

Figure 2.7(b) describes the Overhauser field as components parallel and perpendicular

to the QD growth axis. In addition to the dipole term of the Hamiltonian describing the interaction of the four-level system with light, there is the interaction with the Overhauser field, B_N:

$$\begin{aligned}\hat{\mathrm{H}}_{\mathrm{HF}} &= \frac{1}{2}\mu_B \mathrm{g}_e \overrightarrow{\boldsymbol{B}}_{\boldsymbol{N}} \cdot \overrightarrow{\sigma} \\ &= \frac{1}{2}\mu_B \mathrm{g}_e \Big(B_{\parallel}(\sigma_{11} - \sigma_{22}) + B_{\perp}(e^{i\theta}\sigma_{21} + e^{-i\theta}\sigma_{12}) \Big),\end{aligned} \tag{2.6}$$

where we define the projection operators $\sigma_{ij} = |i\rangle \langle j|$, with i, j = 1...4 corresponding to one of the four levels of X^{1-}. The angle θ is indicated in Fig. 2.7(b). The second term produces a mixing between the two Faraday-geometry spin eigenstates, and this allows the otherwise forbidden diagonal transitions to occur. In essence, it is the Voigt geometry contribution to the overall Hamiltonian.

For the Overhauser field vector we choose an isotropic Gaussian distribution (equation 2.4). A numerical integration over this distribution is used, and the resultant average lineshape is a starting point for the model of electric field fluctuations.

The sub-linewidth ground state splitting results in a broadened absorption lineshape as indicated in Figure 2.8. For the two-level system the curve represents the expected power-broadened Lorentzian. Interestingly, in the case of the X^{1-} level structure, the lineshape is still very much indistinguishable from a Lorentzian, albeit broadened. The absorption profile is not obviously split as 25mT corresponds to $\sim$ 200 MHz, which compares to the radiative linewidth $\approx$ 220 MHz and the absorption is integrated over a range of values of B_{nuc} from zero to the extremes of the distribution. The amplitude of both curves have been scaled to unity here, while in actual fact, the intensity is reduced in the four-level case, partially due to spin pumping of population away from the ground state momentarily addressed by resonant excitation. This becomes possible as the Overhauser field creates a Voigt-like geometry [128]. In general the apparent lineshape for a single frozen fluctuation of the Overhauser field is a complex interplay of detuning and selection rules.

Our experimental data contain several processes on different timescales associated with electric field fluctuations, however we are able to characterize the combined noise averaged over full measurement times with a single field distribution function [27]. In this case it is the sum of noise amplitudes that we are concerned with and therefore a model which treats dynamics on multiple timescales is not required. We assume that during the measurement time of 100—200 s the full range of possible electric field values is explored. The transition frequency distribution $P(\Delta\delta)$ is represented by a Gaussian distribution about a central resonant frequency:

$$P(\Delta\delta) = \frac{1}{\sqrt{2\pi\sigma_E^2}} \exp\Big[-\frac{1}{2}\Big(\frac{\Delta\delta}{\sigma_E}\Big)^2 \Big]. \tag{2.7}$$

Here $\Delta\delta$ is the change in detuning due to the Stark shift of the instanteous resonant frequency relative to the central (mean) resonant frequency. In other words, $P(\Delta\delta)$ is

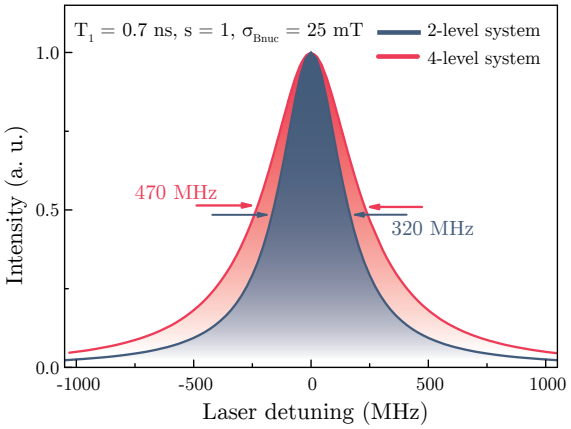

Figure 2.8: Absorption lineshape of two and four-level systems, resulting from calculations where in the four-level case absorption is integrated over the results from Overhauser fields with $\sigma_B = 25$ mT. A radiative lifetime $T_1 = 0.7$ ns is assumed.

the probability distribution of momentary shifts in detuning compared to the measured value, which is extracted from time-averaged absorption measurements of the quantum dot spectrum. The distribution has a standard deviation, σ_E, corresponding to a full-width at half-maximum $\Delta_{\mathrm{FWHM}} = \sqrt{8 \ln 2}\, \sigma_E$. The width of this distribution indicates the relative contribution of electric field noise to the resulting spectral linewidth.

Intensity autocorrelations The intensity autocorrelation of a time-binned signal written as $\{x_1, x_2, \ldots, x_N\}$ with mean $\langle I(t) \rangle = \bar{x}$ has a zero time delay amplitude given by:

$$g^{(2)}(0) = \frac{1}{N} \frac{\sum_i x_i^2}{\bar{x}^2}. \tag{2.8}$$

This can be written directly in terms of the variance σ^2 and the mean as

$$g^{(2)}(0) - 1 = \frac{\sigma^2}{\bar{x}^2}. \tag{2.9}$$

We therefore may relate the variance of our entire signal time trace to the full amplitude of the bunching in the autocorrelation, and likewise make this comparison between the variance found from the model and the experimental bunching amplitudes.

Parameters required by the model The sensitivity to electric and Overhauser field fluctuations is determined by the underlying Lorentzian absorption spectrum of a QD transition. The radiative lifetime T_1 gives directly the natural linewidth of the transition, the linewidth is broadened under excitation, $\Gamma_{\mathrm{FWHM}} = (2\pi T_1)^{-1}\sqrt{1+s}$. Consequently, the sensitivity to both electric and magnetic field noise drops as the QD transition is saturated. To model the bunching amplitudes for a particular QD it is necessary to measure both the radiative lifetime and saturation behaviour of every QD.

The excited state lifetime T_1 is measured under pulsed resonant excitation, using an electro-optic modulator with 10 GHz bandwidth driven by voltage pulses with sub-50 ps

rise and fall times. QD resonance fluorescence detection times are recorded in bins of 162 ps width with respect to a trigger signal derived from the pulsed voltage source. Data for QDs A, B and C are plotted in Fig. 2.9, together with single-exponential fit functions. The error is the standard error in the mean for independent fits to decay curves under repeated measurement.

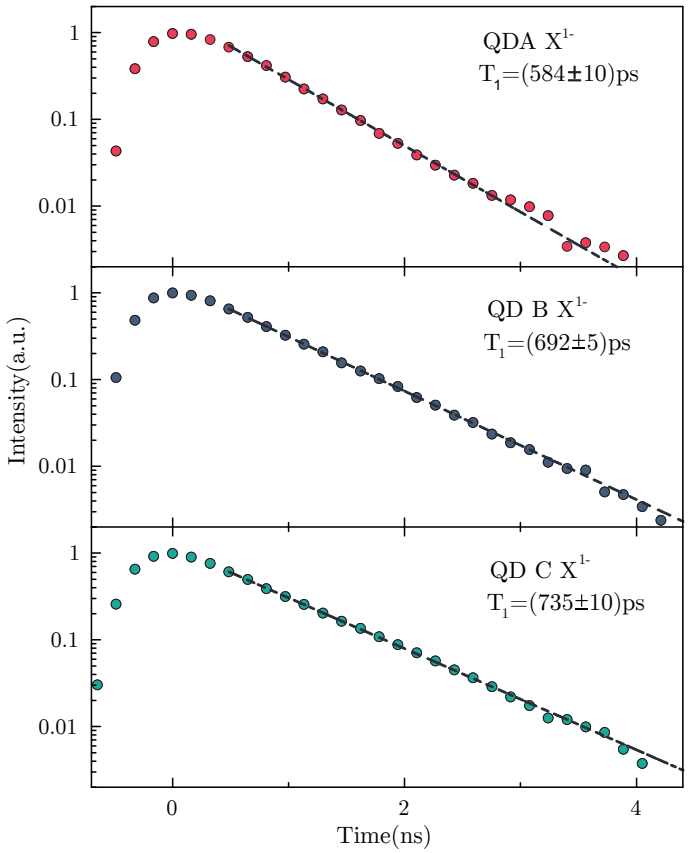

Figure 2.9: Radiative lifetimes of QD A, B and C, measured using weak, pulsed resonant excitation.

A short lifetime translates to a broad natural linewidth $\Gamma = (2\pi T_1)^{-1}$ and consequently a smaller sensitivity to noise in general. For QD C we measure $T_1 = (735 \pm 5)$ ps, yielding a greater overall sensitivity to noise than both QD A and QD B.

2.4.1 Application of the model to electric-field-related bunching amplitudes

In Figure 2.10 the model is applied to the autocorrelation amplitudes. The total amplitude is taken at a time delay where the dominant contributions due to nuclear field fluctuations have decayed ($\tau \sim 200$ μs for QD A), and the noise due to the electric field occurs on all longer timescales. The known values of radiative lifetime and saturation power were used to inform the model, and a series of simulated amplitudes across the entire detuning range for each power were compared to those measured, taking a least-squares approach. The

free parameters are Δ_{FWHM} representing the full-width-half-maximum of the Stark-shift-induced detuning distribution function (equation 2.7) and the standard deviation of the Overhauser field distribution (equation 2.4), σ_{B}.

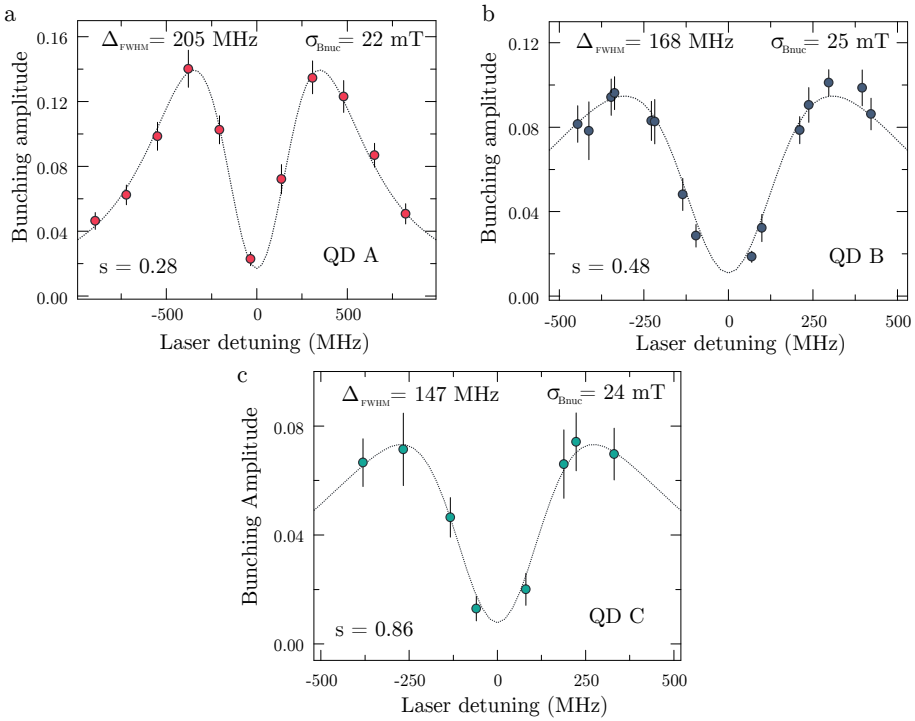

Figure 2.10: Fit of four-level electric field noise model to total electric field bunching amplitudes. The parameters for each dot are represented in the figure and discussed in the text.

In Fig. 2.10(a) this fluctuation amplitude for QD A (data as circles) is described using the time-averaged model (curve). The simulation is in agreement with the data for an Overhauser field with standard deviation σ_{B}= (22±2) mT and an electric field noise broadening Δ_{FWHM} = (205±7) MHz. Taking into account the measured Stark shift for this QD we arrive at an electric field fluctuation distribution with a FWHM of (3.2±0.1)10^3 V/m. For QD B we extract σ_{B} = (25±2) mT and ΔE_{FWHM} = (3.5±0.2)10^3 V/m, which corresponds to a transition frequency broadening of (168±11) MHz [Fig. 2.10(b)]. As a final example, driving QD C at close to saturation (S = 0.86) we find that Δ_{FWHM} = (147±5) MHz, or equivalently ΔE_{FWHM} of $(2.3 \pm 0.1)10^3$ V/m. The Overhauser distribution is σ_{B}= (24 ± 2) mT. The electric field noise in all cases corresponds to sub-radiative linewidth distributions (see Figure 2.9) and as such this sample is relatively 'clean' when compared to the sample studied in Section 2.6.1, for example.

While this model does not include the fluctuation processes of nuclear spins explicitly, it is possible to obtain a characteristic Overhauser field distribution through its impact on the underlying level structure. It is notable that the distribution of values amongst QDs is remarkably small. This is expected because the QDs have similar resonant frequencies (λ

$\approx$ 969nm), and therefore geometries, which fixes the number of nuclear spins interacting with the electron wavefunction. The values of 22-25 mT are consistent with those expected theoretically [126, 137, 162] and measured experimentally [163], where estimates range from 10–50 mT. In particular the values are in close agreement with that recovered in Ref. [164] from a measurement of electron spin dephasing.

The electric field distributions seen by QD A and QD B appear to be quite similar, indicating that the difference in autocorrelation amplitude was due primarily to the different Stark shifts and the power dependence. In fact, QD B is experiencing a marginally larger local electric field distribution but is simply less sensitive. However, the fit to the model suggests that QD C genuinely experiences reduced electrical noise. This is to be expected if the origin of the noise is external charge traps; the precise field distribution then depends upon an individual quantum dot's position [25, 152].

It is interesting that a Gaussian distribution, typically a good description for the overall effect of a large number of contributing processes, is suitable here. Many studies have localized a few charge traps, for example forming in the GaAs/AlGaAs capping layer/blocking barrier interface [151]. However, where N traps can be unoccupied or occupied, this gives 2^N local electric field configurations, so it is not inconceivable that relatively few charges are described by a Gaussian distribution. We must also not discount the possibility that the gates and associated wires leading from the voltage source, and the voltage source itself, could deliver a small amount of electrical noise, although we note that a strong 20 ms timescale that would be expected with 50 Hz noise, for example, is not found in the autocorrelations.

Taken in conjunction with the evidence from Section 2.3 which reveals a number of similar timescales for each QD on this sample, we suggest distinct classes of charging processes with signature timescales, i.e. that the noise correlation times are a global sample property. However, the noise amplitude for a single QD is a local property and while some samples may in general have fewer charge traps than others due to details of growth, it must be determined on a QD by QD basis. This will be explored in more detail in the next Chapter.

This model does not attempt to precisely locate individual charge traps, as previous work has done. Rather, it distinguishes the effect of power broadening and local noisy electric fields of different magnitudes, while confirming that the inherent Overhauser field magnitudes are consistent, both between QDs and with extant literature.

It is important to note that this model was only applied when QDs were driven below their saturation power; the presence of significant power broadening renders the model less sensitive and more speculative. Instead in the next section we focus upon the power dependent dynamics of the fastest timescales. The short timescale bunching in autocorrelations of resonance fluorescence is a direct probe of the changing electron Zeeman energies, and as such it reveals the dynamics of the Overhauser field which have direct consequences for the electron spin coherence.

2.5 Power dependence of nuclear-spin correlation times

QD B has the advantage of a relatively small Stark shift and also a longer radiative lifetime, leading to greater overall sensitivity to noise but a reduced sensitivity to the electric field. For this reason it is used to study the power dependence of the two magnetic field timescales identified in Section 2.3.1. QD B is driven resonantly where the laser powers are varied from a tenth to twice the saturation power, and the resulting autocorrelations are displayed in Figure 2.11(a).

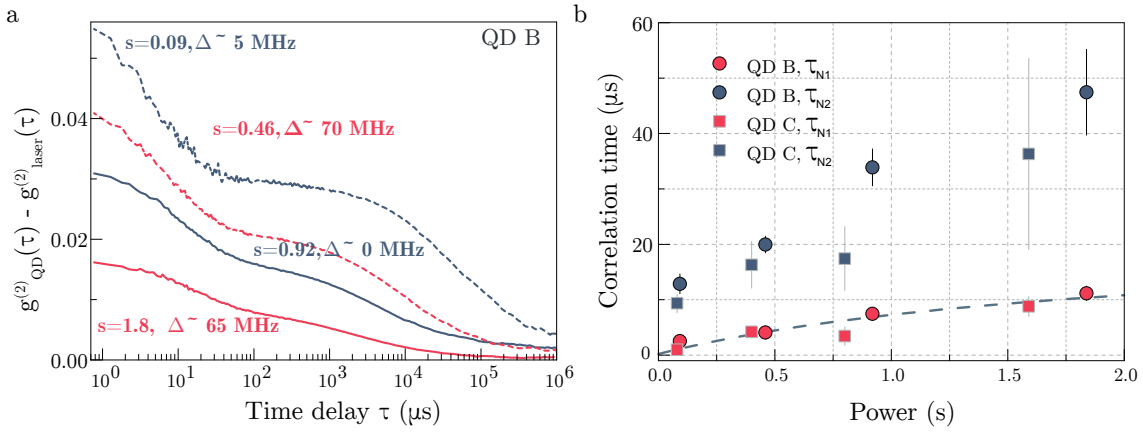

Figure 2.11: Power dependence of nuclear spin correlation times. a) Near-resonantly driven QD B autocorrelations under varied optical power, where the effect of power broadening is apparent. The detuning is an estimate based on an absorption profile extracted from count rates averaged over ¿ 100s, where all values are sufficiently close to the central peak that detuning is not the dominant factor in autocorrelation variation. b) Fits reveal that timescales associated with Overhauser field fluctuations slow down as the driving power is reduced, data for QD C is also included and follows the same trend. The dotted line represents a phenomenological model of Overhauser field fluctuations due to the Knight field of the electron, which becomes motionally narrowed at higher power, and reduced as the ground state electron population is depleted.

The autocorrelation amplitude decreases markedly as a consequence of power broadening, as expected. However, it is notable that the short time dynamics, previously confirmed to be associated with magnetic field fluctuations (see Section 2.3.1), slow down with increasing excitation power. Figure 2.11(b) summarizes the power dependence of the fast timescales for QD B (filled circles). For reference we provide an additional set of data for QD C (light filled squares). Taking QD B data in particular, the correlation times increase from $\tau_{N1} = (2.5\pm0.5)$ μs at $s = 0.09$ to $\tau_{N1} = (11\pm1)$ μs at $s = 1.8$. Similarly, τ_{N2} increases from (13 ± 2) μs to (47 ± 8) μs in the same range. In fact, the ratio of correlation times is approximately constant in our measurements, giving $\tau_{N2}/\tau_{N1} \sim 4.5$ in this case. QD C shows qualitatively the same behavior.

The correlation times measured here can be compared to the established model of nuclear spin dynamics in QDs and their effect on spin dephasing as introduced in Ref. [126].

This measurement technique is sensitive only to the dynamics of the Overhauser field itself, evidenced through the resulting ground state Zeeman splitting of the electron. The power dependence suggests that the nuclear spin dynamics are dependent upon the ground state electron spin, as might be expected for singly charged dots [144]. The nuclear dipole-dipole interactions, which act upon a timescale of $T_{dip} \sim 100$ μs, could be associated with the second timescale τ_{N2}. However, it is possible to exclude direct dipolar coupling of nuclear spins; not only is it a local interaction that depends only weakly on the dynamics of an electron spin, it is a relatively weak interaction and many studies suggest that strain and the resultant effective quadrupole field are capable of suppressing it [144, 148, 165].

The nuclear spins' precession in the Knight field, $T_{K\Delta} \simeq \sqrt{N}T_{\Delta}$, resulting in $T_{K\Delta} \sim 1$ μs for $N = 10^5$ is similar to τ_{N1} at low power. We suggest the fastest timescale, τ_{N1} is due to the effect of the Knight field. Thus a tentative explanation of the τ_{N1} behaviour is possible: first it is noted that the Knight field is present where the QD is in the ground state. The field is negligible in the excited state as the electrons form a spin singlet and the heavy hole has a much weaker hyperfine interaction. Consequently, the rate of Overhauser field change $\gamma_{N1} = 1/\tau_{\mathrm{N1}}$ should decrease in line with the optical saturation and reduction in ground state population ρ_g. Furthermore, the Knight field is affected by the electron spin lifetime, where electron spin flip rates comparable to, or faster than, the nuclear precession rate in the Knight field result in a motional averaging, which suppresses the effect of the Knight field.

The electron spin-flip rate is a combination of spin-flip cotunnelling processes which are negligible ($1/\gamma_{\mathrm{cot}} > 100$ ms^{-1}) for this device at the centre of the X^{1-} plateau [97], and the spin-flip Raman transitions allowed at 0T by Overhauser field configurations that produce an effective Voigt geometry. Spin pumping via this channel occurs on average after three optical cycles in 0T [128]:

$$\gamma\mathrm{sp} = \frac{s}{2\,(1+s)\,\mathrm{T}_1} \times \frac{1}{3}, \tag{2.10}$$

which corresponds to tens of nanoseconds spin lifetime at low excitation power, and shorter as power is increased. This dominates over cotunnelling effects, and is combined with the Knight field in a phenomenological model for these Overhauser field dynamics:

$$\gamma_{\mathrm{N1}} \approx \frac{\gamma_{\mathrm{K}}}{\gamma_{\mathrm{K}} + \gamma_{\mathrm{sp}} + \gamma_{\mathrm{cot}}} \cdot \gamma_{\mathrm{k}}\rho_{\mathrm{g}}, \tag{2.11}$$

where $\gamma_K = 1/T_{K\Delta}$ is the rate of change of Overhauser field due to the Knight field in the absence of motional averaging, and γ_{N1} is reduced by the presence of electron spin flips with rate γsp. The value $T_{K\Delta} \simeq \sqrt{N}T_{\Delta} \sim 200$ns provides reasonable agreement with the data as plotted as a dashed line in Figure 2.11(b). $T_{K\Delta} \sim 200$ ns suggests that N $\sim$ 5 x 10^4.

It is important to note that the expected Knight field of $\ll 10$ mT is relatively weak

compared to the effective field due of quadrupolar coupling $B_Q \sim 100$ mT, and that consequently in an externally applied field it is quadrupolar effects that dominate the dynamics of the Overhauser field [17] as a dominant perturbation to the precession around B_{ext}. However, in the absence of an externally applied field each nucleus can be considered to have a quantization axis determined by a heirarchy of B_Q and then the Knight field [24]. The timescale is power dependent and these results suggest that the electron spin polarization remains relevant to the Overhauser field behaviour at low fields, even if high field behaviour is independent of the Knight field.

Concerning the origin of τ_{N2}, it also increases with power, indicating again that the process permitting nuclear spin bath fluctuations is likely dependent upon ground state spin population, and that optical pumping and ground state depopulation results in a quenching of the process responsible. A possible mechanism is indirect nuclear-nuclear spin flips through a mediating electron [144, 166, 167].

2.6 Further discussion

2.6.1 Identification of noisy samples

In Figure 2.12 we investigate a completely different sample; here the wafer was designed to have a 720 nm sacrificial AlGaAs layer etched out beneath the usual heterostructure, and above a DBR layer, such that a new surface is exposed 155 nm below the quantum dot layer. When etched to produce a gap with n = 1, this could potentially result in increased out-coupling of photons into a collection mode. Several QDs were investigated and this is a good example of RF autocorrelations in use as a rapid characterisation technique.

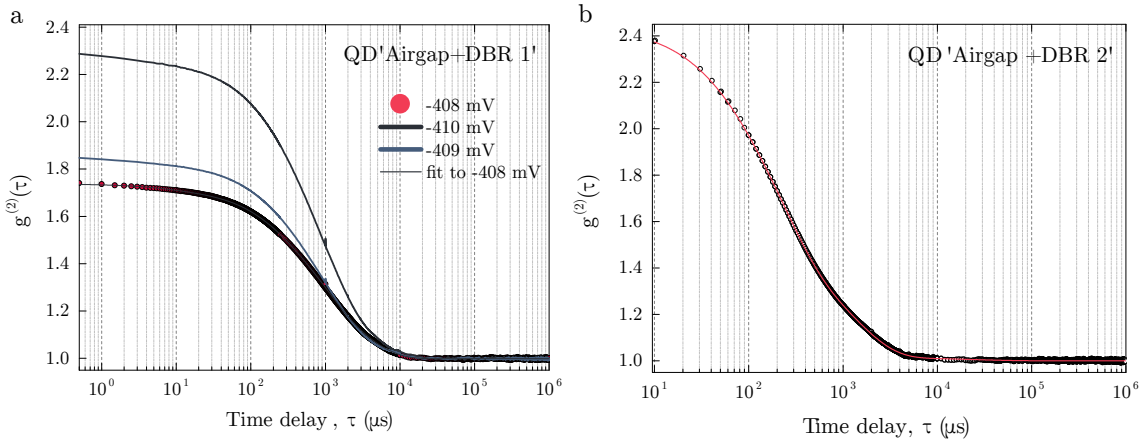

Figure 2.12: Autocorrelations from an alternative sample, with an 'airgap' etched 155nm beneath the QD layer. a) Autocorrelations from QD 1 indicate strong bunching due to processes on timescales associated with electric field noise, and detuning dependence confirms this interpretation. b) Similar data from QD 2 which presents strong bunching due to 'slow' noise processes.

Figure 2.12(a) displays autocorrelations from 'QD 1' driven below saturation power. The total autocorrelation amplitude is markedly higher than for any dot from the sample used in the rest of this chapter, and the dominant decays of 100 μs to 1 ms have been previously identifed with electric field noise. The point corresponding to -408mV gate voltage is approximately resonant. The fit to data at -408 mV is best achieved with four timescales: $\tau_1 \approx 7$ μs, $\tau_2 \approx 200$ μs, $\tau_3 \approx 900$ μs, and $\tau_4 \approx 4$ ms. It is important to note that of the total bunching amplitude of 0.74, 0.62 (or 84 %) is associated with timescales longer than 100 μs. The bunching amplitude is significantly reduced on resonance, which agrees with the interpretation of the dominant timescales as primarily due to electric fields.

Figure 2.12(b) presents data from another QD ('QD 2') from this underetched sample, driven resonantly. The bunching is even more pronounced, and the multi-exponential fit reveals the presence of two dominant decay components at 200 μs and 1300 μs, and a weaker decay at $\approx$ 50 μs. As such, it broadly agrees with the data for QD 1; in general this sample (from a survey of several dots) appears to have much larger bunching on 'slow' timescales associated with electric field noise, possibly due to an increased number of trapped charges on the etched surface that has been exposed within 155 nm of the QDs. While the top surface of the sample remains 140 nm from the QDs, this is created in an MBE grown process and is less likely to be subject to the same level of defects as the bottom surface, as the etching process was found to be somewhat inconsistent and had a tendency to leave residual structures. Having insufficient sample pieces available, it was not possible to directly compare the sample with and without the etching process, however, the amplitude of short timescale autocorrelations here are far above anything seen in any MBE-grown sample we have tested. It is reasonable that the etching process is responsible for a severe reduction in quality of the quantum dot emission.

2.6.2 Comparison to quantum dot hole spin behaviour

It would be remiss in any discussion of the implications of this solid state environment for the electron spin behaviour to completely neglect the impact on a trapped hole spin. We previously mentioned that the predominantly p-type wave-functions of the holes are insensitive to the contact hyperfine interaction by virtue of having zero amplitude at the nucleus. Instead, they must interact with nuclear spins through a dipole-dipole hyperfine interaction, where the magnetic dipole moment of a purely heavy-hole state is along the $\pm$z, resulting in an Ising-like interaction. This means that holes of pure heavy-hole character interact only with the z component of the fluctuating Overhauser field. Measurements of the nuclear spin induced Zeeman splitting place the hole-nuclear interaction at 10 % of the electron-nuclear spin bath coupling [130–132]. It is for this reason that the excited state splitting of the X^{1-} due to nuclear spins was neglected in our model by way of a simplifying approximation.

It is expected that an in-plane magnetic field suppresses the weak anistropic coupling to the Overhauser field, and the hole spin T_2^* should be extended beyond that seen for

an electron spin. We note that a typical electron spin T_2^* measured for our samples is 1.9 ns [17]. Initial experiments placed the T_2^* of the hole at $\approx$ 100ns [168], although in more recent work T_2^* was measured above 460 ns without recourse to nuclear spin bath polarization [169].

Heavy hole character might be dominant but it is not complete, and the mixing with light-hole states and the split off spin-orbit band results in an interaction that is no longer perfectly anisotropic. Such problems could be solved by altering the geometry of quantum dots to force more heavy-hole dominance. It is key however, that holes have an electric field sensitivity in their g-factor due to their spin-orbit coupling [170], which results in hole spin dephasing due to electric field noise in samples. In combination with the poorer quality samples typical available for hole spins this was a strong limitation of the hole T_2^*, but high-quality device growth has enabled this to be overcome [169].

Coherent optical control of the hole spin has been demonstrated, and in particular a spin-echo experiment has initially suggested that the T_2 of a hole is ~ 1 μs [171], although it is important to note that in this experiment the measured T_2^* was only 2.3 ns indicating perhaps that this sample was suffering extensively from charge noise. Coherence times extended beyond the microsecond regime have yet to be demonstrated for hole spins. However, there is great reason to be optimistic if indeed charge noise is the limitation; the timescales of electric field noise indicated here could easily be filtered by appropriate spin-echo or dynamical decoupling schemes.

2.6.3 Summary

In this chapter the timescales and relative amplitudes of noise processes evident in QD resonance fluorescence have been explored through a relatively simple technique that not only can be used for rapid characterization of new samples, but allows for more detailed study. On the basis of these measurements we are able to identify samples which contain the 'cleanest' QDs. The electric field noise characteristics are extrinsic and vary QD-by-QD, but more pronounced differences are found between samples. The 'Chef 2' sample that is the chief focus of this chapter has a relatively small contribution from electric field noise (compared to other available samples) and thus is used in further work in this dissertation. In the next chapter we introduce a rapid characterization method that focuses upon quantifying the spectral diffusion resulting from slow noise.

In contrast, the Overhauser field is an intrinsic and unavoidable aspect of this type of QD. A change in the Overhauser field affects the effective Zeeman splitting of the electron and hence its coherence. In this Chapter the dynamics of the Overhauser field in zero applied magnetic field are shown to be power-dependent and this is evidence that the central electron spin has a direct impact. The perturbation of the Overhauser field is reduced with increasing excitation power, and possible mechanisms are considered, including the motionally-averaged Knight field of the electron as well as electron-mediated indirect nuclear-nuclear interactions.

However, recent work at non-zero applied magnetic field has demonstrated that the dominant mechanism in Overhauser field evolution becomes the nuclear quadrupolar coupling to inhomogeneous electric field gradients present in these strained QDs. This results in a 'hard limit' to the extension of spin coherence through spin echo or dynamical decoupling of $T_2 \sim 1$ μs in these QDs [17], which could only be significantly overcome by the use of unstrained QDs.

In conclusion, the processes governing Overhauser field evolution are complex and dependent upon a number of conditions, where the quadrupolar coupling, electron spin Knight field and nuclear dipole-dipole coupling act as successively smaller perturbations to the evolution of a nuclear spin bath in an external magnetic field. In Section 2.5 we attempted to identify the origin of magnetic field noise components; further work could include systematic measurements away from the centre of the X^{1-} plateau, where the co-tunneling rate is increased. Here the electron spin flip rate γ_{sp} should become large enough to destroy the effect of the Knight field, as such the power dependence of the nuclear spin correlation times would be expected to vanish. Additionally, by examining whether the power-dependent processes are dominated by the combination of an externally applied magnetic field B_{ext} and the quadrupolar coupling it would be possible to confirm the relative importance of the Knight field.

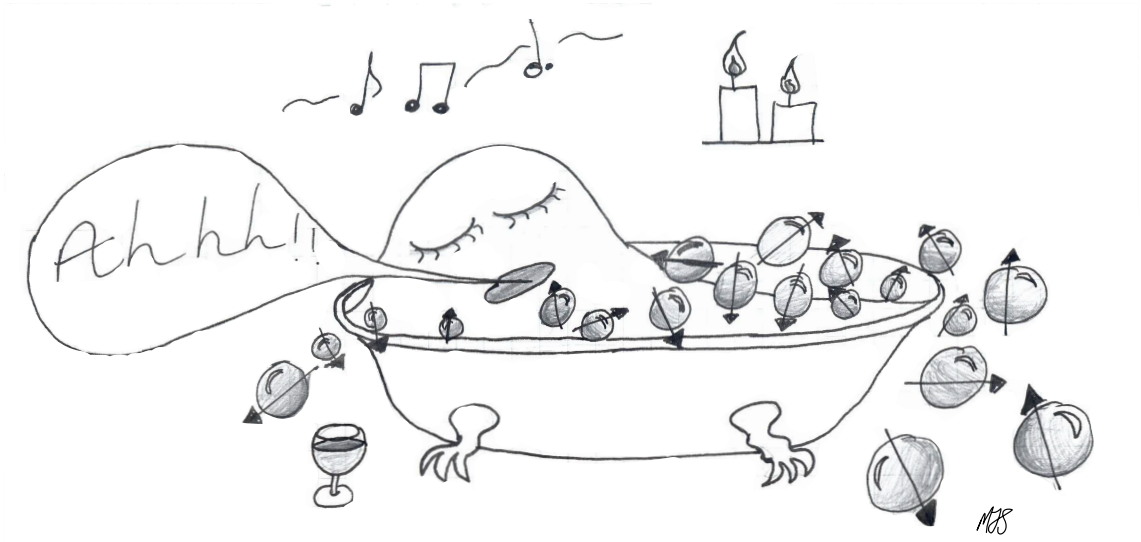

After a long, hard microsecond Felix the electron relaxes in a nuclear spin bath

Chapter 3

Photon counting statistics: a technique for rapid QD characterization

In the previous chapter the timescales of the noise seen in resonance fluorescence were surveyed, and relative contributions of local electric fields and the nuclear Overhauser field could be assigned. In particular, whilst the Overhauser field is reasonably consistent between QDs, there is variation even upon the same sample in terms of electric field noise. Consequently, quantifiying the noise using a rapid characterization method is highly desirable. In this chapter we present such a method based upon single-photon counting statistics, and their deviation from the expected Poisson distribution. This work is published in Reference [27].

First, we lay theoretical foundations and discuss how environment noise impacts upon photon counting statistics. It is demonstrated that the model developed fits well to example QD data. We use this method to quantify the spectral diffusion for QD C, which was studied in the previous chapter, enabling a direct comparison of the two approaches and delineating some of the limitations of this model. Following this a survey of further QDs under changing excitation power and position on the sample is undertaken.

3.1 Diffused Poisson distribution model

Photons scattered by a single emitter display sub-Poissonian intensity statistics, resulting in the well-known antibunching dip in the intensity autocorrelation [106] on the timescale of the radiative lifetime T_1. On timescales much greater than T_1 photons from an ideal two-level system simply follow Poisson statistics characterised by a mean rate of photon emission and a variance equal to the mean, which corresponds to the long-timescale autocorrelation $g^{(2)}(\tau) = 1$ typical of coherent light [116]. The probability distribution of

Poisson statistics is simply given by:

$$P(k_{\text{bin}}) = \frac{m^{k_{\text{bin}}} e^{-m}}{k_{\text{bin}}!}, \tag{3.1}$$

for a mean number of m photons per measurement time bin. In other words, this is the probability distribution of k_{bin} detections per bin, and in general is a peaked function, where the maximum point shifts to increased k_{bin} as m increases.

For a simple two-level system the mean value m is linked to the excited state population and as such depends upon the detuning of the driving field from the transition, as well as the power with which the transition is being driven. Overall, when considering QD fluorescence we may describe the mean counts per bin m as determined by the collection and detection efficiency $\eta_{\text{detection}}$, the duration of a detection bin t_{bin} and the excited state population:

$$m(s, \Delta) = \eta_{\text{detection}} \times t_{\text{bin}} \times \frac{1}{2T_1} \frac{s}{1 + s + 2(2\pi\Delta)^2 T_1 T_2}, \tag{3.2}$$

where the final factor is the rate of QD photon emission, as determined by the excited state population and the radiative lifetime T_1 (see Introduction, Section 1.3.2). Δ is the detuning from resonance and T_2 is the coherence time of the two-level system. The saturation parameter s is linked to the Rabi frequency Ω by $s = \Omega^2 T_1 T_2$, and experimentally $s = 1$ when the scattered intensity is equal to half the maximum value. As a shorthand notation we define the amplitude $a(s)$ to denote the mean counts on resonance $a(s) = m(s, \Delta = 0)$. Thus,

$$a(s) = \eta_{\text{detection}} \times t_{\text{bin}} \times \frac{1}{2T_1} \frac{s}{1 + s}, \tag{3.3}$$

provides a simple link to experimental data. As a result the mean counts to be used in equation 3.1 are detuning and excitation-power dependent.

This concept is illustrated in Figure 3.1. In panel (a) the absorption lineshape of an ideal QD is shown for three distinct values of the detuning relative to the laser frequency. When a laser of fixed power drives the QD transition, the mean fluorescence intensity decreases with laser detuning, $|\Delta|$. Each situation results in a different Poisson distribution. The photon counting intensity histograms arising from these three situations are displayed in the right hand side of the panel using the same colour code.

For a semiconductor QD, the presence of electric field noise in the environment results in a time-dependent detuning between the resonant excitation laser and the QD's instantaneous resonance frequency thereby modifying the photon emission rate. To model the spectral diffusion, we take a weighted sum of the probability distributions over a range of permitted detunings, and the photon counting histograms $P(k_{\text{bin}})$ from equation 3.1 can be modified to:

$$P(k_{\text{bin}}) = \sum_{\Delta} W(\Delta) \frac{m(s, \Delta)^{k_{\text{bin}}} e^{-m(s,\Delta)}}{k_{\text{bin}}!}. \tag{3.4}$$

$W(\Delta)$ is the weighting function given to the contribution at each detuning. $W(\Delta)$ describes

the probability of a particular environmentally-induced resonance shift in an instantaneous measurement, or equivalently a shift in detuning. Chapter 2 modelled the time-dependent resonant frequencies with a Gaussian distribution to good effect, and we therefore return to that assumption here. For sufficiently long measurement times the distribution is fully sampled and we may express the weighting function as the continuous probability distribution:

$$W(\Delta) = \exp\left[-\frac{1}{2}\left(\frac{\Delta - \delta_{\text{average}}}{\Delta_{\text{diffusion}}}\right)^2 8\ln 2\right]. \tag{3.5}$$

The Gaussian distribution is centred on δ_{average} to describe the effect of spectral diffusion when setting the laser at a finite average detuning from the QD resonance. The magnitude of the spectral diffusion is described by the full-width-at-half-maximum $\Delta_{\text{diffusion}}$ of the Gaussian distribution, this is directly comparable to the description used in the discussion surrounding autocorrelation bunching amplitudes, except in that case the detuning is taken as a fixed parameter that is measured relative to a time-averaged absorption lineshape. Here, the detuning is a parameter in the model, although it is informed by the known gate voltage and Stark shift of the QD.

To illustrate the effect of spectral wandering typically observed in our samples, we show in Figure 3.1(b) a theoretical plot derived from the equations above. We have chosen the physically representative parameters $T_1 = 0.65$ ns, $\Delta_{\text{diffusion}} = 250$ MHz and amplitude $a = 100$ counts per bin (which corresponds to a mean count rate on resonance of 1 MHz being binned to $t_{\text{bin}} = 100$ μs). The driving power is assumed to be equivalent to the saturation power such that $s = 1$. In the case of $\delta_{\text{average}} = 0$, the peak of the distribution displayed in the left hand side of Figure 3.1(b) is lower than the value of 100 expected for a pure Poisson distribution. To the right, three histograms are reproduced in the conventional form for specific detunings: 220 MHz (dark blue), 120 MHz (green-blue), 40 MHz (yellow). Histograms can be double-peaked (e.g. around 120 MHz detuning here) and may generally appear to be bi-modal, but we note this is a natural consequence of taking a sum of Poisson distributions sampling over a non-linear function such as a Lorentzian. Small count rates where the laser is positioned at high detuning values naturally give rise to histograms with high amplitude and small variance collecting around low k_{bin}, while high count rates are associated with broad distributions. At the intermediate detuning value the laser is driving the transition at approximately half a linewidth detuning from resonance, where the variation in mean count rate is greatest with respect to small shifts in the resonant frequency. Therefore, the contributions to the mean histogram from the high and low detuning cases are more equally distributed at this point.

The model predicts a unique histogram for each combination of parameters ($\Delta_{\text{diffusion}}$, $\delta_{average}$, a) and next we establish how the model relates to experimental data. The model must be informed by the radiative lifetime of each dot, T_1, which is measured under pulsed excitation, and the saturation parameter s is obtained by a power dependent measurement of the resonance fluorescence count rate. Records of time-resolved RF containing of order

10^7 detection events are used to obtain low-noise histograms, which corresponds to about 10–100s data acquisition time. The time traces are binned to 0.1 –1ms, where the limit in timing resolution is given by the count rate; it is not possible to bin on arbitrarily short times as the histograms tend in the limit of infinite sampling rate to bars centred around $k_{bin} = 0$, not suitable for a good fitting to the model. The minimum bin time determines the bandwidth, or the fastest fluctuations that are accounted for in the model. Increasing the acquisition time improves the signal to noise ratio of the histogram in general but does not permit ever reducing bin times. Additionally, increased acquisition time allows us to capture slower fluctuations.

With the theoretical framework laid out it is important to analyse how well it can be applied in practice.

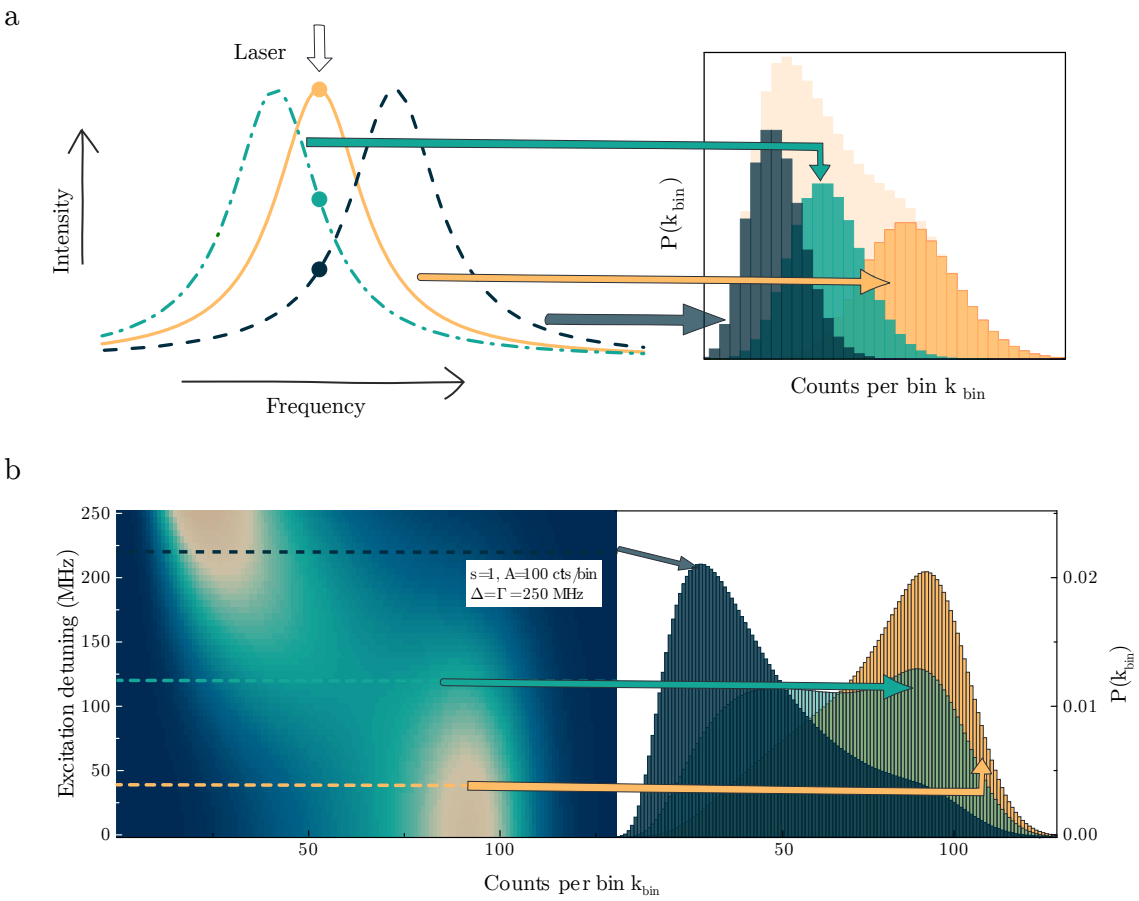

Figure 3.1: Influence of spectral diffusion on resonant photon counting statistics. (a) The QD optical transition frequency shifts as a consequence of local electric field noise such that a laser of fixed frequency drives the transition with a time-dependent detuning. Here we show the absorption lineshape at three points in time. Right panel: intensity histograms corresponding to the three detunings depicted on the left (same colour code). The cumulative histogram (yellow shaded) strongly deviates from the ideal Poissonian distribution. (b) Calculation of full counting statistics histograms for a Gaussian diffusion distribution with a full-width-half-maximum equal to the natural linewidth of 250 MHz. The excitation detuning denotes the average detuning of the laser from the QD resonance. The saturation parameter is s=1, the average count rate on resonance would correspond to 100 counts per bin in the absence of environmental effects. Right panel: Linecuts from the calculation for three detunings, 220 MHz (dark blue), 120 MHz (green-blue), 40 MHz (yellow).

3.2 Application of the model to quantum-dot histograms

Figure 3.2 displays a histogram of resonance fluorescence from the X^{1-} species of QD G, where the data is represented by filled circles. QD G is on 'Sample 2'; 'Sample 1' dots were presented in the previous chapter as QD A, B and C, and both samples are taken from the same wafer ('Chef 2'), thus they were grown under the same conditions with identical sample structure. The QD was driven at s = 1.7 for an acquisition time of nearly 50s, where the data was then placed in 100 μs bins. The mean counts from the 100 μs binned data are 34 counts/bin, with $\sigma = 15.9$, which is clearly much larger than the expected value for Possion statistics alone, $\sigma = \sqrt{\mu} = 5.8$, suggesting that indeed significant spectral diffusion is present. The data is then arranged in as a histogram, which is here termed $c(k_{bin})$, according to counts per bin, k_{bin}. The total number of 100 μs bins in the measurement time is N = 500921, and this is used to normalise the histogram so that the total area is unity, or $P(k_{\mathrm{bin}}) = c(k_{bin})/N$, in other words the probability distribution for k_{bin} counts in 100 μs bins. The error in the value of c itself is assumed to follow a Poisson distribution, such that the error bars of the normalized histogram values are found as $\sigma = \sqrt{c}/N$.

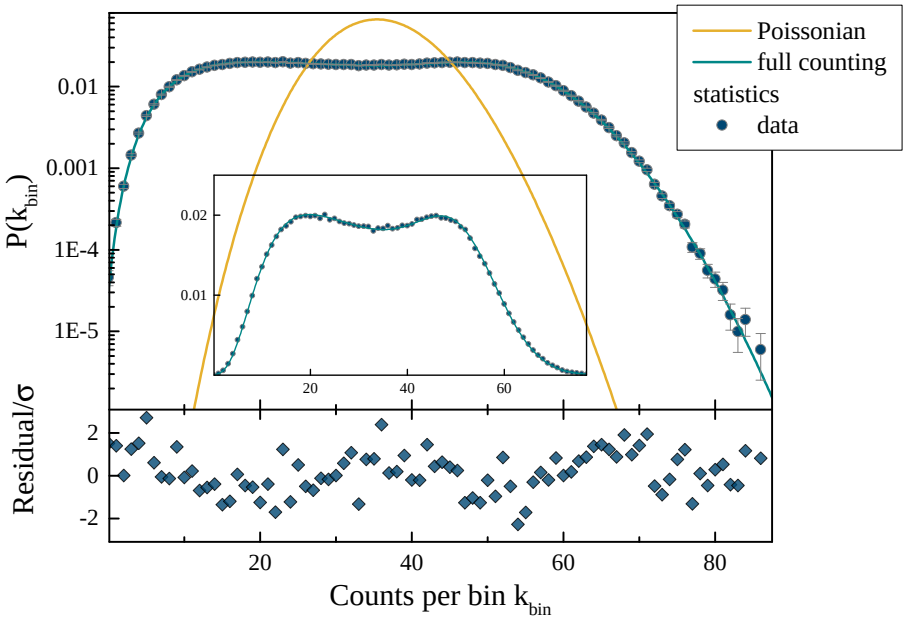

Figure 3.2: Fitting quantum dot resonance fluorescence histograms using full counting statistics. Photon counting histogram of resonance fluorescence intensity for the charged exciton transition ($X1^{1-}$) of QD G at finite detuning, s = 1.7, acquisition time of 50 s and bin size of 100 μs. Data is shown as filled circles, a least-squares fit according the model as blue-green line. The yellow line maps out the expected histogram at the same detuning, but in the absence of spectral diffusion. Fit parameters: amplitude $a = 55.3$, detuning $\delta_{\mathrm{average}} = 148$ MHz, Gaussian diffusion width $\Delta_{\mathrm{diffusion}} = 364$ MHz. Inset: same data and fit on linear scale. Bottom: residual of fit.

The inset to Figure 3.2 shows the histogram on a linear scale, and the double peak

due to spectral diffusion is clear. A least-squares fit to the model of full counting statistics in the presence of spectral diffusion is displayed as a blue curve, with fit parameters a = 55.3, average detuning δ_{average} = 148 MHz and diffusion width $\Delta_{\text{diffusion}}$ = 364 MHz. The parameter a gives us a measure of the expected counts from this quantum dot in the absence of electrical noise; this quantum dot would be expected to emit at 0.55 MHz on resonance at this power, were spectral diffusion removed. In other words, a is a measure of the photon rate scattered from the quantum dot under resonant excitation by a narrow-linewidth laser in the ideal case of no averaging over instances of off-resonant excitation due to spectral diffusion. Below the plot is a summary of the residuals for this model and data, in terms of the error at each data point.

The square of the deviations between the data and model at each point is calculated, and summed over the entire histogram. A three-dimensional grid of this data is represented in Figure 3.3, where all three parameters are allowed to vary broadly and the minimum deviation is represented as blue. In this 3D space a single minimum exists; a plane cutting through at the minimum as detuning is varied, for example, is projected on to the left-hand wall and illustrates the 2D amplitude-diffusion variation, with the resulting minimum as a well-localised point in this plane. This single minimum confirms that the experimental data can be associated with a unique set of parameters, where we give an example of a single detuning point but note that the model works well for a range of detunings and powers. Additionally, we note that the detuning parameter discovered is close to what is expected given the known gate voltage and Stark shift of the transition.

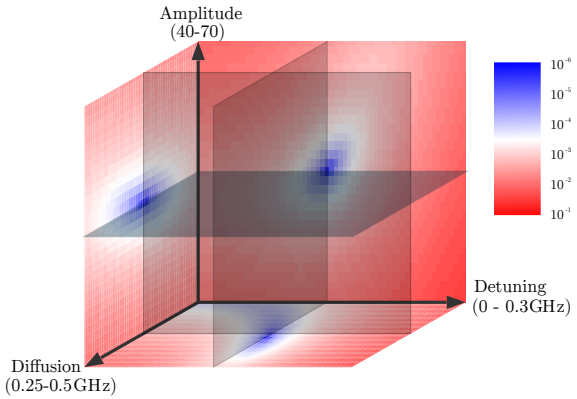

Figure 3.3: Fitting quantum dot resonance fluorescence histograms using full counting statistics - errors. Calculation of least-squares error using the data from Figure 3.2 in the parameter space of amplitude, detuning and diffusion. The sidewalls show projections of plane cuts through the global error minimum. The actual location of the planes in the parameter space is indicated by the shaded squares. The model error has a single well-defined minimum.

In our analysis we aim primarily to keep the model as simple as possible. However, the attentive reader will have noticed that we have omitted a broadening mechanism with comparable amplitude, namely the nuclear Overhauser field. In the next section we explore

the limitations of this model through comparison to the more detailed description from Chapter 2.

3.2.1 Limitations of photon-counting analysis

In Chapter 2 QD C was studied; here in Figure 3.4 we present three typical histograms for this QD. The X^{1-} species was excited close to saturation, $s = 0.85$, where the size of the bins is 200 μs. The natural linewidth of this quantum dot is 216 MHz. Each of the histograms represents a different detuning, with detuning decreasing from Figure 3.4(a) down to Figure 3.4(c). In addition to the data and model fit, distributions for the same detuning and excitation power, but in the absence of spectral diffusion, $\Delta_{\text{diffusion}} = 0$ are presented. As expected, the deviation from the Poisson distribution is largest at δ = -89 MHz, or close to half a linewidth detuning from resonance, as this is the point at which spectral shifts result in the largest change in intensity; it is the point of highest sensitivity. In general, the model (solid lines in Figure 3.4) is a good description of the data, although we note that the spectral diffusion as given by Δ_{diff} is different in order to achieve a good fit for each example in the figure.

To investigate this further, we extract the diffusion width $\Delta_{\text{diffusion}}$ for each detuning probed [Figure 3.5]. Values less than 100 MHz are typical for the QD C X^{1-} resonance at this driving power. The detuning dependence in Figure 3.5 indicates that diffusion width obtained from this model is reduced on resonance, which is in contrast to the physically reasonable expectation that $\Delta_{diffusion}$ is independent of detuning. We have seen that for an X^{1-} the underlying absorption lineshape is modified by a sub-linewidth splitting due to the Overhauser field. As a consequence of this magnetic broadening, the underlying absorption lineshape is effectively a broader Lorentzian, leading to a reduced senstivity when $\Delta = 0$, compared to T_1 and power-broadened form of the lineshape considered in equation 3.2. However, the model here does not account for this reduction in sensitivity, and instead it effectively calculates that there is simply *less* electric field noise at this point. The grey background in the figure indicates a calculation of the absorption lineshape expected with a typical $\Delta_{\text{diffusion}} \approx 80$ MHz, which results in a FWHM of 320 MHz, broadened from the expected value of 290 MHz for a two-level system driven at this excitation power.

Regarding the treatment of data from this quantum dot in Chapter 2, the effective diffusion width extracted from the model of autocorrelation amplitudes was 147 MHz, which is significantly larger than the values uncovered by fitting to the model here, and confirms that there is a systematic underestimate. This underestimate is well understood and as the Overhauser field is consistent between quantum dots it remains reasonable to draw comparisons between quantum dots based upon the spectral diffusion extracted by this model.

With the knowledge of a systematic under-estimate for the X^{1-} species, we turn to X^0. Figure 3.6(a) presents typical histograms for one transition of the X^0 species of QD

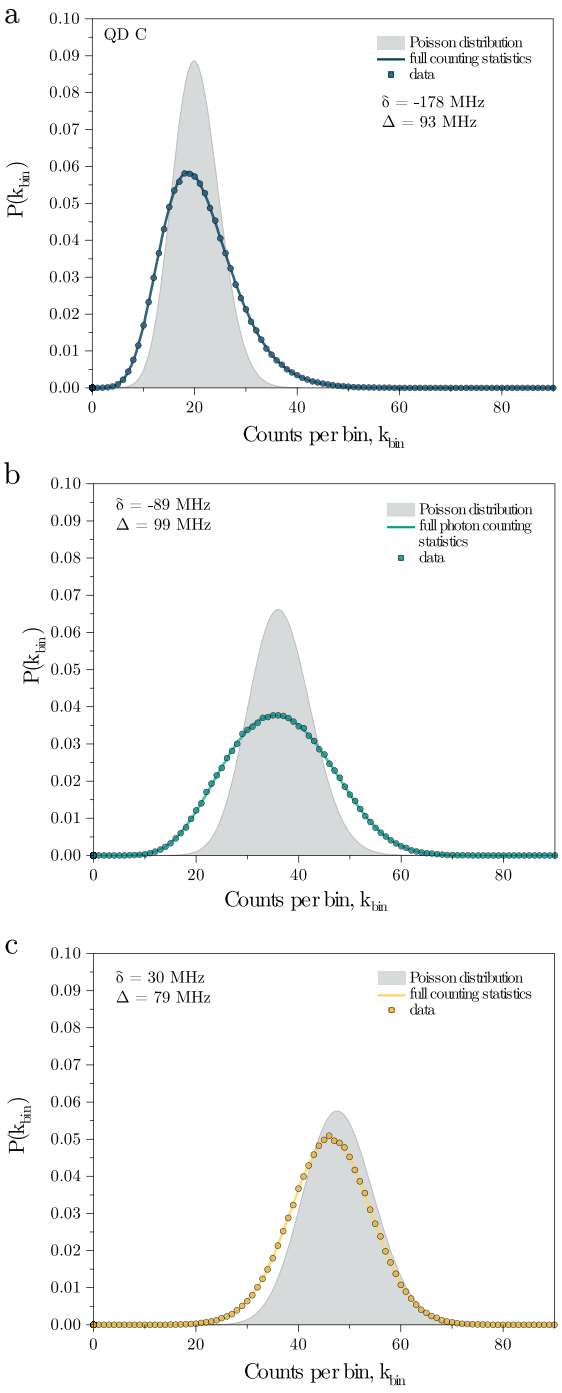

Figure 3.4: Signatures of electric field fluctuations in photon counting histograms of QD C X^{1-} with varied detuning. Data are presented as filled circles, fits as solid lines and Poisson distributions corresponding to the same power (s = 0.85) and mean count rates are represented as filled grey curves. The time bin size is t_{bin} = 200 μs and detuning, δ, decreases from (a) down to (c). The spectral diffusion widths are also given in each figure as Δ.

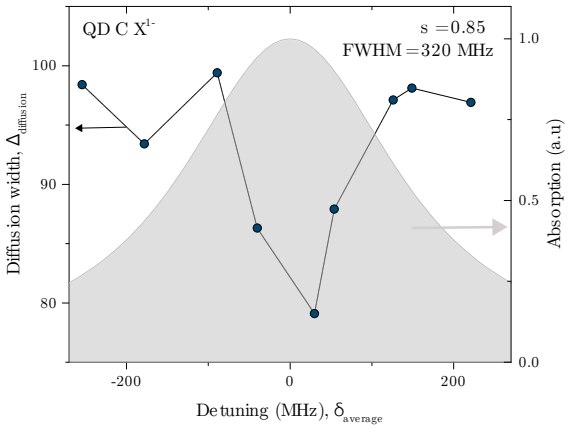

Figure 3.5: Summary of spectral diffusion width for QD C X^{1-}. The data is a summary of all detunings measured, including the histograms displayed in Figure 3.4. The grey background is the absorption that would result from the power-broadened Lorentzian being additionally broadened by the spectral diffusion on resonance, resulting in a typical FWHM of 320 MHz.

C where the bin time was 500 μs at s = 0.8. Figure 3.6(b) summarises the extracted diffusion widths for both t_{bin} = 500 μs and 200 μs. In general there does not appear to be any systematic diffusion width dependence in this case. There is no mechanism for a sub-linewidth splitting which would result in the detuning dependence seen in the case of the X^{1-}, as we are addressing only one of the neutral excitons. Neutral excitons in an asymmetric quantum dot such as this are expected to couple quadratically, with a minimum at zero field, to magnetic fields such as the Overhauser field [88]. Therefore, we expect that an underlying Overhauser field produces a small amount of broadening on the absorption lineshape. As a result, the extracted spectral diffusion for X^0 might be expected to be physically representative of the sample noise at this particular applied gate voltage.

It is also important to note the systematic errors that may occur due to the time resolution fixed by the bin size. For example, in this case the autocorrelation modelling accounted for electric field noise that could act on timescales as short as 50 μs whilst the photon counting statistics account for data in 200 μs time bins where any faster noise is averaged out. In reality, an absorption is further broadened by these faster processes, contributing further to an underestimate of $\Delta_{\text{diffusion}}$ if they are thus excluded from the photon counting statistics.

To examine this further, Figure 3.6(b) records the extracted diffusion widths from the same data, where the length of the time bin was varied from 500 μs to 200 μs. In this case, there is little difference between the two repeats of fitting, suggesting that a timescale lying between 200 μs and 500 μs is not a dominant source of spectral diffusion and t_{bin} is not a limitation of the fit. Therefore this particular limitation is not relevant to this quantum dot.

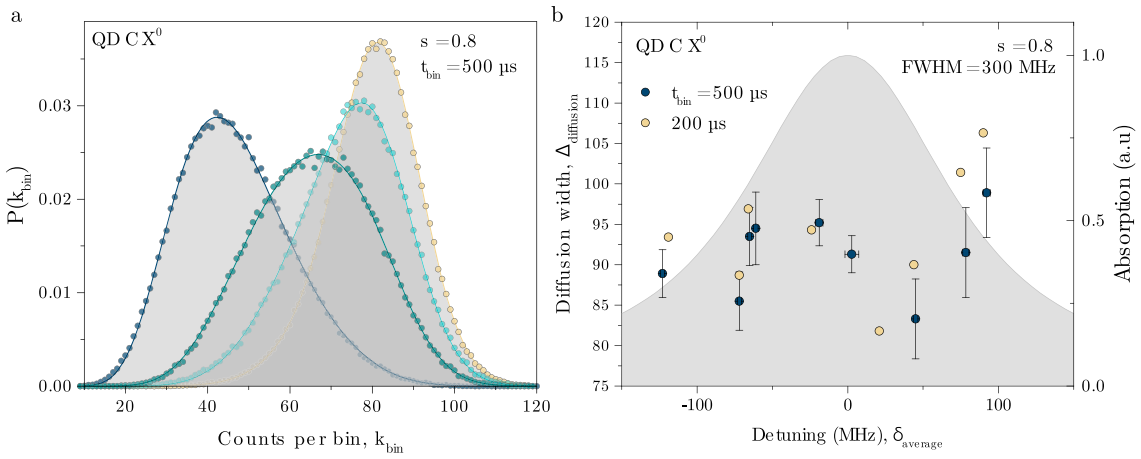

Figure 3.6: Summary of spectral diffusion width for QD C X^0. (a) A set of exemplary histograms for the transition at s = 0.8, where t_{bin} = 500 μs. (b) Summary of spectral diffusion widths with respect to detuning for the X^0 species; both t_{bin} = 500 μs and 200 μs are displayed.

Confirmation of this is provided by turning to the autocorrelation amplitudes: Figure 3.7 summarises the three shortest timescale classes and their dependence on detuning for this QD. Referring to the technique introduced in Chapter 2, only the timescale of $\sim$ 10 μs is associated with Overhauser field fluctuations. However, a significant electric field timescale does not appear below 500 μs, which is in agreement with the invariance of diffusion width with respect to t_{bin} seen in Figure 3.6(b). We note that very similar electric field timescales are found for the X^0 bunching.

In conclusion, the model presented here may be applied to quantum dots with the recognition that there is a systematic but well understood underestimate of the spectral diffusion in the case of X^{1-}, and to a lesser extent for X^0. The primary origin of this underestimate is the nuclear Overhauser field which notably is very similar between quantum dots, as discussed in the previous chapter. In light of this, the technique provides a useful comparison mechanism which is key to selection of suitable quantum dots because the underestimate may reasonably be expected to be consistent, even if it cannot provide a perfect absolute value of the extent of spectral diffusion in each case. For the quantum dot 'QD C' all electric field timescales were captured, but it is necessary to take care that this is the case if this technique is to be applied to other systems.

Having discussed the technique in more detail, including the impact of chosen time bins, and the potential impact of underlying Overhauser field fluctuations, we now turn to a comparison of the behaviour of a number of quantum dots.

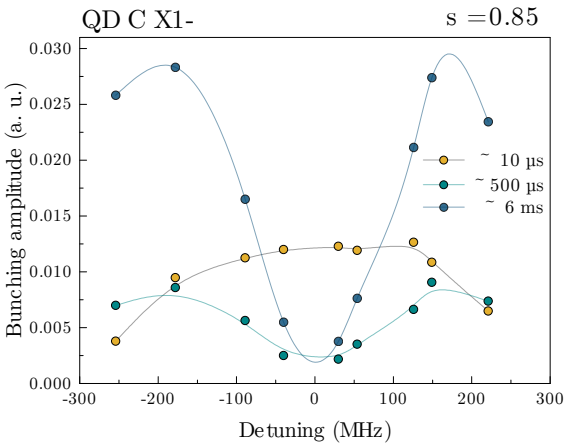

Figure 3.7: Identification of noise timescales for QD C. A summary of the main classes of bunching timescale with their detuning-dependent amplitudes, indicating that electric field noise only occurs on timescales slower than ≈ 500 μs near this QD.

3.3 Survey of photon counting statistics

3.3.1 Power dependence of spectral diffusion

In Figure 3.8 we detail QD Q, found on the same sample as QD C. Example autocorrelations at close to resonant driving for the lowest power, s = 0.2, are given in Figure 3.8(a). The data clearly demonstrate the dominant timescales of intensity noise in the 1 –10 ms range. These autocorrelation amplitudes were found to have a strong detuning dependence that lead to identification as electric field noise. Consequently, a t_{bin} of 100 μs is adequate to capture electric field fluctuations in their entirety. Photon counting histograms for the X^{1-} species were analysed at a range of driving powers and the diffusion widths are presented in Figure 3.8(b). The diffusion width $\Delta_{diffusion}$ suggests systematic detuning dependence as expected for the X^{1-} species, however the large variation in values due to the limited resolution of the fitting technique means this is inconclusive. Rather, we focus on power dependence of the mean (Figure 3.8(c)) and note that there is a very small change in measured $\Delta_{diffusion}$ as driving power is increased.

The apparent change in $\Delta_{diffusion}$ over nearly a factor of 20 in power is only 15 MHz, and as such is barely significant above the error in the mean value for each point. Exploration of power dependence of spectral diffusion in the literature focuses upon the effect of non-resonant excitation; an increased power has been shown to change the local environment to create different timescales and amplitudes of electric field noise. The resulting spectral diffusion creates broadening beyond the linewidth found under resonant excitation [25, 172]. Additionally, it has been found that a reduction in energy of non-resonant excitation results in a reduction of spectral diffusion [173], which also suggests that the excitation of carriers in the local QD environment is associated with electric field noise. However, in the case of resonant excitation we probe the environment more weakly, and it is not

continually populated by photoexcited carriers. The processes allowing carrier escape from traps are therefore likely to be thermally activated, rather than resonantly addressed by a narrow linewidth laser. Whether there is a change in the electronic environment with resonant driving power and why this would occur is not clear and would require a more in-depth study.

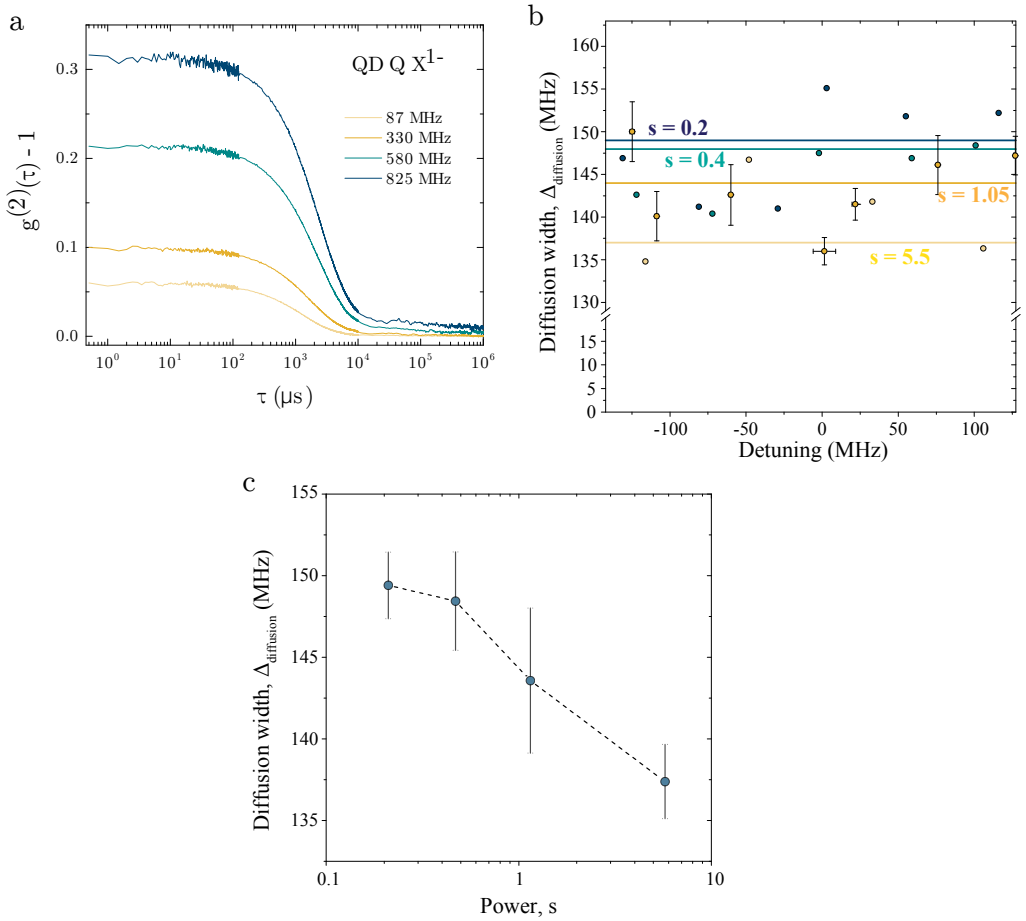

Figure 3.8: Electric field noise in QD Q. (a) Autocorrelation data for QD Q at s = 0.2, for a range of detunings. Bunching decays are around $\sim$ 1 ms, indicating that very slow noise processes with strong electric field detuning dependence are dominant. (b) Results of fitting to histograms with $t_{bin} = 100$ μs for a range of powers, where the mean spectral diffusion widths are indicated by lines, and each line is labelled with the power. (c) The mean spectral diffusion width $\Delta_{diffusion}$ as a function of power.

3.3.2 Comparison of QDs

In Figure 3.9 we summarize some of the parameters extracted by this method for three QDs: QD C, QD G and QD Q. It is clear that systematic variations due to power and detuning are small compared to the variation between QDs. In particular we note that the X^0 and X^{1-} species of QD C are very similar in apparent diffusion width extracted, as expected when the external electric field noise dominates rather than the Overhauser field. The sample of QD G was being operated in the regime where a small current was flowing across the diode (due to a slightly damaged area of the sample), which could lead to anomalous local electric field behaviour and hence the significantly enhanced spectral diffusion with a mean $\Delta_{\text{diffusion}} = 355$ MHz. QDs C and Q are found on the same sample, and have similar behaviour although it is clear that in general Q is a 'noisier' dot. This has informed us as to the quality of QDs we can expect, and how we can compare them. QDs C and Q are some of our best quality QDs, being found on the lowest-noise sample we have yet available, where it appears that $\Delta_{\text{diffusion}} \approx 100$ –150 MHz is a typical value and lies well below the radiative linewidth of the QDs. QD G is an example of a QD on the same sample where the local environment happens to be poor.

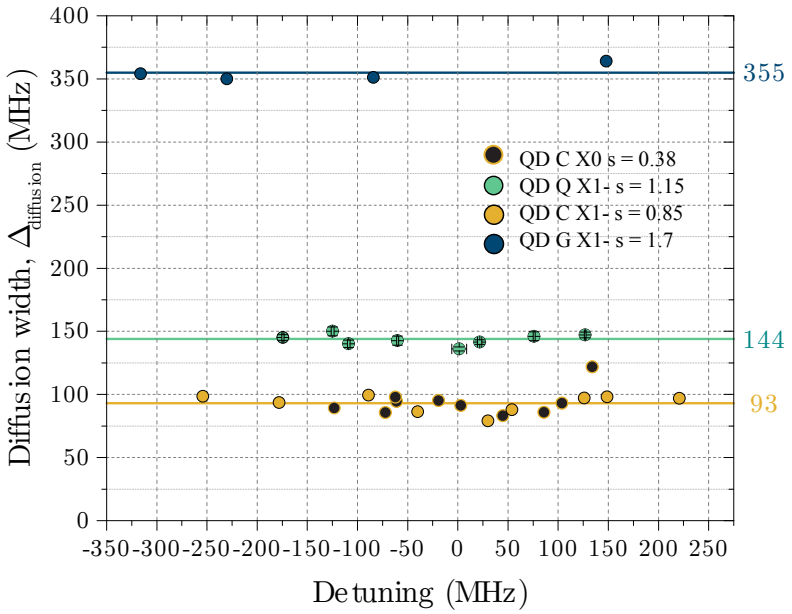

Figure 3.9: Comparison of spectral diffusion widths for three QDs. Spectral diffusion widths extracted from the histogram model are displayed as a function of detuning, with both species of QD C present. The mean values in MHz are given by the numbered lines.

3.3.3 Spectral switching

The discussion of spectral diffusion has focused so far on continuous spectral shifts which can be described by a single (Gaussian) probability distribution. Discontinuous spectral jumps due to a single local charging event have been observed [151, 152, 174]. 'Blinking'

due to the trapping of population in dark states is also known [149, 175, 176], often for samples with a large number of defects or high QD density, and commonly in ungated devices. Blinking denotes the temporary inability of an emitter to scatter photons and is a major issue for colloidal QDs [177]. In contrast, a spectral jump shifts the emitter's resonance with respect to a resonant laser, resulting in a modified scattering rate. Such events can be seen in resonance fluorescence counting statistics. Figure 3.10 presents histogram data for the X^{1-} transition of QD P (yellow curve). Applying the model with a single Gaussian probability distribution for the detuning (c.f. equation 3.5) yields good agreement to part of the data. This fit is shown as a blue shaded area in the main figure. In the panel below, the residual to the data (blue circles) highlights a second mode of the detuning probability distribution is needed to obtain a fit for the full data set. The histogram due to the second mode is shown as a yellow line with shading in the residuals plot. On the right-hand side of Fig. 3.10 the physical process is explained in a sketch. The local electric field switches discontinuously between two values and consequently the QD resonance frequency jumps between two values. The exciting laser is blue-detuned with respect to the two resonance frequencies here. The mode closer to the laser is populated with high probability (96—97%). A spectral jump into the second mode reduces the fluorescence intensity; it shows up on the histogram as a distribution with lower typical k_{bin}. By tuning the excitation laser to lower frequencies we observe the dominant mode moving through a maximum in intensity before weakening. At these lower frequencies a spectral jump brings the QD closer to resonance with the excitation, such that we observe the less-likely second mode at higher counts in the histogram, or in other words the small hump in the residuals shifts to the higher k_{bin}.

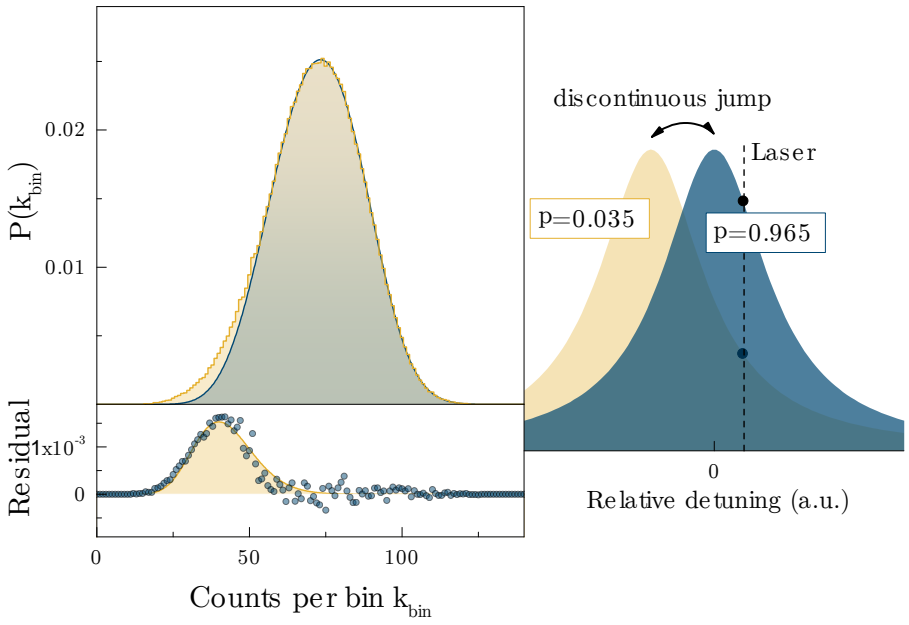

Figure 3.10: Identifying spectral jumps through the photon statistics. LHS: Intensity histogram for the X^{1-} transition of QD P (s = 0.8, $\delta_{\text{average}} = 70$MHz, $\Delta_{\text{diffusion}} = 70$MHz). Applying full counting statistics reveals a bimodal detuning probability distribution. The data is shown as yellow stepped curve with yellow shading; the blue curve with blue shading shows a fit to the dominant of the distribution modes. Bottom, the residual (data as blue circles) reveals the second weaker mode. RHS: Sketch of the physical process. The QD resonance switches discontinuously between two frequencies. Relative frequency denotes the detuning between laser and the QD resonance in the dominant distribution mode. The fit from the left-hand side puts the probability to be in the brighter (darker) mode to 0.965 (0.035).

3.4 Conclusion

We have demonstrated that it is possible to use the photon counting statistics of QD resonance fluorescence, in combination with a simple model of spectral diffusion based upon a Gaussian distribution of possible local electric field values, to characterize a QD sample. We note that previous work has used a Lorentzian probability distribution for spectral diffusion [168], but this does not give good results in our case. The long tails of the Lorentzian give rise to contributions from Poisson distributions with small means, significantly overestimating the histogram amplitudes at small k_{bin}.

Whilst this model does not accurately capture all the aspects of the QD environment, in particular the Overhauser field fluctuations, it is possible to distinguish the local environments of different QDs on the same sample. Incorporating the Overhauser field fluctuations would give more accurate physical parameters in situations where the nuclear spin physics plays an important role. However, the simple Gaussian diffusion model can reproduce intensity fluctuations correctly, primarily due to the dominance of electric field noise for the timing resolution of the present measurements. The nuclear spin baths in

QDs of similar wavelengths would be expected to be quite similar as they are intrinsic to this type of QDs. Local charge traps, on the other hand, are likely subject to more variation and a method of comparing QDs becomes useful. Whilst some of the differences may arise due to the difference in Stark shift coefficient between QDs rather than actual difference in the local electric field fluctuations, in practical circumstances we are most interested in the actual magnitude of spectral shift of a QD resonance however it occurs.

As to the origin of these electric field fluctuations, the electric field noise occurs despite the absence of non-resonant excitation, suggesting we are not dealing with photoexcited carriers being captured, or photoactivated escape of charges from traps. A possible mechanism is a group of charge traps that forms directly above each QD in the interface between the capping layer and blocking barrier, due to propagation of the strain field from the QD [151]. This would mean that every QD would have such a collection of charge traps and be subject to unavoidable electric field noise, although the precise quantity can vary QD-by-QD. There is also the possibility that growth can be contaminated by carbon dopants [178], which may be the origin of some samples being notably worse than those presented here.

Whilst the electric field fluctuations appear in general unavoidable and we must seek a QD with the smallest contribution from these processes, it is possible to actively stabilize the resonant frequency of a QD by lock-in detection of the filtered-out phonon sideband [117] and active feedback on the applied gate voltage which, for example, resulted in a reduction of the spectral diffusion width from $\approx$ 150 MHz to 20 MHz. In this dissertation the technique will not be used due to practical considerations, but in principle it is a powerful technique to minimise the effect of spectral diffusion.

The measurement technique gives reliable results for moderate sample sizes (10^7 detection events, $\sim$ 10 s acquisition time) with easily accessible timing resolution (100 μs is possible with our data acquisition cards). In contrast to direct spectral measurements of spectral diffusion [172] the frequency selectivity of resonance fluorescence allows us to quantify spectral diffusion below the radiative linewidth, with a resolution of $\approx$ 20 MHz or 0.1 μeV. The simplicity of the model makes it widely applicable; in this case it has enabled us to identify our best samples with which we proceed for the remainder of this dissertation.

Chapter 4

An entangled state of two electron spins

Having considered in the introduction to this dissertation the *why* of producing entangled states of matter, and also why we would wish to attempt this in a solid-state environment with carriers trapped in quantum dots, we now turn to the *how*. Prior to this point we have considered the impact of the solid-state environment on the behaviour of the quantum dot as evidenced in the scattered photon statistics. The solid-state environment exerts a large influence on both the photon spectral purity and the spin coherence. It has been anticipated that high performance with regards to both of these properties is necessary if quantum dots are to be utilised in quantum optical networks, along with the usual requirement of being able to perform unitary operations and high-fidelity read-out on our qubits [1]. While there are soli-state effects that appear unfavourable in comparison to more isolated systems such as trapped atoms, we wish to investigate whether entangled states can be generated between two quantum dots and how the limitations dictated by the environment become apparent. Indeed, having quantified the impact of the environment, we may tailor our protocols to circumvent its effects.

In this Chapter, we demonstrate that electron spins in quantum dots can be entangled in spite of a reduction in apparent emitter 'quality' as compared to atomic, ionic, superconducting or diamond-defect systems. We begin by surveying photon-mediated entanglement schemes, and then discuss the scheme to be implemented in this work including the requirements it will place upon our system. Following this we assess the suitability of the chosen quantum dots. We then describe the experimental set up used to generate entanglement, control and measure electron spins, and also quantify the quality of our control sequence. Finally, we extract three-photon correlations that unambiguously confirm creation of an entangled state, and quantify the fidelity of the state in comparison to the ideal case.

The demonstration of spin-spin entanglement was a complex experiment jointly performed by several key team members, including postdoctoral researchers Claire Le Gall and Clemens Matthiesen. In the preparation for the experiment, three PhD students each

focused upon a different aspect: Robert Stockill on optical spin rotation and generation of pulse sequences, Lukas Huthmacher on data acquisition and data analysis, and I focused upon arranging the optics necessary for this experiment, inclusive of a stabilised interferometer with phase control and the photon filtering set-up.

4.1 Photon-mediated entanglement schemes

In Section 1.1.2 the advantages of quantum optical networks were introduced, where photonic links are used to distribute quantum information between matter qubits sitting at the nodes. One approach to producing an entangled state distributed across the nodes is to directly send photons from one node to another, where the matter qubits within the nodes are placed within optical cavities in order that they interact strongly with a photonic mode [78–81]. However, this can be challenging to implement, for example the electrodes of ion traps can be difficult to incorporate into the geometry required by such a cavity. There has been recent development of micro-pillar cavities with photonic modes which can be coupled to quantum-dot transitions [179, 180] where in addition it is now possible to tune the transitions electrically [181].

However, we are not yet in a position of combining strong coupling to photonic modes of a cavity with the control [15], initialization [14], and readout [13] of our spin qubits in the way that is available for self-assembled QDs embedded in the more simple structures introduced in Section 1.2.2. The quality of these structures is such that, in concert with Stark-shift tuning of the resonances, otherwise non-resonant systems can be carefully matched to then generate highly indistinguishable photons [182]. We therefore turn to probabilistic entanglement schemes where detection of one or more photons projects the system into an entangled state. Such schemes are robust against losses in the photonic channels that result in decaying fidelity of communication for the direct node-to-node schemes [82, 183].

There are two main types of probabilistic entanglement scheme [184], where both involve as a first step the generation of entanglement between the state of the matter qubit and an emitted photon.

In a **Type I** scheme a system initially with all population in a single ground state is weakly excited, where there is a finite probability p of an inelastic scattering process and a transition to another ground state concomitant with emission of a spectrally distinct photon. Therefore, the state of the matter qubit is entangled with the occupancy of this photonic mode. Simultaneous treatment of two systems in this manner, and subsequent interference of the photonic mode on a 50:50 beam-splitter, erases the which-path information regarding the origin of the photon. Detection of a single photon is then sufficient to project the system into an entangled state of the two matter qubits, where there is an inherent infidelity given by p due to our inability to distinguish such cases where both systems emit a photon but only one can be detected, for which we would require perfect

collection and detection efficiency and number-resolving detectors. As a result, p is chosen to be deliberately low, thus limiting the entanglement generation rate. This scheme was proposed by Cabrillo et al. [185], and is similarly proposed for use in the DLCZ protocol which addresses how to entangle separate atomic ensembles and cascade the entanglement out to further systems [82]. It is important to note that in this scheme the state is inherently sensitive to optical phase, and therefore the positions of the matter qubits with respect to each other and the beam-splitter must be well maintained. This scheme has been successfully implemented in trapped ion systems [186] and with quantum-dot heavy-hole spins [83].

A **Type II** scheme takes a similar form. However, the initial state of the matter qubit is deterministically transferred to a superposition of two states which is entangled with a property of the emitted photon such as polarization. The protocol was first described in Ref. [187]. Following the generation of matter-photon entanglement between two systems, the photons are interfered on a beam-splitter and loss of which-path information creates a photonic Bell state correlated with a matter-qubit Bell state. Various implementations then measure this photonic Bell state in order to project the matter qubits into an entangled state, but rely in general upon two-photon detection events to project the systems into a spin singlet. Such a scheme has been used to successfully generate entanglement between ions and atoms in separate traps [77, 188, 189], and also most recently between superconducting qubits [190].

In this way, the low probability of emitting a state-projecting photon in each attempt is removed, and additionally the protocol does not require carefully maintained positioning of the components. However, it does require that two photons are detected to successfully project an entangled state, which is disadvantageous when the collection and detection efficiency are low.

If we take p_c to be our photon collection probability, and η_d to be detection efficiency, the Type I entanglement probability per attempt is $pp_c\eta_d$ if we assume that any polarization of the scattered mode can be collected. For Type II this becomes $p^2p_c^2\eta_d^2/2$, where $p = 1$, due to the required two photon detection and the probability of the photons emerging from the beam-splitter on to different detectors. Consequently, Type I is more likely to produce an entangled state if $p > p_c\eta_d/2$, where an initial conservative estimate of $p_c\eta_d$ for our system based upon using superconducting nanowire single photon detectors (SNSPDs) with detection efficiencies of $\eta_d \approx 80$ % and a collection efficiency of 2 %, is 0.84 %.

As an alternative, a 'double-heralding' scheme relies upon the detection of a single photon in the first instance, but then this is followed by a π-rotation of the qubit at each node and a second excitation, where detection of a second photon heralds an entangled state with high fidelity [191]. The contribution to the state associated with two photon scattering events in the first round, and the optical path-length sensitivity of the state, are both removed. Such a protocol enabled high fidelity entanglement to be produced between two electron spins localized in NV centres in diamond [192, 193], culminating in a

'loophole-free' test of Bell's inequality due to the space-like interval between the two qubits and the availability of event-ready information [33]. In this case an estimated entangled state fidelity of 92 % was achieved, but the requirement of two-photon detection events reduced the probability of entanglement generation per attempt to 6.4×10^{-9}.

Such schemes succeed in spite of lower entanglement generation probability, as they merely require patience. However, confirming the presence of a Bell state also relies upon detection of further photons to measure the state of the qubits. In systems such as the NV centres, there exist cycling transitions that scatter many photons before decaying to a dark state, allowing readout of a state generated by a single entanglement event with high probability [194], which counteracts the effect of low generation probability. Our chosen method of electron spin rotation in quantum dots requires that we work in the Voigt geometry, where the near-single-shot read out available in Faraday geometry [98] cannot be used. Therefore, with limitations on collection and detection efficiency we attempt to implement a Type I single photon detection scheme, where we aim to demonstrate rapid entanglement distribution between quantum dot nodes.

4.2 A single-photon detection scheme

In Figure 4.1 we outline the components of the scheme proposed by Cabrillo et al. [185] where we define single spatial photonic modes as shown in Figure 4.1(a), and we label two detectors 1 and 2. The matter qubits are labelled A and B, and in our implementation these are the sites of two quantum dots. Figure 4.1(b) indicates the general three-level Λ-scheme that is required for this protocol. The qubit is provided by the ground state electron spin with a quantization axis defined by a magnetic field in Voigt geometry (ground states $|\uparrow\rangle$ and $|\downarrow\rangle$), where the excited state consists of an X^{1-} species with a single unpaired hole spin ($\uparrow\downarrow\Downarrow$). The ground states are split in energy by the Larmor frequency, ω_L, and the branching ratio for decay of the excited state to each ground state is equal in this geometry. A second excited state is available, but under sufficient magnetic field one Λ-scheme can be isolated.

Before entanglement generation begins, the population of a single ground state spin must be equal to unity. Weak, simultaneous excitation of both systems follows using a pulse resonant with the transition between the initial spin state and the excited state. In the figure, this frequency is labelled as ω_l. This pulse is introduced via the first beam-splitter in Figure 4.1(a), and the transition is driven so that an excited state is created with probability $\epsilon \ll 1$. Following spontaneous decay at rate $\Gamma/2$ into the photon modes at ω_l and ω_R with equal probability, each QD will now be in a superposition of spin states, where the spin is entangled with the occupancy of the emitted photon modes. In this work the inelastically scattered photons (from the higher energy transition of the Λ-scheme) are frequently referred to as the 'Raman' or 'blue' photons while their elastically scattered counterparts are therefore called the 'red' photons.

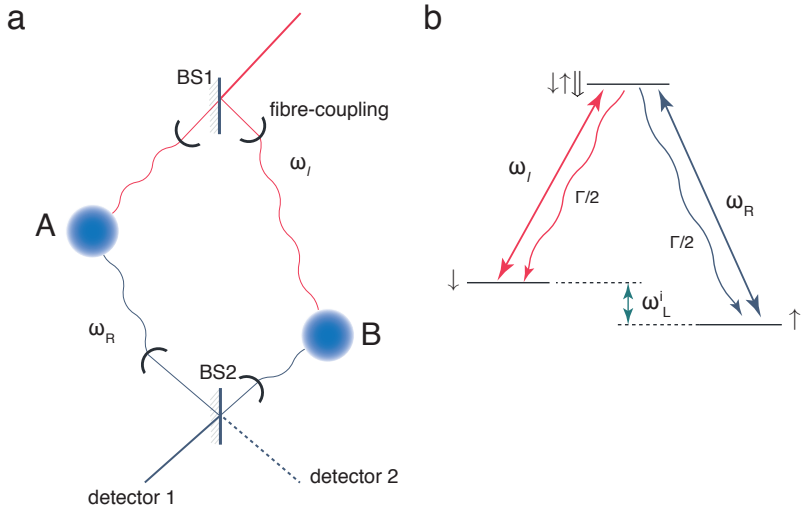

Figure 4.1: Schematic of the single-photon detection scheme. (a) Outline of the Mach-Zehnder interferometer, including the placement of the two qubits, A and B, and the location of detectors. Following a first beam-splitter, where in this figure wavy lines reflect flexibility with regards to spatial arrangement of the qubits following coupling of light in to optical fibres after the first beam-splitter, and prior to the second. The frequencies of excitation (ω_l) and the state-projecting photon (ω_R) are included. (b) The Λ-scheme of a single QD, where an X^{1-} species is used as the excited state and the single trapped electron spin provides the qubit at a single node. The ground-state energy splitting, ω_L^i, is indicated.

The states of the photonic modes and electron spins can be described during the process as follows [82, 195], where we first assign projection operators to the spin i, σ_i, where:

$$\sigma_i^+ = |\uparrow\rangle\langle\downarrow| \tag{4.1a}$$

$$\sigma_i^- = |\downarrow\rangle\langle\uparrow|\,, \tag{4.1b}$$

which 'raise' $|\downarrow\rangle$ state to the final state $|\uparrow\rangle$. There also exist operators S_i which act on the photonic mode at frequency ω_R originating at each QD:

$$S_i^+ = |1\rangle\langle 0| \tag{4.2a}$$

$$S_i^- = |0\rangle\langle 1|\,. \tag{4.2b}$$

We now define p as the probability of $|\downarrow\rangle$ population being transferred to $|\uparrow\rangle$. Following an approach taken in Ref. [82], the spin-photon entanglement for a single QD_i can be represented as:

$$|QD_i\rangle = \left(\sqrt{1-p} + \sqrt{p}e^{i\phi_i}S_i^+\sigma_i^+\right)|0\rangle_i\,|\downarrow\rangle_i\,, \tag{4.3}$$

where the case of repopulation of $|\downarrow\rangle$ with emission of a photon at ω_l has been included as part of the first term. In other words we anticipate tracing over the occupation of the photonic mode at ω_l. It is also important to note that the spin operator inherits the

phase of the incoming excitation pulse ϕ_i as this is a coherent excitation process [119]. More specifically, the excitation process creates coherence between the $\downarrow$ ground state and the excited state, and the later detection of the inelastically scattered photon maps this coherence on to the state of the ground state spins. In essence, this is the reason that there is an interferometer, where the entire path length is crucial to the entangled state phase. We discuss in more detail in the next chapter the implications of these phase terms and the impact of the noisy environment thereon.

Therefore, the total state of both systems prior to the beam-splitter BS2 ($|\Psi\rangle = |QD_A\rangle \otimes |QD_B\rangle$) is expressed as:

$$|\Psi\rangle = \left[(1-p) + \sqrt{p\,(1-p)}\left(e^{i\phi_A} S_A^+ \sigma_A^+ + i e^{i\phi_B} S_B^+ \sigma_B^+\right)\right] |0\rangle_A |0\rangle_B |\downarrow\rangle_A |\downarrow\rangle_B + \left[p e^{i(\phi_A+\phi_B)} S_A^+ S_B^+ \sigma_A^+ \sigma_B^+\right] |0\rangle_A |0\rangle_B |\downarrow\rangle_A |\downarrow\rangle_B . \quad (4.4)$$

Here the first beam-splitter introduces a $\pi/2$ phase shift between the excitation modes addressing the two quantum dots. The photonic mode operators evolve prior to the beam-splitter gaining some phase ξ_i. The modes directed towards detectors 1 and 2 are represented by operators d_1 and d_2, and are written in terms of the incoming modes as [196]:

$$S_A^+ = \frac{1}{\sqrt{2}}\left(i d_1^+ + d_2^+\right) \quad (4.5a)$$

$$S_B^+ = \frac{1}{\sqrt{2}}\left(d_1^+ + i d_2^+\right). \quad (4.5b)$$

Therefore, the state after the beam-splitter can be written as:

$$\begin{aligned} |\Psi\rangle = {} & (1-p)\,|0\rangle_A |0\rangle_B |\downarrow\rangle_A |\downarrow\rangle_B \\ & + \sqrt{p\,(1-p)/2}\left[\left(i d_1^+ + d_2^+\right) e^{i\phi_A} e^{i\xi_A} |0\rangle_1 |0\rangle_2 |\uparrow\rangle_A |\downarrow\rangle_B\right] \\ & + i\sqrt{p\,(1-p)/2}\left[\left(d_1^+ + i d_2^+\right) e^{i\phi_B} e^{i\xi_B} |0\rangle_1 |0\rangle_2 |\downarrow\rangle_A |\uparrow\rangle_B\right] \\ & + ip/\sqrt{2} e^{i(\phi_A+\phi_B)} e^{i(\xi_A+\xi_B)} \left(i d_1^+ i d_1^+ + i d_2^+ i d_2^+\right) |0\rangle_1 |0\rangle_2 |e\rangle_A |e\rangle_B . \end{aligned} \quad (4.6)$$

The which-path information that gives information on the origin of the photon is now lost, and we see that the photonic entangled state produced by a beam-splitter is at the heart of the entanglement generation.

Finally, the detection of a single photon transfers the entanglement generated between the photons onto the spins alone. The parts of equation 4.6 corresponding to detection of a single photon in mode 1 or 2 can be singled out. Following a single photon detection in mode 1 we now have the state:

$$|\Psi_+\rangle = \frac{1}{\sqrt{2}}\left(|\uparrow\downarrow\rangle + e^{i\phi_i} |\downarrow\uparrow\rangle\right), \quad (4.7)$$

while detection of a single photon in mode 2 leads to the state:

$$|\Psi_-\rangle = \frac{1}{\sqrt{2}}\left(|\uparrow\downarrow\rangle - e^{i\phi_i}|\downarrow\uparrow\rangle\right), \tag{4.8}$$

where there is the introduction of an additional $\pi/2$ phase difference between the two due to the second beam-splitter resulting in a total π phase difference between the states associated with different detection modes. The state can be more generally written $|\Psi\rangle = \frac{1}{\sqrt{2}}\left(|\uparrow\downarrow\rangle + e^{i\theta}e^{i\phi_i}|\downarrow\uparrow\rangle\right)$, where $\theta \in \{0,\pi\}$. The importance of the phase ϕ_i will be discussed more thoroughly in the next chapter. In reality the created states are not in fact pure Bell states due to the final term in 4.6. In this term, the modes leading to each detector can be occupied with two photons; detecting a single photon and being unable to detect the presence of the other leads to the contribution in the overall mixed state of the form $|\uparrow\rangle_A|\uparrow\rangle_B$ with a relative probability p.

In the above discussion we assumed that the Λ-schemes were identical, and that photons at ω_{R} are emitted by both systems. This indistinguishability of the emitted photons is essential to create an entangled state with high fidelity [191]. Any possible knowledge of where a photon originated adds a component to the final state that is not entangled, and terms associated with knowledge of which QD emitted a photon,

$$|\uparrow\rangle_A \otimes \left(\sqrt{p}\,|\uparrow\rangle_B + \sqrt{1-p}\,|\downarrow\rangle_B\right), \tag{4.9}$$

$$|\uparrow\rangle_B \otimes \left(\sqrt{p}\,|\uparrow\rangle_A + \sqrt{1-p}\,|\downarrow\rangle_A\right), \tag{4.10}$$

must be added to the overall density operator of the mixed state, $\rho = \sum_i p_i\rho_i$ for probability p_i of contribution ρ_i. Such contributions do not contain coherence between the spatially separated spins.

Quantum dots suffer from a degree of spectral diffusion and variation in the nuclear Overhauser field leading to a fluctuating ground state spin splitting ω_L^i. Our strategy must be to find matching QDs with the minimum spectral diffusion available. A broadened photon energy due to the ground state splitting appears as $\omega_{\mathrm{R}}^i = \omega_l + \omega_L^i$. If the detection time window is long enough, $\tau_{det} = 2\pi/(\omega_L^A - \omega_L^B)$, the two photon modes can be distinguished. If $\tau_{det} \ll 2\pi/(\omega_L^A - \omega_L^B)$, the spectral resolution is lost and the two frequencies cannot be distinguished; which-path information regarding the origin of the photon is not revealed and entanglement is possible [197].

However, a very short time detection window is detrimental to the rate of entangled state production so there is a trade-off between this and state fidelity [198], as we shall see in Section 4.5. We now turn to quantifying the indistinguishability of the photons from our chosen QDs.

4.3 Indistinguishable photons from two quantum dots

The which-path information regarding the photons after the beam-splitter must be minimised in order to produce the desired entangled state with good fidelity. We are confronted with the dual challenge of identifying two quantum dots that contain Λ schemes within Stark shift tuning range of each other, while not compromising on spectral quality. In chapter 3 we identified a 'good' sample, upon two pieces of which we find our two quantum dots.

Two quantum dots were chosen, where wavelengths were sufficiently close that a combination of Stark-shift tuning along the X^{1-} plateau and application of a magnetic field create two identical Λ-systems. Gate voltages were chosen far from the edges of the charging plateau to maintain long electron spin T_1 times on the order of milliseconds in the absence of significant cotunnelling [97]. Figure 4.2 shows very similar radiative lifetimes as measured by time-resolved detection following weak (≪ saturation) excitation pulses on the red transition: (762(9) ps for QD A and 797(11) ps for QD B), thereby guaranteeing overlap of the photon wavepackets in time.

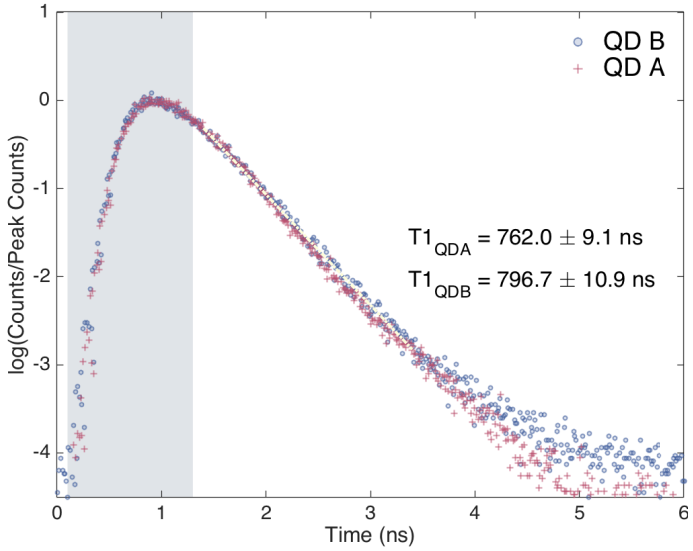

Figure 4.2: Radiative lifetime measurements of QD A and QD B. Photons from the 'blue' transition are collected following weak excitation of the 'red' transition. The time-resolved detection is presented normalized to the peak detected counts, and a fit to the exponential decay reveals the radiative lifetime of the excited state: 762(9) ps for QD A and 797(11) ps for QD B. The grey box bounds the window in which photon detection events that contribute to the entanglement results are found, where this represents ≈ 51 % of collected photons.

Figure 4.3 shows the results of intensity correlation measurements on each quantum dot independently, confirming the single-photon nature of the emission. The counts are recorded during pulses applied to the red transition of the Λ-scheme, where data is collected independently for each dot, and it is clear that $g^2(\tau = 0) \approx 0$ for both. The counts here

are detected from the blue transition, resulting in not only background-free emission, but also a spin-blockaded process where emission of a second Raman photon cannot occur until the $\downarrow$ spin population is reinitialised. There is near-perfect antibunching; this is not limited by detector dark counts, which contribute at a rate of 1 Hz to the photons detected during this weak pulse, or 1 in 3500 in normal operation.

a) Intensity autocorrelation measurement for QD A, $g^2(0) = 0$.

b) Intensity autocorrelation measurement for QD B, $g^2(0) = 0.08$ %.

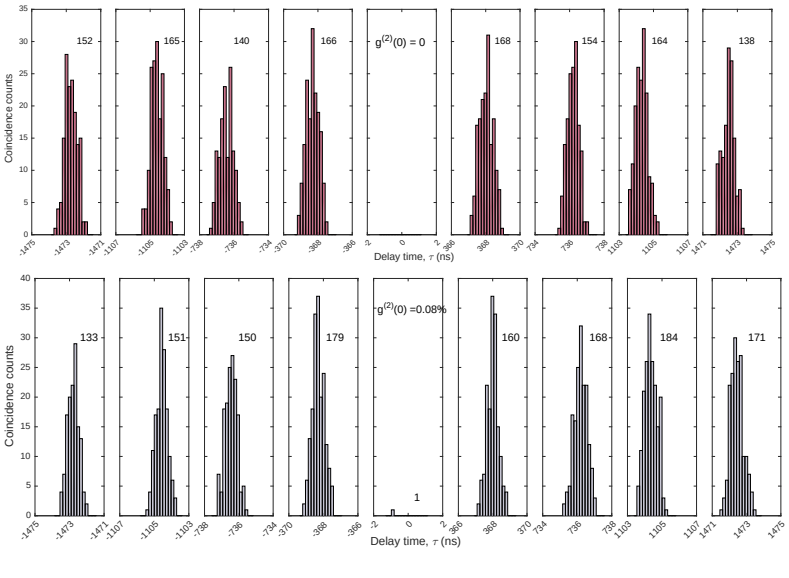

Figure 4.3: Intensity autocorrelation measurements for QDs A and B. The quantum dots are excited on the red transition by weak pulses of light, and correlations between those emitted at the blue transition frequency are recorded here, for a total of three minutes. The QDs display near-perfect single photon emission, where the measurement is limited here by background counts only.

4.3.1 Ramsey interferometry

In order to match the ground-state splitting of the two quantum dots, essential to both the indistinguishability of emitted photon frequencies and ensuring that the final entangled state does not precess in the laboratory frame, we employ Ramsey interferometry [199]. A coherent superposition of $|\uparrow\rangle$ and $|\downarrow\rangle$ is created by a $\pi/2$ rotation of the spin and allowed to evolve for a known time τ, before a second $\pi/2$ rotation maps the acquired phase on to the spin populations. The phase acquired is simply $\omega_L\tau$.

Figure 4.4a illustrates the pulse sequence. The spin is initially prepared in the $|\downarrow\rangle$ state by a resonant laser driving the blue transition at ω_R, and the spin is measured after rotation by recording the number of photons scattered from a second pulse of this resonant laser. Figure 4.4b illustrates the signal we record from this measurement pulse as a function of inter-rotation delay, τ, for an example QD, 'QD C', where the externally applied field is ≈ 4 T. For reasons that will become clear during later discussion around the behaviour of the Larmor frequency (see Chapter 5), we keep an additional weak pulse driving the red transition at ω_l. This does not impact upon our ability to measure a Larmor frequency as

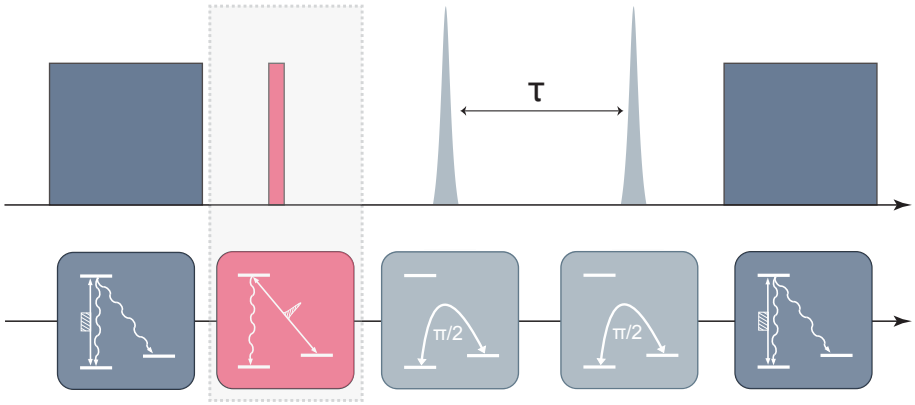

a) The optical pulse sequence used in Ramsey interferometry. The variable delay time between two $\pi/2$ rotation pulses is given by τ. The blue transition is driven during the initial pulse, and spin read-out and reinitialization are performed using the blue transition also. The weak driving pulse on the red transition remains to provide an accurate measure of the Larmor frequency under conditions used in the running of the entanglement experiment.

b) An example of a Ramsey interferometry signal for QD C. As the delay is increased, the effect of dynamic nuclear spin polarization becomes evident as a departure from sinusoidal oscillations.

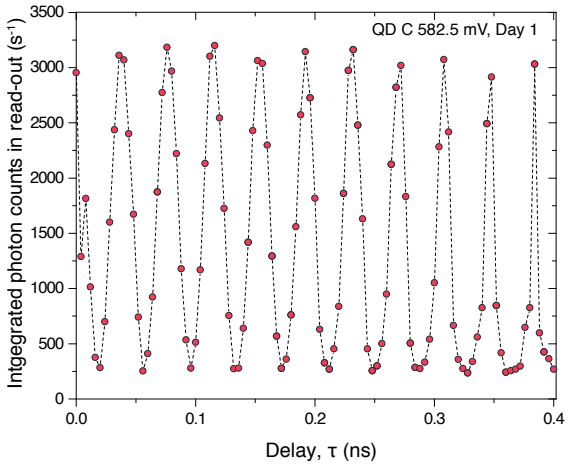

Figure 4.4: Ramsey interferometry of a single electron spin.

it means that we simply start with a density matrix where the population in the $\downarrow$ state has been reduced to 90 %.

At short delays, the signal exhibits sinusoidal behaviour as expected. At longer delays $\tau \sim T_2^*$, the envelope of the signal is expected to decay exponentially as the spin precession dephases; during the ~ 1 s measurement time of each point ω_L samples the full distribution of the Overhauser field. However, in reality the signal from single electron spins in these QDs exhibits a 'saw-tooth' profile at longer times. This behaviour, as well as hysteresis dependent upon the direction of delay scanning, has been observed and explored in more detail elsewhere [17, 200]. The behaviour is due to a nuclear spin polarization that occurs within the measurement. Larmor frequency measurements are limited to short time delays where we thus extract a mean value of ω_L.

By fitting a sinusoidal curve to the short time delay signal, we are able to extract the Larmor frequency of each QD. The dominant error is due to the fit; the assumption of

a sinusoidal curve neglects the distortion produced by nuclear spin polarization, and also very slow fluctuations in the readout signal due to electric field noise result in a changing amplitude of the interference fringes. A typical error in the fit is 0.15 GHz.

In Figure 4.5 we present the Ramsey interferometry signal from QD A and QD B, where small adjustments have been made to the externally applied magnetic field on QD B in order to produce well-matched ground state energies. The spin splitting is set to $2\pi \times (25.2 \pm 0.1)$ GHz.

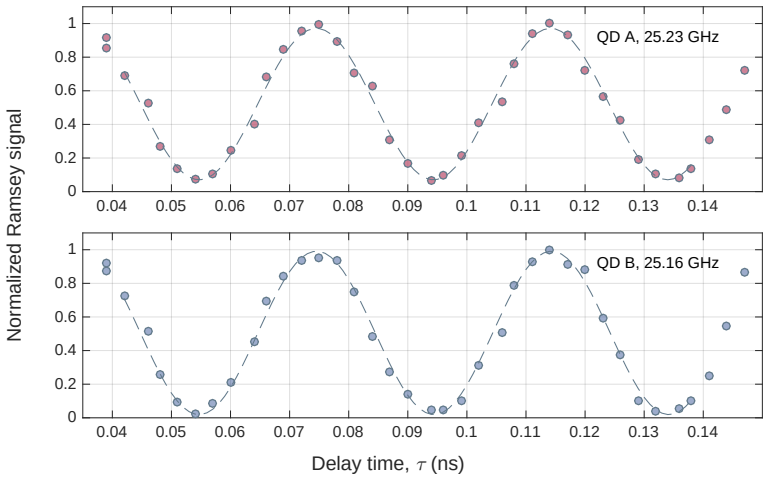

Figure 4.5: Ramsey interferometry of QD A and QD B. Fine adjustment of the externally applied magnetic field has been made to match the Larmor frequencies at 25.2 GHz, within the error of fitting these curves at small time delays, τ.

4.3.2 Hong-Ou-Mandel interferometry

The ultimate test of photon indistinguishability is Hong-Ou-Mandel interferometry [201]. Photons incident on opposite ports of a beam-splitter will exit on the same port if they overlap spatially, in time, central frequency, and linewidth. For an input state in modes a and b, $|1\rangle_a |1\rangle_b$, the output state can then be written:

$$|\Psi\rangle_{BS} = \frac{1}{\sqrt{2}} \left(|2\rangle_1 |0\rangle_2 + |0\rangle_1 |2\rangle_2 \right), \tag{4.11}$$

for the output modes 1 and 2 [196]. It is therefore expected that if two well-aligned modes are coincident upon a perfectly balanced beam-splitter, there will be no chance of detecting the coincidence of a photon on each output port, provided the photons are indistinguishable.

In Figure 4.6 the results of a Hong-Ou-Mandel (HOM) analysis of Raman-scattered photon counts emitted during a weak pulse exciting the red transition are presented. The lack of photon coincidences in the central peak is a signature of photon coalescence. The counts in each pulse (red and blue bars) are noted. We only consider photons within a

1.2ns window of the start of the pulse in order to stay within the joint two-QD inhomogeneous spin dephasing time, $T^*_{2,joint} = T^*_{2,i}/\sqrt{2}$. Typically, one would perform a second measurement where a photon mode is deliberately rotated in polarization by 90° in order to render the photons distinguishable and thus act as a calibration.

Here, this is not possible due to the presence of gratings in the detection filtering set-up which require prior polarization matching. We may alternatively compare the counts in the zero-delay pulse to the outer peaks; these peaks represent interference between completely time-distinguishable photons. However, there is the possibility of detecting correlated photons from the same QD, therefore the mean counts in the side peaks are multiplied by a factor of 0.5, or in other words the HOM visibility, V_{HOM}, is estimated as:

$$V_{HOM} = \frac{\mu - 2 * c}{\mu}, \tag{4.12}$$

where μ is the mean count number in each side peak and c is the count number in the zero-time delay peak.

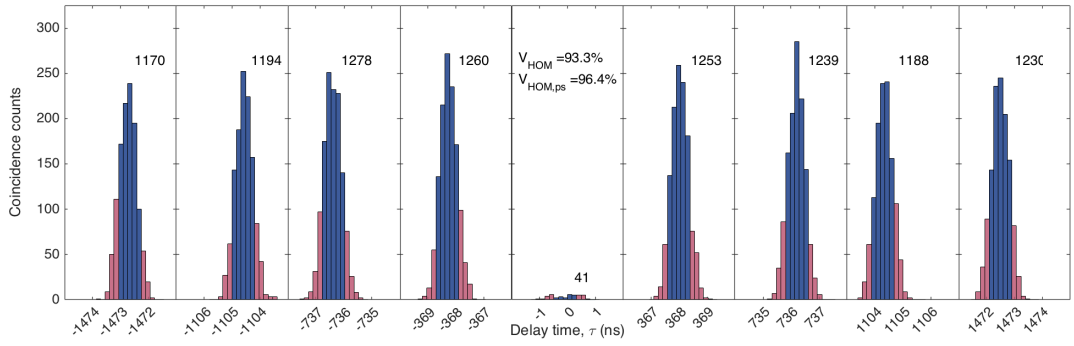

Figure 4.6: Hong-Ou-Mandel indistinguishability measurement for photons scattered from QD A and QD B. Photons scattered at ω_R are collected during a 1.2 ns window coincident with a weak excitation pulse applied to the red transition at ω_l, where both interferometer arms are open, such that both QDs contribute equally to the total counts. The visibility measured is $\mathrm{V}_{HOM} = 93.3$ %, where the peaks representing the full detection window are integrated over. The total coincidence counts integrated over the full 1.2 ns correlation window are recorded in the figure.

For this data, we find $\mathrm{V}_{HOM} = 93.3$ %, which is comparable to the best results available for this type of quantum dot [120, 182]. This can be achieved due to the relatively low spectral diffusion, and good time overlap of the photon wavepackets. The contribution to the emission from the phonon sideband is filtered by our grating and etalon set-up and also does not contribute to a reduction in the photon indistinguishability. Figure 4.7 focuses upon the central peak from Figure 4.6; as the time between photon detection events increases, the inhomogeneous dephasing (time-dependence of ground state splitting, varying by $\simeq$ 190 MHz between the two QDs) results in some distinguishability of the photons. However, there is a compromise to be made; we cannot arbitrarily limit the detection time window without drastically reducing our entanglement generation rate.

Within our detection window as shown in Figure 4.2 as a grey box, we shall assign ≈ 50 % of the single photons emitted in the entanglement pulse to actual entanglement events.

We explore the impact of limiting the detection time difference between photons to 400 ps by selecting the centre of the peaks (blue bars in Figures 4.6 and 4.7), where now $V_{HOM,ps} = 96.4\%$. The visibility saturates as the permitted time difference of photon detection is reduced below 400 ps; we use this to place an upper bound on the reduction in interference due to imperfect polarization control, beam-splitter imbalance and imperfect interferometer alignment of 4%.

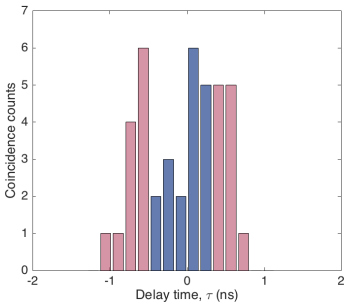

Figure 4.7: Zero time delay of HOM measurement, detail.

4.4 An optical entanglement-generation machine

Prior to this point this dissertation has focused upon the suitability of quantum dots as an experimental system and how adequate quantum dots can be identified. In addition to a suitable sample and the basic requirement of indistinguishability of emitted photons, the experimental set-up is demanding and requires a number of steps. It is necessary that:

- the Raman-scattered photons can be identified, in order that the state is projected to a two-spin entangled state.
- a constant optical phase can be maintained throughout the entire system illustrated in Figure 4.1.
- the state can be verified by measurement of each of the two spins.
- the electron spins in each quantum dot can be rotated independently.

The experimental set up is illustrated in Figure 4.8. In Fig. 4.8(a) the points of input for optical entanglement generation, spin control and measurement are displayed. Quantum dots are within the cryostat and microscope set-ups as described in Section 1.3.3. The 'entanglement pulse' weakly excites each QD, resulting in the Raman-scattered photons which generate the entangled state upon detection; in this case they are at a higher energy than the excitation laser. The entanglement pulse is directed to a first beam-splitter, BS1, and the modes outgoing from the QDs are combined on the second beam-splitter (BS2) prior to photon detection.

Following BS2, photons are filtered using the optics indicated in Figure 4.8b. Each output has an identical set of downstream optics, including a 1200 groove/mm holographic grating (Edmund Optics) which is used in the first instance to remove any unsuppressed background from the detuned rotation pulse (see section 4.4.2). Our QD photons are at 309703GHz (Raman, or inelastically scattered, photons) and 309728GHz (Elastically scattered photons). The two frequencies can be distinguished by high finesse Fabry-Pérot etalons (Manx Optics) with a FWHM of 5GHz and a free spectral range of 250 GHz. The inelastically-scattered photons are transmitted and detected on the 'T' detectors, while elastically-scattered photons are reflected and collected separately on the 'R' detectors. The etalons permit photon detection at ω_R with a background composed of negligible counts from the other transition due to the high rejection at over 99 percent of the outside band photons.

The optical pulse sequence is illustrated in Figure 4.9. The entanglement pulse on the red transition generates the inital spin-photon entanglement for each quantum dot, and inelastically-scattered photons from the blue transition then project an entangled state if detected, indicated as Step 1. The read out of the QD spin populations is via a resonant excitation of the blue transition (Step 3), which also serves to optically pump the spin population prior to an entanglement pulse (Step 4). Any photons detected in the readout window indicate the presence of spin $\uparrow$ population, where the quantum dot of origin is distinguished by timing of the pulses. Finally, there are optional spin rotations in order

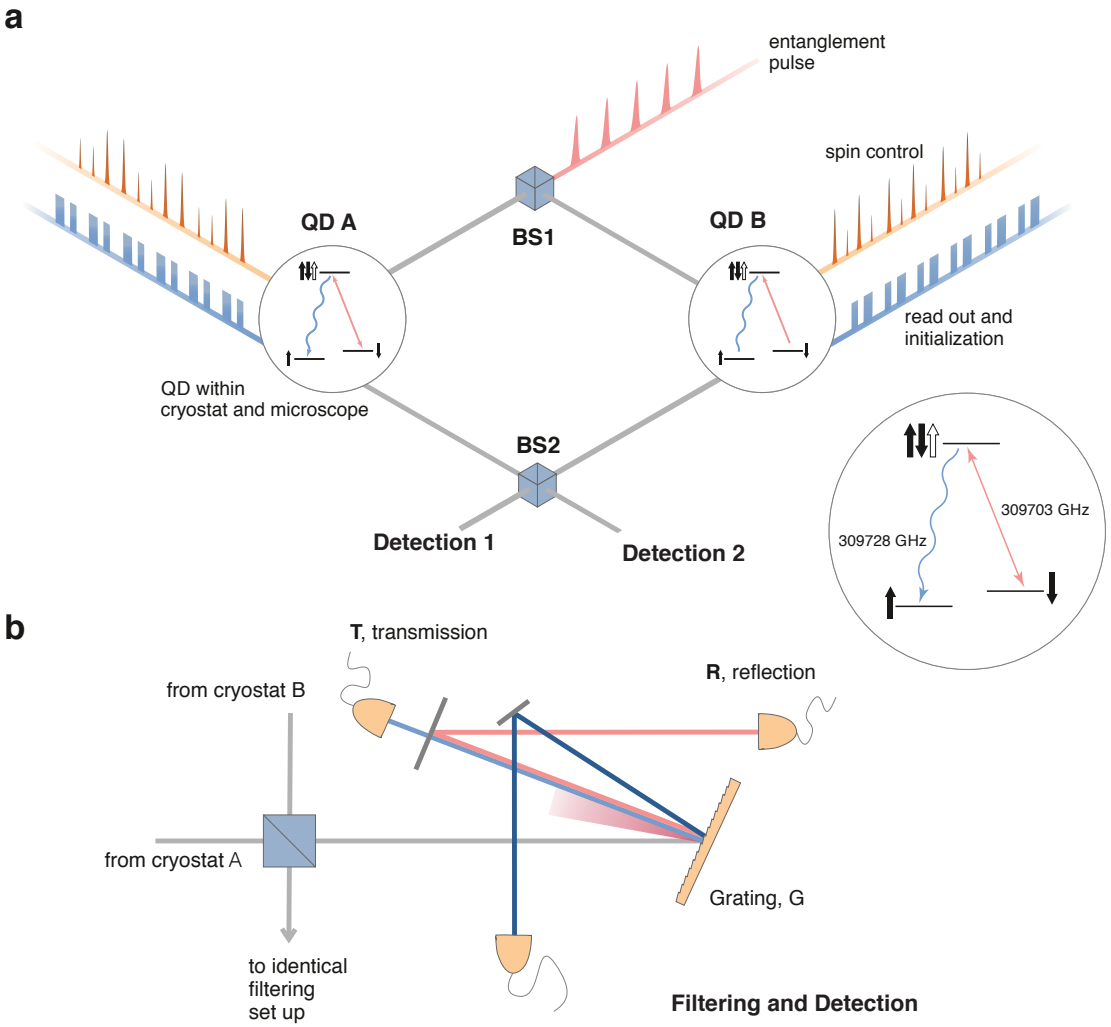

Figure 4.8: The experimental realization of the Cabrillo scheme. a) The Mach-Zehnder interferometer incorporating two QDs, QD A and B. Weak excitation pulses that create the spin-photon entanglement are illustrated entering through BS1. Optical spin control and read-out pulses are independently applied to each QD. (inset) The chosen Λ-scheme, with the transition frequencies at which both QDs are matched. b) A filtering and detection set-up downstream of BS2. A grating first removes the remaining spin rotation pulse background. QD resonance fluorescence is filtered into transmission (T) or reflection (R) via the high-finesse Fabry-Pérot etalon, and finally detected by SNSPDs.

to measure the spin $\downarrow$ population (by first applying a π-rotation), or to rotate the entire state in order to measure along an orthogonal axis (Step 2). By repeatedly applying four combinations of optical spin rotations, the diagonal terms of the density matrix can be mapped out in the basis $\{\downarrow_A\downarrow_B, \downarrow_A\uparrow_B, \uparrow_A\downarrow_B, \uparrow_A\uparrow_B\}$.

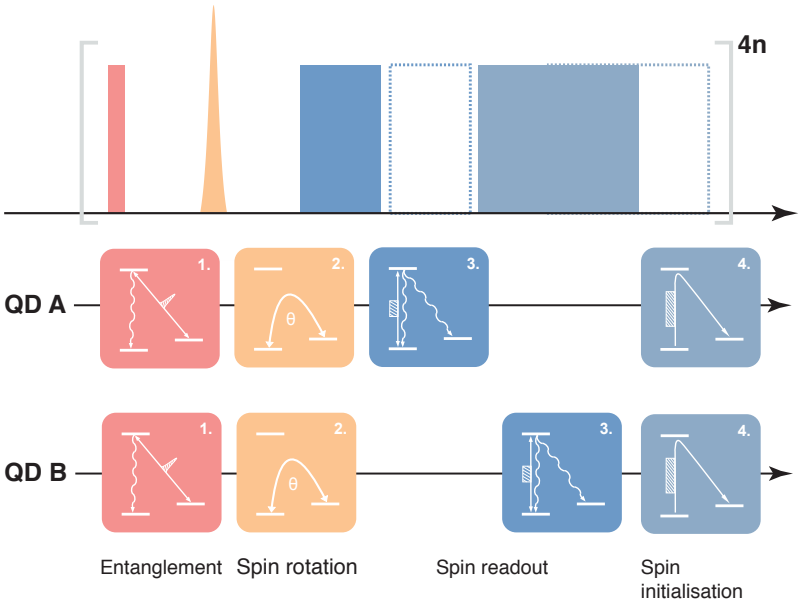

Figure 4.9: An entanglement generation and confirmation pulse sequence. A short, weak pulse is applied to the red transition to intiate spin-photon entanglement, which is projected on to spin-spin entanglement upon detection of an inelastically scattered photon from the blue transition. Optional spin rotation allows selection of the spin population and direction to be measured. Read-out pulses resonant with the blue transitions are applied to each QD, separated in time to allow the measurement to be distinguished, and are followed by further pumping to ensure good spin initialization into $\downarrow$. The sequence is repeated in four ways to allow measurement of all the spin combinations, and the entire sequence is then repeated to obtain statistics and thus reconstruct a density matrix of the created state.

In Figure 4.10 the practical arrangement of this pulse sequence is outlined. A pick-off of a mode-locked laser (Coherent MIRA 900 pumped by Verdi V-5) with a repetition rate of 76 MHz is detected by a 1.4 GHz bandwidth photodiode. This signal acts as a clock for the experiment, via the arbitrary waveform generator illustrated. The signal is also fed to a digital delay generator (Stanford DG645) and divided by 360 to produce a trigger at 211 kHz. The AWG uses this to trigger a time-to-digital converter (qutools quTAU), which is used to time-tag all photon detection events.

The entanglement pulse is supplied by electrical modulation of an amplitude EOM (EOspace), where a tunable CW laser (Toptica TA pro) is fibre coupled into the input. Likewise, the read-out pulses introduced through additional beam-splitters in the excitation paths (Fig. 4.8(a)) are created by EOM modulation (Jenoptik) of a tunable CW input (New Focus). Beam pick-offs allow the mean intensity to be monitored, which permits the

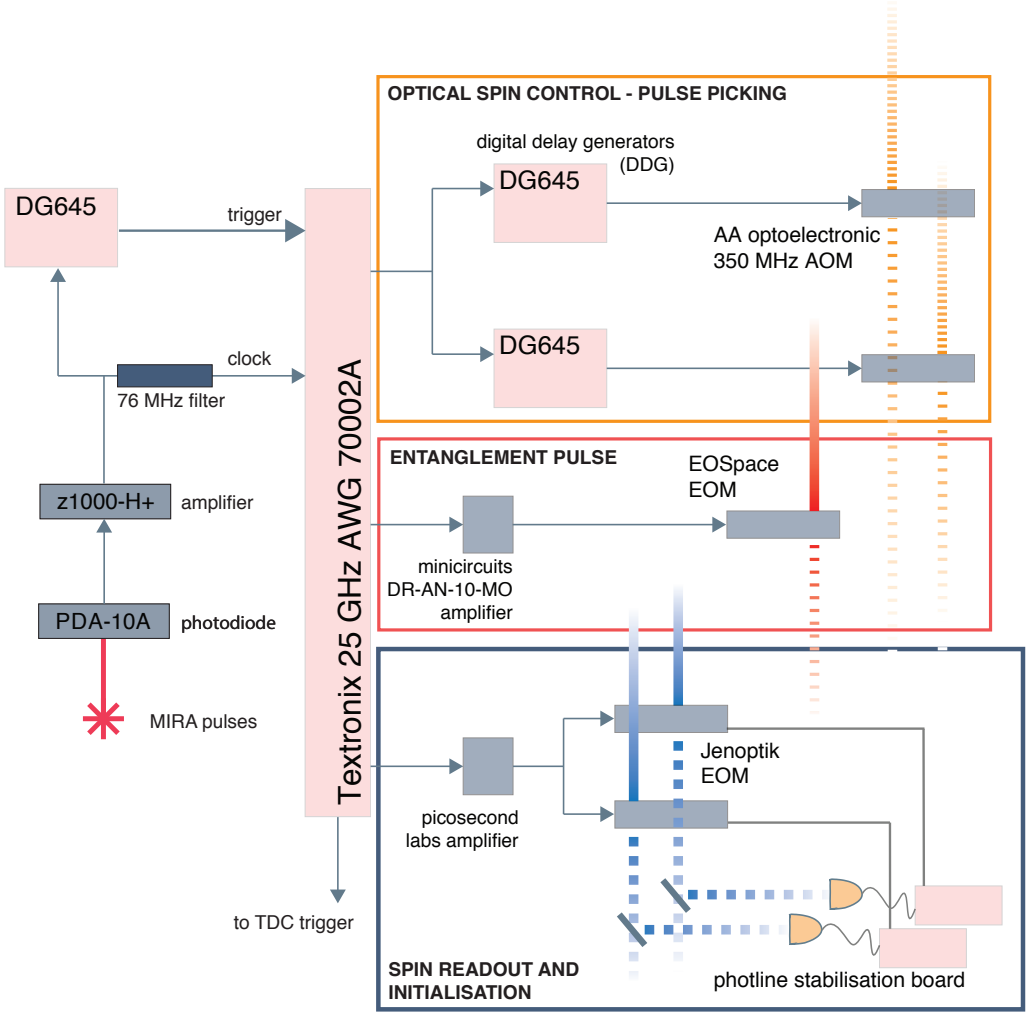

Figure 4.10: Experimental arrangement of the pulse sequence. The mode-locked laser acts as a clock for the experiment, to which the AWG is locked, and additionally provides a trigger for the pulse sequence. The AWG provides the electrical modulation of the lasers, via fast AOMs and EOMs, where amplifiers are required for some signals. The mode-locked laser pulses are selected by AOMs where the signal from the AWG is further modified by digital delay generators. This permits us to select 4/28 pulses, with tunability of intensity for each pulse.

operation of the EOMs to be controlled by stabilization boards (Photline). Consequently the on/off ratios of the CW-derived pulses are ≈ 300:1.

Finally, optical spin rotation pulses are provided by the MIRA system. Pulses are picked from the continuous train at 76 MHz as the first-order diffraction from acoustic optical modulators (AA Optoelectronic) which operate at a frequency of 350 MHz. The ∼ 4 ps long pulses can be selected and amplitude modulated pulse-to-pulse. Overall the effect is to pick 4 of every 28 pulses, and the repetition rate is hardware limited at this point. The input signals to the AOMs are provided by digital delay generators triggered by the AWG.

Photon detection utilises superconducting nanowire single photon detectors (SNSPDs, Quantum Opus) with detection efficiencies of 80 % and a 50 ps timing resolution. However, overall timing resolution is mainly limited by the time-to-digital converter setup, where the bin size is 162 ps. One detector is at each of the 'T and 'R' output ports of the interferometer as illustrated in Figure 4.8(b).

Figure 4.11 illustrates time-tagged photons detected during the pulse sequence in Figure 4.9, as detected in transmission through the FP-etalons. Dotted lines mark the barrier between each repetition with a different optical rotation pulse combination for each. The read-out pulses measure population in the $|\uparrow\rangle$ state only so application of a π pulse here allows readout of the $|\downarrow\rangle$ population, which results, for example, in the contrast in counts between the first two readout pulses for QD A and the final two. Figure 4.11b highlights a single repetition where a π pulse is applied to QD A directly after the entanglement pulse.

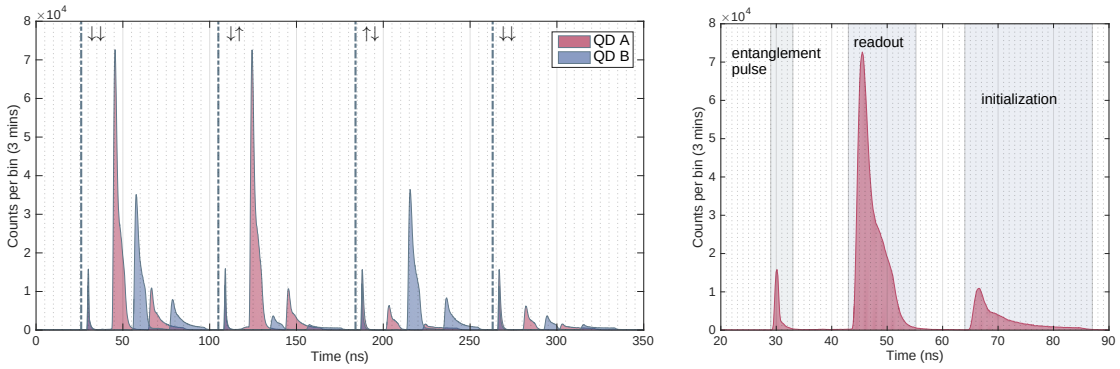

a) Four repetitions of the entanglement generation and measurement sequence, with a different optical rotation pulse combination for each. The spin populations measured in each repetition are indicated. Photons are collected from each quantum dot separately.

b) A single repeat of the pulse sequence, photons scattered from QD A. Each component of the pulse sequence as detected on the 'transmission' detectors is labelled.

Figure 4.11: Detection of entanglement pulse sequence. A histogram of the photons detected from each quantum dot while excited by the pulse sequence, on the detectors behind the Fabry-Pérot etalons.

4.4.1 Spin read-out

Read-out photons can be scattered at both red and blue frequencies, although the 20 ns dead time removes one of the blue detectors from this role following detection of a state-projecting photon. The equal branching ratio of the excited state results in spin pumping with 2 photons scattered on average and a spin pumping time of < 10 ns. Figure 4.12 shows the proportion of photons found in the read-out pulse as compared to read-out and re-initialization pulses combined for the case of QD A. Our detection window is limited to 7 ns due to the need to keep the pulse scheme short. In this 7 ns, we reach a steady state of ≈ 70 % of total scattered photons occuring within our detection window. We choose the lowest power that achieves this, or the onset of saturation at ≈ 0.05 μW, to maximise the signal-to-noise ratio in our read-out. The 70% of total scattered photons corresponds to 1.4 photons per $\uparrow$ spin available to be measured. In this way we preserve read-out fidelity from background signal, while maximising the rate at which our pulse sequence operates.

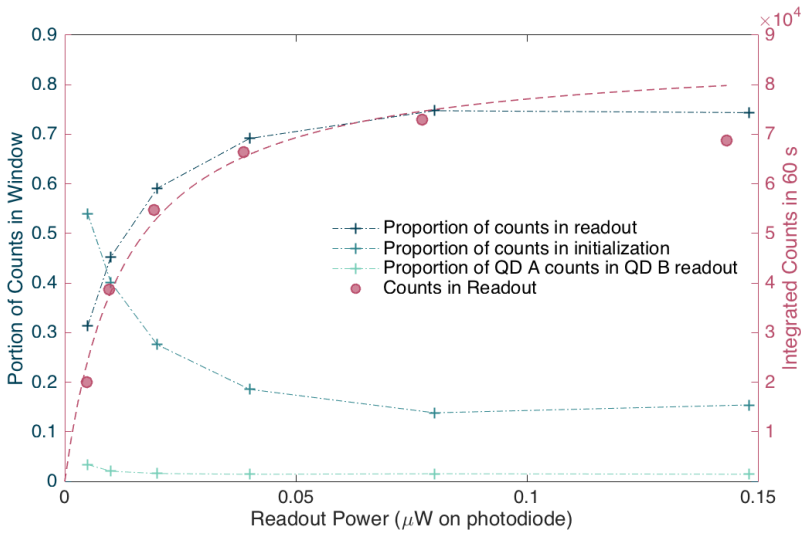

Figure 4.12: Optical spin read-out of a single quantum dot. Photons scattered from the blue transition saturate as the power of the read-out laser is increased. The limit of ≈ 70 % is due to the 7 ns window during which read-out photons may be detected, and we set the read-out power to the onset of saturation.

The figure also displays the proportion of counts from QD A that appear in the readout window of QD B. These counts are composed of background and the driving of QD A under imperfect EOM suppression of CW laser between pulses, but account for less than 2 % of all the counts. A similar estimate is made by considering the identical case of QD B readout.

4.4.2 Optical spin rotation

Fast optical rotation of the electron spin is achieved using ~ 4 ps pulses from the mode-locked laser, highly detuned from the optical transitions, in this case close to 971 nm. This process may be expressed as a stimulated Raman transition that coherently transfers population from one ground state to another, with no intermediate population of the excited state and therefore no loss of coherence due to spontaneous relaxation from this state [15]. Alternatively, the optical Stark shift induced by the laser can be considered to hybridise the ground states for a period during which the resultant superposition evolves and effectively rotates the spin. In other words, for the duration of the pulse, the optical Stark shift may overcome the external magnetic field, and the states as defined in Voigt geometry are projected to the superpositions of eigenstates in the Faraday geometry, with consequent time evolution. At the end of the pulse they fall into eigenstates of the Voigt geometry once more, with spin rotation dependent upon time duration and power of the pulse [102].

However, the spin rotation axis is not perfectly perpendicular to that defined by the pulse rotation, as the external magnetic field contributes a perturbation. To compensate for this we utilize composite pulses where, for example, a π-rotation is broken into a $\pi/2$-rotation, a delay to allow near complete precession of the state around the axis defined by the magnetic field, and a second $\pi/2$-rotation [202, 203]. The delay is adjusted to produce the maximum amplitude of the spin Rabi oscillations.

In Figure 4.13 we present optically-induced Rabi oscillations of an electron spin, where spin population in the $|\uparrow\rangle$ state is measured by a CW laser driving the blue transition. The figure displays detected counts emitted at the lower energy of the Λ-scheme, and is therefore resonant-background free. However, the linearly increasing background is from the rotation pulses themselves and is accounted for as an addition to the otherwise sinusoidal fit.

Once appropriate optical powers are found to allow full inversion of an electron spin ('π-power'), the power of the spin rotation inputs is feedback-controlled through a second set of AOMs (80 MHz frequency). Excess power is removed and placed in the first-order diffracted beam.

4.4.3 Two-photon correlation measurements

Figure 4.14 presents the results of two-photon correlation analysis within the pulse sequence for each QD; the first photon occurs during the entanglement pulse on the blue transition (a Raman-scattered photon), the second photon during the read-out pulse. The bars indicate the probability with which a photon detected during the entanglement pulse predicts the spin measurement proceeding directly after it; in a perfect pulse sequence, the emission of a Raman photon *must* be correlated with spin $\uparrow$. Each was measured independently so contributions from the other QD have no direct effect. The results indicate

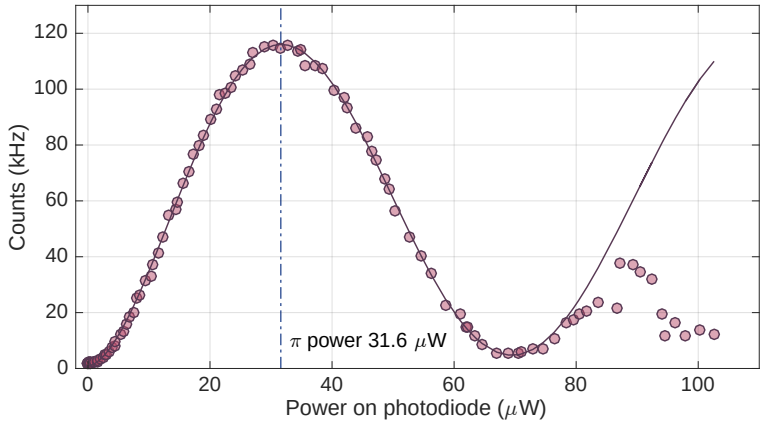

Figure 4.13: Optical electron spin rotation; Rabi oscillations. Counts are the scattered photons detected from the lower energy transition, while the Λ-scheme is driven at the higher energy. The power of the optical pulses applied by the mode-locked laser is varied, and consequently the power at which a full inversion of the electron spin ('π-power') can be found.

that there is strong correlation between the expected result and that measured.

The bars are close to 100 % but do not demonstrate perfect fidelity for several possible reasons. First, the read-out pulses are generated from a CW laser with EOMs, where the region between pulses has suppression of the CW power limited by a maximum factor of $\approx$ 300. In the region between the entanglement pulse and read-out pulses, this allows a small percentage ($\sim 0.5\%$) of the spins to be repumped to the initial state ($\downarrow$), as a consequence $\uparrow$ is erroneously measured to be $\downarrow$. Additionally, by tuning the QDs away from resonance with gate voltage, we measure a background averaging 0.77% of counts in the entanglement pulse. This contributes 'false heralds' which are more likely to be associated with a $\downarrow$ spin than $\uparrow$ due to the weak spin-pumping in the entanglement pulse. The background is a combination of dark counts and residual resonant background from the driving of the blue transition. Finally, imperfect spin rotation results in measurement of a larger $\downarrow$ population than actually exists (when correlated with a Raman photon detection).

Therefore, we identify these limits primarily with any imperfection in the spin rotations; checking two-photon correlations is a final step in ensuring the power settings for these optical pulses are optimal. The values of 96.2 % and 97.3 % are limits in the read-out fidelity for QD A and QD B respectively.

Thus far, we have explored the suitability of the quantum dots and outlined the experimental protocol, along with the limitations arising from both of these sources. We now present results that indicate the generation of a two-electron spin-entangled state.

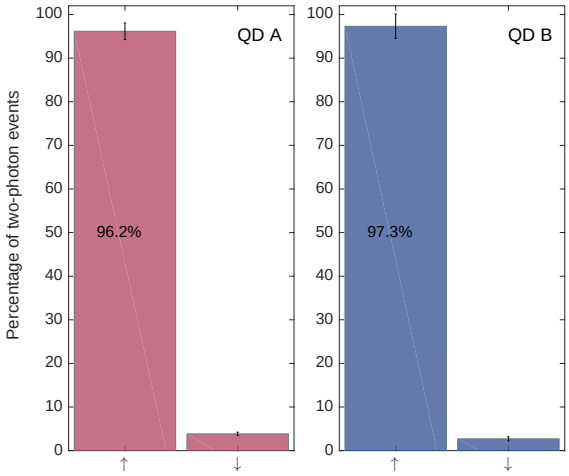

Figure 4.14: Two-photon correlations during the pulse sequence. Following detection of a single photon scattered at the blue frequency during the entanglement pulse, the spin population measured directly afterwards is recorded. If the read-out and spin rotation pulses are correct, this should always be ↑. The fidelity of this process is 96.2 % and 97.3 % for QD A and B respectively.

4.5 Results of two-spin state measurement

4.5.1 Measurement in the population basis

Reconstructing the state created proceeds by identifying three-photon coincidences: first, a photon is detected within 1.2 ns of the start of the entanglement pulse, signalling creation of a state. Next, a photon detection in the readout window of QD A indicates a spin ↑ or ↓ population, dependent upon the preceding spin rotation. The final photon similarly must arise from the readout window of QD B.

In Figure 4.15 the results of these correlations in the computational, or population basis, are presented, where the components of the joint spin basis are $\{\downarrow_A\downarrow_B, \downarrow_A\uparrow_B, \uparrow_A\downarrow_B, \uparrow_A\uparrow_B\}$. The state is thus written in terms of the spins defined in Figure 4.1(b), parallel to the externally applied magnetic field. Measuring the normalized populations of the different spin combinations constitutes a measurement of the diagonal terms in the joint density matrix of the overall state.

The results can be compared to the two extreme cases of a randomly mixed state and a maximally entangled state; in the former case all bars are expected to be equal height as there should be no correlation between the spin populations. A maximally entangled state of the form $|\Psi\rangle = \frac{1}{\sqrt{2}}\left(|\uparrow\downarrow\rangle + e^{i(\theta+\phi_i)}|\downarrow\uparrow\rangle\right)$ should present all population associated with the '↓↑' and '↑↓' components of the basis, as indicted by the dash-outlined bars in the figure.

In this measurement, the total population in the anti-correlated components $\uparrow_A\downarrow_B$ and $\downarrow_A\uparrow_B$ is $\rho_{\uparrow\downarrow} + \rho_{\downarrow\uparrow} = 85.7 \pm 3.8$ %, where the error is given by the shot noise of the 603

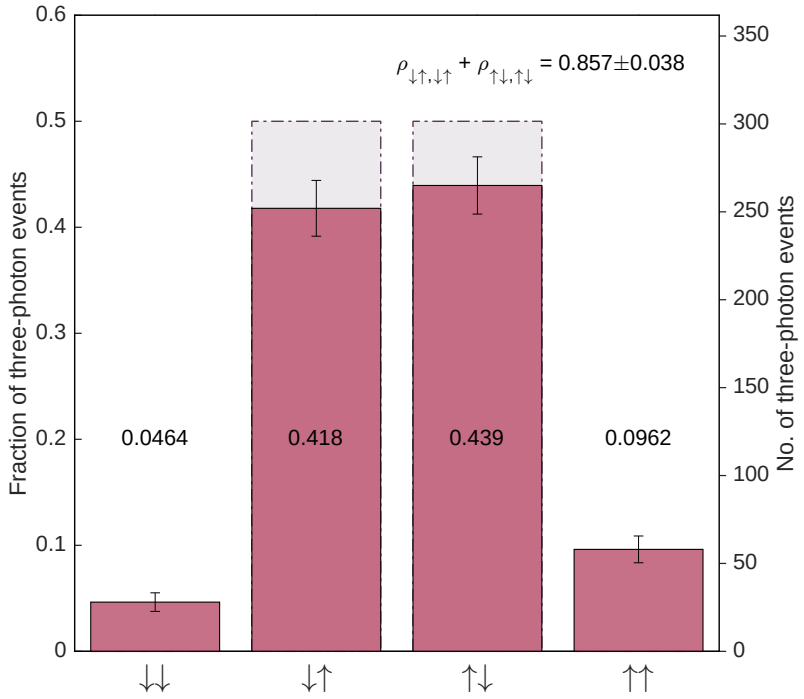

Figure 4.15: Population basis measurement of generated two-spin state. Following detection of a state-projecting photon, the population of ↑ and ↓ spins for both quantum dots is measured. The histogram records the number of occurrences, partitioned into the diagonal terms of a joint spin density matrix. The anti-correlated spin populations, expected in the case of a maximally entangled state, represent 85.7 ± 3.8 % of the events.

three-photon events.

The population in the $\uparrow_A\uparrow_B$ component is due to the inherent error of the entanglement generation scheme. From a comparison of the maximum Raman counts available from each QD in our pulse sequence (122.8 kHz and 85.3 kHz for A and B respectively), and noting that we collect only 50 % of the photons in the entanglement pulse (Figure 4.2), an entanglement event detection rate of 7 kHz corresponds to an average $p = 0.07$. The contribution to the three-photon correlations from ↑↑ is entirely due to creation of this component in the Cabrillo scheme and thus we expect a contribution of 7%. We note that it is essential that the count rate arising from each quantum dot is identical, or there is some which-path information available regarding an individual photon's origin, as one QD becomes a more likely source. For this reason, we must refer to the average value of p.

However, the two-photon correlations of Figure 4.14 indicate an infidelity of the spin measurement for each quantum dot, primarily due to imperfect spin rotations, which therefore impact the measurement of ↓ spin population. We make the assumption that the probability of measuring the ↓ population correctly is 96.2% and 97.3% for QD A and QD B respectively, where other smaller contributions are neglected. This would reduce the central bars to 0.48 and 0.49. As to the origin of ↓↓ population following a Raman photon detection, there are a number of possible explanations. A false herald where no

Raman emission process happens in either QD will result in such a measurement, and is likely to happen ≈ 0.77 % of the time. In the case where a single QD emits a photon with concurrent spin-flip, inadequate rotation of the population from $\uparrow$ results in a larger than expected $\downarrow$ population, which on average would be expected to occur with 3.2 % probability. The combination of these two processes may account for the population in the $\downarrow\downarrow$ state. Therefore, it seems that read-out infidelity accounts approximately for the data, although we note that the precise balance of readout probabilities is sensitive to rotation pulse powers and subject to some fluctuation during the measurement of all 603 events.

The computational basis measurement is sensitive only to the populations of the resultant density matrix and therefore cannot be used to find the off-diagonal components that demonstrate quantum coherence in the entangled state superposition. Rotating the measurement basis to an orthogonal axis projects the phase of the Bell states into the measurable diagonal terms of the resultant density matrix.

4.5.2 Measurement in an orthogonal basis

Following the entanglement generation pulse, the optical spin rotations are supplemented by $\pi/2$ (that is, a total of $\pi/2$ or $3\pi/2$). This maps the state created onto orthogonal eigenstates, and the coherences of the initial density matrix onto the population terms in the rotated density matrix. Rotation pulses are applied directly after the detection window for the state-projecting photon, to reduce the deleterious effect of inhomogeneous spin dephasing upon the measured coherences. It is important to note, therefore, that the spin rotations, and indeed spin measurements, are performed upon a two-spin state that does not yet exist, as the state-projecting photon must travel ~ 5 m (≈ 16 ns) prior to detection. However, we may consider that the projection photon merely selects a subset of the state in equation 4.6 and this does not affect any demonstration of entanglement in this form.

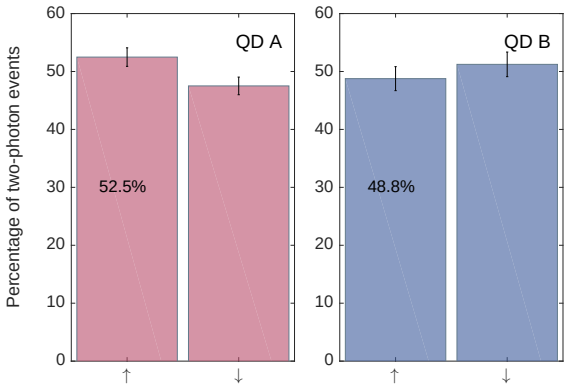

Figure 4.16: Two-photon correlations during the pulse sequence, measurement in rotated basis. Results presented as in Figure 4.14, where an optical $\pi/2$-rotation precedes the spin measurement.

Figure 4.16 gives the results of a two-photon correlation measurement for each QD in the rotated basis. A formerly $\uparrow$ ($\downarrow$) spin is now rotated to the superposition $\propto |\uparrow\rangle + |\downarrow\rangle$ ($|\uparrow\rangle$ - $|\downarrow\rangle$), such that a measurement of the spin following detection of an entanglement-projecting photon yields $\uparrow$ and $\downarrow$ with equal probability. Similar to the computational basis case, deviations are due to imperfect spin rotations, resulting in unequal weightings of the $\uparrow$ and $\downarrow$ components of the superposition. However, we note that deviations are small, and we take account of these errors when considering the final results.

Figure 4.17 presents the three-photon correlation measurements. The filled bars are our results. The pale bars represent measurement of an ideal state with a perfect fidelity compared to the Bell states, and the dashed outlines correspond to the values expected for an entirely mixed state.

Results are presented for two possible Bell states; three-photon correlations are partitioned according to whether the Raman photon was in the same output port as constructive or destructive elastically-scattered photon interference. Therefore, since the phase of a state is the sum of the contributions from the interferometer and the beam-splitter ($\theta + \phi_i$), the events assigned to the state Ψ_+ are those that emerge on detector 1, where the interferometer phase is $\phi_i = 0$ (constructive interference on this output port) or those on detector 2 where $\phi_i = \pi$. These results are shown in Figure 4.17a. The converse situation gives us the events to be associated with Ψ_-, Figure 4.17b. It is important to note that the the Raman photons emerge randomly and are equally distributed between the two output ports of the beam-splitter. This is because there is no Raman photon coherence between the quantum dots, as the initial ground state of the two QD spins has no joint coherence to be mapped onto a coherent photonic state.

Both outputs give the same results in the population basis, as the spins are necessarily anti-correlated. However, by considering the rotation of a joint spin density matrix for an ideal maximally entangled state, it is expected that the visibility, or contrast between correlated and anti-correlated spin populations, is negative for Ψ_+ following a $\pi/2$-rotation of the joint density matrix, and positive for Ψ_-. The results are at first glance somewhat further from the ideal maximally entangled state than the measurements in the computational basis. Measurements in the population basis are susceptible to T_1 processes, whereas in the rotated basis it is T_2 processes that degrade the apparent entangled state, and in some sense it is in the coherences of a state where the truly quantum nature lies. Therefore, we expect the measurement in the rotated basis to be more sensitive to destruction by uncontrolled environmental fields. In order to clarify the quality of the state we have created, we next calculate the state fidelity.

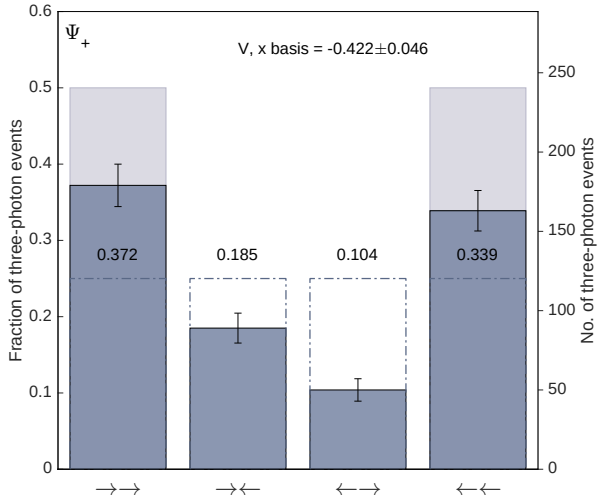

a) Measured two-spin correlations following detection of a state-projecting photon on detector 1 (2) where the interferometer phase was 0 (π), corresponding to attempted creation of the Ψ_+ state. The visibility is -0.380 $\pm$ 0.038.

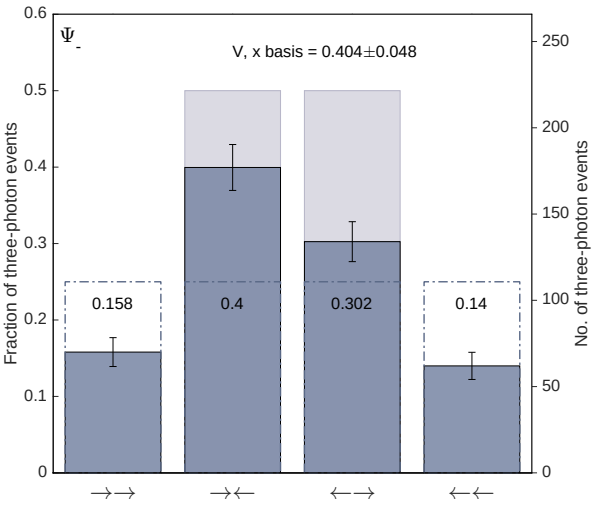

b) Measured two-spin correlations following detection of a state-projecting photon on detector 1 (2) where the interferometer phase was π (0), corresponding to attempted creation of the Ψ_- state. The visibility is 0.357 $\pm$ 0.038.

Figure 4.17: Measurement of entangled state creation in a rotated basis. Following detection of a state-projecting photon, the population of spins is measured where a $\pi/2$ rotation pulse is first applied, a measurement of the populations of $\propto |\uparrow\rangle + |\downarrow\rangle$ ($|\uparrow\rangle$ - $|\downarrow\rangle$). The histogram records the number of occurrences, partitioned into the diagonal terms of the rotated joint spin-density matrix. The visibility is dependent upon which Bell state was created.

4.5.3 Fidelity of created states

The fidelity is defined as

$$F = \langle \Psi | \, \rho \, | \Psi \rangle \tag{4.13}$$

for a measured density matrix ρ, compared to a desired state Ψ. For a general maximally entangled state, the fidelity can be written in terms of a measurable density matrix as

$$F = \frac{1}{2} \left(\rho_{\downarrow\uparrow,\downarrow\uparrow} + \rho_{\uparrow\downarrow,\uparrow\downarrow} + 2Re\{\rho_{\downarrow\uparrow,\uparrow\downarrow}\} \right). \tag{4.14}$$

The computational basis measurement directly provides $\rho_{\downarrow\uparrow,\downarrow\uparrow} + \rho_{\uparrow\downarrow,\uparrow\downarrow} = 0.857 \pm 0.038$. The coherences of the density matrix, or off-diagonal components, are available from the measurement following a $\pi/2$ rotation, where they are transferred to the diagonal terms. The visibility in this basis is written as

$$V = \tilde{\rho}_{\downarrow\uparrow,\downarrow\uparrow} + \tilde{\rho}_{\uparrow\downarrow,\uparrow\downarrow} - \tilde{\rho}_{\downarrow\downarrow,\downarrow\downarrow} - \tilde{\rho}_{\uparrow\uparrow,\uparrow\uparrow}, \tag{4.15}$$

in terms of the rotated density matrix $\tilde{\rho}$. By applying $X_{\pi/2}$ rotations for each spin to the unrotated joint density matrix we identify that

$$V = 2Re\{\rho_{\downarrow\uparrow,\uparrow\downarrow}\} + 2Re\{\rho_{\downarrow\downarrow,\uparrow\uparrow}\}, \tag{4.16}$$

in the case where we rotate the spins such that they may evolve for the same time. In other words, we do not wish the coherence $\rho_{\downarrow\uparrow,\uparrow\downarrow}$ to evolve prior to our spin rotation and subsequent measurement. The term $\rho_{\downarrow\downarrow,\uparrow\uparrow}$ evolves rapidly at $2\omega_L$ in the laboratory frame and therefore averages to zero over the course of any measurement, as the evolution at $\approx$ 50 GHz would require timing resolution better than 20 ps and we are ultimately limited to 50 ps by the detectors. While the term $\rho_{\downarrow\downarrow,\uparrow\uparrow}$ can exist in any single measurement, we are simply insensitive to it, and thus in our *measured* density matrix we may assume these terms are zero.

In summary, the visibility of each state is given in Figure 4.17 and this can be directly identified with $\rho_{\downarrow\uparrow,\uparrow\downarrow}$ [188], leading to the fidelity via equation 4.14. For Ψ_+ we measure F = (64.0 $\pm$ 3.0) % and for Ψ_- we measure (63.1 $\pm$ 3.0) %.

In the case of a classical mixed state no correlation exists between the two electron spins, and any coherence between the two spins vanishes, resulting in a maximum fidelity of a measurement of the density matrix, when compared to the maximally entangled state, of 0.5. For Ψ_+ we therefore violate the classical limit by 4.7 standard deviations of the mean, and for Ψ_- this figure is 4.3.

4.5.3.1 Limitations to state fidelity

The state fidelity reached is evidently less than the perfect value, where a combination of experimental inaccuracies and the solid state environment are responsible. First, the

single-photon detection scheme has an in-built error due to weak driving with probability p; this reduces the overall fidelity to (1-p), a factor of 0.93 here. Next, considering the distinguishability of the Raman photons, any possible knowledge of Raman photon origin leads to components of the measured density matrix associated with the states given in Equations 4.9 and 4.10. The two components of this form are weighted by (1-V_{HOM}) in a total density matrix which reduces the total expected fidelity to F = 0.899 and the rotated basis visibility to 0.87. The reduction of indistinguishability only impacts the coherence terms and therefore the visibility as measured in the rotated basis alone.

Figure 4.16 suggests that the rotation to an orthogonal basis is imperfect; a correction for this makes a negligible change to the fidelity, F = 0.896, where a 5% error in the rotation is permitted. The expected visibility measured in the rotated basis would then be 0.86. Similarly, we again account for the error due to the imperfect spin measurement fidelity discussed in Section 4.4.3, where the lower bound for readout accuracy is 95 %, leading to F = 0.85.

Thus far we have neglected inadequate spin initialization, where an estimate based upon the remaining fluorescence at the end of the spin initialization pulse suggests that electron spin population can be considered to be 98% $\downarrow$ upon beginning the pulse sequence. If a QD spin population begins in the $\uparrow$ state, a subsequently detected photon must have originated from the other QD, contributing further to the $\uparrow\uparrow$ component of the state. This may be responsible for the 9%, rather than 7%, population measured for $\uparrow\uparrow$ in Figure 4.15, and taking this into account reduces the expected fidelity to 0.83.

Finally, we consider the effect of the nuclear Overhauser field. Inhomogeneous electron spin dephasing occurs within the time between emission of a Raman photon and the projection of the time-dependent state coherences onto the spin populations. We estimate the effect by taking a joint dephasing time of the two spins, $T^*_{2,joint} = 1.2$ ns, and allowing photons to be detected within this window from the start of the entanglement pulse, as the optical rotation occurs directly afterwards. The Larmor precession frequencies of each entangled state are assumed to be normally distributed about a mean value of zero. The leads to a factor of 0.82 that acts to reduce the rotated basis visibility alone, resulting in a final fidelity of 0.76, which remains in excess of our measurement. However, it is not easy to take into account the effects of slow, QD-dependent drift in the Larmor frequencies, which arises due to very slow electric field noise and is discussed in the next chapter. Such drifts will result in not only increased photon distinguishability, but also precession of the entangled state in the laboratory frame. Additionally, the stability of the state created is sensitively dependent upon the phase ϕ. The origin of fluctuations and steps taken to maintain stability of this phase are the topic of the next chapter. We anticipate the results of the next chapter, where we find evidence that the fast electric field noise is directly translated on to the phase of the entangled state, resulting in a further reduction of fidelity.

4.6 Discussion and conclusions

In Figure 4.18 we compare the fidelities achieved for optically mediated entanglement schemes in current literature. The value obtained in this experiment for the Ψ_+ state is included, as well as results from Type I, Type II, and double-heralding schemes thus far used exclusively to entangle electron spins within distant NV centres in diamond samples. The references are given in the figure caption.

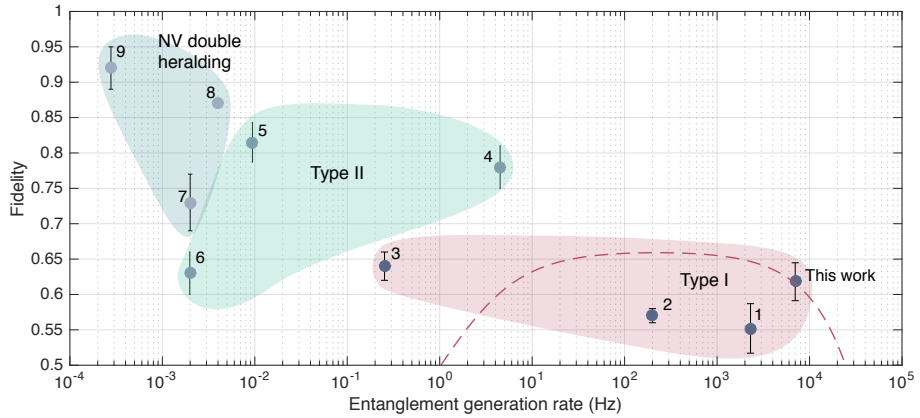

a) Entangled state fidelity as a function of generation rate. The reported fidelity for a series of different experiments, using each of the three photon-mediated entanglement methods discussed, is presented as a function of the generation rate achieved.

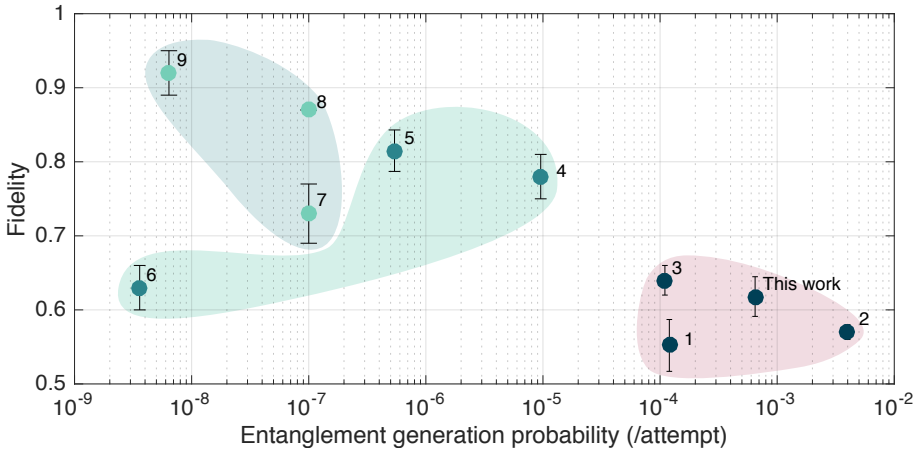

b) The reported fidelity is presented against the success probability during an entanglement generation attempt.

Figure 4.18: Comparison of results to current literature reports. The results presented here are compared to other implementations of Type I schemes, Refs. 1 [83], 2 [190], and 3 [186], Type II schemes, Refs. 4 [77], 5 [189], and 6 [188] and double-heralding schemes which have been used in NV centres in bulk diamond only, Refs. 7 [192], 8 [193], and 9 [33].

In Figure 4.18a the general trend is of a trade-off between fidelity and entanglement generation rate. Applications of the double-heralding scheme [191] and Type II schemes are slow due to the requirement of two-photon detection events in addition to spin readout,

however there is no inherent limitation to the entanglement fidelity 'built-in' to the scheme. On the other hand, single-photon detection schemes inherently permit faster entanglement distribution but do so at the cost of an imperfect state.

The results obtained in this chapter are of comparable fidelity to other single-photon detection schemes. The figure also includes a projection of the fidelity that would result if p were reduced by driving the optical transition more weakly during the entanglement pulse (red dashed line). Fidelity improves as the resulting generation rate decreases, false heralds due to laser background from both cryostats combined can contribute 0.77 % of the counts, but this necessarily decreases with p. Instead, the detector dark counts contribute 1 Hz of false heralds, negligible at the $\approx$ 7 kHz operating rate of this experiment, but dominant as p is reduced. If other limitations upon fidelity such as inhomogeneous spin dephasing and incorrect read-out events are not addressed, the maximum fidelity that could have been achieved in this work is 65.9 %, with a sacrifice of generation rate to $<$ 1 kHz. In the other direction, generation rate is limited to $\approx$ 25 kHz if F $>$ 0.5 is to be maintained.

To distinguish the effect of repetition rate from success probability, Figure 4.18b summarizes the same references as reported in Figure 4.18a, but instead the probability of success in each attempt is calculated. The division between single-photon and two-photon detection schemes is more pronounced; displaying entanglement generation rate alone concealed experiment-dependent factors such as the requirement of trap loading for ion implementations. We are able to operate continuously at 10.8 MHz, limited as yet by hardware rather than the capabilities of the quantum dots themselves. The total photon detection probability inclusive of the sample out-coupling, microscope, filtering set-up, and detector efficiency is 11.3 %, and only 4.1 % of the useful Raman-scattered photons are coupled from the sample into the collection mode. Therefore, the total Raman photon detection efficiency, $p_c\eta_d$, is 0.5 %. Combined with $p = 0.07$ for each quantum dot, this takes a 10.8 MHz possible operating rate and reduces it to the $\approx$ 7 kHz we see here. The implications of possible operation rate will be discussed more in the conclusion to this dissertation.

It was necessary in the course of this work to measure the two-electron spin states prior to detection of the state-projecting photon, and we note that the inhomogeneous dephasing time currently limits the creation of a single, shot-by-shot stable entangled state to a photon detection window of $\approx$ 1.2 ns, the joint spin T_2^*. In order to circumvent the electron spin inhomogeneous dephasing, one may apply a spin-echo sequence to the quantum dots, as demonstrated in Ref. [17], where microseconds of spin coherence permits a photon path length of hundreds of metres.

As an alternative, it has been suggested that the nuclear spins in a quantum dot become locked in a coherent population trapping process [204], where this may provide a route to extend the T_2^* if incorporated into these experiments. It is also possible to work with hole spins where the T_2^* is extended $>$ 20 ns [83]. The very best reported T_2^* of holes

thus far reported is 460 ns, indicating that there may be large gains in a slightly different choice of spin qubit [169]. Reference [169] argues that the variation in apparent T_2^* for holes is likely due to the inconsistent amount of electrical field noise in each sample (due to the electric-field sensitivity being rather dominant as discussed in Chapter 2), as well as the differing profile of the quantum dot wave-functions, and as yet there is no definitive answer for the final limitations of hole spin coherence.

In the conclusion to this dissertation we will turn to a more detailed discussion of the advantages of quantum dots and their limitations, and the necessary developments that would be required to realize quantum technologies in this context. This dissertation has thus far neglected the entangled state phase stabilization and control. In the next chapter, the ability of the operator of the 'entangled state generation machine' to choose and control this phase is demonstrated, and a range of entangled states are created through optical phase tuning.

Chapter 5

Entangled state control through optical phase tuning

In the previous chapter a two-electron spin-entangled state was realized. However, the scheme we adopt results in a mapping of the optical phase on to the spin-spin state [82, 185], therefore requiring the stabilization and control of the state as exercised through the Mach-Zehnder interferometer. In this way it is possible to create states of the form $\Psi = \frac{1}{\sqrt{2}}\left(|\uparrow\downarrow\rangle + e^{i\Phi_I}|\downarrow\uparrow\rangle\right)$ where a choice regarding Φ_I can be made and 'programmed' via the physical control of optical phase.

This chapter addresses the form of the entangled state phase in terms of optical path lengths and the resulting requirements with regard to stability and path-length matching in the experiment. The phase is also sensitive to the ground state splitting of the Λ-scheme, and here we explore in more detail the variation of the Larmor frequency due to slow electric field noise. We detail how the active stabilization of the phase is achieved in a fibre-based interferometer, and finally demonstrate that the phase of the entangled state can be pre-determined by the operator of our 'entanglement-generation machine'.

5.1 Phase of the entangled state: optical-path-length mapping to a spin state

In the previous Chapter, the phase of the state created by the 'Cabrillo scheme' is written as:

$$\Phi_e = (\phi_B + \xi_B) - (\phi_A + \xi_A) + \theta \tag{5.1}$$

where $\theta \in \{0,\pi\}$ depends upon which side of the beam-splitter the inelastically scattered photon emerges from. The phase of the excitation laser is ϕ_i prior to a quantum dot where the first beam-splitter acts as a reference point, prior to the second beam-splitter the phase accumulated by the photon emitted in a spin-flip scattering process is ξ_i.

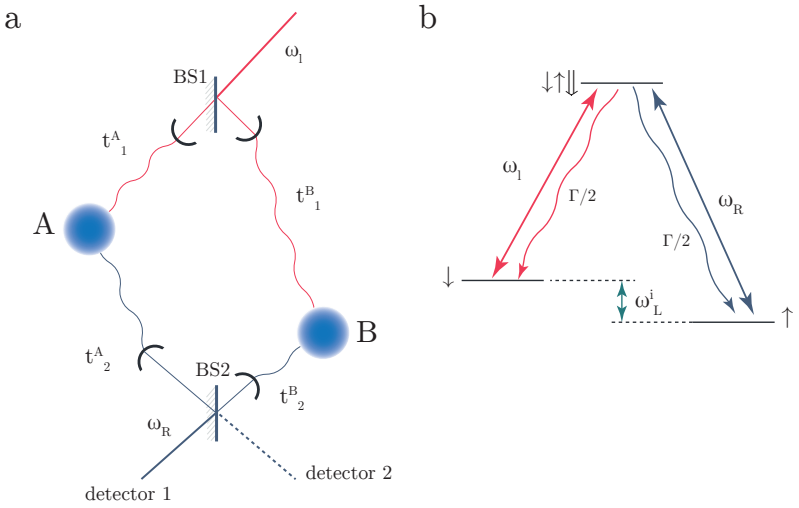

Figure 5.1: Schematic of phase origin in single-photon detection scheme. a) Outline of the Mach-Zehnder interferometer including the time of flight of photons along each of the four component paths. b) The Λ-scheme of a single quantum dot, reproduced to aid discussion.

In Figure 5.1 the optical path travel times in the interferometer are defined, and the general Λ-scheme is reproduced as a reference. The phase of the entangled state can be expressed as:

$$\Phi_e = \omega_l \left(t_1^B - t_1^A\right) + \omega_R \left(t_2^B - t_2^A\right) \tag{5.2}$$

where the values $\Delta t_i = t_i^B - t_i^A$ are non-zero in the case of an interferometer with asymmetric arms. We may restate the phase as:

$$\Phi_e = \omega_l \Delta t_1 + \omega_R \Delta t_2. \tag{5.3}$$

This raises three crucial points regarding the physical implementation of this scheme:

- The optical phase of the entire interferometer illustrated in Figure 5.1(a) is imprinted on the entangled state phase, and only if it is constant is a single entangled state created. Therefore we actively stabilize the path length of the interferometer. The technique and limitations of the phase stabilisation are the topic of Section 5.2.

- The presence of any *changing* asymmetry in the arms will result in a phase drift because the 'before-qubit' and 'after-qubit' paths are associated with separate optical frequencies. In Equation 5.3 it is clear that even if the overall phase of the interferometer is stabilised so that $\Delta t_1 + \Delta t_2 = constant$, it is possible that there is some change $\delta\Delta t_1 = -\delta\Delta t_2$ which will result in a change in entangled state phase:

$$\Delta\Phi_e = \delta\Delta t_2 \left(\omega_R - \omega_l\right). \tag{5.4}$$

The experimental results of the last chapter were found using QDs where $\Delta\omega = \omega_R$

- $\omega_{\mathrm{l}} = 25 \times 2\pi$ GHz. As a result, the phase drift is $2\pi \times 8.3 \times 10^{-3}$ /$(100\ \mu\mathrm{m})^{-1}$, or $3^{\circ}/(100\ \mu\mathrm{m})^{-1}$ in terms of optical path length. We find a maximum unavoidable phase drift of $\approx 4.5\ ^{\circ}$ when using our fibre-based interferometer primarily due to the temperature-dependent refractive index of the optical fibres, which results in a typical drift of 150 μm.

- The phase of the interferometer as apparent from interference of just the frequency ω_l is not the phase of the entangled state.

Regarding the third point, in our experiment the interference of the elastically-scattered photons is the only way to measure entangled state phase. This is the interferometer phase Φ_{I} given by:

$$\Phi_I = \omega_l \Delta t_1 + \omega_l \Delta t_2. \tag{5.5}$$

It is clearly not the same as the phase of the generated entangled state, Φ_e, where the difference can be written:

$$\Delta\Phi = \Phi_e - \Phi_I \tag{5.6}$$

$$= (\omega_R - \omega_l)\, \Delta t_2. \tag{5.7}$$

Hence, the dephasing of the red and blue frequencies over the 'post-qubit' optical path differences Δt_2 prohibits a direct prediction of the entangled state phase from the elastically scattered photons; it is not possible for us to directly measure Δt_2 with sufficient accuracy (a few tens of μm in length) to deduce the difference between the 'measured' phase and the 'real' phase of the state.

However, by correctly timing the $\pi/2$ rotation pulses used to map the density matrix coherence terms onto spin populations, we may unwind the phase difference and directly identify the phase of the interferometer with that of the measured state. In order to achieve rotation pulses with this timing, we set the delay of the interferometer to zero, as detailed below. By deriving the pulses from a single pulsed source using a beam-splitter, and then applying the pulses separately to each QD, we create a second larger interferometer overlapping with the second half of the 'entanglement' Mach-Zehnder. We set the delay of this second interferometer to zero by requiring maximal interference of the optical rotation pulses at the outputs of BS2 (see Figure 5.2). A full 2π phase difference $\Delta\Phi$ is developed if the offset from zero delay is 40 ps, or 1.2 cm in free space, so we must aim to match the interferometer arms with an offset far below this value. Details of the delay matching achieved are covered below in Section 5.2.3.2.

So far, we have considered the impact of the spatial arrangement of experimental equipment and mechanical stability thereof. It is also necessary to consider the impact of non-identical Λ-schemes, for as discussed in chapter 2, the electron ground state spin splitting is susceptible to the variable nuclear Overhauser field.

Although the necessity of indistinguishable photons has been established as inherent

to the erasure of which-path information, any difference in ω_R between the two systems also becomes apparent through the phase of the state. If we describe the difference in the ground state energy splittings as $\delta\omega_{Larmor}$, we find that the entangled state can be restated:

$$\Phi_e = \omega_l(\Delta t_1) + \omega_R(\Delta t_2) + \frac{\delta\omega_{Larmor}}{2}\left(t_2^B + t_2^A\right), \tag{5.8}$$

where ω_R represents the mean Raman photon frequency. We have gained a third term which exposes the phase to variation due to path length and a time-dependent $\delta\omega_{Larmor}$. Regarding the variation in path length, the maximum variation in $t_2^B + t_2^A$ was measured to be ~ 150 μm, which corresponds to $\Delta\Phi_e/\delta\omega_{Larmor} \approx 5 \times 10^{-13} \times 2\pi$ radians GHz^{-1}. As an example, if $\delta\omega_{Larmor}$ takes the physically reasonable value of 200 MHz and the path changes by 150 μm, $\Delta\Phi_e$, the change in the state phase, is 3.6×10^{-11} degrees. In other words, if the difference in ground state splittings is fixed during a measurement, changes in the optical paths result in negligible dephasing.

However, the requirement of a fixed difference in ground state splittings ($\delta\omega_{Larmor}$) is more challenging. In the third term of equation 5.8, variation in $\delta\omega_{Larmor}$ limits the maximum $\left(t_2^B + t_2^A\right)$ that is allowed if the state phase is to be maintained. In other words, it acts to limit the distance over which entanglement can be distributed. Here, if $\delta\omega_{Larmor}$ varies by 100 MHz from one entanglement attempt to the next, in order to maintain an entangled state phase within 10° of the chosen value, $\left(t_2^B + t_2^A\right) \times c < 16$ cm in free space. In our experiment we work at > 5 m, which corresponds to a distribution of Φ_e across $0.83 \times 2\pi$ radians, or 300 degrees. By rotating the state with $\pi/2$-rotation pulses directly after the state-creating photon detection window, we seek to render ourselves blind to this component of the phase by projecting state coherence terms onto spin populations before they can dephase. To mitigate this effect entirely we would need to extend the T_2^* of the spin qubit, or perform a Hahn-echo type control sequence to undo the random phase accumulation in each state generation event.

It is also important to note, as we shall discuss in Section 5.4, that the Larmor frequencies are not only susceptible to fast inhomogeneous dephasing, but that there is slow drift between our two quantum dots due to the effect of slow charge noise.

5.1.1 Phase noise of the scattered photons and the entangled state

We now turn to the coherent properties of the light and its phase stability. For a simple two-level system in these quantum dots the photons are coherently scattered with a dephasing time limited by the lifetime of the excited state, where additional excited state pure dephasing can be neglected [11]. With a Λ-scheme the Raman-scattered photons have a coherence limited by the ground state spin dephasing. Coherent excitation of a single quantum dot from a initial $\downarrow$ state is projected to a coherence between the ground state spins when a first Raman photon is detected. This coherence decays according to the T_2^* value of a single electron or hole, such that interference with a second Raman-scattered

photon scattered a time τ later will have vanishing visbility as τ extends beyond the T_2^*. The decay of Raman photon coherence has been used to measure the T_2^* value of a single electron or hole [127].

While individual elastically scattered photons are coherent with an excitation laser, there is a phase shift upon scattering that is detuning dependent. When photons scattered from a single quantum dot are interfered with the excitation laser in a homodyning experiment, the phase-locking is lost on the timescale of the spectral wandering [119]. For the sample used here we expect timescales of electric field noise ranging from 500 μs to seconds to cause a shift in relative laser-QD photon phase.

In this experiment we are interfering the elastically and inelastically scattered photons from two *separate* quantum dots and therefore we must account for mutual dephasing.

If the elastically-scattered photons emitted by the two quantum dots were phase-locked to the excitation laser, we would expect high visibility interference between these photon modes after the quantum dots, with the only phase noise arising from path length drift of the interferometer. However, the time-dependent detuning of the excitation laser from the red transition of the quantum dots due to independent environmental noise sources (where we must include the Overhauser field as it shifts the energy of the ground state spin, as well as electric field noise) results in random relative phase shifts between the QDs. This is at the heart of the reduction in visibility of elastically-scattered photon interference that we measure below in Section 5.3.

We therefore add a term $\Delta\phi_{random}(t)$ to the overall phase of the elastically-scattered photons (the 'interferometer phase') here:

$$\Phi_{\mathrm{I}} = \omega_l \Delta t_1 + \omega_l \Delta t_2 + \Delta\phi_{random}(t), \tag{5.9}$$

It is important to recall that the phase of the elastically-scattered photons does not represent the entangled state as given in equation 5.2, but rather is merely an *indicator* of what the phase is. However, the impact of the random addition to the interferometer phase remains on the entangled state. In equation 4.3, which represents the generation of spin-photon entanglement by a single quantum dot prior to the beam-splitter, the state carries the phase of the excitation laser in the coherence developed between the two terms [19]. A time-dependent detuning applies the additional random phase term, $\Delta\phi_{random}(t)$, as seen above. In the case of a single spin-photon entangled state such phase terms are not seen as they become a global phase. Here, however, we interfere the photonic modes from two quantum dots and the phase in the spin-photon entangled state of each is mapped onto the entangled spin state.

We may simply append the same random phase term to the entangled state as used in the case of the elastically-scattered photons in equation 5.9:

$$\Phi_e = \omega_l \Delta t_1 + \omega_R \Delta t_2 + \frac{\Delta\omega_{Larmor}}{2}\left(t_2^B + t_2^A\right) + \Delta\phi_{random}(t). \tag{5.10}$$

This means that we expect the time-dependent detuning of the entanglement pulse from the red transition of our Λ-schemes to result in fluctuating entangled state phase. The processes responsible are uncontrolled electric fields, as well as the Overhauser field from the nuclear spins, and therefore we expect the variation to occur on timescales from ~ 1 μs to seconds.

In the experiment there is no initial coherence between the spins in two separate quantum dots. Therefore, even if the T_2^* of both spins was extended we do not expect to see interference between the Raman photons at the output of the second beam-splitter. However, once an entangled state is created a coherence now exists between the quantum dot spins, and a second weak scattering from the QDs allows this to be measured [83].

The interference of the elastically-photons at the output of the interferometer will be particularly useful in what follows; it is examined about a net interferometer delay of zero in order to find Φ_e. However, the reduction in visibility of the elastically scattered photons also indicates the extent to which the noisy environment impacts upon the final entangled state through the jitter on the red transition, and we discuss this in the conclusion to this chapter.

From this discussion we have established the origin of the phase of our entangled state, Φ_e and the mechanisms that can change it. In order to produce a controlled state, the phase must be stabilized. In addition, we must perform spin rotations with the correct timing offset to know the entangled state. Finally, we find limitations due to drifts in the asymmetry of the interferometer, the inhomogeneous dephasing of the electron spin, and the phase noise between the excitation laser and elastically scattered photons from each quantum dot.

5.2 Phase-stabilization of a fibre-based interferometer

The interferometer stabilisation is achieved through phase monitoring and direct feedback, the components indicated in Figure 5.2. First, there must be a phase reference that is independent of quantum dot state preparation and read out. This is provided by a laser tuned to 313171 GHz, or 958 nm, far from optical transitions of the quantum dots. The phase reference is introduced at BS1 as indicated in Figure 5.2(a). It follows the path of the entanglement excitation laser and the photons scattered from the QDs, impinging finally on BS2. After BS2 all laser modes are incident on the downstream optics, where the reference is filtered out by using the gratings G1 and G2 and directed to fibre collection via a pick-off mirror, see Figure 5.2(b). There is an additional advantage to having a far-detuned laser as a phase reference; the background suppression using crossed polarization is highly chromatic leading to count rates of at least 5 MHz available from each cryostat in normal operation.

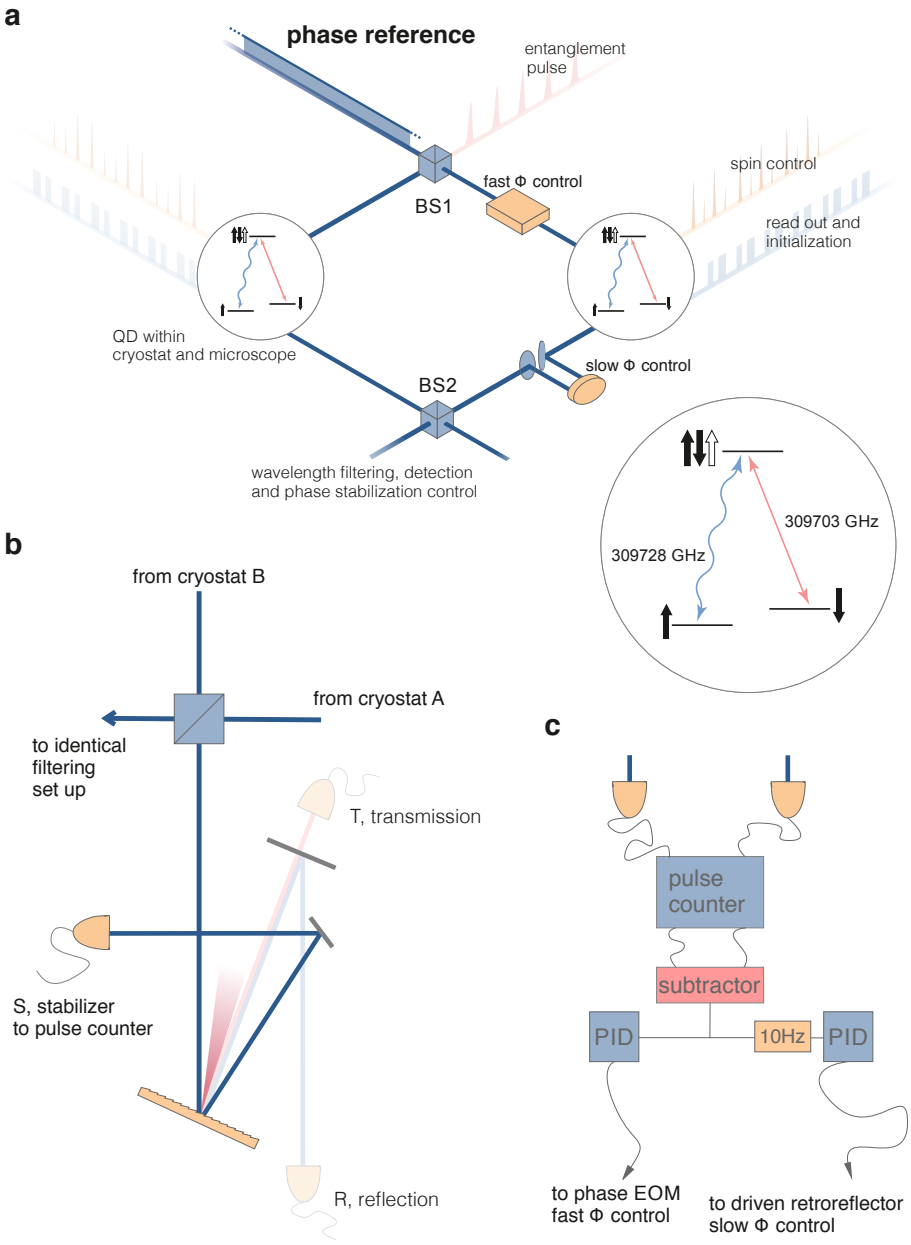

Figure 5.2: Experimental phase stabilization and control. a) The Mach-Zehnder interferometer where the far-detuned CW phase reference laser is highlighted. The other components of the experiment are included as a background. Phase stabilization is achieved through a combination of 'fast' and 'slow' control, where both a fast phase EOM and a retroreflector mounted on a piezo-driven stage participate in a PID-controlled feedback loop. b) The post-BS2 filtering arrangement, inclusive of a pick-off mirror downstream of the grating, that enables detection of the phase reference signal by APDs. c) The phase stabilization feedback loop; APD counts are converted to a voltage signal, and subtracted detection removes the impact of intensity noise. A 10 Hz low-pass filter is used prior to the feedback control of the piezo-driven retroreflector, and the phase EOM is subject to a second PID controller, operating at a bandwidth limited by the pulse counters.

5.2.1 Homodyne measurement of phase noise

We elucidate the typical frequencies of noise and necessary bandwidth for phase stabilization using the reference fringes detected by a fast photodiode (PD, Femto), Figure 5.3.

Figure 5.3a indicates the phase evolution of the entire interferometer, detected on a single output of BS2. There is apparent phase drift at sub-Hz frequencies, and higher frequency phase noise less than a full fringe height. The detection bandwidth is 10 kHz. By blocking each arm of the interferometer we can also see noise contributions from laser intensity and the PD detection. The intensities of the two arms are not equal because input power to each cryostat cannot be adjusted to compensate for microscope-dependent background suppression at this wavelength. However, the homodyne measurement enables the signal to be amplified by the high intensity arm.

From a comparison of the fringe height and single arm intensities, the mode overlap is nearly 100%. Specifically, for two detectors S1 and S2, the expected intensities in the case of perfect spatial mode overlap are:

$$\mathrm{I_{S1}} = \mathrm{I_0}\left(1 + \alpha + 2\sqrt{\alpha}\cos\phi\right) \tag{5.11a}$$

$$\mathrm{I_{S2}} = \mathrm{I_0}\left(1 + \alpha - 2\sqrt{\alpha}\cos\phi\right), \tag{5.11b}$$

where ϕ is the relative phase of the two paths, $\mathrm{I_0}$ is the higher intensity and α is the factor by which the other path intensity is reduced, $\mathrm{I_{weaker}} = \alpha \mathrm{I_0}$. In this example intensity is proportional to voltage, $\mathrm{I_0}$ is 0.14 V and $\alpha = 0.86$.

The maximum possible visibility with perfect mode overlap in an interferometer with unbalanced arm intensities is given by:

$$\mathrm{V_{max}} = \frac{2\sqrt{\alpha}}{1+\alpha}, \tag{5.12}$$

which due to the very similar intensities here results in $\mathrm{V_{max}} = 99.7\%$. The data here indeed has an apparent fringe visibility of $\mathrm{V_{max}}$, within error of the photodiode measurement.

Figure 5.3b displays the fast Fourier Transform (FFT) of the voltage signals in Figure 5.3a. There are three main features in the spectra: a 1/f-like behaviour both in the case of interference and where each arm is taken separately; a white noise floor reached at around 3 kHz; and finally, only in the case of interference between the arms, there is a series of broad peaks between 10 Hz and 1kHz.

True phase noise is the difference between curves in the presence or absence of interference. It can therefore be identified as the peaks in the very low audio range. There is a slow phase wander as well that is not illustrated on the FFT for convenience. The background is a combination of detector electronics noise, and light intensity noise. It has a $1/f^2$ spectrum at low frequencies, and at approximately 3 kHz it flattens to a white noise spectrum. The $1/f^2$ spectrum is intensity noise of the reference laser input to the

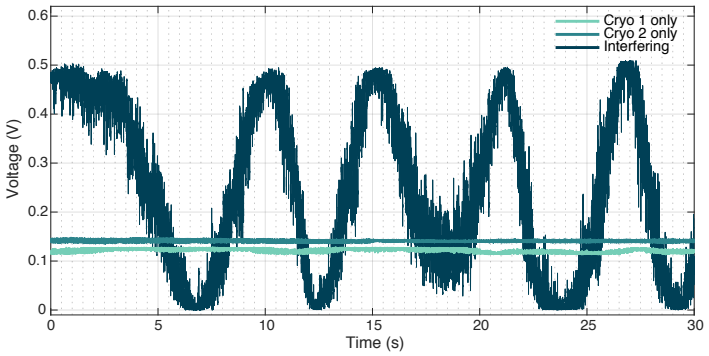

a) Interference fringes of full Mach-Zehnder interferometer in time domain, compared to the case of each arm blocked prior to the second beamsplitter.

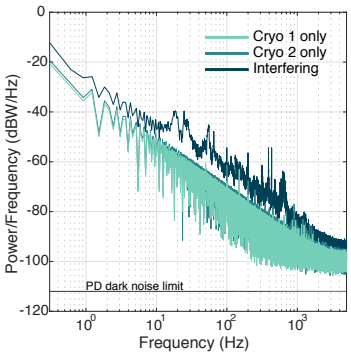

b) FFT of the photodiode detected interference fringes. The photodiode dark noise limit according to specifications is indicated as a dark line.

Figure 5.3: Two-cryostat Mach-Zehnder interference detected on a fast photodiode.

microscope.

Overall, this data suggests that any stabilization system must have a bandwidth of up to 1 kHz to effectively remove phase noise. Additionally, long-term tracking of the phase evolution indicates that the path length evolves through a maximum of $\approx$ 150 μm. Therefore, the stabilization must be able to remove audio-frequency noise while compensating slow, relatively large shifts in the path length.

5.2.2 Characterisation of phase reference detection

The resonant background is suppressed at experiment run time, reducing the phase reference laser signal below the noise level of the photodiodes. APDs (Perkin Elmer) replace PDs, and the electrical pulses (2.3 V pulse height with a width $\approx$ 16 ns) are converted to a voltage by a home-built 'pulse counter'. This pulse counter is based upon a peak detector circuit and was built by our electrical technician Stephen Topliss.

In Figure 5.4 we display the responses in time and Fourier domains of three pulse counters to an input photon rate of 2.5 MHz, where one arm of the interferometer is blocked and we detect only on one APD. It is clear that pulse counter 6 (# 6) is noisy in the time domain. Intensity fluctuations of the laser are apparent in the time domain at low frequency, and turning to the FFT all pulse counters return the same low-frequency spectrum, differing only in the low-frequency component/offset of the curve, due to different D.C. offsets as a result of slightly different gains. The high-frequency spectra display different noise floors as a consequence of the effective bandwidth of each. Regardless of the precise origin of the noise floor, Counter # 4 has the lowest noise characteristics in the frequency range of interest and so is used for the final stabilization setup. A typical figure for the white-noise floor apparent at high frequencies is -80 dBW/Hz.

The impact of common-mode intensity noise can be reduced by taking the output of

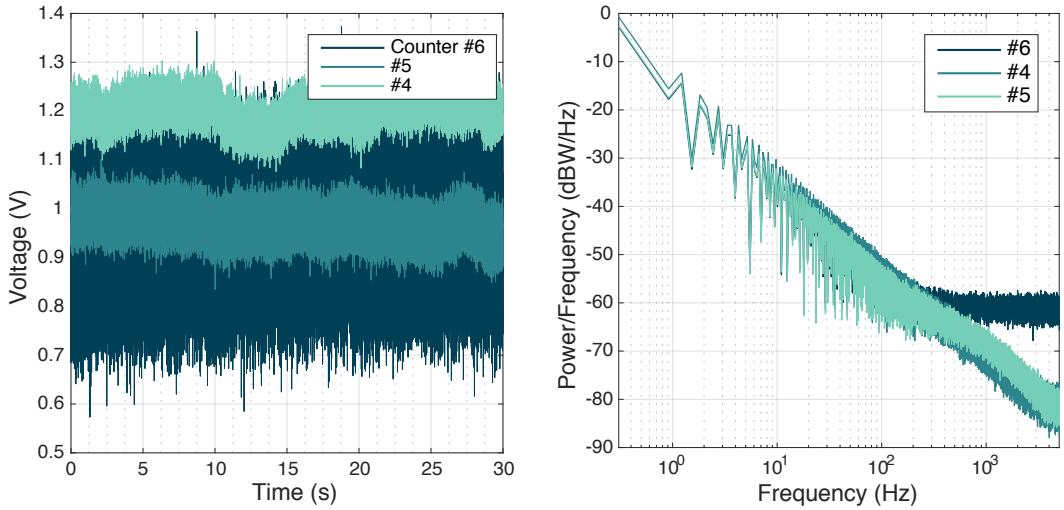

a) Output of three pulse counters in response to pulses from a Perkin-Elmer APD receiving a mean photon count rate of 2.5 MHz.

b) FFT of the signals from each of three pulse counters.

Figure 5.4: Response of pulse counters to single APD inputs. All tests were performed with an arm of the interferometer blocked and the signal from a single APD receiving 2.5 MHz mean photon rate.

one detector and subtracting the other [205]. Attempting to stabilise at a single voltage value without subtracted detection would result in a sensitivity to intensity noise in first order as the interference fringe height wanders. If one chooses to stabilise at the centre of the fringes in subtracted detection, the signal is sensitive to the wandering input intensity in the derivative of the signal only. The two outputs of the beam-splitter are converted to voltages by the pulse counter prior to subtraction. It is necessary in this scheme that the signals are balanced, which is achieved with a near-perfect 50:50 beam-splitter.

5.2.3 Phase stabilisation performance

With all the components of an error signal detection in place and well characterised we turn to the phase stabilization. Figure 5.5 illustrates the progression from a free-running interferometer to a phase-stabilised configuration in both the time and Fourier domains. The PID setpoint is 0 V with parameters chosen to narrow the distribution as much as possible.

The error signal is split and one component is fed to a low-pass filter with a bandwidth of ≈ 10 Hz. The low frequency signal is used to run a PID where actuation, or the 'slow ϕ control' of Figure 5.2, is supplied by a retroreflector on a piezo-driven stage. This enables the slow phase drift to be compensated for. The full bandwidth signal is an input to PID control of a phase-EOM (EOSpace, bandwidth 40 GHz), which enables the 'fast ϕ control'. In Figure 5.5b the phase signal as the first slow stabilization system is implemented has an average signal around zero and a reduction in the low frequency component of the

spectrum. The central point of the fringe represents the greatest sensitivity to phase noise, which results in a concurrent increase in some frequency components. However, once the second fast stabilization is brought in, the power in the total noise spectrum is reduced dramatically, by a factor of ≈ 260.

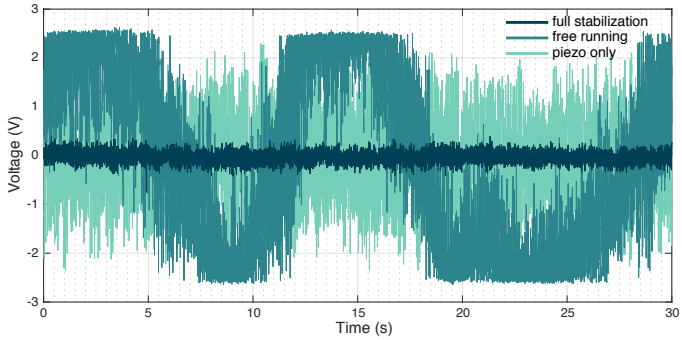

a) Time domain signal from the interferometer, prior to an entanglement measurement. A progression from free running to fully stabilized, via an intermediate step where the phase EOM component was not yet on-line, is illustrated. The fully stabilized signal is seen as a narrow distribution around 0 V.

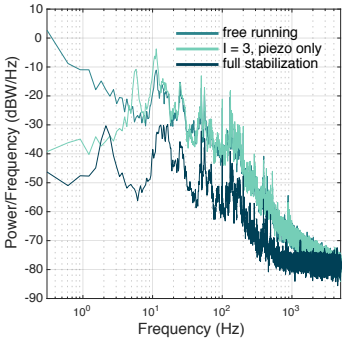

b) The noise spectra in a configuration where the interferometer is both free running and stabilized, with an intermediate step of 'slow' stabilization only. A significant reduction of audio noise power is evident.

Figure 5.5: Phase stabilization prior to an entanglement measurement.

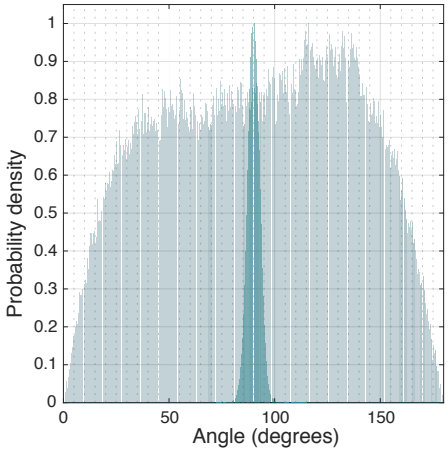

Figure 5.6: Phase stabilization of the Mach-Zehnder interferometer. A histogram of the voltage signal from the interferometer mapped to phase angle, over the 30 s measurement period. The broad peak is due to the interferometer phase evolving freely, and the FWHM of the narrow, stabilized, peak is 6.8 °.

A useful figure of merit is the relative distribution of the phase when stabilised compared to the full fringe height, which is shown in Figure 5.6. The full fringe height represents a phase change of 180°, and the full-width-half-maximum when the interferometer is stabilised is 6.8°, or $\approx \pi/25$. The phase can be maintained in this distribution over a period of hours.

5.2.3.1 Phase stabilisation at quantum dot frequencies

Figure 5.7 displays phase-stabilized unsuppressed background at the wavelength of QD elastically-scattered photons. The data demonstrates that the phase Φ_I can be freely chosen. In the figure, four different phase-stabilisation points are displayed, at each of which both outputs of BS2 are given. In Figure 5.7b, the distribution in phase of the two extreme points is analysed; the apparent phase distribution during stabilization has a full-width-half-maximum of 8 degrees, or better than $\pi/20$. This data was taken with an integration time of 1ms.

Practically, jumping to an alternative set-point Φ_I is achieved by applying a step change to a D.C. offset on the piezo stage. The PID system returns to a stable position but several fringes of the phase reference have been skipped in the process, due to the dephasing between the quantum dot frequencies and the far blue-detuned phase reference. In order to produce a full 2π phase shift between the reference and quantum dots, we need to generate a jump of ≈ 87 μm, or 91 reference wavelengths. In practice, we wish to tune by a maximum π shift, or just 44 μm, far below the restrictions on interferometer asymmetry and zero total delay.

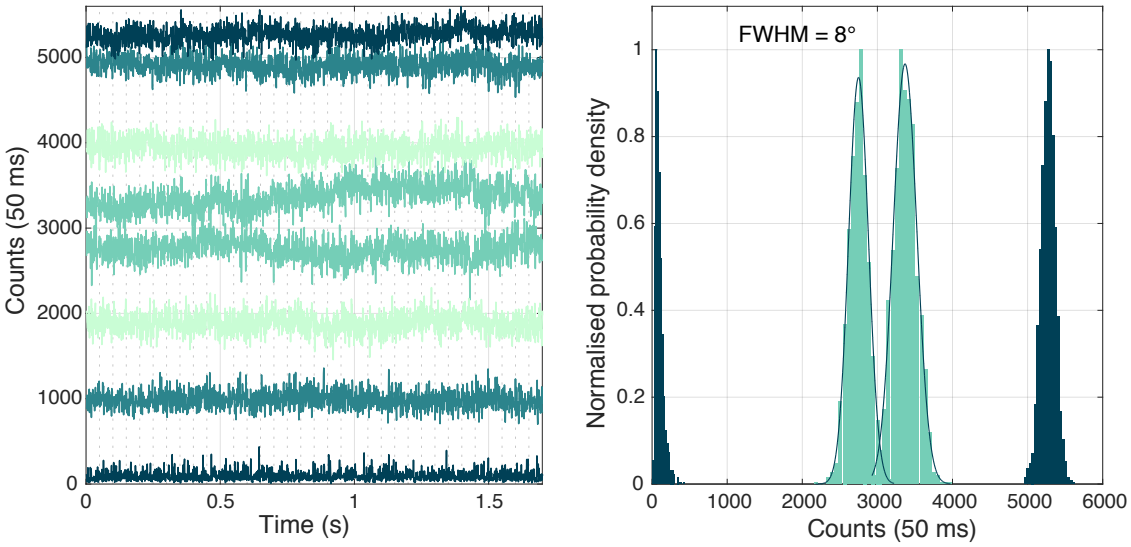

a) The unsuppressed background as measured on detectors R1 and R2 whilst the phase stabilization is in operation. Several set points are possible by applying a step voltage offset to the piezo causing it to 'jump' fringes of the quantum dot frequency.

b) Histograms of the two extreme set points from (a). Using the outermost points to calibrate, the inner point is stabilised with a FWHM of 8°.

Figure 5.7: Phase stabilization at quantum dot frequencies.

5.2.3.2 Setting the zero-delay point of the interferometer

As discussed in Section 5.1, the phase of the entangled state is not directly that of the interferometer at the lower energy quantum dot frequency. To compensate and effectively

'unwind' this additional phase, the $\pi/2$-rotation pulses must arrive at the QDs with the same time delay that the entanglement pulses have. By setting the interferometer delay to zero, a reference point for the rotation pulses is established, and a zero delay in arrival time of the rotation pulses at BS2 corresponds to correct pulse timing.

The short resonant pulse used to generate entanglement (160 ps) passes through the entire interferometer and allows the delay to be coarsely adjusted to zero. However, the timing jitter of $\approx$ 160 ps in detection prevents the delay being set to zero with sufficient accuracy of $\sim$ 1 ps.

We use a method similar to the technique of white light interferometry [206]: by finding the point at which the interference fringes for all frequencies overlap, the position of zero delay is found. Using the frequency resolution of the optical set-up we monitor the interference of two different lasers passing through the interferometer (one at $\nu = 309728$ GHz, transmitted by the Fabry-Pérot etalons, and one at $\nu + \Delta\nu$ with $\Delta\nu \in [15, 25$ GHz], reflected by the etalons). We use a slow piezo modulation (5 μm, 0.1 Hz) to generate fringes. The normalised difference of the fringe magnitudes for two frequencies is expected to follow the total delay as:

$$4\left|\mathrm{Sin}\left(\frac{\pi(d-d_0)\Delta\nu}{c}\right)\right|. \tag{5.13}$$

Here (d-d_0) is the delay, d_0 is the current position. The delay (d-d_o) is set manually using the micrometer screw on a delay stage.

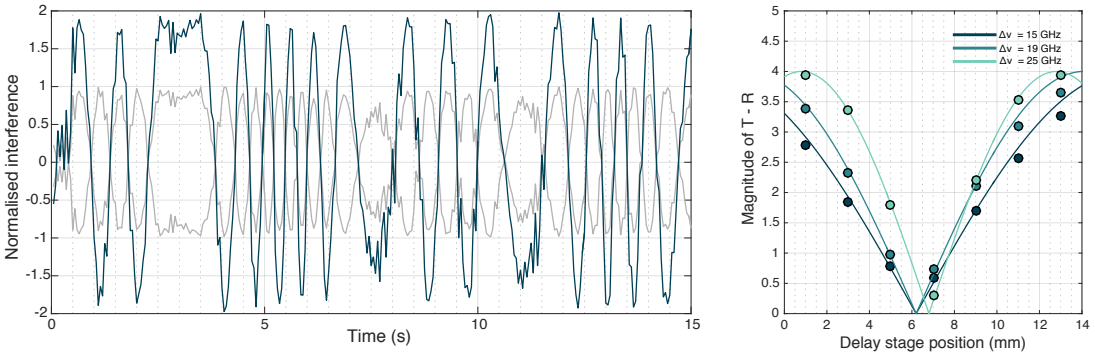

a) Example of the normalised fringes, T_1 - T_2 and R_1 - R_2 in grey, with the difference in blue. The two frequencies are on different inputs of BS1 so the out of phase fringes here indicate the delay is not zero (it would be if T_2 - T_1 fringes were used instead, for example).

b) The magnitude of the fringe difference for different frequency separations $\Delta\nu$. All three curves coincide between 6 and 7 mm, indicating this is the zero.

Figure 5.8: Setting the zero delay path of the interferometer.

In Figure 5.8 the magnitude of fringe differences and the model are displayed. The point where all frequency differences coincide (and the curve reaches zero) is the zero delay. In this particular case the position of zero delay was at 6.2 mm for two frequency differences but 6.8 mm for another, where a shift occurred due to backlash of the stage

in this example, and care is taken to avoid this by checking that the interference fringes overlap upon returning to the apparent zero. The maximum uncertainty in the zero delay of 0.6 mm (2 ps) corresponds to 5 % of the distance over which Raman and elastically scattered photons with $\Delta\nu = 25$ GHz dephase, suggesting that the largest possible shift between measured phase and real entangled-state phase is 18°, but in true operation it is likely to be much smaller. Thus we identify the phase of interferometer, as evidenced in the interference of elastically scattered photons, with the phase of the entangled state.

5.3 Phase-controlled interference of elastically scattered photons

The effect of the phase stabilization can be seen upon the elastically-scattered photons from the quantum dots. Measuring the interference of unsuppressed laser background indicated that the mode overlap can be made near perfect for the quantum dot frequencies (Figure 5.7), but the best test of phase stabilization is the realistic case where the background is fully suppressed. In this case we detect at least 1 MHz on each of the phase reference detectors from each cryostat, where typical operating fringes peak at 3-5 MHz.

The interference of QD photons is shown in Figure 5.9. This figure shows the counts on all detectors from an excitation pulse resonant with the low energy transition of the selected Λ-scheme. The counts are from an $\approx$ 1ns bin starting with the pulse, integrated during 0.5 s. Interference is seen only for the elastically-scattered photons (detected on R1 and R2) because the Raman-scattered photons (detected on T1 and T2) follow the mutual ground state spin coherence between the two quantum dots, which is not generated in this experiment (as discussed in Section 5.1.1). Over the first 10 s there is some 'wandering' in the detuning of one of the dots, indicated by the reduction in counts on detectors T1 and T2. Thereafter, the fringes of a freely evolving interferometer are imprinted in the quantum dot fluorescence.

In Table 5.1 we record the counts on all detectors for each QD and the background from each arm of the interferometer. We estimate the average background contribution to our state-projecting photons detected on T1 and T2 at 0.77 %. The difference in the number of counts on each detector (from a single QD) is due to variations in coupling to the fibre directly prior to each detector, a wavelength-dependent ratio of the beam-splitter at which QD fluorescence is combined, and the efficiency of each detector. There is also a mismatch in the rates detected at each frequency. This is largely due to the polarization of detection in the microscope which in this case happens to be biased towards detecting the higher energy transition here for both QDs. Here, the overall state-projecting Raman count rates from each quantum dot are not being matched, but they must be in entanglement generation to ensure which-path information is destroyed.

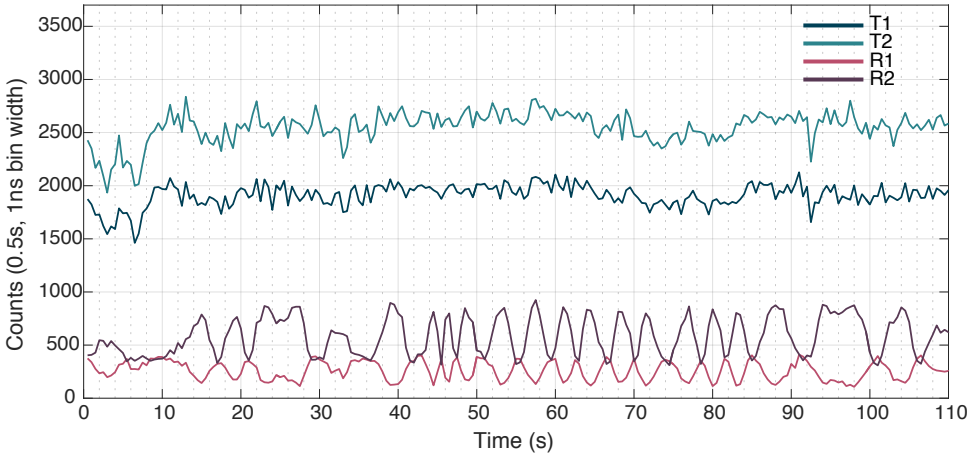

Figure 5.9: Two QD elastically-scattered photon interference in the unstabilized interferometer. Photons are detected during the 1 ns bin starting with the entanglement pulse, integrating for 0.5 s. The detectors 'T' pick up the inelastically-scattered, incoherent photons and therefore no interference is seen. The 'R' detectors are exposed to the elastically-scattered coherent photons, thus interference fringes for two light scattered from two quantum dots is seen.

	Detector			
	T1	T2	R1	R2
cryostat A arm only	2564	3338	164	300
cryostat A background	6	20	6	10
cryostat B arm only	1840	2672	370	986
cryostat B background	16	34	96	242
Visibility of interference			0.59	0.50

Table 5.1 – The average counts on each of the four detectors, for 1 ns of the entanglement pulse, in Hz. The arms of the interferometer from each of the cryostats, A and B, containing the QDs, are treated independently. The apparent visibility of the interference between the two QD photon streams is also indicated.

It is notable that the elastically-scattered photon fringes do not appear to have a high visibility even though the interferometer is aligned with near-perfect (> 98 %) mode overlap at all frequencies; the apparent visibilities during time periods in which the quantum dots are resonant with the laser are also indicated in table 5.1. Using the detected count rates from the independent interferometer arms, in the case of the near-perfect interferometer we expect a visibility of $V_{R1} = 0.92$ and $V_{R2} = 0.85$, using equation 5.12.

The elastically-scattered photons from each of the QDs are expected to interfere with the laser background [119]; this interference is used in differential reflectivity and transmission measurements [207], for example. The relative phase of the background depends sensitively upon the detuning of the QD with respect to the laser and may have changed

between the blocked-arm tests recorded in the table and the measurement of the interference in Figure 5.9, but accounting for this only produces $V_{R1} \approx 88$ % in the 'worst-case' scenario of the relative phase shifting by π between measurements.

It is clear that V_{R1} is much higher than the experimentally observed visibility $V_{R1} = 0.59$. A first loss of visibility is due to the fraction of the scattered photons that can be considered incoherent in contrast to an ideal two-level system. Even for weak driving of the transition, scattering is not 100 % coherent as there is a second decay channel available to decohere the excited state. Applying a 160 ps pulse to the red transition of the Λ-scheme, where the average probability of causing a Raman photon emission with concurrent spin-flip is $p = 0.07$, results in 87 % of the emission being coherent on average (following a full density matrix calculation that we do not reproduce here). Accounting for incoherent emission reduces the expected visibility V_{R1} to 0.8. A negligible reduction is present due to remaining uncompensated mechanical noise. We note that the excitation pulse itself is also spectrally broad. However, the coherence between the excitation at the two quantum dots is maintained and this should not reduce the visibility of the elastically-scattered photons.

For the remaining visibility loss, the fringes are being washed out by QD optical transition noise faster than the 0.5 s integration time. In Chapter 2 we explored the relative timescales of environmental noise sources, and both electric and nuclear Overhauser field are faster than 2 Hz. In Section 5.1.1 we discussed the implication of this environmental noise for the interferometer phase Φ_I, and the random phase $\Delta\phi_{random}(t)$ given to the elastically scattered fluorescence is likely to cause the reduction of fringe visibility here.

One might ask how much spectral diffusion is required to produce a reduction in fringe visibility from $\sim$ 80 % to only 59 %. The phase of the scattered light is modelled as that of a simple harmonic oscillator with respect to detuning, creating a $\pi/2$ phase shift between excitation and scattered light on resonance, and a π phase shift movng across the resonance. We make the assumption that the Overhauser field distribution at this magnetic field results in a $\sim$ 50 MHz broadening of the spin ground state of each QD independently (corresponding to a $T_2^* = 2$ ns). As a result, to reach the reduction in fringe visibility seen would require the addition of a further $\approx$ 300 MHz spectral diffusion acting upon each quantum dot. However, this neglects the destruction of fringe visibility due to amplitude noise from the same sources, and including this in the simple model of a 206 MHz radiative linewidth transition yields an estimate of 230 MHz average spectral diffusion. This is physically reasonable in comparison to the values found for the same sample in Chapter 2.

Figure 5.10a displays the counts on all detectors, where at 85 s the phase stabilization is applied. The elastically-scattered counts (R1 and R2) appear reasonably constant, but the phase of the fluorescence is highly sensitive to relative detuning of the QD and the laser, resulting in phase noise. To illustrate this further, in figure 5.10c the interferometer is phase stabilized and QD B is held at a constant gate voltage. A gate voltage sweep of 11

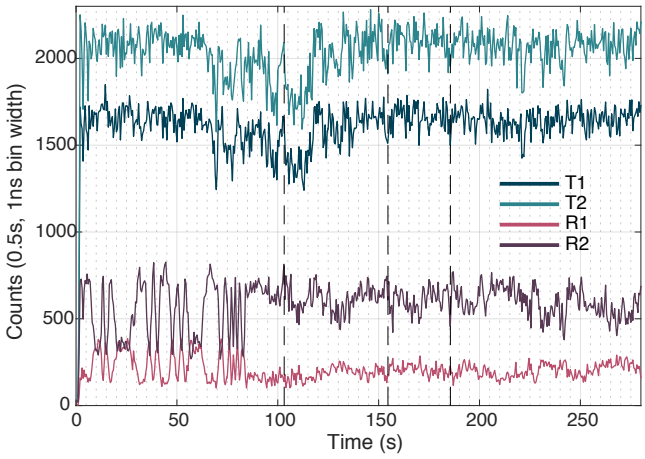

a) Photons detected during the entanglement pulse, integrated for 0.5s, where stabilization is applied at $\approx$ 85 s.

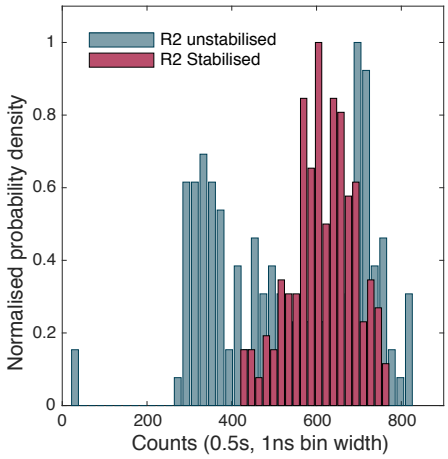

b) Histogram of elastically-scattered photon counts detected during the entanglement pulse. Application of phase stabilization creates a peak of counts in contrast to the spread seen in free-running conditions. A distribution with a FWHM of nearly $\pi/3$ is measured.

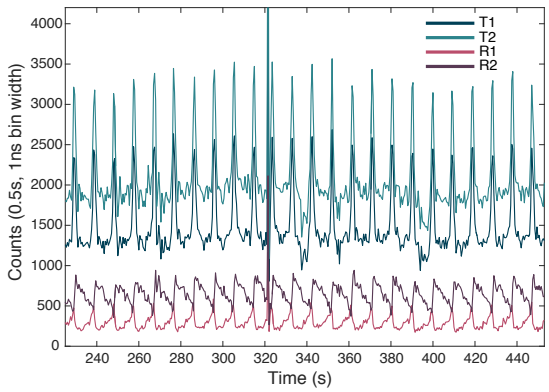

c) Interference of two QD fluorescence as the resonance of one QD is tuned across the other by a periodic gate voltage sweep.

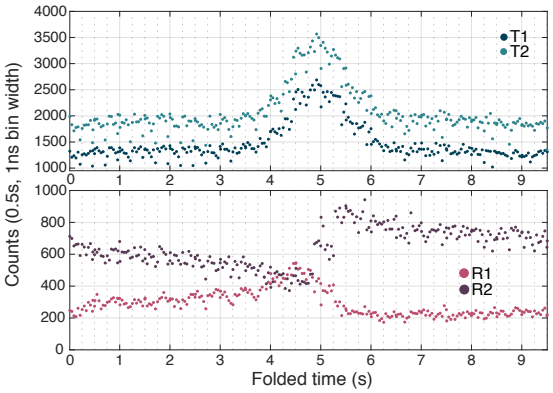

d) Folding of data presented in Figure 5.10c. The sharp relative phase change in elastically scattered light is seen on resonance.

Figure 5.10: The phase of quantum dot resonance fluorescence in a stabilized interferometer.

mV triangular wave at 105 mHz is applied to QD A, causing the lower energy resonance to be swept across the entanglement laser frequency. As a result, the Raman-scattered photons (T1 and T2) map the Lorentzian line shape of the resonance whilst R1 and R2 indicate that the relative phase of the light from the two quantum dots sweeps through π. Figure 5.10d folds this data to illuminate the time coincidence between the resonance and a sharp relative phase change of QD fluorescence. In particular, the sensitivity to very small detuning jitter poses a significant challenge to analysis of the three-photon events, and indeed to the creation of a stable entangled state.

In Figure 5.10b the photon counts on R2 for the freely evolving and stabilized periods in Figure 5.10a are presented in a histogram. The freely evolving fringes are approximately 330-700 in height, with the peak of the stabilized distribution centred around 620, or approximately $\pi/3$ radians. However, it is clear from the FWHM of nearly $\pi/3$ that despite active phase stabilization there is an unstable relative phase of light elastically-scattered by the two QDs and this exceeds what should be seen from shot noise alone, and the underlying mechanical stability of the interferometer. We shall be required to filter our three-photon detection events based upon apparent phase as we do not actively stabilize the quantum dot transitions here [117].

In summary, we are able to stabilize the interferometer to better than $\pi/20$ at the frequencies of interest, but the relative phase between the photons scattered from two QDs drifts in reality. This is a very sensitive probe of the inherently noisy environment of a quantum dot through its action on a single quantum dot transition.

5.4 Larmor frequency variation

We rely upon well-matched Λ-schemes to ensure a high fidelity of our entangled state as it influences the indistinguishability of the state-projection photonic modes, the entangled state phase, and any precession of the entangled state after a projection event. Frequent checking of ω_L for both QDs is a necessity, and we do so by performing Ramsey interferometry within the entanglement pulse sequence, where we utilise the components of the compound pulses as the necessary $\pi/2$ rotations. We ensure that a QD is resonant prior to the measurement by maximising the Raman-scattered photons. The gate voltage required varies due to very slow electric field noise processes in each QD. In QD A, the timescale of such processes is many hours, whilst in QD B this change can occur after $\sim$ 20 minutes.

Figure 5.11 illustrates the Ramsey interferometry signal for another QD on which we explore the Larmor frequency behaviour further, QD C. The data is taken on two consecutive days. There is an apparent shift of $\approx 400 \times 2\pi$ MHz, equivalent to an external magnetic field shift of $\Delta B_{ext} = 7.6$ mT. However, the external magnetic field has a high stability and we thus seek an alternative explanation.

In Figure 5.12 the measured Larmor frequencies on Day 1 are summarised as a function of applied gate voltage. In this case $\omega_l = 309702.75 \times 2\pi$ GHz, and $\Delta = \omega_R$ - ω_l is 25

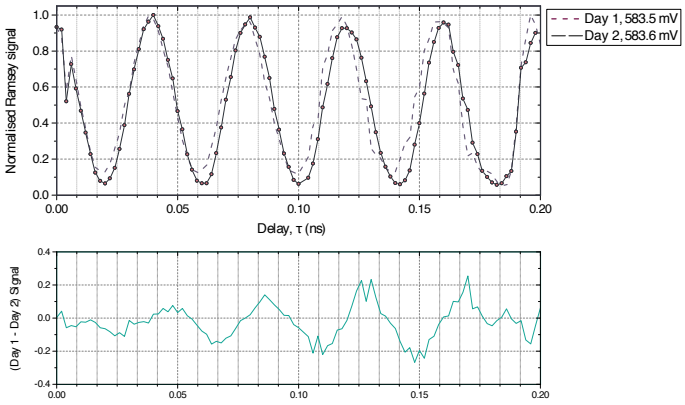

Figure 5.11: Variation of Larmor frequencies: QD C Ramsey interferometry. (upper) Repeats of Ramsey interferometry performed on QD C, on two consecutive days. (lower) The residuals of the sinusoidal fits, illustrating a dephasing due to a shift in apparent Larmor frequency by 400 $\times$ 2π MHz.

$\times$ 2π GHz. The Larmor frequency is a smooth function of gate voltage, implying that there is detuning dependent polarization of the nuclear spins, which results in a shift of the apparent Larmor frequency around that set by the external magnetic field.

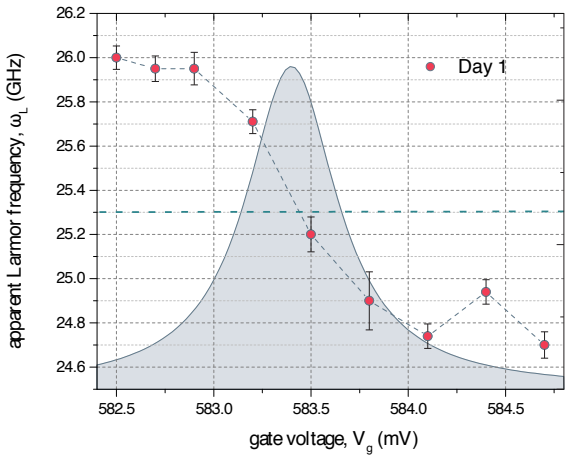

Figure 5.12: QD C Larmor frequency variation with gate voltage. An ideal absorption lineshape is included in the background for reference.

A tentative explanation is provided by considering the phenomenon of 'dragging' [208], whereby a QD resonance is locked to the excitation laser due to favourable polarization of the nuclear spin bath that compensates for positive and negative detuning. In our protocol, the driving power of the spin read-out laser at ω_R is a factor of ~ 10 above that of the ω_l laser. It is therefore likely to dominate any nuclear spin polarization processes, and if an initial detuning between ω_R and the addressed transition exists, the nuclear spins polarize in order to compensate. Therefore the Larmor frequency is reduced as the transition is pulled into resonance with an initially blue detuned laser. The change in ω_L is reduced at large detunings, where the nuclear spin polarization rate is suppressed.

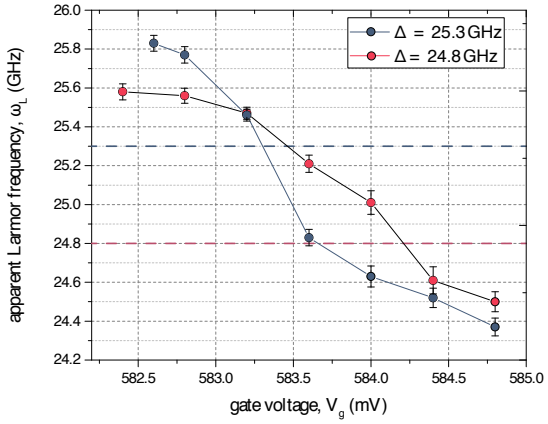

a) A scan of Larmor frequency as a function of gate voltage for QD C, where the wavelength of the red laser is shifted, blue laser wavelength maintained. Two relative laser detunings of 25.3 GHz and 24.8 GHz are shown.

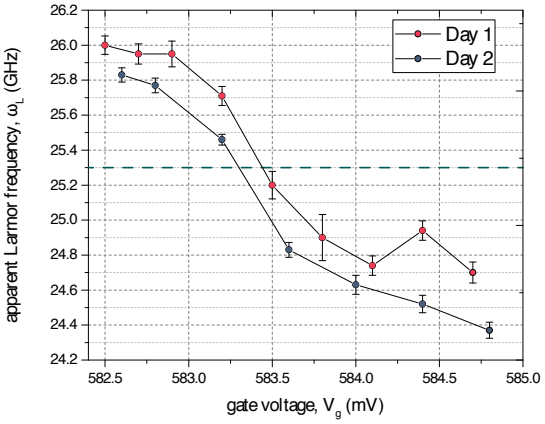

b) Gate-voltage sweeps of the Larmor frequency on two days, where a shift of the resonant gate voltage takes place between the two due to slow charging events.

Figure 5.13: Investigation of Larmor frequency variation.

To further explore this phenomenon, Figure 5.13a presents data where the relative laser detuning, Δ, is varied, but the frequency of the blue laser ω_R is maintained. As Δ is decreased the curve appears to shift and centre around a reduced Larmor frequency, despite the constant blue wavelength. This indicates that the weaker red excitation may also play a role in nuclear spin behaviour during the time for which the red transition is driven by the 'entanglement pulse'. Finally, figure 5.13b presents data from Day 1 and Day 2 for QD C under the same Δ conditions, where now we note that the curve shifts along the gate voltage axis as the resonant frequency of the QD transitions varies under slow electric field noise. However, the origin of the slight downwards shift despite identical laser frequencies is unclear.

Practically, it is the slow variation in resonant frequency due to electric field noise that results in a shifting Larmor frequency for both quantum dots. Fine adjustment of the gate voltage applied to a sample must be made beyond simply maximising photon scattering from the red transition; figure 5.12 also includes the absorption spectrum expected for this QD with power broadening as expected for s = 0.2, which illustrates a shift of ω_L by up to 800 MHz across the linewidth of transition. The measured Larmor frequency is highly sensitive to the detuning of a Λ-scheme from two driving laser frequencies, and as such it is necessary to make repeated checks and adjustments of gate voltage to match the two quantum dots during our measurement. The origin of this behaviour is thought to be the 'locking' of the blue and red optical transitions to the driving laser due to underlying polarization of the nuclear spin bath.

5.5 Phase-controlled measurements: a tunable two-electron spin-entangled state

Having explored how the phase of an entangled two-electron spin state is to be created and maintained, we now turn to the three photon correlations under phase tuning. In the previous chapter, we presented only the results where the phase was set to 0 or π. The phase of the state is found by examining the interference of the elastically-scattered photons detected on R1 and R2, and indeed this allows us to 'dial up' the state we create using the technique outlined in Section 5.2.3.1.

In Figure 5.14 we present the results of a two-spin measurement in the rotated basis conditioned upon detection of a single state-projecting photon, where results are now partitioned by which detector (D1 or D2) registered the photon during the entanglement pulse, and are arranged according to the set phase of the interferometer. It is notable that, for a single-phase set-point, the correlations display opposite behaviour to those where the entanglement event was registered on the other detector. This is entirely a by-product of the phase introduced to the photonic modes by the beam-splitters, and yet appears in the state of two electron spins. In general, the trend in these results would be expected as an outcome of this entanglement scheme; at $\pi/2$ set point, for example, the visibilities vanish as there is a term proportional to $\cos(\phi)$ in the expression for the visibility.

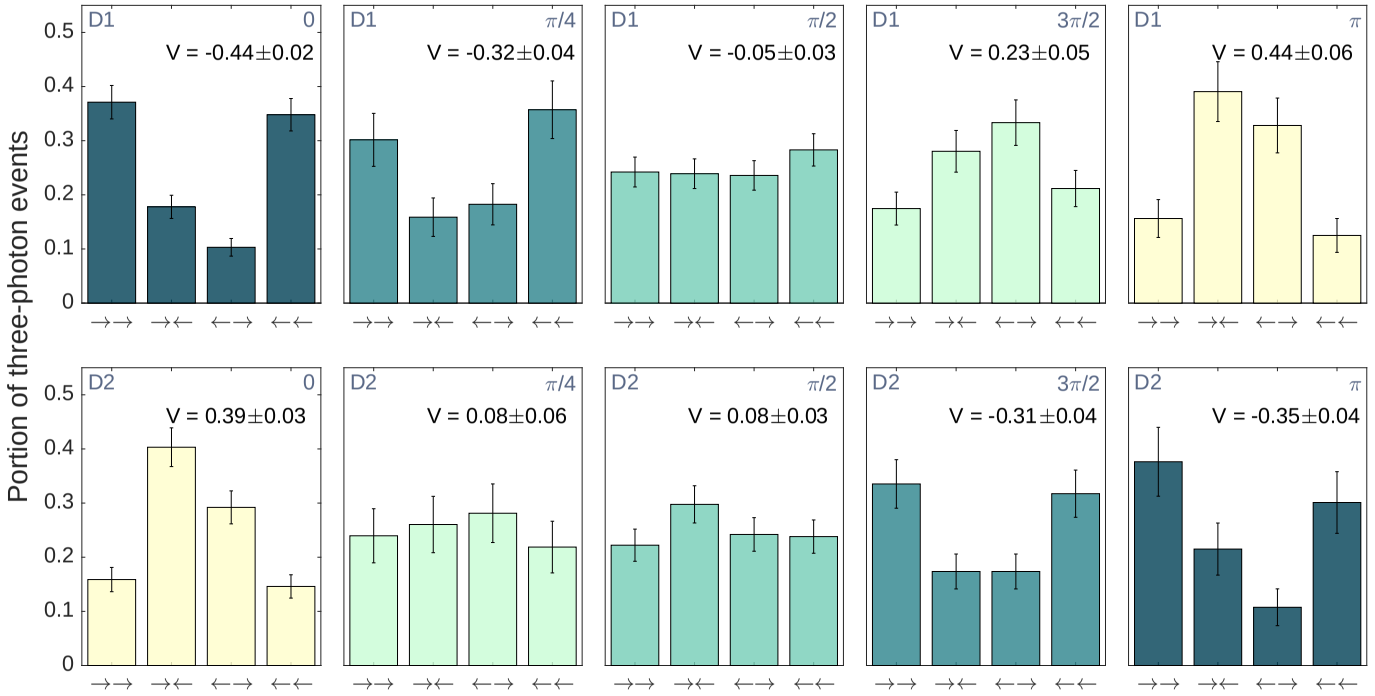

Figure 5.14: Two electron spin measurements in the rotated basis; full phase tuning. Results are presented for five set points of the interferometer, where the results are partitioned according to the detector that registered the state-projection photon. The four extreme points contributed to the calculated fidelities of Ψ_+ and Ψ_- in the previous chapter.

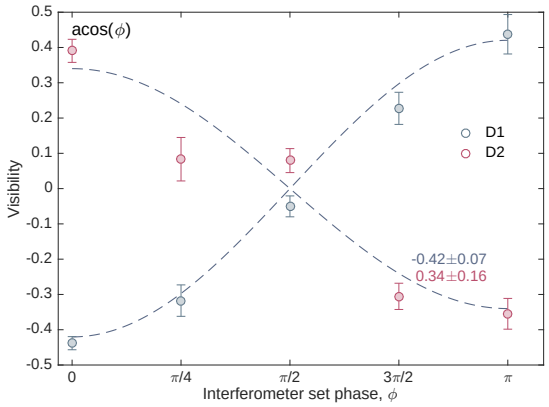

a) Visibility as a function of interferometer set phase, ϕ, where the post-selection window of QD fluorescence phase is set to $\pm$ 10 degrees.

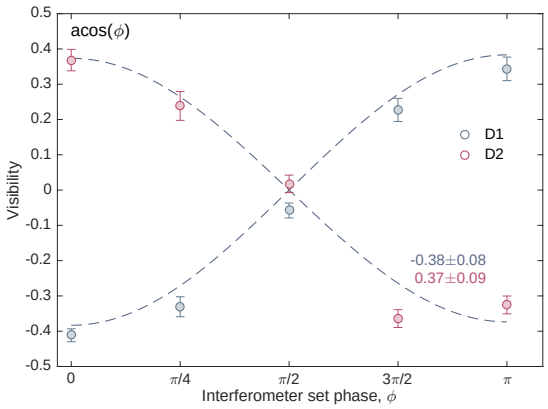

b) Visibility as a function of interferometer set phase, ϕ, where the post-selection window of QD fluorescence phase is set to $\pm$ 20 degrees.

Figure 5.15: Summary of the phase-tunable entangled states. The visibility of the correlations as a function of interferometer set phase, with a $\cos(\phi)$ fit constrained to $V(\phi{=}\pi/2) = 0$.

The results are summarized in Figure 5.15a, where the visibility of correlations, V, is presented as a function of interferometer set phase. The dashed lines represent sinusoidal fits under the constraint of passing through zero at $\pi/2$, and the data roughly agrees with the expected $\cos(\phi)$ dependence. Taking the amplitudes of these fits to represent a 'global' visibility of the experiment, the resulting fidelity with respect to the full range of states $\frac{1}{\sqrt{2}}\left(|\uparrow\downarrow\rangle + e^{i\phi}|\downarrow\uparrow\rangle\right)$ is ≈ 62 % although we note that the fits are not within the error bars of the individual points.

A reason for this is the phase noise introduced to the entangled state by both electric field and nuclear Overhauser field acting upon the lower energy transition of the Λ scheme. Evidence of this was found in the interference of the elastically scattered photons, see for example Figure 5.10. In order to gain sufficient statistics, it became necessary to allow a wide range of apparent phases to contribute to final results. Data was selected by

examining the elastically-scattered RF interference and permitting events within apparent phase ranges of different widths, where detailed data analysis is the work of my colleague Lukas Huthmacher. The data presented here, and prior to this point, permitted a ± 10° phase range.

Figure 5.15b presents the results where now the selection window is ± 20 degrees in phase. As a result, the statistics are improved as there are simply more events that may be included into each measurement run. Therefore, the results more closely follow the expected Cosine curve of visibilities. Averaging over the local range of phase results in a reduction in the overall amplitude of the curve. It is for this reason that the smaller selection window of 10 degrees results in the highest measured fidelities at the extreme points of 0 and π phase.

5.6 Conclusions: phase tunable entanglement generation.

In this chapter we have demonstrated a method for control and tuning of the state generated by a single-photon detection technique. It has been possible not only to generate entangled states of electron spins, but also to choose *which* state we create from the full range of the general form $\frac{1}{\sqrt{2}}\left(|\uparrow\downarrow\rangle + e^{i\phi}|\downarrow\uparrow\rangle\right)$. While this does not provide access to all of the maximally entangled states, the remaining are available through simple local operations, such as a π-rotation pulse on the electron spin at QD A, which would take Ψ_+ and create Φ_+, for example.

Such phase-tunable entangled states have previously been created [186], but this has not been the case in self-assembled quantum dots [83], so a phase-stabilized fibre-based interferometer represents a modest but useful addition to this body of work. This is also the first demonstration where an optical interferometer has been used over macroscopic distances; the prior demonstration utilised a single ion trap. Practically however, we can study this technique in light of technologies where the quantum dots are unlikely to be separated by several metres interconnected by optical fibres. We might envisage a collection of 'on-chip' interferometers, for example, as our quantum network. Initial work towards wave-guide-based interconnects in GaAs is in progress [209–211]. There the phase shifts due to path length are likely to be small and easier to control.

It was also found in the course of this work that we clearly see a detuning-dependent Larmor frequency. The precise explanation is not clear, however it appears that dynamic nuclear spin polarization by the read-out laser on the blue transition of the Λ-scheme makes a dominant contribution, with a secondary effect due to the weaker 'entanglement' laser driving the red transition also taking place. The polarization occurs due to a detuning that develops due to a change in the local electric field environment, where in particular slow noise processes allow the nuclear spins to track the transition and keep it resonant with the excitation.

Future work aims to improve the fidelity of the state we create. As discussed in the

previous chapter and in the conclusion to this dissertation, a key reduction in fidelity is due to the inhomogeneous spin dephasing, which could be improved by finding methods to polarize the nuclear spin bath, or alternatively by turning to hole spins in samples with a low contribution from electric field noise [169].

However, due to the marked sensitivity of fluorescence phase to small detunings, it appears that electric field noise becomes a larger problem when the phase of the scattered light is key to the protocol. We discussed the origin of the term in the entangled state phase that represents random phase shifts of the scattered light, Equation 5.10, and found evidence of this noise taking effect in Section 5.3. The interference visibility of the elastically scattered photons would be reduced by 0.8 due to the presence of incoherent emission, but the additional factor of ≈ 0.75 represents the total effect of all random phases $\Delta\phi_{random}(t)$ introduced in equation 5.9, regardless of source. This is the same phase noise term that acts in the entangled state phase and therefore the reduction in visibility of the entangled state would be expected to be the same. Referring to the analysis of limitations to state fidelity from the previous chapter, our final estimation of the entangled state fidelity based upon known reductions was 0.76. If the factor of 0.75 attributable to electric and Overhauser noise on the red transition is taken into account we reach a final fidelity of 0.67, which approaches our measured value. While this is a simple estimate of the origin of reductions to the fidelity, it suggests that a scheme insensitive to phase noise could raise the fidelity above 75 %.

With this in mind, improvement of the phase stability in this scheme requires more stable quantum dot resonances, or careful choice of only the very best examples. An alternative is to use a two-photon detection scheme where optical phase does not impact upon the state; it may be possible to improve photon collection efficiency through careful structural modification of the GaAs surrounding a quantum dot, where recent approaches include both microcavities and photonic trumpets [212]. In the previous chapter, we noted the trade-off made in Type I and Type II detection schemes, where the gain in fidelity made in a Type II scheme comes at a cost of slow entanglement generation. If limitations to the rate of entanglement generation are overcome, however, the issue of phase stability is side-stepped altogether.

Chapter 6

Conclusion

In the introduction to this work, we posed the question of what is the impact of the inherent semiconductor environment on a single trapped electron and associated optical transitions in a self-assembled quantum dot, and given these known limitations, can such systems form the basic building blocks of a quantum computational technology?

It is possible to investigate the effect of the solid state environment in resonance fluorescence via the spectral fluctuations that result in intensity noise of resonance fluorescence. Fluctuations were measured with timescales down to 1 μs. We were able to distinguish electric and magnetic field contributions through the detuning dependence of the noise amplitudes for the case of optical transitions of the X^{1-} species. In particular we measured slowing dynamics of the Overhauser field with increased optical driving power. As this system consists of a single electron interacting with a nuclear spin bath, we ascribe a portion of this behaviour to the Knight field of the resident electron acting upon the nuclear spins.

These measurements took place at zero applied magnetic field and focused on the spectral signatures of the nuclear spin bath, and as such are different to direct measurements of the spin coherence and dephasing [16, 17, 24]. However, they highlight the importance of an electron-spin dependent process on the Overhauser field dynamics in the absence of magnetic field. Beyond the quantization provided by an external magnetic field, there is a hierarchy of contributions to the Hamiltonian describing each nuclear spin, of which the quadrupolar coupling to electric field gradients is known to be dominant [17, 145]. Therefore, we suggest that the Knight field acts as an additional smaller perturbation to the nuclear spin dynamics, becoming relevant when the external field does not provide the dominant term.

A model of the fluctuation amplitudes provides good agreement with the data. The model takes a four-level system representation of the X^{1-} and allows electric field fluctuations. As a result we may extract the underlying standard deviation of the Overhauser field where we find values of 22-25 mT for the chosen QDs at zero applied magnetic field, in

accord with the literature. The spectral broadening due to local electric field fluctuations was typically 150-200 MHz for these QDs, and it is important to note that even on the same sample there is some variation in electric field noise as it is due to factors outside of the quantum dots themselves. For the latter half of this work we have chosen the sample with the smallest spectral diffusion available, although noise amplitudes differ slight between QDs. This is indicative of a common source, perhaps a layer of defects above each dot due to the strain it creates propagating to the GaAs-blocking barrier interface [25]. However, there were more marked differences when compared to other samples such as those with exposed surfaces close to the QD layer, which demonstrates this technique's utility in sample comparison.

Further exploration of spectral diffusion was enabled by a simple model of photon counting statistics. A systematic offset from the results obtained by the full noise spectroscopy model does exist but is a well understood consequence of the simplicity of the model. The simplicity of the model, and the fact that the Overhauser field is consistent between quantum dots, means that this technique has a place in the rapid characterization of samples where the spectral wandering due to electric field noise is the critical parameter of interest. It also permits us to compare quantum dots that may be in future used to generate entanglement, where reduction of the spectral diffusion below that seen in the sample here should result in an increase in entangled state fidelity.

Having identified a sample with spectral diffusion less than or comparable to the radiative linewidth, we aimed to demonstrate the most basic step in building a quantum network. Using the scheme described by Cabrillo et al. [185], two electron spins are entangled by detection of a single photon, where the fidelity of both the Ψ_+ and Ψ_- states violated the classical limit by over four standard deviations of the mean. The fidelity of the entangled state is eroded by distinguishability of the photons, however we find that the 'best' samples we identified produced clean enough photons (with two-QD Hong-Ou-Mandel visibility of 93.3 %) that an entangled state could be generated. In addition, the necessary optical phase control required by single photon detection schemes was achieved, and as such we generated a full range of linear combinations of Ψ_+ and Ψ_-, where we note that simple local operations on the single electron spins would produce the remaining Bell states.

In order to demonstrate an entangled state it was necessary to perform a spin rotation within 1.2 ns of the beginning of the 'entanglement pulse' from which the state-projecting photons were selected. This is due to the inhomogeneous dephasing of the electron spins, or the joint T_2^*. If the rotation of the spin coherence terms in the density matrix were performed later, we would expect the fidelity of the measured state compared to the desired Bell state to have deteriorated further. A relatively simple extension (so far limited by hardware) to this work is the implementation of a spin-echo sequence [16] within the entanglement protocol in order that we can measure the state after the state-projecting photon has been detected. However, this presents an additional complication to any architecture

if the overall coherence of a system must be artifically maintained, and it would perhaps be more useful in the long term to find methods of extending the T_2^* of our electron spins beyond $\approx$ 2 ns. Current work is focusing upon manipulating the nuclear spins, creating a more stable polarization using coherent population trapping methods [204]. This would present a major step towards improving the fidelity of the Bell states.

It is possible that the use of hole spins presents a solution to problem presented by inhomogeneous dephasing, and indeed entangled states of hole spins have been generated [83], where the single quantum dot hole T_2^* exceeded 22 ns. In high quality samples the T_2^* has exceeded 460 ns [169], and as such one would not need to select such a small portion of the emitted state-projecting photons, as T_2^* far exceeds the radiative lifetime. However, whether the hole spin coherence time T_2 may be extended beyond the microsecond regime remains to be seen [171]. It is clear for both electron and hole spins the challenges in increasing fidelity and coherence time of entangled states lies in engineering the environment, whether through charge noise reduction, or careful modification of quantum dot geometry to reduce the impact of strain which currently presents the hard limit to electron spin coherence [17].

In this work we did not address Bell tests by making measurements of more than one observable perpendicular to the population basis. As there is only one axis of rotation available with this optical spin rotation technique, we would need to allow Larmor precession by an extra quarter of a period (10 ps) before performing the rotation. However, a loophole-free Bell test requires space-like separation of the two qubit measurement events, where microseconds of coherence provided by the addition of spin-echo sequences give $\approx$ 600 m maximum inter-qubit distance if creation of the state is to be possible (in the best-case scenario of assuming that detection takes zero time). This presents the challenge of being able to randomly choose the measurement basis in a sufficiently short time that it cannot have influenced the entangled state created, in order that the state can be measured before it decoheres. It is not yet clear whether this is technically possible.

Here, the entanglement protocol chosen in fact calls not only for indistinguishable photons, but also requires that these photons are phase stable. Phase variation is largest on resonance. As such, the phase of the created state is highly susceptible the noisy solid state environment of a quantum dot, and it is possible the impact of $\approx$ 230 MHz spectral broadening reduced our state fidelity by at least 7 %. There are a number of potential solutions. It may be necessary to simply find or grow higher quality quantum dot samples. As an alternative, the resonance of the quantum dots could be actively stabilised using feedback from the intensity of the phonon sideband [117]. Deliberately addressing the optical transitions at a half-detuned point would reduce the phase sensitivity to electric field noise but consequently increase intensity noise. Regardless of the exact solution, this experiment demonstrates that a Bell state with fidelity of $\approx$ 63 % can be achieved with a Type I protocol, for the known amount of electric field noise on this sample ($\approx$ 200 MHz linewidth broadening).

It may however be better to use a two-photon detection scheme where the optical phase is no longer relevant to the entangled state, provided our photon detection efficiency is sufficient. An additional advantage of 'Type II' schemes is that the inherent error in the created state due to a finite two-photon scattering probability is removed.

The challenge in using two-photon schemes is to maintain the entanglement generation rate, and to be able to measure the state generated in an experiment or computation. In regard to the latter, our quantum dots with a single λ-scheme do not permit single shot read-out. Therefore, in a probabilistic entanglement generation scheme we not only have the success probability to consider, but also the single shot probability of measuring both spins, $p^2_{readout} \ll 1$. This factor can be removed by having one spin coupled to a cycling transition. For example, in a vertically stacked, coupled double quantum dot arrangement one of the quantum dots acts to provide an ancillary spin-readout transition. This transition is on resonance with a fixed driving laser dependent upon the spin state of the other quantum dot [213]. It should then be in theory possible to verify every state heralded by a single detected Raman photon, or indeed two photons if a Type II scheme were being used.

In the conclusion to chapter 4 we highlighted that the entangled state generation rate of ≈ 7 kHz is the fastest optically-mediated distribution to date. This is enabled by the use of a single photon detection scheme, bright emitters in the form of our quantum dots, and high efficiency single photon detectors. With an attempt rate of 10.8 MHz, driving at $p = 0.07$, we conclude that the total product of photon collection and detection efficiency, $p_c\eta_d$ is 0.46 %. In a Type II, or two photon detection scheme, the expected generation rate would therefore be reduced to 114 Hz allowing for $p = 1$ in this case. In our experiment, we are able to generate and *verify* spin-spin entangled states at over 8 per minute; in the case of a two photon experiment 114 Hz would be reduced by the factor 0.005^2 to an average of one event every 6.9 minutes.

All is not lost however; by considering the losses between the sample and the detector we find that only 4.1 % of useful Raman-scattered photons are coupled from our sample in to the collection mode. State-of-the-art electrically-tunable micropillar samples could increase this to 52 % [181], raising $p_c\eta_d$ to 5.9 %. Our single photon detection scheme would be therefore able to operate at a minimum rate of ≈ 44 kHz and potentially verify a state created every second, whilst the two-photon schemes would operate at 19 kHz. Placing quantum dots in micropillar cavities not only increases the percentage of photons coupled out but should also reduce the radiative lifetime by Purcell enhancement and permit faster operation of the pulse sequence. In addition, it ensures that a higher percentage of photons are emitted within the T_2^*, again increasing the possible entanglement rate. Pushing the collection efficiency further using photonic trumpets (although no method yet exists for tuning the resonances of a quantum dot within them) it has been suggested that coupling from the quantum dot to the collection optics could be as high as 95 % [212]. At this point, it is our microscope, filtering set-up and detection that become the limiting factor, as the

single-photon scheme would be expected to generate entangled states at 81.2 kHz, and the two-photon scheme at 61.8 kHz. This highlights the crucial crossover in the scheme that is more likely to succeed that occurs once the photon detection probabilty is increased; the low driving probability of Type I schemes becomes a limitation.

It is important to ask what rate is required and whether we are close to reaching it. In a simple picture, in order to create a network of entangled spins it must be possible to generate pairwise entangled states faster than the states can decohere. With electron spins so far this time is perhaps 2 μs if inhomogeneous dephasing is mitigated [17], requiring an absolute minimum rate of 0.5 MHz. The attempt rate could be increased if read-out steps were to be neglected, for example, and spin repumping within $2 \times T_1 \approx$ 750 ps would allow a fastest possible rate of operation $\sim$ 0.65 GHz (although we note this neglects no doubt necessary additional steps to remove the spin dephasing). However, at our current operation rate of 10.8 MHz we would require a success probability of 4.6 %, which in a two-photon scheme means $p_c\eta_d$ is 0.3, and we are approaching the realm of deterministic photon transfer between systems. A more subtle version of such an optical network uses probabilistic connection between 'communication qubits' within nodes, where these qubits then transfer entanglement to more suitable memory qubits with longer decoherence times [214]. The optically-addressed electrons in quantum dots make excellent communication qubits as they are coupled to strong optical dipole transitions, but as yet do not function as memory qubits. In diamond systems local nuclear spins provide such a memory [215], but here the nuclear spin bath is too large. A recent proposal capacitively couples self-assembled quantum dots as communication qubits to an underlying set of gate-defined QD memory qubits [216].

Turning to the fidelity of the state we create it is clear that it is currently rather low, although we know that it can be improved by looking for samples with lower spectral diffusion and seeking to extend the T_2^* of the electron. Architectures that permit a greater than 10 % error on the links generated between nodes have been envisaged [41] although it is a challenge to implement this in extant experimental systems of this kind.

Finally, an alternative is to explore one way quantum computing [28, 217]. Networks of entangled qubits represent a cluster state, and specific measurements of qubits project the cluster into subsets. Single qubit operations are then able to create the required state. Running a series of measurements followed by single qubit operations is equivalent to running a program of the quantum computer. In particular, it has been proposed that quantum dots as a source of photons entangled with electron spins could be used to produce long streams of photons all participating in such cluster states [218], and a possible extension could be to use an entangled pair of electron spins to produce a two-dimensional cluster state.

In conclusion, quantum dots continue to show great promise as a light-matter interface for networked quantum information, and we were able to demonstrate the baby step of a two-electron 'network' where the impact of the solid state environment on the state we

create is understood. Some of the key outstanding questions surrounding such quantum dots are: whether the fundamental material and geometry be improved to obtain longer spin coherence times in combination with spectral consistency; whether many quantum dots can be grown that overlap spectrally or must QD-by-QD tuning always occur; finally, whether quantum dots can be incorporated into devices that improve photon collection efficiency while maintaining a low noise solid state environment. The possibility of using these quantum dots as communication nodes in hybrid quantum networks is also an intriguing possibility.

Bibliography

[1] David P. DiVincenzo. The Physical Implementation of Quantum Computation. *Fortschritte der Physik*, 48(9-11):771–783, 2000.

[2] T. D. Ladd, F. Jelezko, R. Laflamme, Y. Nakamura, C. Monroe, and J. L. O'Brien. Quantum computers. *Nature*, 464(7285):45–53, 2010.

[3] C Monroe. Quantum information processing with atoms and photons. *Nature*, 416(6877):238–246, 2002.

[4] P Neumann, R Kolesov, B Naydenov, J Beck, F Rempp, M Steiner, V Jacques, G Balasubramanian, M L Markham, D J Twitchen, S Pezzagna, J Meijer, J Twamley, F Jelezko, and J Wrachtrup. Quantum register based on coupled electron spins in a room-temperature solid. *Nature Physics*, 6(4):249–253, 2010.

[5] Benjamin Pingault, Jonas N. Becker, Carsten H H Schulte, Carsten Arend, Christian Hepp, Tillmann Godde, Alexander I. Tartakovskii, Matthew Markham, Christoph Becher, and Mete Atat´ure. All-optical formation of coherent dark states of silicon-vacancy spins in diamond. *Physical Review Letters*, 113(26), 2014.

[6] Helena S Knowles, Dhiren M Kara, and Mete Atatüre. Observing bulk diamond spin coherence in high-purity nanodiamonds. *Nature materials*, 13(1):21–5, 2014.

[7] Floris A. Zwanenburg, Andrew S. Dzurak, Andrea Morello, Michelle Y. Simmons, Lloyd C L Hollenberg, Gerhard Klimeck, Sven Rogge, Susan N. Coppersmith, and Mark A. Eriksson. Silicon quantum electronics. *Reviews of Modern Physics*, 85(3):961–1019, 2013.

[8] John Clarke and Frank K. Wilhelm. Superconducting quantum bits. *Nature*, 453(7198):1031–1042, 2008.

[9] Emanuel Knill, Raymond Laflamme, and Gerald J. Milburn. A scheme for efficient quantum computation with linear optics. *Nature*, 409(6816):46–52, 2001.

[10] R. Hanson, L. P. Kouwenhoven, J. R. Petta, S. Tarucha, and L. M K Vandersypen. Spins in few-electron quantum dots. *Reviews of Modern Physics*, 79(4):1217–1265, 2007.

[11] Clemens Matthiesen, Anthony Vamivakas, and Mete Atatüre. Subnatural Linewidth Single Photons from a Quantum Dot. *Physical Review Letters*, 108(9):1–4, 2012.

[12] R. J. Warburton, C. Schäflein, D Haft, F Bickel, A Lorke, K Karrai, J. M. Garcia, W Schoenfeld, and P. M. Petroff. Optical emission from a charge-tunable quantum ring. *Nature*, 405(6789):926–929, 2000.

[13] Anthony Nickolas Vamivakas, Yong Zhao, Chao-Yang Lu, and Mete Atatüre. Spin-resolved quantum-dot resonance fluorescence. *Nature Physics*, 5(3):198–202, 2009.

[14] M. Atature, J. Dreiser, A. Badolato, A. Högele, K. Karrai, and A. Imamolu. Quantum-Dot Spin-State Preparation with Near-Unity Fidelity. *Science*, 312(5773):551–553, 2006.

[15] David Press, Thaddeus D Ladd, Bingyang Zhang, and Yoshihisa Yamamoto. Complete quantum control of a single quantum dot spin using ultrafast optical pulses. *Nature*, 456(7219):218–221, 2008.

[16] D Press, K De Greve, P L McMahon, T D Ladd, B Friess, C Schneider, M Kamp, S Hofling, A Forchel, and Y Yamamoto. Ultrafast optical spin echo in a single quantum dot. *Nature Photonics*, 4(6):367–370, 2010.

[17] R. Stockill, C. Le Gall, C. Matthiesen, L. Huthmacher, E. Clarke, M. Hugues, and M. Atatüre. Quantum dot spin coherence governed by a strained nuclear environment. *Nature Communications*, 7:12745, 2016.

[18] H J Kimble. The quantum internet. *Nature*, 453(7198):1023–1030, 2008.

[19] Kristiaan De Greve, Leo Yu, Peter L McMahon, Jason S Pelc, Chandra M Natarajan, Na Young Kim, Eisuke Abe, Sebastian Maier, Christian Schneider, Martin Kamp, Sven Höfling, Robert H Hadfield, Alfred Forchel, M M Fejer, and Yoshihisa Yamamoto. Quantum-dot spinphoton entanglement via frequency downconversion to telecom wavelength. *Nature*, 491(7424):421–425, 2012.

[20] W B Gao, P Fallahi, E Togan, J Miguel-Sanchez, and A Imamoglu. Observation of entanglement between a quantum dot spin and a single photon. *Nature*, 491(7424):426–430, 2012.

[21] J. R. Schaibley, A. P. Burgers, G. A. McCracken, L.-M. Duan, P. R. Berman, D. G. Steel, A. S. Bracker, D. Gammon, and L. J. Sham. Demonstration of Quantum Entanglement between a Single Electron Spin Confined to an InAs Quantum Dot and a Photon. *Physical Review Letters*, 110(16):167401, 2013.

[22] Alexander Högele, Stefan Seidl, Martin Kroner, Khaled Karrai, Richard J. Warburton, Brian D. Gerardot, and Pierre M. Petroff. Voltage-controlled optics of a quantum dot. *Physical Review Letters*, 93(21):19–22, 2004.

[23] Bernhard Urbaszek, Xavier Marie, Thierry Amand, Olivier Krebs, Paul Voisin, Patrick Maletinsky, Alexander Högele, and Atac Imamoglu. Nuclear spin physics in quantum dots: An optical investigation. *Reviews of Modern Physics*, 85(1):79–133, 2013.

[24] Alexander Bechtold, Dominik Rauch, Fuxiang Li, Tobias Simmet, Per-Lennart Ardelt, Armin Regler, Kai Müller, Nikolai A Sinitsyn, and Jonathan J Finley. Three-stage decoherence dynamics of an electron spin qubit in an optically active quantum dot. *Nature Physics*, 11(12):1005–1008, 2015.

[25] Andreas V. Kuhlmann, Julien Houel, Arne Ludwig, Lukas Greuter, Dirk Reuter, Andreas D. Wieck, Martino Poggio, and Richard J. Warburton. Charge noise and spin noise in a semiconductor quantum device. *Nature Physics*, 9(9):570–575, 2013.

[26] M. J. Stanley, C. Matthiesen, J. Hansom, C. Le Gall, C. H H Schulte, E. Clarke, and M. Atatüre. Dynamics of a mesoscopic nuclear spin ensemble interacting with an optically driven electron spin. *Physical Review B*, 90(19):195305, 2014.

[27] Clemens Matthiesen, Megan J Stanley, Maxime Hugues, Edmund Clarke, and Mete Atatüre. Full counting statistics of quantum dot resonance fluorescence. *Scientific reports*, 4:4911, 2014.

[28] Stephen M. Barnett. *Quantum Information*. Oxford University Press, 2009.

[29] A. Einstein, B. Podolsky, and N. Rosen. Can Quantum-Mechanical Description of Physical Reality Be Considered Complete? *Physical Review*, 47(10):777–780, 1935.

[30] J. S. Bell. On the Einstein Podolsky Rosen Paradox. *Physics*, 1(3):195–200, 1964.

[31] John F. Clauser, Michael A Horne, Abner Shimony, and Richard A Holt. Proposed Experiment to Test Local Hidden-Variable Theories. *Physical Review Letters*, 23(15):880–884, 1969.

[32] Alain Aspect, Jean Dalibard, and Gérard Roger. Experimental test of Bell's inequalities using time- varying analyzers. *Physical Review Letters*, 49(25):1804–1807, 1982.

[33] B. Hensen, H. Bernien, A. E. Dréau, A. Reiserer, N. Kalb, M. S. Blok, J. Ruitenberg, R. F. L. Vermeulen, R. N. Schouten, C. Abellán, W. Amaya, V. Pruneri, M. W. Mitchell, M. Markham, D. J. Twitchen, D. Elkouss, S. Wehner, T. H. Taminiau, and R. Hanson. Loophole-free Bell inequality violation using electron spins separated by 1.3 kilometres. *Nature*, 526(7575):682–686, 2015.

[34] M. Zukowski, A. Zeilinger, M. A. Horne, and A. K. Ekert. "Event-ready-detectors" Bell experiment via entanglement swapping. *Physical Review Letters*, 71(26):4287–4290, 1993.

[35] Anupam Garg and N. D. Mermin. Detector inefficiencies in the Einstein-Podolsky-Rosen experiment. *Physical Review D*, 35(12):3831–3835, 1987.

[36] Richard Jozsa. Entanglement and quantum computation. In *Geometric Issues in the Foundations of Science*, 1997.

[37] Michael A. Nielsen and Isaac L. Chuang. *Quantum computation and quantum information*. Cambridge University Press, 2000.

[38] D. Aharonov. Quantum Computation. In *Annual Reviews of Computational Physics VI*, pages 259–346. 1999.

[39] Peter W Shor. Polynomial-Time Algorithms for Prime Factorization and Discrete Logarithms on a Quantum Computer. *SIAM Journal on Computing*, 26(5):1484–1509, 1997.

[40] Peter W. Shor. Scheme for reducing decoherence in quantum computer memory. *Physical Review A*, 52(4):R2493–R2496, 1995.

[41] Naomi H Nickerson, Ying Li, and Simon C Benjamin. *Nature Communications*, 4:1756, 2013.

[42] W. K. Wootters. Quantum entanglement as a quantifiable resource. *Philosophical Transactions of the Royal Society A: Mathematical, Physical and Engineering Sciences*, 356(1743):1717–1731, 1998.

[43] Nicolas Gisin, Grégoire Ribordy, Wolfgang Tittel, and Hugo Zbinden. Quantum cryptography. *Reviews of Modern Physics*, 74(1):145–195, 2002.

[44] Charles H. Bennett and Gilles Brassard. Quantum cryptography: Public key distribution and coin tossing. In *International Conference on Computers, Systems and Signal Processing*, Bangalore, India, 1984.

[45] Charles H. Bennett, Gilles Brassard, and N. David Mermin. Quantum cryptography without Bell's theorem. *Physical Review Letters*, 68(5):557–559, 1992.

[46] Artur K Ekert. Quantum cryptography based on Bell's theorem. *Physical Review Letters*, 67(6):661–663, 1991.

[47] Thomas Jennewein, Christoph Simon, Gregor Weihs, Harald Weinfurter, and Anton Zeilinger. Quantum cryptography with entangled photons. *Physical review letters*, 84(20):4729–32, 2000.

[48] W Tittel, J Brendel, H Zbinden, and N Gisin. Quantum cryptography using entangled photons in energy-time bell states. *Physical review letters*, 84(20):4737–40, 2000.

[49] D. S. Naik, C. G. Peterson, A. G. White, A. J. Berglund, and P. G. Kwiat. Entangled State Quantum Cryptography: Eavesdropping on the Ekert Protocol. *Physical Review Letters*, 84(20):4733–4736, 2000.

[50] Charles H. Bennett, Gilles Brassard, Claude Crépeau, Richard Jozsa, Asher Peres, and William K. Wootters. Teleporting an unknown quantum state via dual classical and Einstein-Podolsky-Rosen channels. *Physical Review Letters*, 70(13):1895–1899, 1993.

[51] W. K. Wootters and W. H. Zurek. A single quantum cannot be cloned. *Nature*, 299(5886):802–803, 1982.

[52] Vittorio Giovannetti, Seth Lloyd, and Lorenzo Maccone. Quantum-enhanced measurements: beating the standard quantum limit. *Science*, 306(5700):1330–6, 2004.

[53] Jonathan P Dowling. Correlated input-port, matter-wave interferometer: Quantum-noise limits to the atom-laser gyroscope. *Physical Review A*, 57(6):4736–4746, 1998.

[54] M. W. Mitchell, J. S. Lundeen, and A. M. Steinberg. Super-resolving phase measurements with a multiphoton entangled state. *Nature*, 429:161, 2004.

[55] S.F. F Huelga, Chiara Macchiavello, T. Pellizzari, a.K. K Ekert, M.B. B Plenio, and J. I Cirac. Improvement of Frequency Standards with Quantum Entanglement. *Physical Review Letters*, 79(20):3865–3868, 1997.

[56] J. Bollinger, Wayne Itano, D. Wineland, and D. Heinzen. Optimal frequency measurements with maximally correlated states. *Physical Review A*, 54(6):R4649–R4652, 1996.

[57] A.N. Boto, P. Kok, D.S. Abrams, S.L. Braunstein, C.P. Williams, and J.P. Dowling. Quantum interferometric lithography: exploiting entanglement to beat the diffraction limit. *Physical Review Letters*, 85(13):2733–2736, 2000.

[58] J. N. Gannaway and C. J. R. Sheppard. Second-harmonic imaging in the scanning optical microscope. *Optical and Quantum Electronics*, 10(5):435–439, 1978.

[59] Ulrich W. Rathe and Marlan O. Scully. Theoretical basis for a new subnatural spectroscopy via correlation interferometry. *Letters in Mathematical Physics*, 34(3):297–307, 1995.

[60] Alain Aspect, Philippe Grangier, and Gérard Roger. Experimental Tests of Realistic Local Theories via Bell's Theorem. *Physical Review Letters*, 47(7):460–463, 1981.

[61] Z. Y. Ou and L. Mandel. Violation of Bell's Inequality and Classical Probability in a Two-Photon Correlation Experiment. *Physical Review Letters*, 61(1):50–53, 1988.

[62] Adrien Dousse, Jan Suffczyński, Alexios Beveratos, Olivier Krebs, Aristide Lemaître, Isabelle Sagnes, Jacqueline Bloch, Paul Voisin, and Pascale Senellart. Ultrabright source of entangled photon pairs. *Nature*, 466(7303):217–220, 2010.

[63] R M Stevenson, R J Young, P Atkinson, K Cooper, D A Ritchie, and A J Shields. A semiconductor source of triggered entangled photon pairs. *Nature*, 439(7073):179–82, 2006.

[64] P. Pathak and S. Hughes. Generation of entangled photon pairs from a single quantum dot embedded in a planar photonic-crystal cavity. *Physical Review B*, 79(20):1–6, 2009.

[65] Harishankar Jayakumar, Ana Predojević, Thomas Kauten, Tobias Huber, Glenn S Solomon, and Gregor Weihs. Time-bin entangled photons from a quantum dot. *Nature communications*, 5:4251, 2014.

[66] Ying Li, Peter C. Humphreys, Gabriel J. Mendoza, and Simon C. Benjamin. Resource costs for fault-tolerant linear optical quantum computing. *Physical Review X*, 5(4):1–15, 2015.

[67] Rainer Blatt and David Wineland. Entangled states of trapped atomic ions. *Nature*, 453(19):1008–1015, 2008.

[68] J. I. Cirac and P. Zoller. Quantum computations with cold trapped ions. *Physical Review Letters*, 74(20):4091–4094, 1995.

[69] F. Schmidt-Kaler, H. Häffner, S. Gulde, M. Riebe, G. P T Lancaster, T. Deuschle, C. Becher, W. Hänsel, J. Eschner, C. F. Roos, and R. Blatt. How to realize a universal quantum gate with trapped ions. *Applied Physics B: Lasers and Optics*, 77(8):789–796, 2003.

[70] F. Schmidt-Kaler, H. Häffner, M. Riebe, S. Guide, G. P T Lancaster, T. Deuschle, C. Becher, C. Roos, J. Eschner, and R. Blatt. Realisation of the Cirac-Zoller controlled-NOT quantum gate. *2003 European Quantum Electronics Conference, EQEC 2003*, 422:384, 2003.

[71] C. Monroe, D. M. Meekhof, B. E. King, W. M. Itano, and D. J. Wineland. Demonstration of a Fundamental Quantum Logic Gate. *Physical Review Letters*, 75(25):4714–4717, 1995.

[72] L M Vandersypen, Matthias Steffen, Gregory Breyta, Costantino S. Yannoni, Mark H. Sherwood, and Isaac L. Chuang. Experimental realization of Shor's quan-

tum factoring algorithm using nuclear magnetic resonance. *Nature*, 414(6866):883–887, 2001.

[73] Thomas Monz, Daniel Nigg, Esteban A. Martinez, Matthias F. Brandl, Philipp Schindler, Richard Rines, Shannon X. Wang, Isaac L. Chuang, and Rainer Blatt. Realization of a scalable Shor algorithm. *Science*, 351(6277):1068–1070, 2016.

[74] J R Petta. Coherent Manipulation of Coupled Electron Spins in Semiconductor Quantum Dots. *Science*, 309(5744):2180–2184, 2005.

[75] M. D. Shulman, O. E. Dial, S. P. Harvey, H. Bluhm, V. Umansky, and A. Yacoby. Demonstration of Entanglement of Electrostatically Coupled Singlet-Triplet Qubits. *Science*, 336(6078):202–205, 2012.

[76] Austin G. Fowler, Matteo Mariantoni, John M. Martinis, and Andrew N. Cleland. Surface codes: Towards practical large-scale quantum computation. *Physical Review A*, 86(3):032324, 2012.

[77] D Hucul, I V Inlek, G Vittorini, C Crocker, S Debnath, S M Clark, and C Monroe. Modular entanglement of atomic qubits using photons and phonons. *Nature Physics*, 11(1):37–42, 2014.

[78] J. I. Cirac, P. Zoller, H. J. Kimble, and H. Mabuchi. Quantum State Transfer and Entanglement Distribution among Distant Nodes in a Quantum Network. *Physical Review Letters*, 78(16):3221–3224, 1997.

[79] A. D. Boozer, A. Boca, R. Miller, T. E. Northup, and H. J. Kimble. Reversible state transfer between light and a single trapped atom. *Physical Review Letters*, 98(19):1–4, 2007.

[80] Tatjana Wilk, Simon C Webster, Axel Kuhn, and Gerhard Rempe. Single-Atom Single-Photon Quantum Interface. *Science*, 317(5837):488–490, 2007.

[81] Stephan Ritter, Christian Nölleke, Carolin Hahn, Andreas Reiserer, Andreas Neuzner, Manuel Uphoff, Martin Mücke, Eden Figueroa, Joerg Bochmann, and Gerhard Rempe. An elementary quantum network of single atoms in optical cavities. *Nature*, 484(7393):195–200, 2012.

[82] L M Duan, M D Lukin, J I Cirac, and P Zoller. Long-distance quantum communication with atomic ensembles and linear optics. *Nature*, 414(6862):413–418, 2001.

[83] Aymeric Delteil, Zhe Sun, Wei-bo Gao, Emre Togan, Stefan Faelt, and Ataç Imamoğlu. Generation of heralded entanglement between distant hole spins. *Nature Physics*, 12(3):218–223, 2015.

[84] D. Leonard, K. Pond, and P. M. Petroff. Critical layer thickness for self-assembled InAs islands on GaAs. *Physical Review B*, 50(16):11687–11692, 1994.

[85] Richard J Warburton. Single spins in self-assembled quantum dots. *Nature Materials*, 12(6):483–493, 2013.

[86] O. Gywat, H. Krenner, and J Berezovsky. *Spins in optically active quantum dots*. Wiley-VCH, 2010.

[87] D Gammon, Es Snow, Bv Shanabrook, Ds Katzer, and D Park. Fine structure splitting in the optical spectra of single GaAs quantum dots. *Physical review letters*, 76(16):3005–3008, 1996.

[88] M. Bayer, G. Ortner, O. Stern, a. Kuther, a. Gorbunov, a. Forchel, P. Hawrylak, S. Fafard, K. Hinzer, T. Reinecke, S. Walck, J. Reithmaier, F. Klopf, and F. Schäfer. Fine structure of neutral and charged excitons in self-assembled In(Ga)As/(Al)GaAs quantum dots. *Physical Review B*, 65(19):1–23, 2002.

[89] a Högele, B Alèn, F Bickel, R.J Warburton, P.M Petroff, and K Karrai. Exciton fine structure splitting of single InGaAs self-assembled quantum dots. *Physica E: Low-dimensional Systems and Nanostructures*, 21(2-4):175–179, 2004.

[90] M. Müller, S. Bounouar, K. D. Jöns, M. Glässl, and P. Michler. On-demand generation of indistinguishable polarization-entangled photon pairs. *Nature Photonics*, 8(3):224–228, 2014.

[91] R. Ferreira and G. Bastard. Carrier Capture and Intra-Dot Auger Relaxation in Quantum Dots. *physica status solidi (a)*, 178(1):327–330, 2000.

[92] P. W. Fry, J. J. Finley, L. R. Wilson, a. Lemaitre, D. J. Mowbray, M. S. Skolnick, M. Hopkinson, G. Hill, and J. C. Clark. Electric-field-dependent carrier capture and escape in self-assembled InAs/GaAs quantum dots. *Applied Physics Letters*, 77(26):4344, 2000.

[93] M. Ediger. *Photoluminescence from charged excitons in single quantum dots*. PhD thesis, Heriot-Watt University, 2006.

[94] M. Ediger, P. a. Dalgarno, J. M. Smith, B. D. Gerardot, R. J. Warburton, K. Karrai, and P. M. Petroff. Controlled generation of neutral, negatively-charged and positively-charged excitons in the same single quantum dot. *Applied Physics Letters*, 86(21):211909, 2005.

[95] B. Alen, F. Bickel, K. Karrai, R.J. Warburton, and P.M. Petroff. Stark-shift modulation absorption spectroscopy of single quantum dots. *Applied Physics Letters*, 83(11):2235, 2003.

[96] A. J. Bennett, Raj B. Patel, Joanna Skiba-Szymanska, Christine a. Nicoll, Ian Farrer, David a. Ritchie, and Andrew J. Shields. Giant Stark effect in the emission of single semiconductor quantum dots. *Applied Physics Letters*, 97(3):031104, 2010.

[97] C.-Y. Lu, Y. Zhao, a. N. Vamivakas, C. Matthiesen, S. Fält, a. Badolato, and M. Atatüre. Direct measurement of spin dynamics in InAs/GaAs quantum dots using time-resolved resonance fluorescence. *Physical Review B*, 81(3):3–7, 2010.

[98] Aymeric Delteil, Wei-bo Gao, Parisa Fallahi, Javier Miguel-Sanchez, and Atac Imamolu. Observation of Quantum Jumps of a Single Quantum Dot Spin Using Submicrosecond Single-Shot Optical Readout. *Physical Review Letters*, 112(11):116802, 2014.

[99] J. M. Smith, P. a. Dalgarno, R. J. Warburton, a. O. Govorov, K. Karrai, B. D. Gerardot, and P. M. Petroff. Voltage control of the spin dynamics of an exciton in a semiconductor quantum dot. *Physical Review Letters*, 94:1–4, 2005.

[100] Susan M Clark, Kai Mei C Fu, Thaddeus D Ladd, and Yoshihisa Yamamoto. Quantum computers based on electron spins controlled by ultrafast off-resonant single optical pulses. *Physical Review Letters*, 99(4):2–5, 2007.

[101] Alex Greilich, Samuel G. Carter, Danny Kim, Allan S. Bracker, and Daniel Gammon. Optical control of one and two hole spins in interacting quantum dots. *Nature Photonics*, 5:702, 2011.

[102] J Berezovsky, M H Mikkelsen, N G Stoltz, L A Coldren, and D D Awschalom. Picosecond Coherent Optical Manipulation of a Single Electron Spin in a Quantum Dot. *Science*, 320(5874):349–352, 2008.

[103] C Schneider, S Hofling, and A Forchel. Growth of III-V semiconductor quantum dots. In A Tartakovskii, editor, *Quantum Dots: Optics, Electron transport and Future applications*, chapter 1, pages 4–7. Cambridge University Press, 2012.

[104] B. R. Mollow. Power Spectrum of Light Scattered by Two-Level Systems. *Physical Review*, 188(5):1969–1975, 1969.

[105] F Schuda, CR R Stroud, and M Hercher. Observation of the resonant Stark effect at optical frequencies. *Journal of Physics B: Atomic and Molecular Physics*, 7(7):198–202, 1974.

[106] H. J. Kimble, M. Dagenais, and L. Mandel. Photon Antibunching in Resonance Fluorescence. *Physical Review Letters*, 39(11):691–695, 1977.

[107] T. Hoffges, H.W. Baldauf, and J. Lange. Heterodyne measurement of the resonance fluorescence of a single ion. *Journal of Modern Optics*, 44(10):1999–2010, 1997.

[108] Carsten H H Schulte, Jack Hansom, Alex E Jones, Clemens Matthiesen, Claire Le Gall, and Mete Atatüre. Quadrature squeezed photons from a two-level system. *Nature*, 525(7568):222–5, 2015.

[109] H. M. Meyer, R. Stockill, M. Steiner, C. Le Gall, C. Matthiesen, E. Clarke, A. Ludwig, J. Reichel, M. Atatüre, and M. Köhl. Direct photonic coupling of a semiconductor quantum dot and a trapped ion. *Physical Review Letters*, 114(12):1–5, 2015.

[110] Rodney Loudon. *The Quantum Theory of Light*. Oxford Science Publications, 3rd editio edition, 2000.

[111] Pierre Meystre and Murray Sargent. *Elements of Quantum Optics*. Springer-Verlag, 1991.

[112] C. J. Foot. *Atomic Phyics*. Oxford University Press, 2004.

[113] Marlan Scully and M. Zubairy. *Quantum Optics*. Cambridge University Press, 1997.

[114] Alexander V. Khaetskii and Yuli V. Nazarov. Spin-flip transitions between Zeeman sublevels in semiconductor quantum dots. *Physical Review B*, 64(12):125316, 2001.

[115] P Michler, a Kiraz, C Becher, W V Schoenfeld, P M Petroff, L Zhang, E Hu, and a Imamoglu. A quantum dot single-photon turnstile device. *Science*, 290(5500):2282–5, 2000.

[116] Mark Fox. *Quantum Optics: An Introduction*. Oxford University Press, 2006.

[117] Jack Hansom, Carsten H H Schulte, Clemens Matthiesen, Megan J. Stanley, and Mete Atature. Frequency stabilization of the zero-phonon line of a quantum dot via phonon-assisted active feedback. *Applied Physics Letters*, 105(17), 2014.

[118] Andreas V. Kuhlmann, Julien Houel, Daniel Brunner, Arne Ludwig, Dirk Reuter, Andreas D. Wieck, and Richard J. Warburton. A dark-field microscope for background-free detection of resonance fluorescence from single semiconductor quantum dots operating in a set-and-forget mode. *Review of Scientific Instruments*, 84(7):1–17, 2013.

[119] Clemens Matthiesen, Martin Geller, Carsten H H Schulte, Claire Le Gall, Jack Hansom, Zhengyong Li, Maxime Hugues, Edmund Clarke, and Mete Atatüre. Phase-locked indistinguishable photons with synthesized waveforms from a solid-state source. *Nature communications*, 4:1600, 2013.

[120] Yu-Ming He, Yu He, Yu-Jia Wei, Dian Wu, Mete Atatüre, Christian Schneider, Sven Höfling, Martin Kamp, Chao-Yang Lu, and Jian-Wei Pan. On-demand semiconductor single-photon source with near-unity indistinguishability. *Nature Nanotechnology*, 8(3):213–217, 2013.

[121] Charles Santori, David Fattal, Jelena Vucković, Glenn S Solomon, and Yoshihisa Yamamoto. Indistinguishable photons from a single-photon device. *Nature*, 419(6907):594–597, 2002.

[122] Edward B. Flagg, Andreas Muller, Sergey V. Polyakov, Alex Ling, Alan Migdall, and Glenn S. Solomon. Interference of single photons from two separate semiconductor quantum dots. *Physical Review Letters*, 104(13):1–4, 2010.

[123] P. Gold, A. Thoma, S. Maier, S. Reitzenstein, C. Schneider, S. Höfling, and M. Kamp. Two-photon interference from remote quantum dots with inhomogeneously broadened linewidths. *Physical Review B - Condensed Matter and Materials Physics*, 89(3):1–7, 2014.

[124] W.B. Gao, P Fallahi, E Togan, A Delteil, Y.S. Chin, J Miguel-Sanchez, and A Imamoğlu. Quantum teleportation from a propagating photon to a solid-state spin qubit. *Nature Communications*, 4:2744, 2013.

[125] A. V. Kuhlmann, J. H. Prechtel, J. Houel, A. Ludwig, D. Reuter, A. D. Wieck, and R. J. Warburton. Transform-limited single photons from a single quantum dot. *Nature Communications*, 6:8204, 2015.

[126] I A Merkulov and M Rosen. Electron spin relaxation by nuclei in semiconductor quantum dots. *Physical Review B*, 65:1–8, 2002.

[127] Zhe Sun, Aymeric Delteil, Stefan Faelt, and A. Imamoğlu. Measurement of spin coherence using Raman scattering. *Physical Review B*, 93(24):241302, 2016.

[128] Jack Hansom, Carsten H. H. Schulte, Claire Le Gall, Clemens Matthiesen, Edmund Clarke, Maxime Hugues, Jacob M. Taylor, and Mete Atatüre. Environment-assisted quantum control of a solid-state spin via coherent dark states. *Nature Physics*, 10:1–21, 2014.

[129] Jan Fischer, Mircea Trif, W. A. Coish, and Daniel Loss. Spin interactions, relaxation and decoherence in quantum dots. *Solid State Communications*, 149(35-36):1443–1450, 2009.

[130] P. Fallahi, S. T. YIlmaz, and A. Imamolu. Measurement of a heavy-hole hyperfine interaction in ingaas quantum dots using resonance fluorescence. *Physical Review Letters*, 105(25):1–4, 2010.

[131] E. A. Chekhovich, A. B. Krysa, M. S. Skolnick, and A. I. Tartakovskii. Direct measurement of the hole-nuclear spin interaction in single InP/GaInP quantum dots using photoluminescence spectroscopy. *Physical Review Letters*, 106(2):1–4, 2011.

[132] P. Desfonds, B. Eble, F. Fras, C. Testelin, F. Bernardot, M. Chamarro, B. Urbaszek, T. Amand, X. Marie, J. M. rard, V. Thierry-Mieg, A. Miard, and A. Lemàtre. Electron and hole spin cooling efficiency in InAs quantum dots: The role of nuclear field. *Applied Physics Letters*, 96(17), 2010.

[133] D Gammon, A L Efros, T Kennedy, M Rosen, D S Katzer, D Park, S W Brown, V L Korenev, and I A Merkulov. Electron and nuclear spin interactions in the optical spectra of single GaAs quantum dots. *Physical review letters*, 86(22):5176–5179, 2001.

[134] A Abragam. *Principles of Nuclear Magnetism*. Oxford University Press, 1961.

[135] C. Testelin, F. Bernardot, B. Eble, and M. Chamarro. Hole-spin dephasing time associated with hyperfine interaction in quantum dots. *Physical Review B - Condensed Matter and Materials Physics*, 79(19):1–13, 2009.

[136] C. Lai, P. Maletinsky, a. Badolato, and a. Imamoglu. Knight-Field-Enabled Nuclear Spin Polarization in Single Quantum Dots. *Physical Review Letters*, 96(16):167403, 2006.

[137] Alexander V Khaetskii, Daniel Loss, and Leonid Glazman. Electron spin decoherence in quantum dots due to interaction with nuclei. *Physical review letters*, 88(18):186802, 2002.

[138] B. Eble, O. Krebs, A. Lemaître, K. Kowalik, A. Kudelski, P. Voisin, B. Urbaszek, X. Marie, and T. Amand. Dynamic nuclear polarization of a single charge-tunable InAs GaAs quantum dot. *Physical Review B*, 74(8):081306, 2006.

[139] E A Chekhovich, K V Kavokin, J Puebla, A B Krysa, M Hopkinson, A D Andreev, A. M. Sanchez, R. Beanland, M. S. Skolnick, and A. I. Tartakovskii. Structural analysis of strained quantum dots using nuclear magnetic resonance. *Nature Nanotechnology*, 7(10):646–650, 2012.

[140] B. Urbaszek, P. F. Braun, T. Amand, O. Krebs, T. Belhadj, A. Lemaítre, P. Voisin, and X. Marie. Efficient dynamical nuclear polarization in quantum dots: Temperature dependence. *Physical Review B - Condensed Matter and Materials Physics*, 76(20):1–4, 2007.

[141] A. I. Tartakovskii, T. Wright, A. Russell, V. I. Fal'Ko, A. B. Van'Kov, J. Skiba-Szymanska, I. Drouzas, R. S. Kolodka, M. S. Skolnick, P. W. Fry, A. Tahraoui, H. Y. Liu, and M. Hopkinson. Nuclear spin switch in semiconductor quantum dots. *Physical Review Letters*, 98(2):1–4, 2007.

[142] P. Maletinsky, C. W. Lai, A. Badolato, and A. Imamoglu. Nonlinear dynamics of quantum dot nuclear spins. *Physical Review B - Condensed Matter and Materials Physics*, 75(3):1–7, 2007.

[143] P. Maletinsky, a. Badolato, and a. Imamoglu. Dynamics of quantum dot nuclear spin polarization controlled by a single electron. *Physical Review Letters*, 99(5):1–4, 2007.

[144] Christian Latta, Ajit Srivastava, and Atac Imamolu. Hyperfine interaction-dominated dynamics of nuclear spins in self-assembled InGaAs quantum dots. *Physical Review Letters*, 107(16):1–5, 2011.

[145] Ceyhun Bulutay. Quadrupolar spectra of nuclear spins in strained In xGa 1-xAs quantum dots. *Physical Review B - Condensed Matter and Materials Physics*, 85(11):1–12, 2012.

[146] Patrick Maletinsky, Martin Kroner, and Ataç Imamolu. Breakdown of the nuclear-spin-temperature approach in quantum-dot demagnetization experiments. *Nature Physics*, 5(6):407–411, 2009.

[147] N. A. Sinitsyn, Yan Li, S. A. Crooker, A. Saxena, and D. L. Smith. Role of nuclear quadrupole coupling on decoherence and relaxation of central spins in quantum dots. *Physical Review Letters*, 109(16):1–5, 2012.

[148] E. A. Chekhovich, M. Hopkinson, M. S. Skolnick, and A. I. Tartakovskii. Quadrupolar induced suppression of nuclear spin bath fluctuations in self-assembled quantum dots. *Nature Communications*, 6:1–7, 2014.

[149] Marcelo Davanço, C. Stephen Hellberg, Serkan Ates, Antonio Badolato, and Kartik Srinivasan. Multiple time scale blinking in InAs quantum dot single-photon sources. *Physical Review B - Condensed Matter and Materials Physics*, 89(16):1–5, 2014.

[150] A. N. Vamivakas, Y. Zhao, S. Fält, A. Badolato, J. M. Taylor, and M. Atatüre. Nanoscale Optical Electrometer. *Physical Review Letters*, 107(16):166802, 2011.

[151] J. Houel, A. V. Kuhlmann, L. Greuter, F. Xue, M. Poggio, R. J. Warburton, B. D. Gerardot, P. A. Dalgarno, A. Badolato, P. M. Petroff, A. Ludwig, D. Reuter, and A. D. Wieck. Probing single-charge fluctuations at a GaAs/AlAs interface using laser spectroscopy on a nearby InGaAs quantum dot. *Physical Review Letters*, 108(10):1–5, 2012.

[152] Disheng Chen, Gary R. Lander, Kyle S. Krowpman, Glenn S. Solomon, and Edward B. Flagg. Characterization of the local charge environment of a single quantum dot via resonance fluorescence. *Physical Review B - Condensed Matter and Materials Physics*, 93(11):1–9, 2016.

[153] Hai Son Nguyen, Gregory Sallen, Marco Abbarchi, Robson Ferreira, Christophe Voisin, Philippe Roussignol, Guillaume Cassabois, and Carole Diederichs. Photoneutralization and slow capture of carriers in quantum dots probed by resonant exci-

tation spectroscopy. *Physical Review B - Condensed Matter and Materials Physics*, 87(11):1–15, 2013.

[154] R. Warburton, C. Schulhauser, D. Haft, C. Schäflein, K. Karrai, J. Garcia, W. Schoenfeld, and P. Petroff. Giant permanent dipole moments of excitons in semiconductor nanostructures. *Physical Review B*, 65(11):2–5, 2002.

[155] A. Kuther, M. Bayer, A. Forchel, A. Gorbunov, V. B. Timofeev, F. Schäfer, and J. P. Reithmaier. Zeeman splitting of excitons and biexcitons in single InGaAs/GaAs self-assembled quantum dots. *Physical Review B*, 58(12):R7508–R7511, 1998.

[156] Douglas Magde, Elliot Elson, and W. W. Webb. Thermodynamic fluctuations in a reacting system measurement by fluorescence correlation spectroscopy. *Physical Review Letters*, 29(11):705–708, 1972.

[157] Oleg Krichevsky. Fluorescence correlation spectroscopy : the technique. *Reports on Progress in Physics*, 65:251–297, 2002.

[158] Markus Lippitz, Florian Kulzer, and Michel Orrit. Statistical evaluation of single nano-object fluorescence. *ChemPhysChem*, 6(5):770–789, 2005.

[159] Stefan Machlup. Noise in Semiconductors: Spectrum of a Two-Parameter Random Signal. *Journal of Applied Physics*, 25(3):341, 1954.

[160] Alice Berthelot, Ivan Favero, Guillaume Cassabois, Christophe Voisin, Claude Delalande, Philippe Roussignol, Robson Ferreira, and J. M. Gérard. Unconventional motional narrowing in the optical spectrum of a semiconductor quantum dot. *Nature Physics*, 2(11):759–764, 2006.

[161] Marco Abbarchi, Takashi Kuroda, Takaaki Mano, Massimo Gurioli, and Kazuaki Sakoda. Bunched photon statistics of the spectrally diffusive photoluminescence of single self-assembled GaAs quantum dots. *Physical Review B - Condensed Matter and Materials Physics*, 86(11):1–4, 2012.

[162] E A Chekhovich, M N Makhonin, A I Tartakovskii, A Yacoby, H Bluhm, K C Nowack, and L M K Vandersypen. Nuclear spin effects in semiconductor quantum dots. *Nature Materials*, 12(6):494–504, 2013.

[163] Jan Dreiser, Mete Atatüre, Christophe Galland, Tina Müller, Antonio Badolato, and Atac Imamoglu. Optical investigations of quantum dot spin dynamics as a function of external electric and magnetic fields. *Physical Review B - Condensed Matter and Materials Physics*, 77(7):1–15, 2008.

[164] P.-F. Braun, X Marie, L Lombez, B Urbaszek, T Amand, P Renucci, V K Kalevich, K V Kavokin, O Krebs, P. Voisin, and Y. Masumoto. Direct Observation of the

Electron Spin Relaxation Induced by Nuclei in Quantum Dots. *Physical Review Letters*, 94(11):116601, 2005.

[165] R I Dzhioev and V L Korenev. Stabilization of the Electron-Nuclear Spin Orientation in Quantum Dots by the Nuclear Quadrupole Interaction. *Physical Review Letters*, 99(3):037401, 2007.

[166] Changxue Deng and Xuedong Hu. Electron-spin dephasing via hyperfine interaction in a quantum dot: An equation-of-motion calculation of electron-spin correlation functions. *Physical Review B - Condensed Matter and Materials Physics*, 78(24):245301, 2008.

[167] Gunter Wüst, Mathieu Munsch, Franziska Maier, Andreas V. Kuhlmann, Arne Ludwig, Andreas D. Wieck, Daniel Loss, Martino Poggio, and Richard J. Warburton. Role of the electron spin in determining the coherence of the nuclear spins in a quantum dot. *Nature Nanotechnology*, pages 1–6, 2016.

[168] Daniel Brunner, Brian D Gerardot, Paul A Dalgarno, G. Wust, Khaled Karrai, Nick G Stoltz, Pierre M Petroff, and R. J. Warburton. A Coherent Single-Hole Spin in a Semiconductor. *Science*, 325(5936):70–72, 2009.

[169] Jonathan H Prechtel, Andreas V Kuhlmann, Julien Houel, Arne Ludwig, Sascha R Valentin, Andreas D Wieck, and Richard J Warburton. Decoupling a hole spin qubit from the nuclear spins. *Nature Materials*, 15(9):981–986, 2016.

[170] Jonathan H Prechtel, Franziska Maier, Julien Houel, Andreas V Kuhlmann, Arne Ludwig, Andreas D Wieck, Daniel Loss, and Richard J Warburton. Electrically tunable hole g factor of an optically active quantum dot for fast spin rotations. *Physical Review B*, 91(16):165304, 2015.

[171] Kristiaan De Greve, Peter L. McMahon, David Press, Thaddeus D Ladd, Dirk Bisping, Christian Schneider, Martin Kamp, Lukas Worschech, Sven Hoefling, Alfred Forchel, and Yoshihisa Yamamoto. Coherent control and suppressed nuclear feedback of a single quantum dot hole qubit. *Nature Physics*, 7(11):5, 2011.

[172] H. Robinson and B. Goldberg. Light-induced spectral diffusion in single self-assembled quantum dots. *Physical Review B*, 61(8):R5086–R5089, 2000.

[173] C. Kammerer, C. Voisin, G. Cassabois, C. Delalande, Ph. Roussignol, F. Klopf, J. Reithmaier, a. Forchel, and J. Gérard. Line narrowing in single semiconductor quantum dots: Toward the control of environment effects. *Physical Review B*, 66(4):1–4, 2002.

[174] C. Arnold, V. Loo, A. Lemaître, I. Sagnes, O. Krebs, P. Voisin, P. Senellart, and L. Lanco. Cavity-Enhanced Real-Time Monitoring of Single-Charge Jumps at the Microsecond Time Scale. *Physical Review X*, 4(2):021004, 2014.

[175] A. Ulhaq, S. Weiler, S. M. Ulrich, R. Roßbach, M. Jetter, and P. Michler. Cascaded single-photon emission from the Mollow triplet sidebands of a quantum dot. *Nature Photonics*, 6(4):238–242, 2012.

[176] Charles Santori, David Fattal, Jelena Vučković, Glenn S. Solomon, Edo Waks, and Yoshihisa Yamamoto. Submicrosecond correlations in photoluminescence from InAs quantum dots. *Physical Review B*, 69(20):205324, 2004.

[177] Ewa Zbydniewska, Anna Duzynska, Michka Popoff, Djamila Hourlier, Stéphane Lenfant, Jaroslaw Judek, Mariusz Zdrojek, and Thierry Mélin. Charge Blinking Statistics of Semiconductor Nanocrystals Revealed by Carbon Nanotube Single Charge Sensors. *Nano Letters*, 15(10):6349–6356, 2015.

[178] M. Hauck, F. Seilmeier, S. E. Beavan, A. Badolato, P. M. Petroff, and A. Högele. Locating environmental charge impurities with confluent laser spectroscopy of multiple quantum dots. *Physical Review B*, 90(23):235306, 2014.

[179] E. Peter, P. Senellart, D. Martrou, a. Lemaître, J. Hours, J. M. Gérard, and J. Bloch. Exciton-photon strong-coupling regime for a single quantum dot embedded in a microcavity. *Physical Review Letters*, 95:1–4, 2005.

[180] A. Dousse, L. Lanco, J. Suffczyński, E. Semenova, A. Miard, A. Lemaître, I. Sagnes, C. Roblin, J. Bloch, and P. Senellart. Controlled Light-Matter Coupling for a Single Quantum Dot Embedded in a Pillar Microcavity Using Far-Field Optical Lithography. *Physical Review Letters*, 101(26):30–33, 2008.

[181] A K Nowak, S L Portalupi, V Giesz, O Gazzano, C Dal Savio, P-F Braun, K Karrai, C Arnold, L Lanco, I Sagnes, A Lemaître, and P Senellart. Deterministic and electrically tunable bright single-photon source. *Nature Communications*, 5:3240, 2014.

[182] Hui Wang, Z. C. Duan, Y. H. Li, Si Chen, J. P. Li, Y. M. He, M. C. Chen, Yu He, X. Ding, Cheng Zhi Peng, Christian Schneider, Martin Kamp, Sven Höfling, Chao Yang Lu, and Jian Wei Pan. Near-Transform-Limited Single Photons from an Efficient Solid-State Quantum Emitter. *Physical Review Letters*, 116(21):1–6, 2016.

[183] S. Bose, P. L. Knight, M. B. Plenio, and V. Vedral. Proposal for Teleportation of an Atomic State via Cavity Decay. *Physical Review Letters*, 83(24):5158–5161, dec 1999.

[184] L. M. Duan, B. B. Blinov, D. L. Moehring, and C. Monroe. Scalable Trapped Ion Quantum Computation with a Probabilistic Ion-Photon Mapping. *Quantum Information and Computation*, 4(3):165–173, 2004.

[185] C. Cabrillo, J. I. Cirac, P. García-Fernández, and P. Zoller. Creation of entangled states of distant atoms by interference. *Physical Review A*, 59(2):1025–1033, 1999.

[186] L. Slodička, G. Hétet, N. Röck, P. Schindler, M. Hennrich, and R. Blatt. Atom-Atom Entanglement by Single-Photon Detection. *Physical Review Letters*, 110(8):083603, 2013.

[187] Efficient engineering of multiatom entanglement through single-photon detections. *Physical Review Letters*, 90(25 Pt 1):253601, 2003.

[188] D L Moehring, P Maunz, S Olmschenk, K C Younge, D N Matsukevich, L-M Duan, and C Monroe. Entanglement of single-atom quantum bits at a distance. *Nature*, 449(7158):68–71, 2007.

[189] Julian Hofmann, Michael Krug, Norbert Ortegel, L. Gerard, Markus Weber, W. Rosenfeld, and H. Weinfurter. Heralded Entanglement Between Widely Separated Atoms. *Science*, 337(6090):72–75, 2012.

[190] A. Narla, S. Shankar, M. Hatridge, Z. Leghtas, K. M. Sliwa, E. Zalys-Geller, S. O. Mundhada, W. Pfaff, L. Frunzio, R. J. Schoelkopf, and M. H. Devoret. Robust Concurrent Remote Entanglement Between Two Superconducting Qubits. *Physical Review X*, 6(3):031036, 2016.

[191] Sean D. Barrett and Pieter Kok. Efficient high-fidelity quantum computation using matter qubits and linear optics. *Physical Review A*, 71(6):060310, 2005.

[192] Hannes Bernien, Bas Hensen, Wolfgang Pfaff, Gerwin Koolstra, Machiel S Blok, Lucio Robledo, T. H. Taminiau, Matthew Markham, Daniel J Twitchen, Lilian Childress, and Ronald Hanson. Heralded entanglement between solid-state qubits separated by three metres. *Nature*, 497(7447):86–90, 2013.

[193] Wolfgang Pfaff, B. J. Hensen, Hannes Bernien, Suzanne B. van Dam, Machiel S Blok, Tim H Taminiau, Marijn J Tiggelman, Raymond N Schouten, Matthew Markham, Daniel J Twitchen, and Ronald Hanson. Unconditional quantum teleportation between distant solid-state quantum bits. *Science*, 345(6196):532–535, 2014.

[194] Lucio Robledo, Lilian Childress, Hannes Bernien, Bas Hensen, Paul F. A. Alkemade, and Ronald Hanson. High-fidelity projective read-out of a solid-state spin quantum register. *Nature*, 477(7366):574–578, 2011.

[195] Nicolas Sangouard, Christoph Simon, Hugues de Riedmatten, and Nicolas Gisin. Quantum repeaters based on atomic ensembles and linear optics. *Reviews of Modern Physics*, 83(1):33–80, 2011.

[196] Christopher C. Gerry and P. L. Knight. *Introductory quantum optics*. Cambridge University Press, first edition, 2005.

[197] G. Vittorini, D. Hucul, I. V. Inlek, C. Crocker, and C. Monroe. Entanglement of distinguishable quantum memories. *Physical Review A - Atomic, Molecular, and Optical Physics*, 90(4):1–5, 2014.

[198] A. M. Dyckovsky and S. Olmschenk. Analysis of photon-mediated entanglement between distinguishable matter qubits. *Physical Review A - Atomic, Molecular, and Optical Physics*, 85(5):17–19, 2012.

[199] Norman F. Ramsey. A molecular beam resonance method with separated oscillating fields. *Physical Review*, 78(6):695–699, 1950.

[200] Thaddeus D. Ladd, David Press, Kristiaan De Greve, Peter L. McMahon, Benedikt Friess, Christian Schneider, Martin Kamp, Sven Höfling, Alfred Forchel, and Yoshihisa Yamamoto. Pulsed Nuclear Pumping and Spin Diffusion in a Single Charged Quantum Dot. *Physical Review Letters*, 105(10):107401, 2010.

[201] C. K. Hong, Z. Y. Ou, and L. Mandel. Measurement of subpicosecond time intervals between two photons by interference. *Physical Review Letters*, 59(18):2044–2046, 1987.

[202] J. Mizrahi, B. Neyenhuis, K. G. Johnson, W. C. Campbell, C. Senko, D. Hayes, and C. Monroe. Quantum control of qubits and atomic motion using ultrafast laser pulses. *Applied Physics B*, 114(1-2):45–61, 2014.

[203] Malcolm H. Levitt. Composite Pulses. In *Encyclopedia of Magnetic Resonance*. John Wiley & Sons, Ltd, Chichester, UK, 2007.

[204] Xiaodong Xu, Wang Yao, Bo Sun, Duncan G Steel, Allan S Bracker, Daniel Gammon, and L J Sham. Optically controlled locking of the nuclear field via coherent dark-state spectroscopy. *Nature*, 459(7250):1105–1109, 2009.

[205] R. Stierlin, R. Bättig, P. D. Henchoz, and H. P. Weber. Excess-noise suppression in a fibre-optic balanced heterodyne detection system. *Optical and Quantum Electronics*, 18(6):445–454, 1986.

[206] Karthick Sathiamoorthy and Tanjim Ahmed. *Construction and Validation of a White Light Interferometer*. PhD thesis, Halmstad University, 2010.

[207] Khaled Karrai and Richard J. Warburton. Optical transmission and reflection spectroscopy of single quantum dots. *Superlattices and Microstructures*, 33(5-6):311–337, 2003.

[208] C Latta, A Högele, Y Zhao, A N Vamivakas, P Maletinsky, M Kroner, J Dreiser, I Carusotto, A Badolato, D Schuh, W Wegscheider, M Atature, and A Imamoglu. Confluence of resonant laser excitation and bidirectional quantum-dot nuclear-spin polarization. *Nature Physics*, 5(10):758–763, 2009.

[209] C. Bentham, I. E. Itskevich, R. J. Coles, B. Royall, E. Clarke, J. O'Hara, N. Prtljaga, A. M. Fox, M. S. Skolnick, and L. R. Wilson. On-chip electrically controlled routing of photons from a single quantum dot. *Applied Physics Letters*, 106(22):0–5, 2015.

[210] N. Prtljaga, C. Bentham, J. O'Hara, B. Royall, E. Clarke, L. R. Wilson, M. S. Skolnick, and A. M. Fox. On-chip interference of single photons from an embedded quantum dot and an external laser. *Applied Physics Letters*, 108(25), 2016.

[211] M Arcari, I Söllner, A Javadi, S Lindskov Hansen, S Mahmoodian, J Liu, H Thyrrestrup, E H Lee, J D Song, S Stobbe, and P Lodahl. Near-Unity Coupling Efficiency of a Quantum Emitter to a Photonic Crystal Waveguide. *Physical Review Letters*, 113:093603, 2014.

[212] P. Stepanov, Adrien Delga, Niels Gregersen, Emanuel Peinke, Mathieu Munsch, Jean Teissier, Jesper Mørk, Maxime Richard, Joël Bleuse, Jean Michel Gérard, and Julien Claudon. Highly directive and Gaussian far-field emission from "giant" photonic trumpets. *Applied Physics Letters*, 107(14):13–17, 2015.

[213] A. N. Vamivakas, C.-Y. Lu, C. Matthiesen, Y. Zhao, S. Fält, Antonio Badolato, and Mete Atatüre. Observation of spin-dependent quantum jumps via quantum dot resonance fluorescence. *Nature*, 467(7313):297–300, 2010.

[214] C. Monroe, R. Raussendorf, A. Ruthven, K. R. Brown, P. Maunz, L.-M. Duan, and J. Kim. Large-scale modular quantum-computer architecture with atomic memory and photonic interconnects. *Physical Review A*, 89(2):022317, 2014.

[215] A. Reiserer, N. Kalb, Machiel S. Blok, Koen J. M. van Bemmelen, Tim H. Taminiau, Ronald Hanson, Daniel J. Twitchen, and Matthew Markham. Robust Quantum-Network Memory Using Decoherence-Protected Subspaces of Nuclear Spins. *Physical Review X*, 6(2):021040, 2016.

[216] D. Kim, A. A. Kiselev, R. S. Ross, M. T. Rakher, C. Jones, and T. D. Ladd. Optically Loaded Semiconductor Quantum Memory Register. *Physical Review Applied*, 5(2):024014, 2016.

[217] Robert Raussendorf and Hans J. Briegel. A One-Way Quantum Computer. *Physical Review Letters*, 86(22):5188–5191, 2001.

[218] Netanel H. Lindner and Terry Rudolph. Proposal for Pulsed On-Demand Sources of Photonic Cluster State Strings. *Physical Review Letters*, 103(11):113602, 2009.